The failure of graphite arc-furnace electrodes

Kenneth George Middleton

THE FAILURE OF GRAPHITE ARC-FURNACE ELECTRODES

by

KENNETH GEORGE MIDDLETON B.Sc.

Department of Engineering
University of Durham

A thesis submitted for the degree of
Doctor of Philosophy of the University of Durham

APRIL 1985

Dedicated to my wife Ellen
and to my parents

ABSTRACT

Graphite electrodes used in steelmaking are joined together by threaded, tapered connectors (nipples) of similar material. The jointed regions are subjected to arduous thermal and mechanical stresses during use. Mechanical stresses arise from electrode self-weight and tightening torque, and the thermal stresses from the high furnace operating temperatures which ensure a high radiative surface cooling rate as the electrode is removed from the furnace. This thermal shock effect is thought to contribute to particular types of electrode failure.

In this computer-aided analysis of the stresses induced by the above effects, a commercial finite element program is used in conjunction with a purpose-written finite difference program. Mechanical loads due to electrode self-weight and pretightening torque are evaluated and applied with suitable restraints to an axisymmetric finite element mesh, to obtain a mechanical stress analysis. The finite difference program is then used to calculate the time-variant temperature field experienced by an electrode on being removed from the furnace. An interpolation program is used to assign temperatures at the nodes of the same finite element mesh, the thermal stresses then being evaluated by the commercial finite element program.

A 'failure envelope' analysis of the results identifies the critically-stressed regions of the joint and shows that in some such areas the thermal-shock stresses act to relieve the mechanically-induced stresses. A statistical analysis based on Weibull theory predicts a high incidence of crack formation due to thermal stresses.

Finally, consideration is given to the effect of thermal orthotropy and temperature-dependent material properties.

ACKNOWLEDGEMENTS

The work described in this thesis was financed jointly by the S.E.R.C. and by the British Steel Corporation Research Laboratories in Rotherham, and I wish to express my thanks to both of these bodies.

On a more personal level, I am extremely grateful to Prof. P.M. Braiden, of the Department of Mechanical Engineering, University of Newcastle, for the initial setting up of the project, and for his help and enthusiasm throughout; also to John Kirk, Geoff Payne, John Lakin, Bob Montgomery and Tony Nicholson, all of B.S.C., for their helpful comments and information.

Thanks are due to all members of the staff of the Computer Unit for their help in the fine adjustment of my computer programs, and to Christine Wright of the Engineering Department for help with printing.

Lastly I would like to thank my wife, Ellen, for much of the typing of the thesis on the word-processor, and for her unfailing encouragement and understanding throughout the project.

CONTENTS

LIST OF ILLUSTRATIONS

LIST OF TABLES

NOTATION (secondary usage in brackets)

c	Specific heat capacity (semi crack length) .
d	Diameter of electrode section.
D	Diffusivity.
D_r	Radial diffusivity.
D_z	Axial diffusivity.
E	Young's modulus.
F_j	j-th rank value.
h	Convevtion coefficient.
H	Heaviside unit operator.
j	Rank Number.
k	Thermal conductivity.
k_r	Radial thermal conductivity.
k_z	Axial thermal conductivity.
k_θ	Cicumferential thermal conductivity.
K	Stress intensity factor.
l	length of electrode section.
m	Weibull modulus.
n	Number of Observations.
N	Number of ELements in Structure.
p	Thread pitch.
P	Interelectrode force.
P_f	Probability of failure.
r	Radial coord (distance from crack tip).
R	Electrode radius.
S	Stephan's constant of radiation (probabili ty of Survival).

t	Time.
T	Electrode tightening torque.
v	Unit volume.
V	Volume of body.
W	Work.
z	Axial coordinate.
α	Expansion coefficient (reflectivity, ratio of compressive to tensile strength)
β	Angle of maximum principal stress to global x-axis.
γ	Surface Energy per Unit Area.
Δr	Finite difference radial increment.
Δz	Finite difference axial increment.
Δt	Finite difference time increment.
$\Delta\phi$	Increment of torque rotation.
Δx	Infinitesimal compression of electrode end .
ΔW	Work done in achieving Δx.
ε	Emissivity (strain).
θ_A	Ambient temperature.
$\theta_{r,z,t}$	Temperature at time t at point r,z.
ρ	Density.
σ	Electrical conductivity.
σ_1	Maximum (most positive) principal stress.
σ_2	Minimum (most negative) principal stress.
σ_3	Hoop stress.
σ_f	Failure stress.
σ_{fv}	Mean unit volume uniaxial tensile strength .

σ_{nom}	Nominal stress.
σ_{max}	Individual breaking stress.
$\sum$	Stress volume integral.
τ_{max}	Maximum shear stress.
μ	Friction Coefficient.
Y	Poisson's Ratio.

CHAPTER 1

INTRODUCTION

1.1 The Electrode Column

The graphite electrodes which are the subject of this investigation are used in arc-furnaces for the production of special steels. A simplified diagram of such an arc-furnace is shown in Fig. 1.1, the general construction being similar for all furnace sizes. A large vessel, lined with refractory bricks, is supported on a horizontal platform which may be tilted hydraulically through about 30°. The vessel is provided with a door, and a tapping spout through which the molten steel is poured off into ingots. A refractory-lined lid covers the furnace, and this can be swung aside to allow recharging with steel scrap from the top. Three holes are provided in the lid for the insertion of graphite electrodes, which are arranged in triad formation as shown in Fig. 1.2 and connected one to each phase of a three-phase supply. The electrodes are supported by a water-cooled clamping system whose height may be varied under computer control. When required, the clamping system may be raised to remove all three electrodes to allow the furnace lid to be removed, or a single electrode may be removed for replacement using a gantry crane fitted with a special lifting device. In either case, the electrode will be red-white hot, producing considerable thermal shock.

The electric current passing through a single electrode may be up to 70 kA, and the furnace itself may produce up to 130 tonnes of steel in one melt.

Graphite electrodes are made in a variety of sizes. The largest in general use are 600mm in diameter, and approximately 2.5m in length. In use, up to three electrode sections are joined together by means of threaded, tapered connectors (nipples) between adjacent sections. Details of this arrangement are shown in Fig. 1.3. As the electrode erodes from the bottom, it is dropped further into the furnace, until new material needs to be added in the form of a new nipple and section, suitably pretightened. The dimensions of the nipple jointing system for a 600mm electrode are given in Fig. 1.4, and a detail of the thread profile for both electrode and nipple is given in Fig. 1.5. This is an asymmetric form in which the load-bearing face is smaller in area than the flank face, the angle between the two being 60°. The difference in size of the faces arises from the fact that the thread is cut on a 1:6 taper. The geometry of the thread form is such that the teeth do not come to a point, but are slightly flattened, and the thread roots are radiused to reduce stress concentrations. The pitch of the screw thread is 1/4".

The socket machined into the end of the electrode is deeper than half the height of the nipple. Thus, provided the nipple is equally divided between the two

electrode sections, there will be a gap between the end of the nipple and the bottom of the electrode socket. This gap is intended to accommodate differential expansion between the nipple and electrode.

The faced end of the electrode is counterbored to approximately 0.075" greater than the thread form major diameter, which means that the thread does not start at the electrode end surface, but becomes fully developed over one complete revolution, to give a total number of 27-28 complete helixes (on 600mm electrodes). A detailed examination of the geometry of the thread form reveals that approximately one complete helix may be disengaged at the base of both electrode sockets.

A fillet radius of 5/16" is left between the socket base and the beginning of the thread form. This is provided for the reduction of stress concentration effects at the base of the electrode socket.

The joint between two 600mm electrodes is given a tightening preload of 1500 lb-ft (2030 N-m) using a strap wrench. In some cases, plugs of pitch are inserted into radial holes in the nipple. When the electrode reaches operating temperature, the molten pitch helps to cement the joint together.

1.2 Manufacture of Graphite Electrodes

Electrodes are made in two grades for the steel industry. The 'regular' grade is usually used in relatively low-power applications, and the 'premium' grade is intended

for the modern ultra-high-power furnaces. This improved grade offers certain advantages in terms of strength and current-carrying capacity.

Fig. 1.6 is a the flow diagram representing the manufacture of graphite electrodes (Ince, 1979). Petroleum coke and coal-tar pitch are the raw materials; for the largest electrodes the coke used has a layered structure and is referred to as 'needle coke'. The coke is first crushed to give particles of a carefully selected size, and mixed with the coal tar pitch at 160°C. The homogeneity of this mixture is important for the production of uniform material properties in the final graphite. The mixture is then allowed to cool to 120°C (when the viscosity increases to a value suitable for forming), and extruded to the desired shape (introducing orthotropy into the material properties). The pitch binder is converted into a permanent cement by slowly baking the extruded blocks for 6-10 days at 800°C. The next stage depends on the type of electrode being produced. If regular grade electrodes are required the material is heated to about 2800°C in an electric furnace where the charge itself is the resistor. This takes about 4-6 days, followed by a much longer cooling period of several weeks. The rate of cooling is controlled by removing just the right amount of insulating material from around the furnace. This cooling process is known as 'graphitisation' and is characterised by the growth of graphite crystals, and the appearance of the final graphite

properties such as softness and electrical conductivity. If premium grade electrodes are required the electrode is first impregnated with pitch. This involves raising the electrode to high temperature in a chamber containing molten pitch. The chamber is maintained at high pressure for several days, forcing the pitch into the pores of the graphite. The electrode is then rebaked and graphitised as before, increasing the bend strength from 5.9 to 8.6 MPa (Ince, 1979). An increase in current-carrying capacity is also effected by this process. The electrodes are now core-sampled for quality control (the sample usually being taken from the base of the socket) and then passed to the machine shop to be lathe-turned to ensure roundness, and to have the threads cut to accept the nipple.

The manufacturing methods thus have a considerable effect on the material properties. In particular, the following should be noted:

(i) Initial particle size.

An inappropriate or inhomogeneous initial particle size will leave voids in the final material. The particle size chosen will affect the final crystal size, so this must be carefully monitored.

(ii)Graphitisation.

The degree of completion of the graphitisation process will influence the homogeneity of the final material. Incomplete graphitisation leaves pockets of unconverted coke.

(iii) Forming Method.

Normally, graphite electrodes are extruded, providing a degree of anisotropy in the final material properties. (see Table 2.1)

1.3 Electrode Usage

When the three electrode sections have been joined together, and all three columns lifted into the clamping system, the lid of the furnace is drawn back and the furnace charged with scrap iron from a basket carried by a gantry crane. At this point the furnace is cold. The lid of the furnace is replaced, and the electrode columns are lowered through holes in the top. The arc is struck, and begins to bore down through the steel, the distance of the tip of the electrode from the steel bath being computer controlled to maintain the arc. Heat is transmitted to the steel and to the tip of the electrode from the arc which moves in a random way over the tip of the electrode. The electrode also heats up due to the passage of the electric current which can be up to 70kA. After some time, the temperature of the steel reaches about 1600°C, when the electrode is now receiving heat both from the steel melt and from the furnace wall. The tip of the electrode is at 2500 - 3000°C, and the steel is completely molten. A metallurgical analysis of the steel is performed at this stage. This is a spectroscopic analysis which is computer-controlled and takes place automatically when a sample of the steel is removed on a small test-probe inserted through

the door. When the composition is satisfactory the electrodes are withdrawn, white hot, to allow the furnace to be tilted to draw off the steel melt, and more scrap iron to be added from the top. After the furnace is recharged the electrodes are reinserted, having cooled considerably, and the process is continued. The electrodes are also removed periodically during melt-down for the purpose of topping up the furnace. The steelmaking process is thus a semi-continuous one in which production is stopped only to tap off a steel batch or to replace electrode sections. Warm-up from a completely cold furnace therefore occurs relatively infrequently. Normally, the electrode will be reheated from a relatively low temperature attained while the furnace is being recharged or a new section is being added.

As the electode is eroded from the tip, it is allowed to fall gradually through the clamping system until eventually the column must be removed for the addition of a replacement section at the top. When this situation arises, the electrode is removed directly from the furnace by a gantry crane (using a special lifting attachment which screws into the electrode end) and secured vertically against a scaffold from which the replacement operation is carried out. The procedure is described below.

The threads in the top of the last electrode section are cleared of dust by means of compressed air. A new nipple is screwed in until hand tight and is then backed off approximately one turn. The new electrode section is offered by means of the gantry crane and spun down the exposed nipple until hand tight. A strap wrench is then used to apply the final tightening torque, and the electrode is replaced in the clamping system. The magnitude of this final tightening torque represents a trade-off between the electrical requirement of a good joint between mating surfaces and the mechanical requirement of keeping the stresses as low as possible. For a 600mm electrode 1500lb-ft (2030 N-m) is the torque recommended by the manufacturers as a reasonable compromise.

The above discussion shows that the electrode is subjected to considerable stresses, both thermal and mechanical, in the course of its use. The tightening torque and self-weight load of the electrode impose mechanical stresses on the electrode and nipple. In addition to these mechanical stresses, however, thermal stresses are induced as the electrode heats up from cold (this is a relatively slow process and occurs only infrequently) and while in the furnace. More importantly, when the assembly is removed from the furnace for recharging or replacement the white-hot surface of the electrode cools extremely rapidly and contracts onto the still-hot inner layers, setting up large tensile hoop stresses. Two distinct, but simultaneous

problems therefore exist - a mechanical stress field and a thermal shock stress field.

1.4 The Breakage Problem, and Associated Costs.

In addition to the gradual erosion of electrodes due to oxidation and the action of the arc, sudden loss of electrode material occasionally takes place in the form of breakage. This is of considerable importance to the steel industry, and many attempts have been made to suggest shop practices for the reduction of breakage rate. Whether or not these practices are adhered to is a matter of question but it is interesting to note some of the things which may aggravate the problem, and to examine some of the more common-sense measures which can be taken to counter the adverse conditions in a steelmaking plant.

(i) If the nipple is unevenly distributed between the two adjacent electrode sections, an unequal stress distribution in the two electrode sections may result. It is believed in the industry that this may contribute directly to the failure of an electrode, by causing an increase both in the mechanical stresses due to tightening, and in the thermal stresses induced in the collar by cooling.

(ii) A new electrode section is lifted into position by a gantry crane fitted with a special threaded lifting tool. This lifts the

electrode section from one end, the other end being free to trail across the shop floor. If 'skids' are not used, considerable damage may be sustained by the electrode end. Even worse, the nipple threads may be damaged if it has been fitted into the new electrode end rather than the old one, which is sometimes the case.

(iii) Insufficient or excessive tightening torque applied to the joint can reduce the mating area between two electrode sections, causing the bulk of the arc current to be carried by the nipple, with consequent risk of overheating and subsequent failure.

(iv) A spacer is available to fit temporarily between the mating surfaces of two electrodes when the new section is lowered by the gantry crane. If this is not used, thread damage may occur on both the nipple and the electrode, again increasing the risk of failure

(v) The risk of large pieces of scrap metal colliding with the electrode tip is reduced if they are loaded low down in the furnace.

(vi) Small particles of grit or other foreign matter on the mating surfaces of the electrodes may cause separation of the surfaces and electrical overloads on the

parts of the surface left in contact. Additionally, if the foreign matter is large enough, excessive bending stresses may be imposed on the nipple.

Despite these precautions, electrodes sometimes fail catastrophically, the remains usually falling into the steel melt, forcing the furnace to be shut down.

Electrodes are an expensive bought-in item for the industry. In 1975, the cost of electrodes to the British Steel Corporation was between £10m and £12m, corresponding to the production of 3.5Mt of steel (Nicholson, 1976). Electrode material thus costs approximately £4 per tonne of steel produced. This represents a rate of roughly 5.5kg of electrode material per tonne of hot metal. A reduction in electrode loss of 0.1kg/tonne (about 2%) thus represents an annual saving to the industry of £200,000 per annum. Electrode breakages account for about 10% of total electrode usage. It is unlikely, however, that fracture of the electrodes can ever be completely eliminated, and a projected saving of 4% would be more reasonable, representing a saving of £400,000 p.a. to the industry. The financing of a project to examine the problem is thus worthwhile on the basis of material cost alone. If the additional cost of furnace down-time is also considered, it becomes clear that a solution to the problem would prove a sizeable saving to the industry.

1.5 Approaching the Problem

From the foregoing discussion, it is readily appreciated that the fracture of graphite electrodes is an exceedingly complex problem. Electrodes are made in a multitude of sizes, and for each size the furnace operating conditions are different, so it becomes impossible to achieve a comprehensive analysis of all the possible stress fields. The scope of the investigation was therefore limited as follows:

(i) Only 600mm electrodes were considered, since these are the largest and therefore the most expensive of the electrodes in use.

(ii) Only that part of the work-cycle when the electrode is removed from the furnace was considered. This is likely to represent the worst case because of the frequency of the operation and also the rapid cooling involved. It is also the area which has received least attention.

(iii) Detailed analysis was concentrated on the bottom joint, since this is thought to be the most critical joint for thermal failure.

Several approaches to the problem are possible and these may be divided into three broad groups; analytical, numerical, and experimental. The choice between these approaches must be made with due regard both to the individual suitability of each method in terms of the

modelling requirements mentioned above, and their respective financial constraints.

1.5.1 Analytical Techniques.

Timoshenko et al (1951) derived the equations for the stress components in a uniform cylinder subjected to a radial temperature gradient. These equations were modified by Sato et al. (1974) to include axial temperature gradient effects on a hollow electrode. Given an initial temperature field it is therefore possible to evaluate steady-state thermal stresses analytically for a uniform hollow cylinder subjected to radial and axial temperature gradients, which would be an idealistation of the present problem. Even with these simplifying assumptions, however, the mathematics is extremely complicated. Additionally, the task of predicting analytically the complete temperature field at any given time still remains, if the thermal shock stresses are to be calculated. Analytical techniques are therefore not yet sufficiently developed to cope with this problem.

Evaluation of the mechanical stresses by analytical techniques is more difficult. The main mechanical stresses arise from the pretightening torque and electrode self-weight. The forces due to pretightening torque are applied along the thread pitch line, a region of highly complex geometry which could be assumed to be a straight line (neglecting the details of the thread teeth).

This, however, would also involve the conceptual removal of the nipple from the structure, so the interaction of the nipple and electrode could not be considered. Even with these simplifications, the calculation of a stress function to satisfy the boundary and loading conditions imposed by a simplified socket geometry would be practically impossible, and the task of combining the mechanical stresses with the thermal stresses to give a complete stress field would still remain.

An analytical approach to the problem was therefore rejected on the basis that too many simplifying assumptions were required.

1.5.2 Experimental Techniques.

Photoelastic stress analysis is a very powerful full-field stress analysis technique, and would be an ideal check on any results obtained by other methods. For this problem, its main disadvantage is that it is difficult to analyse thermal stresses directly using the technique. Nevertheless, a photoelastic analysis was attempted, as a check on the Finite Element results for mechanical stresses. A full three-dimensional model of an electrode joint was originally envisaged. This was to be stressed mechanically to simulate the dead weight and tightening-torque effects, and the resulting stresses would then be 'frozen in' by a suitable annealing cycle. Sharples Photomechanics Ltd., of Preston, estimated £2500 for the

construction of a model of an electrode joint and the cutting of a diametral slice for analysis - this was not financially viable. A two-dimensional photoelastic analysis was however attempted, and this is fully described in Appendix VI.

Another experimental technique considered was the use of brittle lacquers. This involves spraying the component, or a model of it, with a special material which cracks at a fairly well-defined value of strain. The component is then loaded up to its working stress and the cracking pattern is observed, allowing the strains, and thus the stresses, to be calculated. Again, however, this is a two-dimensional technique and would involve the sectioning of an electrode, altering the stress state to plane stress.

The possibility of using strain gauges on the surface of an electrode was also considered. The main difficulty with this approach is the problem of simulating the dead weight of two electrode sections on the bottom of the joint. Since the weight of a section is in excess of 1 ton, extremely heavy testing machinery would be required, and this was not available. Construction of a scaled-down model would have involved the same machining difficulties as the production of the photoelastic model in three dimensions.

1.5.3 Numerical Techniques

The analytical and experimental stress analysis techniques discussed so far require fundamental oversimplifications regarding loading conditions and/or geometry. Furthermore, thermal shock stresses are not readily handled by either approach.

A numerical analysis offers the capability of calculating both mechanical and thermal-shock stresses, and of readily combining these to produce a full three-dimensional mechanical/thermal-shock stress analysis. Powerful computing facilities exist at Durham, which is on-line to an IBM370 computer at Newcastle University. The system is well-supported by software packages such as the Program for Automatic Finite Element Calculations (PAFEC), and by subroutine libraries such as the Numerical Analysis Group (NAG). Access to other computing installations (e.g. Rutherford) is also possible at greater cost.

Because of the inability of the analytical and experimental approaches to adequately model the problem, a finite element analysis was chosen. The PAFEC suite of programs, which was still in its development stages at the beginning of the project, was used for the stress analysis. As explained in Chapter IV, a finite difference computer program was written to supplement the thermal stress capabilities of PAFEC, which were inadequate to deal with the problem directly. The development of PAFEC by the suppliers during the course of the project imposed some

limitations on the accuracy of the modelling assumptions available, and these are described in detail in the appropriate chapters.

1.6 SUMMARY

The problem of electrode fracture is of considerable importance to the steel industry.

The root causes of such fracture lie in the mechanical and thermal stresses induced during the work-cycle of the electrode. In particular, thermal shock stresses, arising when the electrode is removed from the furnace, are thought by the industry to be highly significant.

Of the various approaches open for the analysis of such stresses, a numerical technique was chosen, despite the limitations which this imposed.

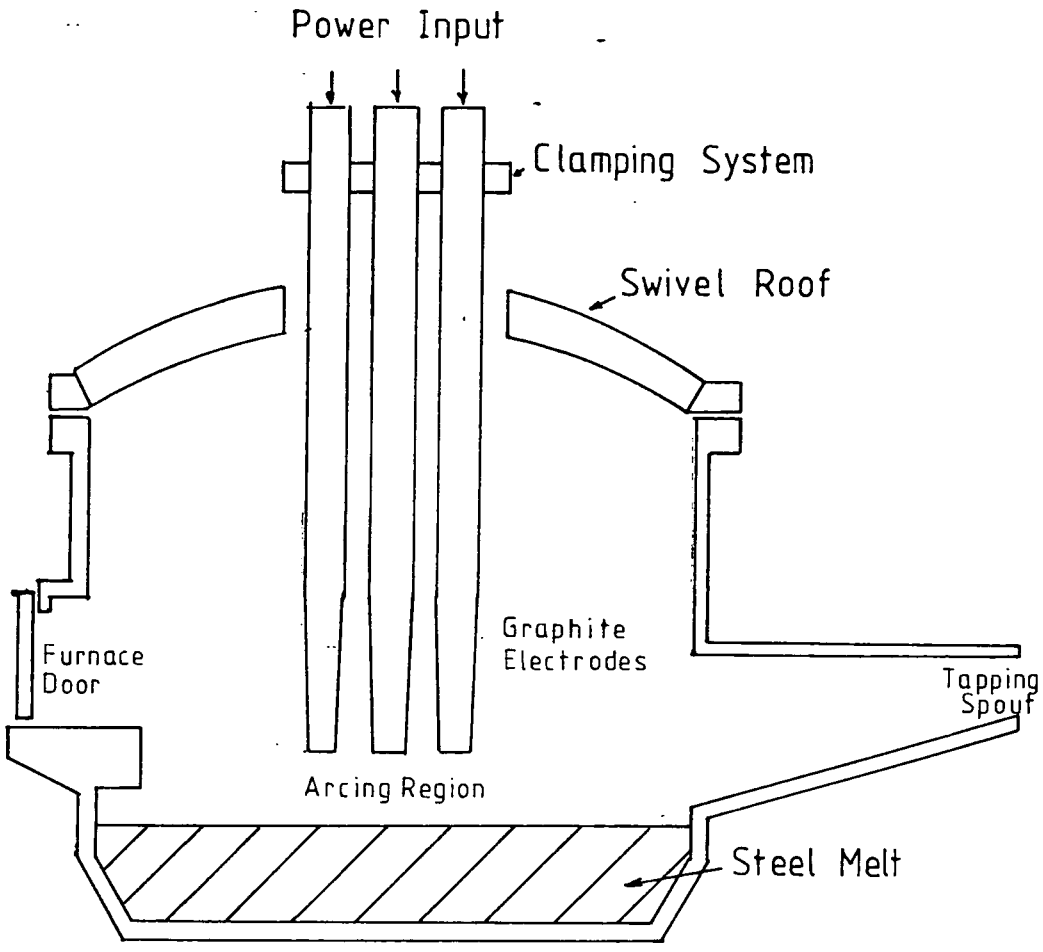

Fig 1.1 Electric-Arc Steel Furnace (Diagrammatic)

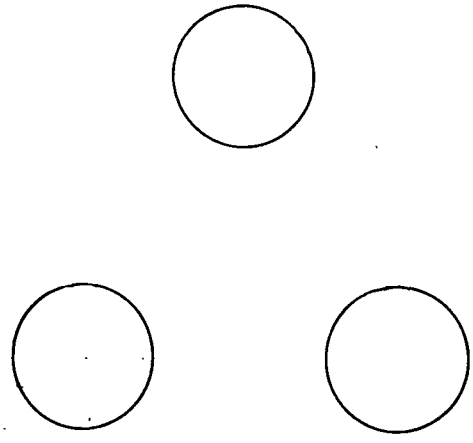

Fig 1.2 Plan View of Electrode Arrangement

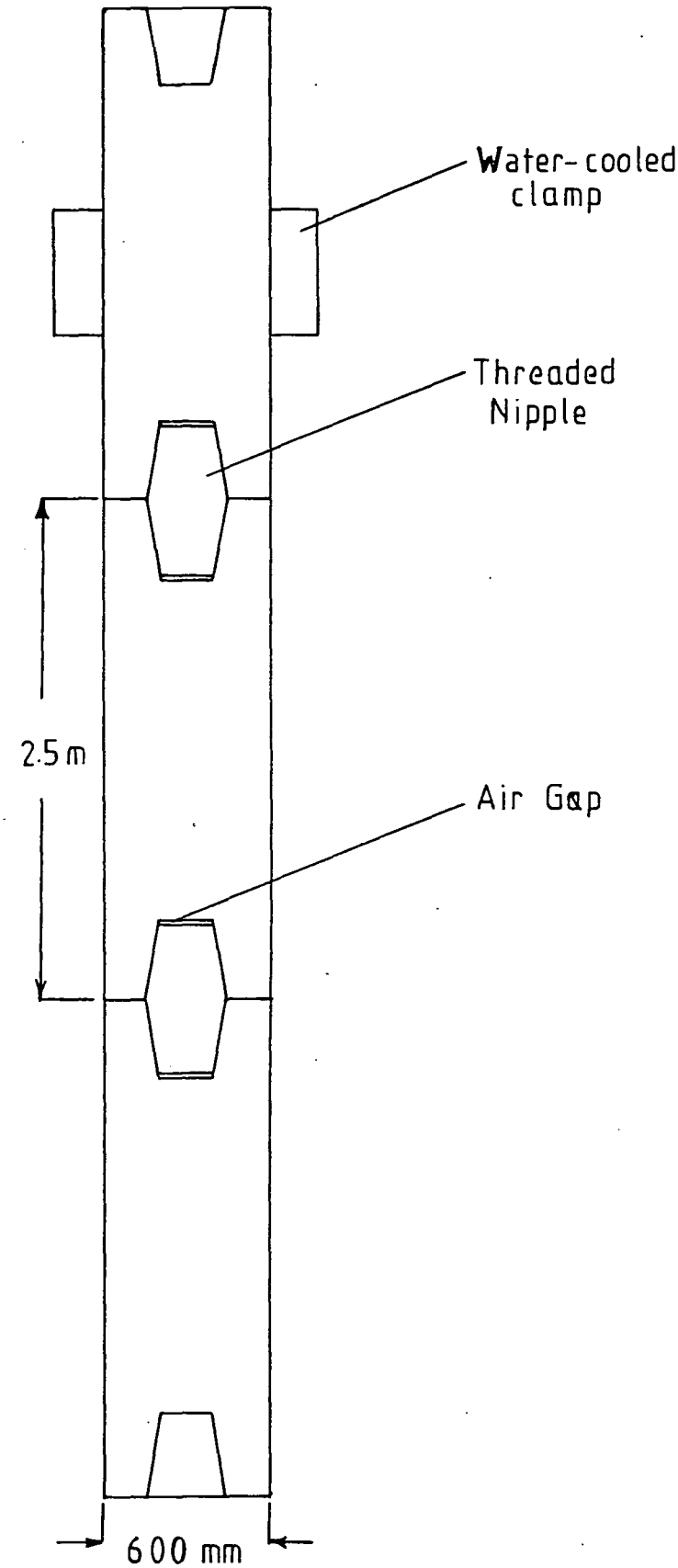

Fig 1.3 Electrode Column Details

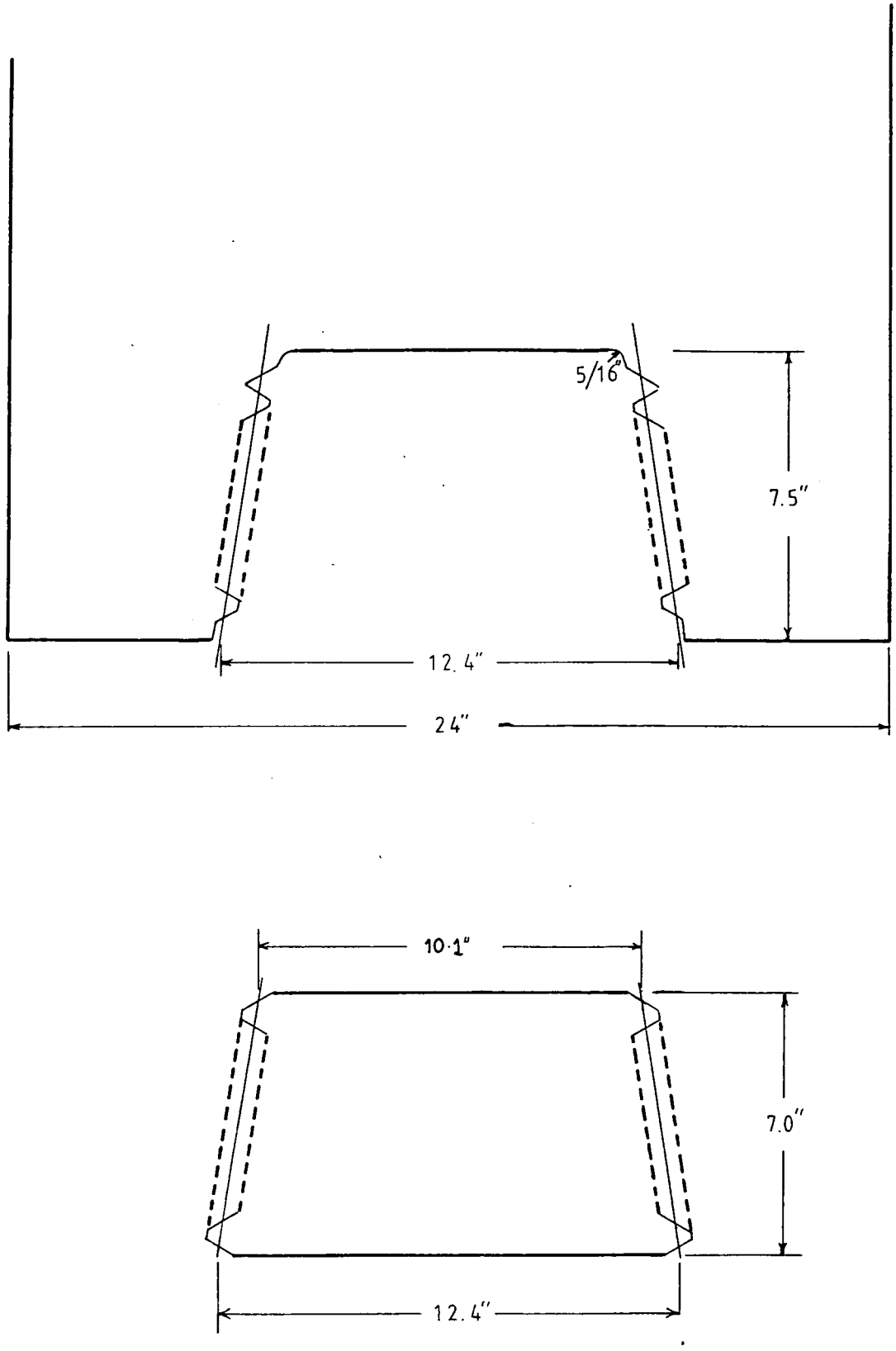

Fig 1.4 Principal Joint Dimensions (thread teeth not to scale)

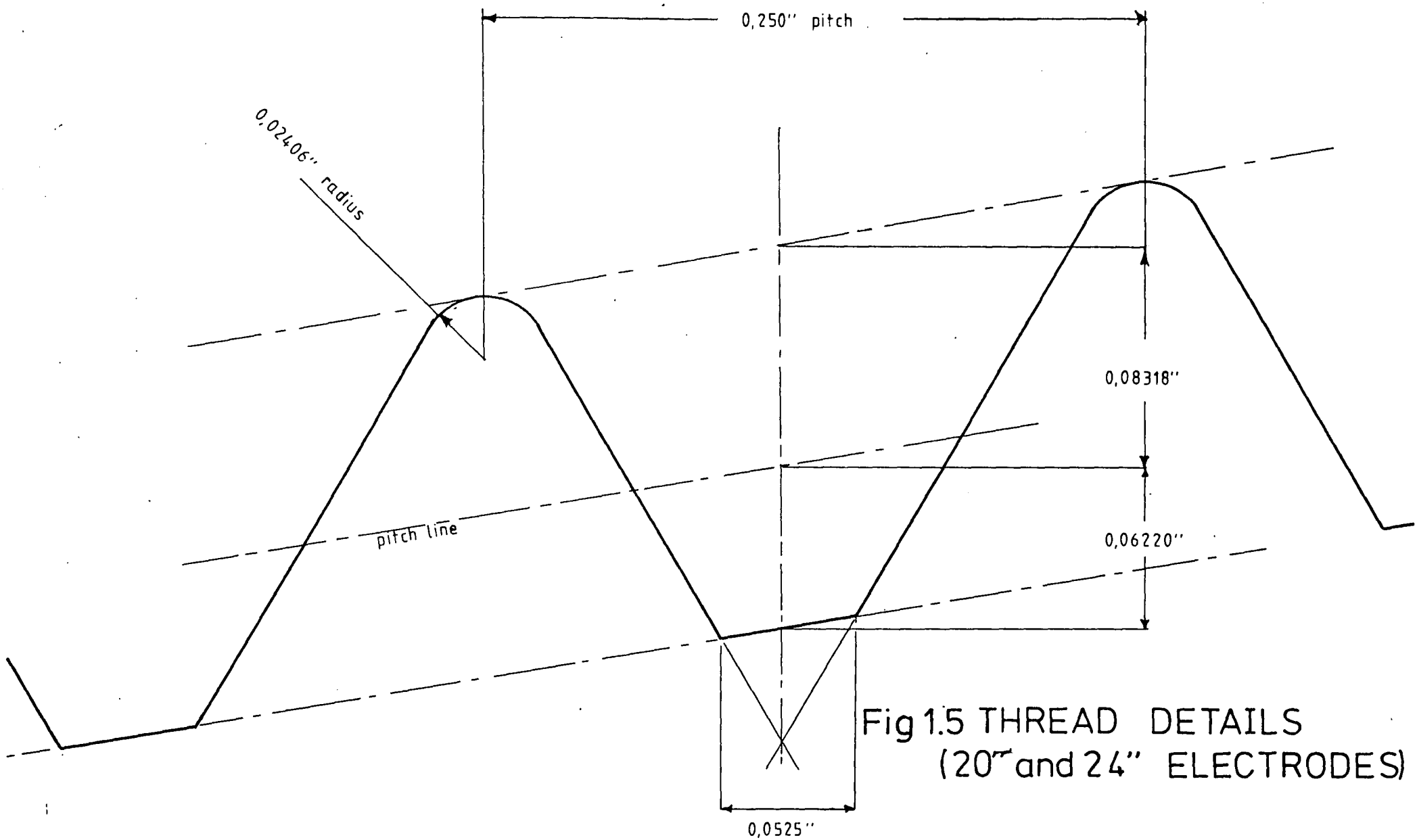

Fig 1.5 THREAD DETAILS
(20" and 24" ELECTRODES)

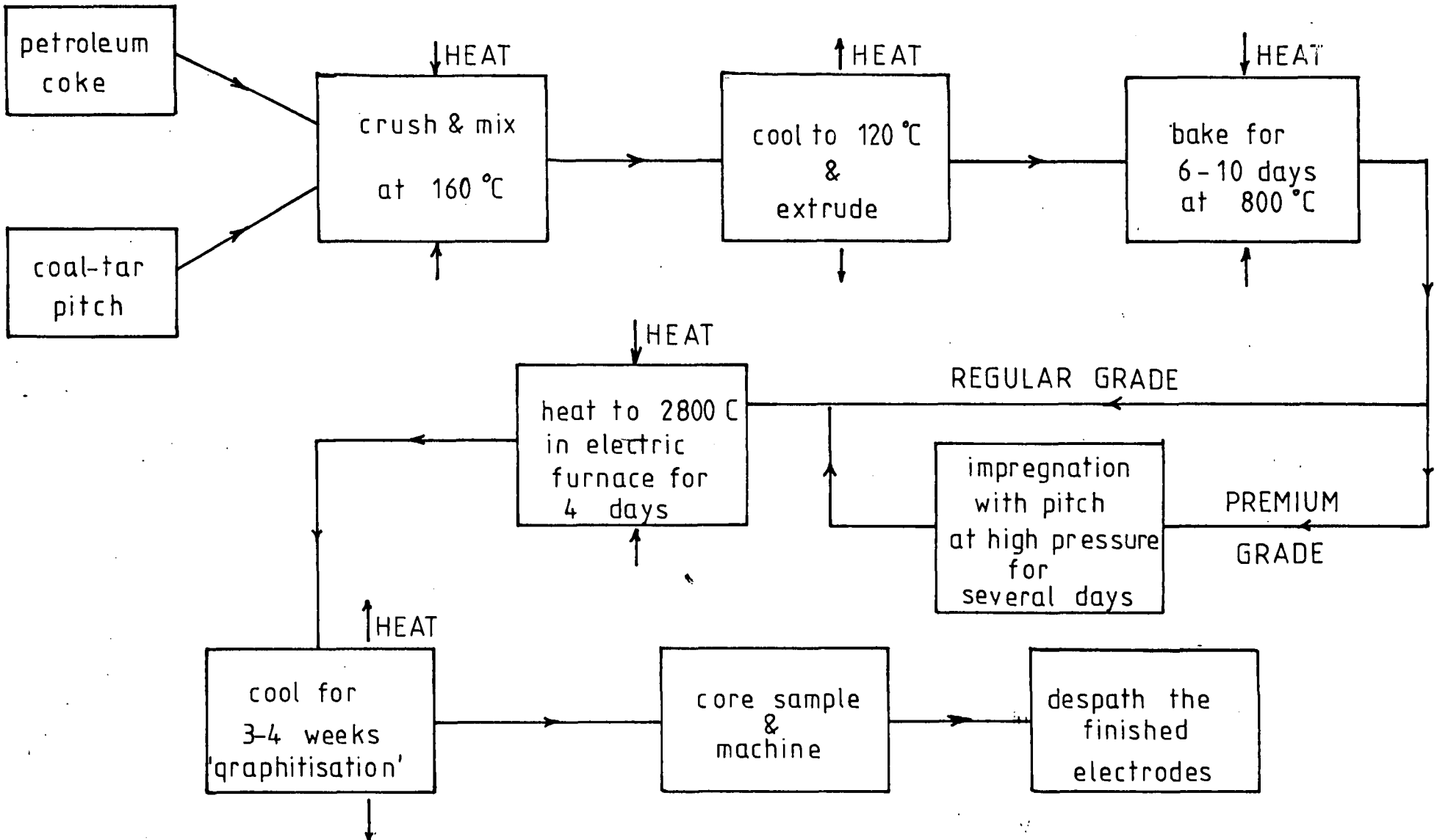

Fig 1.6 Manufacture of Graphite Electrodes

CHAPTER 2

LITERATURE REVIEW

2.1 General Observations

The conditions in an electric steel-making plant make objective assessment of the factors affecting electrode failure extremely difficult. For example, totally enclosed furnaces make it impossible to measure conditions inside with any degree of accuracy, and when the furnaces are uncovered for recharging, or for replacement of an electrode section, the high temperature of large masses of iron and carbon make close physical approach impossible. It is therefore not surprising that information regarding the operating conditions of arc-furnaces is rather sparse, and often of a highly approximate nature. Nevertheless, some progress has been made on certain aspects, despite this lack of reliable data. This chapter is a review of some of the work relating to stress analysis and material properties of graphite electrodes.

2.2 Electrode material loss and replacement

During the course of the electrode work cycle, material can be lost from the electrode in the following ways (Schwabe, 1972)

2.2.1 Sidewall Loss.

Due to the oxidising atmosphere in which the electrode operates, material is lost from the sides of the electrode, the rate of erosion being greatest at the tip, where the temperature is highest. The electrode thus becomes tapered

in use. The rate of oxidation is found to depend on the composition of the furnace gases, and the time of residence of the electrode in the furnace. Moreover, the tapering effect may not be axisymmetric; the mutual radiation between portions of the electrode within the electrode triangle increase the temperature and thus the rate of oxidation in this area. Additionally, the opening and closing of furnace doors, and the use of oxygen lancing contribute to an asymmetric erosion rate.

2.2.2 Tip loss.

Electromagnetic forces cause a concentration of the electric current density around the spot where the arc contacts the electrode. This creates a local 'hot spot' at about 3600-4000°C, while the rest of the electrode is at around 2000°C. The dimensions of this spot are 1/4 to 1/2" and we may visualise the erosion of the electrode around this spot as a simple vapourisation process. This accounts for the bulk of the tip erosion rate, the remainder being made up of abrasion (by metal and slag) and oxidation. It is also suggested (Schwabe, 1972) that expansion of this spot may produce hoop stress of sufficient magnitude for local failure to occur. This would take the form of increased erosion rate due to small pieces of graphite breaking off. The rate of tip erosion is found to increase as the power input to the furnace is increased.

2.2.3 Electrode breakage

Sudden loss of electrode material occurs when an electrode breaks. Fig. 2.1 shows the main modes of failure of a graphite electrode. According to Faircloth (1976) these may be summarised as follows:-

(i) Nipple failure. The nipple, in a state of predominantly tensile stress, fractures along a plane near to its median section. Being of smaller cross-sectional area than the electrode, we would expect the applied forces to produce a correspondingly higher general stress level. Such a failure may be aggravated by other factors, such as insufficient or over-tightening of the joint, increasing interelectrode contact resistance producing a current overload in the nipple itself. Normally, the 'skin effect' ensures that the bulk of the electric current is passed through the mating surfaces of the electrode sections (Fig. 2.2). Undertightening or overtightening, however, may cause the current to flow mainly through the nipple itself, causing local overheating and possible fracture. Additionally, undertightening may place on the nipple bending stresses, when large pieces of metal strike the electrode tip. When combined with the stresses due to tightening torque, the risk of failure could be increased.

(ii) Socket Failure This type of failure results when a large section of the electrode breaks off around the base of the threaded socket. The whole of the 'collar' around the nipple breaks away and the remaining electrode sections fall into the steel melt. This type of failure is often associated with the top joint of an electrode column and Nicholson et al.(1976) found a correlation between the modulus of rupture of electrode material and the number of breakages. On tests in B.S.C. melting shops they discovered that 76% of the electrodes broken had below-average modulus of rupture. It is thought in the industry that this type of failure is due mainly to mechanical stresses. This point is further discussed in later chapters.

(iii) Thermal Failure (sometimes referred to as 'clothes-peg fracture') . As its name implies, this type of failure is thought to be mainly due to the thermal loads imposed on an electrode (Faircloth et al., 1976). A longitudinal crack, originating somewhere near the end of an electrode section, causes a piece of the electrode to break away leaving reduced support for the rest of the lower part of the column which then falls off. This type of failure usually occurs on the bottom joint of an electrode column and is thought to be due to high hoop stresses produced when the outer layers of the electrode contract onto the inner ones as the electrode is removed from the furnace. This supposition

is reinforced by Schwabe (1972).

The relative importance of the above processes in terms of material loss has been summarised by Nicholson (1976) as follows

linear consumption	86%
top joint losses	5%
bottom joint losses	1%
stub end losses	4%
nipple consumption	4%

Note that these figures are recorded in terms of material lost rather than the frequency of occurence of the event.

2.3 Stress Analysis of Electrodes

The problem of calculating the mechanical and thermal stresses in a graphite electrode has been tackled by several workers. Faircloth et al. (1976) used the Finite Element technique with a mesh of over four thousand elements to simulate the behaviour of a joint under the action of tightening torque, electrode self-weight, and thermal stresses due to a uniform temperature of 750°C. The nonlinear stress/strain behaviour of graphite was taken into account, as also was the variation of material properties with temperature. Complete axial symmetry was assumed and sliding was allowed at the electrode/electrode interface by the use of 'zero friction' elements (whose mathematical justification was not explained). The precise method of load application and boundary conditions were not discussed, and only one thermal load case was considered,

as described above. Critically-stressed areas were identified on the electrode near the last engaged thread teeth, and on the nipple near the first engaged thread teeth. The authors noted that the analysis predicted a tendency for the mating surfaces between the electrodes to roll outwards under the mechanical loads, and found that this tendency was increased by the thermal loads. It is suggested that a small gap may appear between the mating surfaces at the periphery. Such a gap may cause overheating of the nipple (due to an increase in current density) and premature failure. The results of the calculations are in good agreement with the observed failure modes of electrodes, but the paper is devoid of any details regarding restraints or load application. It is, therefore, difficult to assess the validity of the results.

Nedopil & Storzer (1967) attempted to measure the temperature distribution in an electrode during service. Their experiments centred around three techniques for temperature measurement - themoelectric, optical pyrometry, and carbon monitors. The thermocouple technique was abandoned because the temperatures encountered were higher than their equipment could stand, and the pyrometric measurements were discontinued because of the large scatter in the results due to local overheating effects in cracks and fissures in the electrode. The method finally adopted was to measure the permanent change in the properties of carbon cylinders which had been inserted into holes bored

in the electrode prior to use. Several property changes were considered for measurement, but changes in thermal expansion coefficient were found to be the most reliable. The technique involves the insertion of a so-called 'carbon monitor' (a small cylinder of the material) into a hole bored radially in the electrode or nipple. The electrode is then used normally and, on cooling, the insert is removed and reheated in the laboratory. The insert expands as normal up to the temperature which it reached in the furnace, and on further heating it begins to contract. The maximum temperature reached by the monitor during service can thus be determined to within about 10°C. The temperatures measured at various points in the electrode have been used as boundary conditions by later workers. Unfortunately, only a few results were obtained, and these at only approximate locations. However, this does represent a serious attempt to measure some of the operating conditions of the electrode, and appears to be the only reliable set of data available.

Weng & Seldin (1977) attempted to determine theoretically the actual temperature distribution in an electrode under operating conditions. A Finite Difference technique was used to determine the temperature distribution near the tip for both square-ended (unused) and tapered (used) electrodes. The effect of a joint was disregarded in the calculations and the effect of the two adjacent electrodes was neglected. The electrode was

assumed to 'see' a furnace wall at approximately 1500°C and a steel bath at a temperature of 2700°C (this is an 'effective' temperature which the authors justify from the results obtained). Axial heat flow was assumed to cease at a distance from the electrode tip of three electrode radii, an important assumption which has also been used by other workers (for example Montgomery et al., 1979). The method involves assigning a series of 'guessed' temperatures to each cell in a Finite Difference mesh. The resultant heat flow into or out of the element is obtained by a computer program which then minimises these heat 'residues' until they are all effectively zero, corresponding to the steady-state condition. The authors took into account the variation of material properties with temperature, and the heating effect of the electric current, both with and without allowance for the 'skin effect'. The results of the calculations were presented graphically for electrodes of different diameters, and it was concluded that the alteration in the temperature distribution due to the skin effect was negligible. While this analysis produced a useful steady-state temperature field, it took no account of heat loss by convection, movement of the arc over the tip of the electrode, or the fact that the electrode end is normally rounded and not flat. In fact these effects are difficult to incorporate into any mathematical model.

Sato et al. (1974) attempted an analytical solution to the thermal stress problem. In order to make the mathematics tractable, the electrodes were considered as hollow, uniform cylinders which were initially assumed to be infinitely long. An 'end-correction' was then applied to enable the technique to be applied to finite cylinders. The analysis assumed complete axial symmetry, and a temperature distribution of the form

$$\theta(r,z) = (Ar^2 + B)e^{-\beta z}$$

The constants A, B, β, were determined by substitution of data from the experimental observations of other workers (Nedopil, 1967). This technique has the advantage that it is possible to take account of the temperature drop across the mating surfaces, although the authors point out that, for the bottom joint of the column, this temperature drop is negligible. The analysis was performed for several different electrode current densities and it was shown that this has very little effect on the predicted stresses. The mathematics of this approach is rather involved and tends to obscure the underlying physical principles, and unfortunately, only steady-state conditions were considered. The method does not lend itself to easy modification for the inclusion of mechanical stresses or thermal transients. A maximum hoop stress of 0.69 kg/mm^2 (~ 7 MPa) was predicted in this analysis.

Elliott and Yavorsky (1969) considered the transient temperature effects on an electrode during the heating cycle and support the assumption (Weng, 1977) that axial heat flow ceases at distances from the electrode tip greater than three electrode radii. Some useful estimates of boundary conditions on the surface of the electrode were given, and it was found theoretically that the fractional completion of the heating or cooling of the electrode is not significantly influenced by the magnitude of the electrode current or the difference between final and ambient temperatures. The relative importance of convection and radiation effects was considered, and convection effects were shown to be relatively unimportant. A value of 0.77 was suggested for the emissivity of the electrode surface. The effect of the other two electrodes on the temperature distribution was considered and estimated to cause an axial asymmetry of less then 10°C. The differential equations involved were solved numerically by a computer technique which was not described in detail, and again, only thermal stresses were considered. Anisotropy of the thermal properties of the material were taken into account, and a value of 1.25 is suggested for the ratio of axial to radial thermal conductivity. The results obtained indicate that axisymmetric steady-state conditions exist during the later stages of a melt, an important observation which will be used in the present analysis.

Montgomery, et al. (1979) used a Finite Difference technique to predict the variation of temperature distribution in an electrode after removal from a furnace. Using a form of initial distribution similar to that of Sato (1974), with constants determined from the Nedopil & Storzer observations, a series of Finite Difference equations was set up. These were used to predict the temperature field at time $t+\Delta t$ given the field at time t. Using an assumed initial field the distribution at any time after removal from the furnace could thus be calculated by successive application of the equations. The analysis was applied only to the simplest of cases where, for instance, the anisotropy of the material properties is neglected, and the different material properties of the electrode and nipple are not considered. The electrode was assumed to radiate as a black body and to be under the influence of no mechanical forces. Unfortunately, a series of errors in the equations meant that the published temperature fields did not follow from the equations. The authors then went on to calculate the hoop stresses predicted by these temperature fields. This is the only work which is concerned with the thermal shock effects produced on removal from the furnace, which is a very important part of the electrode work cycle.

Because the environment of the electrode is continually changing throughout its work cycle, most research work has concentrated on a small part of the total

fracture problem. The temperature measurements of Nedopil & Storzer (1967) and the 4,000-element mesh of Faircloth (1976) were both directed towards steady-state effects. Although Elliott and Yavorsky (1969) considered transient effects during heating, little attention has been given to the thermal shock encountered by an electrode on removal from the furnace. This operation is likely to produce more severe temperature gradients (and hence thermal stresses) because of the more sudden change in surface temperature, and the work done so far must be considered unsatisfactory in this respect. Additionally, thermal and mechanical stresses have not generally been considered together. Faircloth's analysis (1976) did consider a uniform temperature distribution of 750°C in addition to the mechanical loads, but this can hardly be considered an adequate model of the thermal loads. A more complete analysis, including transients, is required. Finite element techniques have not been widely used in the analysis of the problem, but temperature fields have been determined using Finite Difference methods (Weng, 1977). Although a combination of the two techniques has not been used, such an approach should avoid the complicated mathematics used by Sato (1974), while retaining flexiblity of surface boundary conditions.

None of the work investigated made any attempt to study the effect of the screw thread in detail. Work on mechanical loading of screw threads in general is

plentiful in the literature, but it proved impossible to find any work on the stresses in a highly-tapered thread form (as opposed to a 'taper-fit' type of thread.) Further, none of the work on screw threads paid much attention to thermal stresses.

A paper by Cornwell (1981) gave some interesting observations on the effect of friction in threads, and some useful indications as to how to calculate the axial loading produced by a given tightening torque.

2.4 Material properties of electrode graphite

The material properties of electrode graphite have been investigated by several workers, and some of the numerical results are presented in Table 2.1. Semmler (1967) summarised the reasons for the use of graphite as an industrial material; namely, high melting point and relative insensitivity to thermal stresses. He also measured several material properties, and their variation with temperature. The expansion coefficient was found to vary from 2$\mu\varepsilon$/K to 4.5$\mu\varepsilon$/K between 0°C and 3000°C, and the elastic modulus, measured over the same temperature range, varies between 55 and 80 x 10^3 kg/cm^2 (5 - 7 GPa).

Other workers (Elliott, 1969 Faircloth, 1976) assumed values for the material properties, but the measurement direction and the measurement temperature have not always been stated. It can be seen from Table 2.1 that considerable disagreement exists over some of the material properties. The modulus of rupture of electrode graphite

averages at around 10MPa but the scatter is large. Compressive strength is generally agreed to be about 25 - 30 MPa and the thermal expansion coefficient is about 3.0$\mu\varepsilon$/K but values as low as 0.7$\mu\varepsilon$/K and as high as 4.5$\mu\varepsilon$/K were quoted by Faircloth (1976) and Montgomery (1979) respectively. The elastic modulus is also a matter for some disagreement. Sato (1974) quoted values of around 7 GPa throughout the temperature range (parallel to the extrusion direction) Payne (1980) puts the value at 10 GPa (approximately). Of course, most of the material properties are temperature dependent, and different for regular and premium electrode grades.

The variation of the material properties was extensively investigated in Semmler's paper. The variation of elastic modulus with temperature is shown in Fig. 2.3(a), and shows a similar form to that of the flexural and compressive strength graphs, this being a steady increase with temperature at first, levelling off at about 2000°C, and decreasing slightly above this, but the graphite type is not stated. The strength at 2000°C is about 50% greater than at room temperature (Fig. 2.3(b)). Graphite is a brittle material, so the determination of strength values is best done by three-point bend tests, to avoid difficulties with non-axial load application. Values so obtained are generally referred to as modulus of rupture. This does however create difficulties in obtaining reliable values for uniaxial tensile strength, which may

differ from the modulus of rupture values by a factor as large as 2.

Values of thermal conductivity show a considerable decrease with temperature. From a room temperature value of 150 W/mK (parallel to the grain), the conductivity drops to about 25 W/mK at 3000°C. Fig. 2.4 shows the mean of several measurements of thermal conductivity over a range of temperatures taken from 'The Graphite Engineering Handbook', an industrial publication of which only a small part was available for reference.

Table 2.1 shows all the available material property determinations available at the start of the project. The property set chosen is shown in Table 2.2.

An examination of the values shown in the above tables shows the difficulty in selecting a sensible set of material properties. This difficulty arises from three sources:

(i) Many determinations are at unstated temperatures and most of the material properties are temperature-dependant.

(ii) The graphite type (regular, premium, or other) is often not stated.

(iii) The measurement direction is not always stated. Where it is, the appropriate value to use is not always obvious since the present document does not consider material anisotropy.

To circumvent these difficulties, some fairly arbitrary decisions had to be made. These were as follows:

(a) Attempt to obtain properties for premium grade graphite wherever possible, evaluated at a temperature at or around 1500°C.

(b) Where a choice must be made between material properties in orthogonal directions, choose the one most likely to result in the worst possible case of stresses.

The following are notes on some individual choices:

ELASTIC MODULUS

Heavy preference to the values listed in E.C.S.C. since graphite type and temperature are both given.

THERMAL EXPANSIVITY

Sufficient disagreement between the British Steel figures (KIRK,BSC1, PAYNE) to justify taking into account the lower figures given by SNYDER and CEGRAM. Chosen value is probably reasonable.

THERMAL CONDUCTIVITY

Value chosen is on the low side - likely to increase thermal stresses - in keeping with 'worst case' philosophy.

M.O.R. / TENSILE STRENGTH / COMPRESSIVE STRENGTH /

For a particular graphite these three are related quantites. it was not therefore felt appropriate to chose

these independently. By far the most results are available for M.O.R. and this is about 15 MPa for electrodes and 20 MPa for nipples at 1400°C (the values for nipples are fairly arbitrary approximations since there is no better data). The other (lower) values are assumed (or are implied) to relate to room temperature. The multitude of values for M.O.R. are thus consistent if viewed in this light. Brocklehurst (1977) indicates that for most extruded graphites (although none of his results are specifically for electrode graphite) M.O.R. is about 1.5 times tensile strength. Thus tensile strength (necessary for failure envelope analysis) was chosen as 10 MPa for electrodes and 12 MPa for nipples. The crushing strength values in the table imply a value of 25 MPa for electrode and 30 MPa for nipples. These are in accord with Brocklehurst's assertion that compressive strength is roughly 3 times tensile strength for graphite.

2.5 Deformation and Fracture of Polycrystalline Graphite

The deformation and fracture properties of polycrystalline graphite were extensively reviewed and discussed by Brocklehurst (1977). Summarising the observations of many workers he shows the deformation characteristics to be affected by two main considerations.

(i) Particle type and size. Graphite crystals are highly anisotropic, and the degree of anisotropy in a collection of such crystals depends upon

(a) the degree of crystallite orientation within a grain

(b) the particle orientation produced by the forming process (in the case of electrode graphite this is normally extrusion).

For example, a highly oriented structure of needle-like grains would have a preferred deformation by slip along the boundaries, whereas a structure consisting of near-spherical crystallites would deform less easily. The directions of anisotropy are generally along and at right angles to the direction of forming.

(ii) Microcracks and voids. The difference between the theoretical density of 2.26 g/cm^3 and the measured densities of 1.7 - 1.9 g/cm^3 indicate a porosity of about 20% in the materials. This porosity results from a wide spectrum of defects:

(a) microcracks, approximately 0.01mm in size and thought to be the result of internal restraints on cooling from the graphitising temperature.

(b) Larger pores varying widely in size up to several millimetres due to unsatisfactory procedures in manufacture. Some background porisity is, however, unavoidable.

The general deformation behaviour of graphite is a nonlinear stress/strain relationship with a hysteresis effect observed on load/unload cycles, producing a permanent set at zero load. This is not plastic deformation, however, and is thought to be attributable to internal friction associated with interlamellar shear. We may thus visualise the deformation occuring with the crystallites sliding over one another, and being restrained by friction.

Cracks have been noted to start in graphite at about half the tensile failure stress, corresponding to strains of about 1%. These cracks appear to initiate at the boundaries of existing pores and can either cleave the grains or pass around their boundaries. Smith (1972) envisages the microfracture as a build-up of nonpropagating microcracks in regions of high stress adjacent to large voids, until a microcrack density is reached where they join together to form a discontinuous microcrack which then propagates.

Groves and Kelly (1963) explain the fracture mechanism in terms of the Von Mises failure criterion, which states that five independent slip systems are required for general homogenous slip-strain. Only two independent slip systems are operable in graphite. This may cause difficulty in matching strain components at grain boundaries, resulting in local stress concentrations. This can lead to fracture, the onset of which may be delayed by

the presence of voids which the grains may deform into.

Brocklehurst (1977) concludes that, although recent graphite failure theories have some common ground there is as yet no universally agreed quantitative description of the failure mechanism.

SOURCE	TYPE	VAL	VAL*	VAL**	TEMP	COMMENTS
B.S.C. 1 (1980)	R		9.5	8.2	N/S	
	P		12.4	11.0	N/S	
PAYNE (1981)	R		7.0	5.0	N/S	
	P		10.0	7.0	N/S	
B.S.C. 3 (1980)	R		9.7	7.4	N/S	AGL LTd
	P		14.0	9.0	N/S	AGL Ltd
	R		9.5	8.2	N/S	Brit Acheson.
	P		12.4	11.0	N/S	Brit Acheson.
MONTGOMERY, PAYNE KIRK (data sect)	R		9.0	8.0	1400	Unsp brand 'A'
	P		12.5	9.5	1400	Unsp brand 'A'
	R		7.0	7.5	1400	Unsp brand 'B'
	P		13.5	10.5	1400	Unsp brand 'B'
MONTGOMERY, PAYNE KIRK-assumed vals	R	9.5			N/S	
	P	3.0			N/S	
SATO et al.(1974)	N/S		10.0	4.5	1400	Max 12 & 7 @ 2000 C
SEMMLER (1967)	N/S		7.0	4.5	1400	Max 8 & 5 @ 2000 C
PAYNE 1 (1981)	COM		13.5		N/S	Nipple Material.
PAYNE 2 (1981)	COM		13.9		N/S	Nipple Material.
FAIRCLOTH (1976)	N/S		13.7	6.8	N/S	
	COM		21.4	10.7	N/S	Nipple Material.
SNYDER (1976)	P	8.7			N/S	Rm temp. implied.
	COM	4.0			N/S	Rm temp. imp.(nip)
UN. CAR. (1959)	COM		*8.5	7.9*	20	A.T.L. Graphite.

*NOTE A.T.L. is an extruded structural graphite whose description and properties were chosen to be as close as possible to the known values for the type being studied.

Table 2.1(a) Elastic Modulus values for graphite (GPa)

SOURCE	TYPE	VAL	VAL*	VAL**	TEMP	COMMENTS
KIRK 1 (1979)	N/S COM		1.4 1.5	1.2 2.3	N/S N/S	Nipple Material.
B.S.C.1 (1980)	R P		3.5 3.8	4.3 4.4	<1400 <1400	
PAYNE 1 (1981)	N/S		2.0	2.9		
PAYNE 2 (1981)	P		1.6	2.3	N/S	Mean of 23 readings.
SATO et al.(1974)	N/S		1.7	2.7	1800	Assumed vals. at 1800
SEMMLER (1967)	N/S		3.5	3.8	1400	
MONTGOMERY, PAYNE KIRK (1979)	N/S	4.5			N/S	
FAIRCLOTH (1976)	N/S		0.7	1.6	N/S	
SNYDER (1976)	P COM		1.4 1.6	2.1 3.2	N/S	Nipples
UN. CAR. (1959)	COM		2.7	3.8	N/S	A.T.L. Graphite.

Table 2.1(b) Thermal expansivity of Graphite (microstrain/K)

SOURCE	TYPE	VAL	VAL*	VAL**	TEMP	COMMENTS
PAYNE (1981)	N/S	58			<300	Considered unreliable.
UN. CAR. (1959)	COM	38			1400	Mean graphite value
SEMMLER (1967)	N/S		52	41	1500	
BOLZ & TUVE(1970)	COM	16			<1000	Refractory graphite.
ELLIOTT/YAVORSKY (1969)	N/S		50	41	N/S	
WENG & SELDIN (1977)	N/S		41	41	N/S	Vals scattered
MONTGOMERY, PAYNE KIRK (1979)	R P	45 45			N/S N/S	
LINCLON et. al. (1975)	COM		*38	*50	2000	ATJ-S Graphite.

* Note ATJ-S is a pressed graphite. The parallel & perpendicular directions are therefore reversed.

Table 2.1(c) Thermal Conductivity of Graphite (W/mK)

SOURCE	TYPE	VAL	VAL*	VAL**	TEMP	COMMENTS
PAYNE 1 (1981)	R		8.5	7.0	N/S	M.O.R.
	P		13.5	9.0	N/S	M.O.R.
	COM	23.0			N/S	M.O.R. Nipples.
B.S.C.1 (1980)	R		9.0	8.5	1400	M.O.R.
	P		16.5	13.5	1400	M.O.R.
PAYNE 2 (1981)						
set 1	P	9.1			N/S	M.O.R.
set 2	COM	9.5			N/S	T.S. Nipple Mat (A)
	COM		23.0		N/S	M.O.R. Nipple Mat (B)
set 3 (CEGRAM)	R	5.2			N/S	Mean of 30 values.
INCE (1979)	P	9.8			N/S	
SATO et al.(1974)	N/S		5.0	3.0	1500	T.S. values.
SEMMLER (1967)	N/S	5.0			1500	T.S. values.
	N/S	11.0			1500	Flexural.
SNYDER (1976)	P	12.4			N/S	
	COM	21.0			N/S	Nipples
UN. CAR. (1959)	COM		15.0	2.9	20	M.O.R.-A.T.L. Graphite.
	COM		9.1	7.9		T.S. - A.T.L. Graphite.

Table 2.1(d) M.O.R. / Tensile Strength Values for Graphite (MPa)

SOURCE	TYPE	VAL	VAL*	VAL**	TEMP	COMMENTS
KIRK 2 (1979)	P R	20.0 15.0			N/S N/S	Mean of 3 results. 1 result only.
PAYNE 2 (1981)	R	8.4			N/S	Mean of 30 results.
SEMMLER (1967)	N/S	26.0			1500	
MANTELL (1977)	COM		30.0	30.0	N/S	P.G.A. Graphite.
UN. CAR. (1959)	COM		37.6	34.6	20	A.T.L. Graphite.

Table 2.1(e) Crushing Strength Values for Graphite (MPa)

SOURCE	TYPE	VAL	VAL*	VAL**	TEMP	COMMENTS
PAYNE 1 (1981)	N/S	0.30			N/S	Tentative.
B.S.C. 1. (1980)	N/S	0.24			N/S	Undedefined lit. value.
SATO et al.(1974)	N/S	0.10			20	0.15 at >1600 c
MONTGOMERY, PAYNE KIRK (1979)	N/S	0.33			N/S	
FAIRCLOTH (1976)	N/S		0.20		N/S	

Table 2.1(f) Poisson's Ratio Values for Graphite

SOURCE	TYPE	VAL	TEMP	COMMENTS
PAYNE (1981)	N/S	1.7	N/S	
MONTGOMERY, PAYNE KIRK (1979)	N/S	2.2	N/S	
MANTELL (1977)	N/S	1.6	N/S	
BOLZ & TUVE (1970)	COM	1.6	N/S	Refr. graph. Units dubious.
LINCOLN et al.(1975)	COM	2.1	2000	ATJ-S Graphite.

Table 2.1(g) Specific Heat Capacity (kJ/kgK)

SOURCE	TYPE	VAL	TEMP	COMMENTS
FAIRCLOTH (1976)	N/S	0.15	N/S	
BOWDEN & TABOR(1964)	COM	0.15	N/S	General Graphite Values

Table 2.1(h) Coefficient of Friction Values

SOURCE	TYPE	VAL	TEMP	COMMENTS
FAIRCLOTH (1976)	N/S	0.77	N/S	
UN. CAR. (1959)	N/S	0.77	N/S	

Table 2.1(i) Emissivity Values of Graphite

SOURCE	TYPE	VAL	TEMP	COMMENTS
B.S.C. 1 (1980)	R	1610	N/S	
	P	1660	N/S	
B.S.C. 3 (1980)	R	1610	N/S	Anglo Great Lakes Ltd
	P	1750	N/S	Anglo Great Lakes Ltd
	R	1610	N/S	British Acheson Ltd.
	P	1660	N/S	British Acheson Ltd.
PAYNE (1981)	R	1600	N/S	
	P	1700	N/S	
	COM	1800	N/S	Nipple Material.
BOLZ & TUVE (1970)	COM	1900	N/S	Refractory Graphite.

Table 2.1(j) Bulk density Values for Graphite (kg/m**3)

PROPERTY	ELECTRODE	NIPPLE	UNITS
ELASTIC MODULUS	13	14	MPa
POISSON'S RATIO	0.25	0.25	
BULK DENSITY	1650	1800	kg/m**3
UNIAXIAL TENSILE STRENGTH	10	12	MPa
MODULUS OF RUPTURE	15	20	MPa
CRUSHING STRENGTH	25	30	MPa
COEFFICIENT OF FRICTION	0.15	0.15	
THERMAL EXPANSIVITY	2.3	2.9	x 10**-6/K
THERMAL CONDUCTIVITY	40	40	W/mK
SPECIFIC HEAT CAPACITY	2.0	2.0	kJ/kgK

Table 2.2 The property set chosen for the investigation

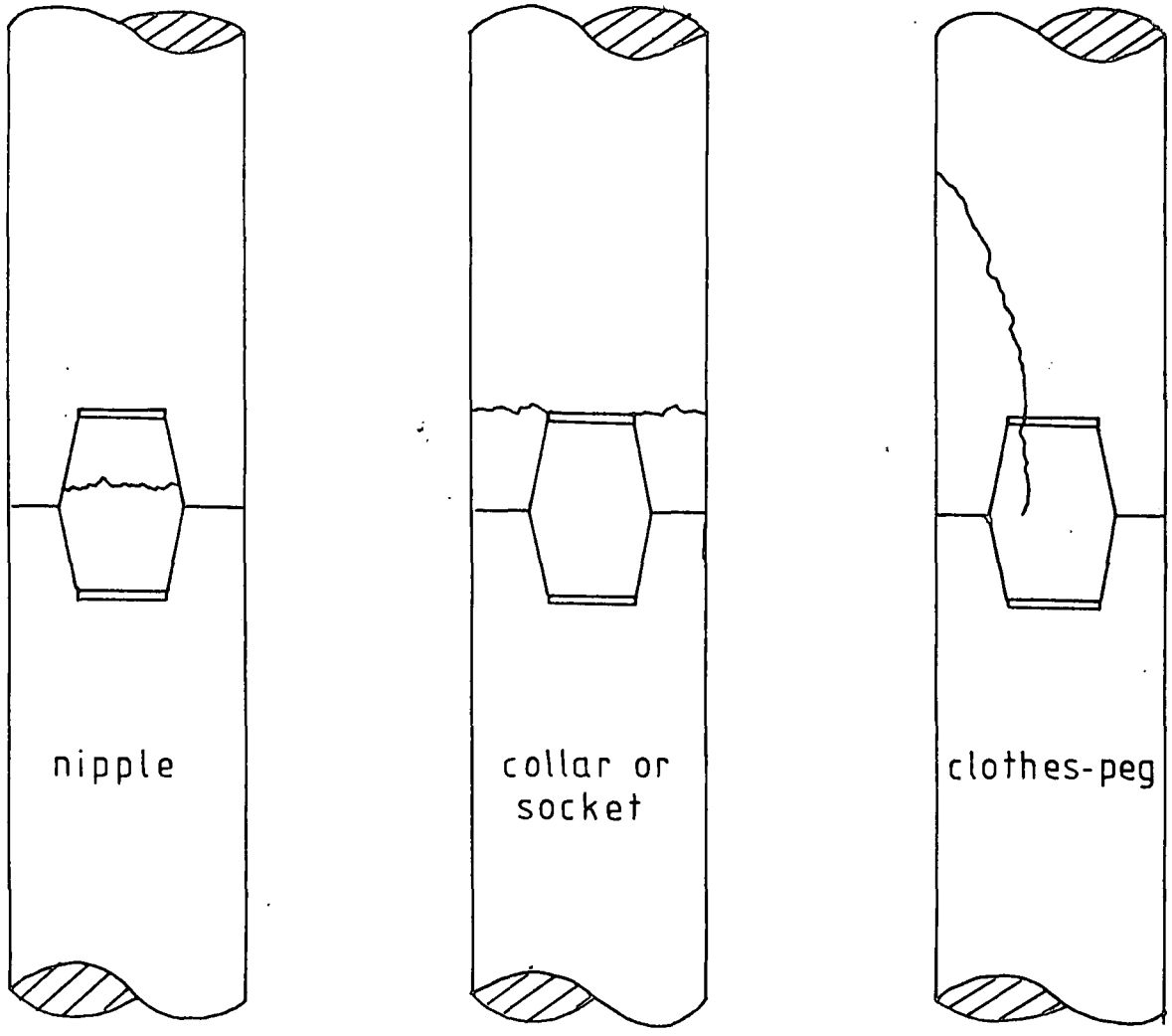

Fig 2.1 Electrode Failure Modes

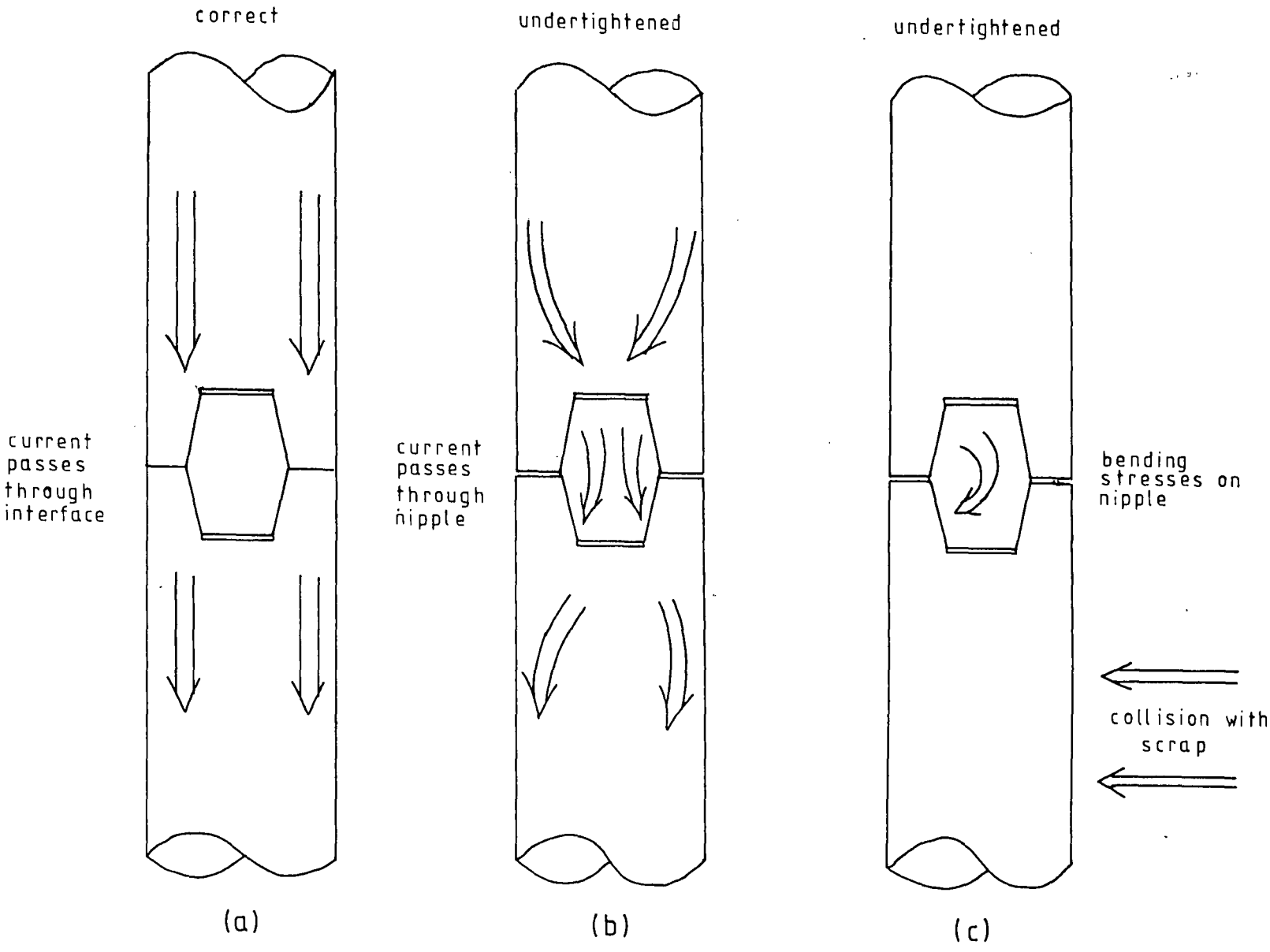

Fig 2.2 The Importance of a tight Joint

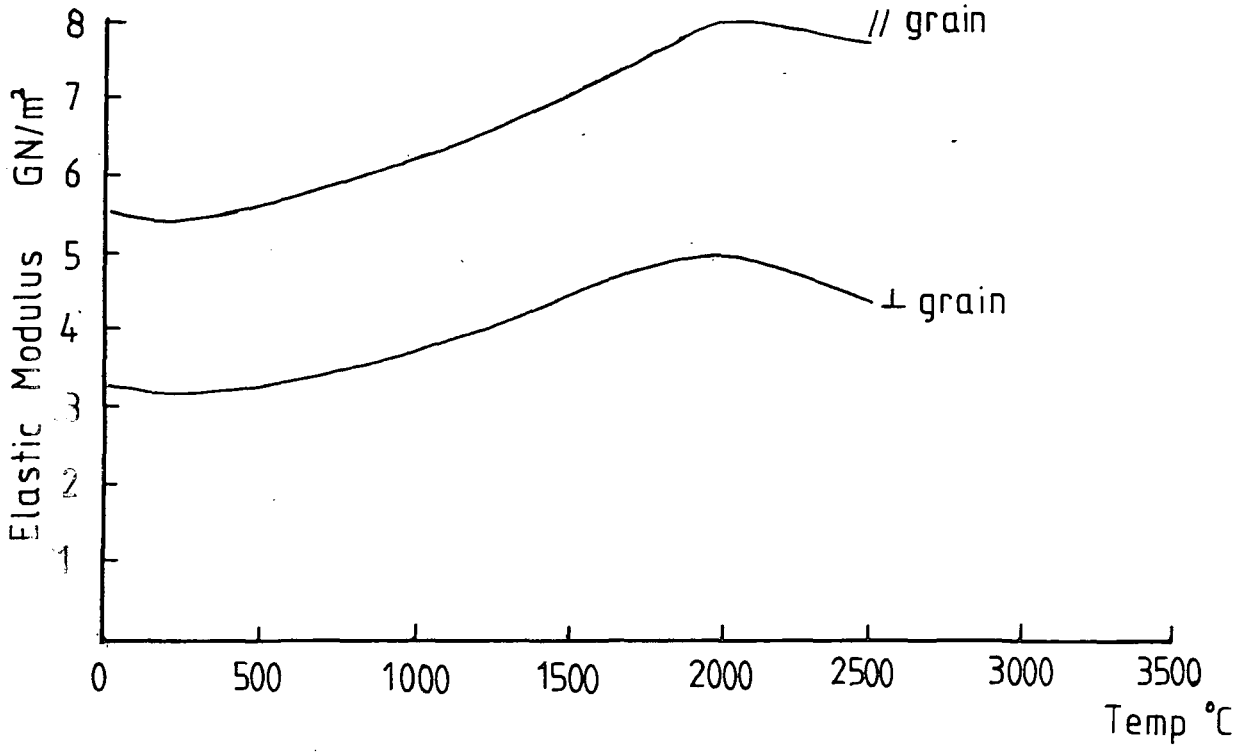

Fig 2.3(a) Elastic Modulus vs Temperature

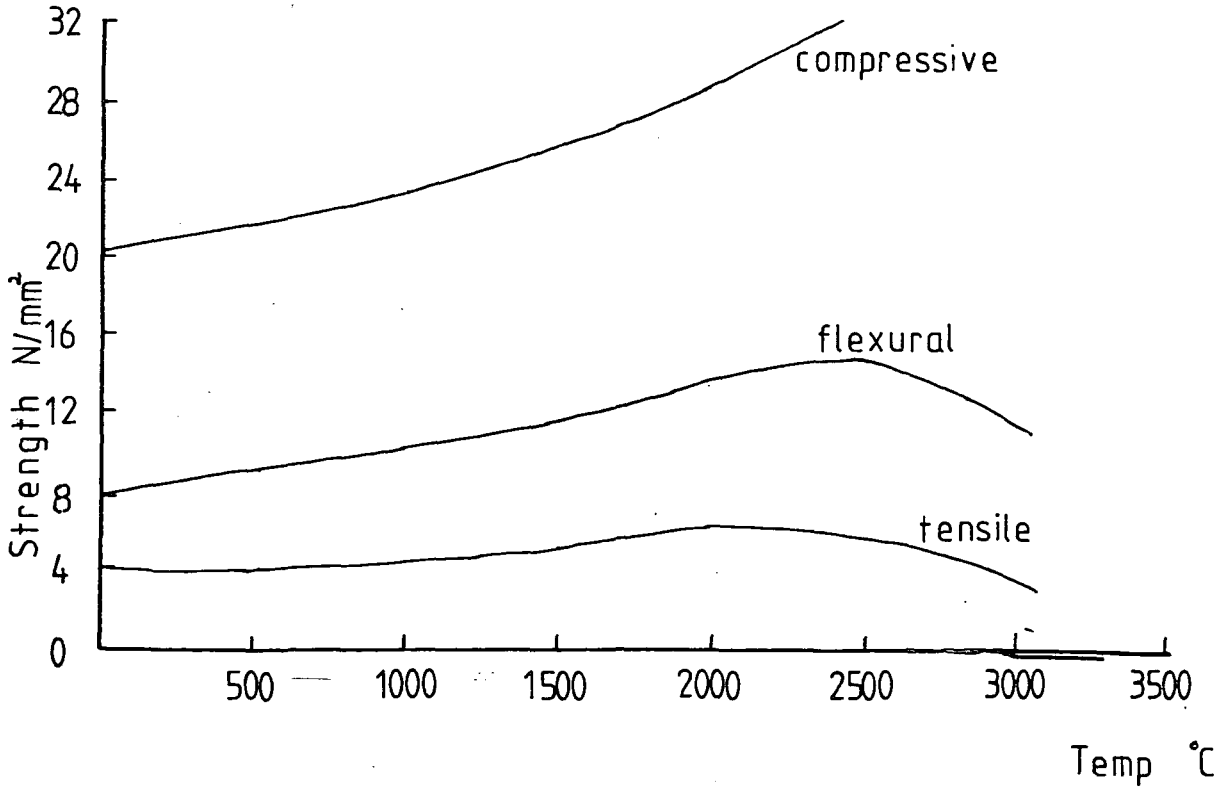

Fig 2.3(b) Tensile Strength vs Temperature

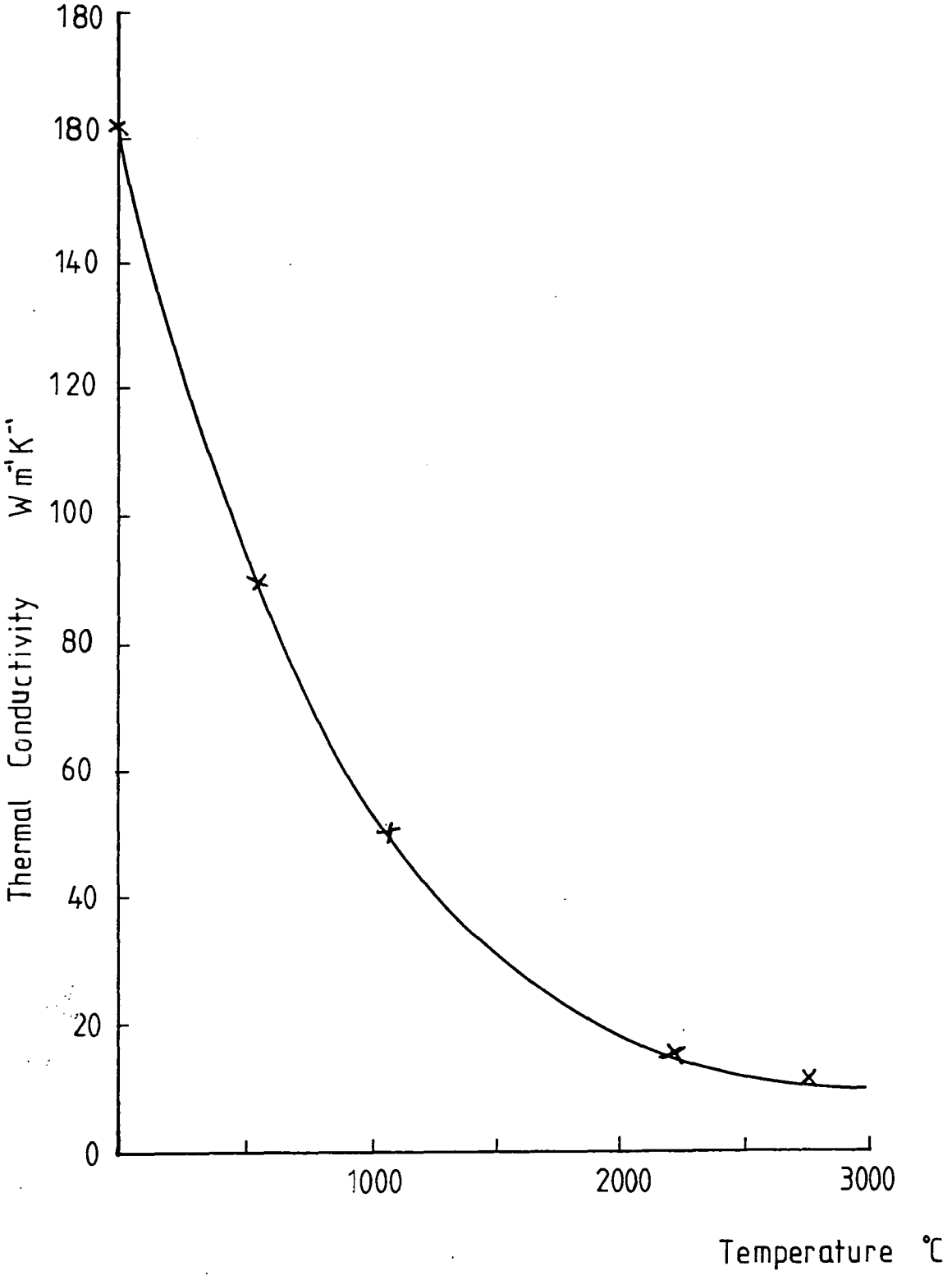

Fig 24 Thermal Conductivity of Graphite vs Temp

CHAPTER 3

STRESSES DUE TO MECHANICAL LOADS

3.1 Sources of Mechanical Stress

Since the loads on a graphite electrode produce a combination of mechanical and thermal stresses, a full analysis of these stresses must include both types of loading. Because the top joint of an electrode column experiences the most severe mechanical loading (self weight + tightening torque), attention was concentrated on this joint for the mechanical analysis.

The mechanical loads on an electrode in service arise from the following sources:

(i) The self-weight of the electrode column. The effect this has on a particular joint depends, of course, on the position of the joint in the column, the top joint experiencing the greatest self-weight load. For any particular joint, the self-weight forces are well-defined and readily calculated.

(ii) The tightening torque applied to the joint. When the column is assembled a torque of 1500 lb-ft (for a 600mm electrode) is applied by means of a strap wrench. Overtightening and undertightening is, however, known to occur in practice.

(iii) Collisions with pieces of scrap metal. During melt-down, large pieces of metal of various sizes may collide with the electrode, producing off-axis forces which cause bending.

(iv) Impulsive forces due to rough handling, collision with furnace lid, etc.

(v) Compressive forces imposed by the clamping system used to support the column at the top.

Of these mechanical forces, only those in sections (i) and (ii) may be readily quantified, and these were therefore the only mechanical forces considered in the model.

3.2 Simplifying Assumptions

Several attempts were made to analyse the stresses due to mechanical loads. The following is a list of assumptions which were applied to the early models.

(i) The coefficient of friction between bearing graphite surfaces is 0.15 (Bowden & Tabor, 1964). This assumption was used in the calculation of inter-electrode force due to tightening torque.

(ii) All thread teeth are initially in contact when the electrodes are first screwed together. Only the application of tightening torque may cause thread teeth to separate.

(iii) The whole problem is axisymmetric. In

particular, we can consider the thread form as a series of concentric hoops. On a thread pitch of 1/4" and a thread length of 7-8" the helix angle is very small. The degree of axial asymmetry produced by the thread helix is thus negligible. The assumption is therefore quite valid on these grounds. On the other hand, an assumption of axisymmetry does preclude analysis of the effect of a sideways collision with a large piece of scrap metal, since only axisymmetric forces may be applied. The use of a fully three-dimensional Finite Element mesh for a problem this size, however, is unrealistic, even without the inclusion of a thread form, because of the increased demand on computing resources.

(iv) The electrode material is homogeneous. Nicholson (1976) has shown that material properties may exhibit quite large deviation (of the order of 30%) from one end of an electrode section to the other. In reality, this variation will be smooth throughout the electrode, and is unlikely to be axisymmetric. Since an axisymmetric analysis is necessary (see above), and a finite element scheme can only deal with step

changes in properties, it was not considered sensible to attempt to take inhomogeneity into account.

(iv) The electrode material is isotropic. This assumption was forced by the fact that the current version of PAFEC did not have facilities for dealing with orthotropic materials.

(vi) The electrode is 'perfect' i.e. no tapering has taken place. If this assumption is not made, the analysis of the thermal stresses becomes extremely difficult (see Chapter IV).

3.3 Loads and Restraints

The method of load application used in the initial models requires some detailed explanation. A Finite Element stress analysis requires accuracy in three main areas; geometry of the element field, application of restraints, and application of loads. Given a sufficiently large computer and unlimited access, satisfactory accuracy may be achieved in all three of the above areas. Unfortunately, limitations on computing resources mean that simplifications must be made. These normally result in an imperfect representation of the true situation, and assessment of results requires careful consideration of the effects of such simplifications. Given a reliable and comprehensive Finite Element program, the most difficult part of the modelling process is the decision on how and

where to apply loads and restraints. In the present situation, there was some difficulty concerning load application.

This difficulty arises fundamentally because an axisymmetric analysis is assumed instead of a full three-dimensional representation. In particular, the load application takes place by a gradual wedging together of the end regions of the electrode under the action of the screw thread due to the turning motion of the electrode sections. An axisymmetric analysis, however, precludes the application of a real torque. The tightening torque loads must therefore be translated into direct loads acting on the thread teeth or some other part of the strucure. Cornwell (1981) has outlined a method for calculating the total axial force produced by the thread teeth and the contacting electrode end-surfaces. This method was used in the analysis.

Fig. 3.1 shows the equilibrium load distribution state when the joint has been tightened. These loads are produced by a complex interaction between the electrode and nipple threads, but are always equal and opposite. Ultimately, it is desired to calculate the thermal/mechanical stress distribution due to tightening torque, self weight and thermal loading.

If we consider the tightening stresses in isolation, it is easily possible, using the work by Braiden (1974) and Cornwell(1981), to calculate the total applied

axial force induced by a given tightening torque. What is more difficult, however, is the decision on how and where to apply these forces. Some possible approaches are as follows.

(i) Consider only the electrode, and set up a finite element mesh with one node corresponding to each thread tooth. Calculate the axial force from Cornwell's equations and apply this load evenly distributed down the thread teeth nodes. When the temperature field has been determined this may be applied in addition to the mechanical loads, thus calculating the complete stress field in a single finite element run.This method was used by Braiden et. al. (1973) and has the advantage of being uncomplicated. However, it suffers from at least two serious drawbacks:

a) There is a non-uniform (in this case, unknown) distribution of load down the thread teeth, caused by the interaction of the nipple with the electrode. This method completely ignores this fact, and will cause errors in the calculated stresses, since it is well-known (Sopwith, 1949) that most of the load in screw threads is borne by the first few thread teeth.

b) When thermal loading is added, the force distribution along the thread teeth will change due to differential expansion of the electrode and nipple. This method represents the action of the nipple by a constant set of forces, which is certainly not the case in practice.

PAFEC is capable of handling mechanical and thermal loading simultaneously, and it is tempting to consider applying some 'reasonable' force distribution down the thread teeth, and imposing the calculated temperature field, along with the self-weight loads. Thus, the total thermal & mechanical stresses would be calculated in one run for each temperature field. However, as with the uniform load application, this method ignores the interaction between the electrode and nipple, which produces a variable set of forces down the thread teeth.

(ii) Model the whole of the electrode and nipple, including the thread teeth (allowing for sliding between them), and apply loads at points remote from the teeth. This is a better approach than (i) since it allows the distribution of load between thread teeth to find its own equilibrium state. Thus it is

conceptually possible to split the nipple along its median section and apply loads equivalent to the tightening torque equal and opposite on this plane (Fig.3.2). Assuming that the load distribution over this plane is known this would be a good representaion of the real tightening torque loads. However, it suffers as method (i) in that,when thermal stresses are added, both the magnitude and direction of these forces change in an unpredictable way, and this model becomes no longer a good representation of the real situation.

(iii) The main problems with methods (i) and (ii) arise from the fact that the boundary conditions (load application, restraints, etc) for the three load cases of tightening torque, self weight and thermal loads, are not identical. This apparent anomaly arises from the fact that an axisymmetric analysis makes it necessary to consider the nipple and electrode separately from the point of view of mechanical stresses. In a full three-dimensional analysis, the tightening torque would have been applied as a real non-axial force, and the self-weight and thermal stresses could be superimposed in one finite

element run for each temperature field, as suggested in option (i). In the present case, however, the application of equal and opposite forces at corresponding points on the electrode and nipple separately mean that the action of the nipple on the electrode, and vice versa, are represented by a set of (constant) forces. To adequately model the situation, these forces must change as the temperature field changes. The method chosen to model mechanical forces must take this into account. Given the fact that the boundary conditions must vary for the three load types, it was decided to model the stress distribution for the three load types (self weight, tightening torque & thermal) separately, and then to combine these by means of a purpose-written program, to obtain the stresses for the combined loads.

3.4 Calculation of Mechanical Loads.

We may calculate, approximately, the inter-electrode force P due to a tightening torque T by the following procedure (Braiden, 1973)

Consider a deformation Δx (in a compressive sense) of the electrode, due to tightening. The work done, ΔW, in producing this compression is then given by

$$\Delta W = P.\Delta x$$

Assuming zero friction, the work done by the torque T is given by

$$\Delta W = T.\Delta\phi$$

where $\Delta\phi$ is the angle of rotation of the torque. We may therefore write

$$T.\Delta\phi = P\Delta x$$

However, if the pitch of the thread form is p, then

$$\Delta x = p.\Delta\phi/2\pi$$

so that

$$T.\Delta\phi = Pp.\Delta\phi/2\pi$$

or

$$P = 2\pi T/p \qquad \ldots\ldots\ldots 3.1$$

This analysis assumes zero coefficient of friction, which in the case of graphite upon graphite may seem a reasonable assumption, since the published value (Bowden & Tabor, 1964) is approximately 0.15.

A more rigorous analysis by Cornwell (1981) shows that, for a coefficient of friction, μ, the total axial force P induced by a tightening torque T is given by

$$P = \frac{(1 - \mu\sec\alpha'\tan\lambda)}{R(\tan\lambda + \mu\sec\alpha')} \qquad 3.2$$

where $\tan\alpha' = \cos\lambda\tan\alpha$, α is the thread flank angle, λ the thread lead angle and R is the mean thread radius. This analysis applies strictly only to a cylindrical thread form; no published work is available on the effect of a

large taper on this force. Additionally, the analysis assumes zero friction between the bearing surfaces other than the screw threads. However, this was the best available estimate of the interelectrode force, so it was decided to use this formula, employing a mean thread radius (0.14 metres) for R. Of course, the value for the thread lead angle λ, where $\lambda = p/2\pi R$, is also variable, so a mean value for R was also substituted here.

Fig. 3.3 shows the variation of induced force P with coefficient of friction calculated form equation 3.2 for a nominal tightening torque of 1500 lb-ft. The heavy dependence of induced force on the frictional coefficient is evident from this graph, showing that a coefficient of 0.15 reduces the induced force by a factor of about 15.

This load is borne by the thread teeth, and an equal and opposite reaction is imposed on the electrode/electrode interface. (However, when the electrode column is suspended vertically, the inter-electrode force on the top joint will be decreased by an amount equal to the self-weight of 2 electrode sections. The force borne by the thread form will be increased by exactly the same amount.)

3.5 Preliminary Model.

To obtain a feel for the forces and stresses involved, and some experience in using the PAFEC finite element suite, a preliminary analysis was carried out on a

simple mesh. The forces were calculated from equation 3.2 as follows.

$$\text{mean value of } \tan\lambda = \text{thread pitch}/2\pi \times \text{mean radius}$$

$$= 7.2 \times 10^{-3}$$

$$\alpha = \text{thread flank angle}$$

$$= 30°$$

$$\tan\alpha = 0.5773$$

Assuming an applied torque of 1500 lb-ft (2036 N-m), equation 3.2 shows the induced axial force to be 80.6 kN, which distributed evenly over 26 thread teeth (see approach (i) in section 3.3) give the individual thread tooth load as 3.1 kN.

The electrode joint has two axes of geometrical symmetry, assuming no tapering has taken place. The major axis of the electrode provides one axis, and the interelectrode boundary the other (in 3-dimensions this is, of course, a plane of symmetry).

A mesh of 344 six-noded isoparametric triangular elements was set up using the automatic mesh generation facilities in PAFEC. This represented the two sides of the electrode joint and the nipple section. The mesh, hereafter referred to as the E8 mesh, is shown in Fig. 3.4. The nodes on the sloping thread form were positioned so that they lay on the thread pitch line, one node corresponding to each thread tooth. The counterbore at the entrance to the socket and the fillet radius at the base were very carefully

modelled to ensure correct geometry. A total of 26 uniformly loaded teeth was assumed (the actual number of teeth depends on the angular position at which the cross-section is taken). From previous work (Braiden, 1973) it was suspected that the fillet radius at the socket base was a region of particular interest, so this was finely meshed. The fineness of the mesh close to the thread teeth is, of course, determined by the number of teeth.

The top and bottom of the mesh was extended well beyond the region of interest because the restraints at the top of the mesh may induce stresses which could be confused with 'real' stresses produced by the torque loading. Any stresses thus induced are incorrect since the restraint in the finite element model is total, whereas in reality some flexibility would exist at the support. By extending the mesh in this way, the magnitude of such 'reflected' stresses is reduced.

Assuming the clamp at the top of the column to be rigid, a total restraint was applied at the top of the column, and the calculated loads input to the PAFEC program which was then used to calculate the stresses. In this preliminary run the nipple elements were omitted and the loads applied only to the electrode.

3.6 Results from Preliminary Model

Although numerical results from this model are not presented because the basic assumtions were later changed considerably, it identified two regions of

interest.

(i) The fillet radius at the socket base, in which largely tensile stresses occur.

(ii) The counterbore at the socket entrance, in which quite high compressive stresses occur.

The magnitude of the stress vectors at the restraints were carefully examined and found to be very low. This was regarded as adequate proof that the extension of the mesh is sufficient to avoid problems with reflected stresses at the restraints, and that the element field covers the whole of the area of interest.

One problem with the preliminary calculation was that interpretation of the digital output was rather difficult because of the way in which the mesh had been constructed, using the automatic mesh-generation facilities of PAFEC. This involves defining large PAFBLOCKS, (groups of elements) by entering the coordinates of relatively few nodes. PAFEC then 'fills in' these blocks with ordinary elements, in a way over which the user has little control. On small meshes this is a very acceptable way of saving time, but the elements and nodes are numbered haphazardly. On the digital printout, nodes which are physically close may thus be at opposite ends of the printout, so interpretation of results becomes tedious and error-prone.

Another difficulty exists if a slight alteration is made to the mesh. For example, if an element or node is removed or added, the whole numbering system of the mesh

will be changed. It therefore becomes very difficult to compare results between similar meshes. Two courses of action were considered as a solution to this problem.

(i) Generate all meshes 'by hand' i.e. define every nodal coordinate and element topology explicitly.

(ii) Write a post-processing program which renumbers the mesh in a more sensible manner.

The latter course of action was chosen as being marginally the quicker of the two possibilities since all the information required to renumber a mesh is, in fact, printed by PAFEC. It was not possible to alter the FORTRAN coding of PAFEC to obtain the required output, so a separate program was written to renumber a PAFEC-generated mesh in a logical fashion, with node numbers increasing from left to right.

3.7 Improved Tightening Torque Stress Calculation.

The preliminary run may be seen as a 'rangefinder', giving basic information on computing time, consistency of results, and an overall appreciation of the magnitude of the problem to be solved.

A major inaccuracy in the preliminary run arises from the fact that the total tightening force is applied uniformly down the thread teeth. It is well-known (Sopwith, 1949), that the majority of the load is borne by the first few thread teeth.

In considering the calculation of loads due to tightening torque, we may imagine two electrode sections lying horizontally and being tightened onto a nipple. Because there are no self-weight effects, the symmetry of the situation dictates that the electrode/electrode interface does not move during the tightening process. As the sections are gradually made hand-tight, we might assume that all thread teeth are initially in contact. As the tightening process continues, the thread teeth will slide over one another along their load-bearing faces in a radial and axial direction. Some thread teeth may become disengaged during the tightening process, leaving a smaller number of teeth to support the load. The load distribution down the thread teeth is thus non-uniform.

What is required is a method of determining the load distribution across the thread form, given the total applied load (as calculated from equation 3.2). As mentioned in section 3.3, this is a fundamental problem caused by being forced to represented a truly three-dimensional situation as an axisymmetric problem. Ideally, a three-dimensional finite element model should be constructed, representing the thread teeth as a helical construction. A real torque could then be applied to the outer circumference of the electrode, and the finite element program would then calculate the equilibrium distribution of load down the thread tooth line, taking

full account of the thread geometry particular to this problem. The computing resources required for such a course of action are, however, totally unrealistic. It is shown in Chapter V that a mesh of 1200 linear two-dimensional elements is just viable given the available system. It is estimated that at least 5000 three-dimensional elements would be required for even an approximate analysis of the type described.

It is relatively easy, using Cornwell's equation, to translate the electrode tightening torque into an equ ivalent axial pull. The difficulty, however, is that, no matter where this calculated load is applied, assumptions must be made about the load distribution.

To achieve an approximation to the load distribution down the thread line, the E8 mesh was modified to produce the structure shown in Fig. 3.5. In this analysis, use is made of the fact that the interface between the electrode ends deforms symmetrically about a staitonary symmetry plane under pure tightening. Thus, region X is a high-modulus material, restrained completely along the line CD. The line of nodes AB are defined as 'GAP' nodes, with coefficient of friction 0.15 in the sliding direction. Similarly the nodes along the line EF (corresponding to the thread teeth) are defined as 'GAP' nodes. The action of PAFEC at these nodes is to use an iterative process to eliminate all tensile reactions. Any pair of nodes which have tensile reactions is released and

the displacements recalculated. This process is continued for a maximum of seven iterations, by which time the process will usually have converged, i.e. all reactions will be compressive. A uniform pressure corresponding to the axial force calculated from equation 3.2 is applied along the line GH. This method removes the load application from the region of interest, reducing its influence on the stresses.

Reactions were calculated for all nodes along the line EF, and these are plotted in Fig. 3.6. The variation shows that the first few thread teeth bear the majority of the load. Of course, the fact that the geometry of the nipple is changed where it joins with the cylindrical section means that the stress distribution over the nipple median section is altered. The assumption inherent in this technique is that this does not significantly alter the load distribution down the line of thread teeth. The forces in Fig. 3.1 are now determined and it remains to find the stress distribution. The calculated reactions and displacements were therefore used as loads for tightening torque stress calculations in all regions near the joint. Fig.3.7 shows the runs which are neccessary, with the appropriate restraints. These runs were as follows:

(i) An initial run exactly as in Fig. 3.5. This was used to obtain the load distribution down the thread form, and the stress distribution in this electrode section.

(ii) The electrode nodal displacements along the line EF obtained from (i) were used along the corresponding line on the adjoining electrode section as input displacements, allowing for 'GAPS' over the interface. This is equivalent to the application of the load distribution from Fig. 3.6 being applied down the thread teeth.

(iii) Finally, the reactions along the line EF were applied symmetrically to both halves of the nipple. The axial restraint along the nipple median section is necessary to satisfy the requirements of the finite element program. It will have no effect on the stresses since, by symmetry, this section remains plane under pure tightening.

Thus the mechanical stresses due to tightening torque were calculated for the electrode joint regions. Of course, this technique is not ideal. The load distribution down the thread teeth will be affected by the incorrect geometry where the nipple joins with the cylindrical section. However, it is considered that this is a more accurate representation of the real situation than the imposition of some arbitrary load distribution over some region of the structure, which appears to be the only other viable option.

3.8 Mechanical stresses due to self-weight

The calculation of mechanical stresses due to self-weight is much easier than that for tightening torque. The self-weight of two electrode sections (appropriate to the conditions of a top-joint) is

$$\pi d^2 l \rho g/4 \text{ Newtons}$$

where l is the total length in m, d the diameter of the electrode in m, ρ the density in kg/m^3 and g the acceleration due to gravity in m/s^2. Assuming each section to be 8ft long (the nominal length), 24" in diameter, and the density of electrode material to be 1650 kg/m^3, the self-weight of two electrode sections is 23 kN.

The mesh shown in Fig. 3.8, was set up for the calculation of self-weight stresses. This requires no geometry change for the correct load application. Line GH was restrained axially and gaps were specified along the lines AC, AE, BD, BF. A force of 23 kN was applied as a uniform pressure across the face IJ. In addition, a gravity loading of 1.0g was applied to the finite element mesh itself so that the weight of the modelled region was included.

3.9 Obtaining the Combined Stress Field.

The output from PAFEC for the element types used contains the following five important items:

(i) most positive principal stress.

(ii) least positive principal stress.

(iii) hoop stress

(iv) maximum shear stress

(v) β, the angle of the most positive principal stress to the global x-axis.

Combining the two stress fields (due to two different loading conditions for example), is therefore not a straightforward matter of simple addition, since the principal stresses will only occasionally be in the same direction in the two cases.

The principal stresses represent the maximum and minimum stresses in the plane respectively. On the principal stress planes the shear stress is zero. To visualise the process of combining two stress fields at a node, consider two stress fields A & B. At a particular node, let σ_1 in stress field A have angle θ_A to the global X-axis, and the corresponding σ_1 due to B have angle θ_B to the global X-axis. In order to combine the two stresses, we must first determine what the stresses B would be if rotated through an angle $\theta_A - \theta_B$ to the orientation of stresses A. If this rotation is performed, the direct stresses due to B will change, and a finite value of shear stress will appear. The direct stresses may then be added together and a new pair of principal stresses equivalent to this sum and the additional shear stress may be determined.

The theory may be found in any good textbook on stress analysis (e.g. Timoshenko & Young (1968)). The following set of equations are appropriate.

$$\sigma_\theta = 0.5(\sigma_x+\sigma_y) + 0.5(\sigma_x-\sigma_y\cos 2\theta) - \tau\sin 2\theta \quad 3.3$$

This gives the direct stress at an angle θ to the global X-axis due to the stresses σ_x, σ_y, τ.

$$\tau_\theta = 0.5(\sigma_x-\sigma_y)\sin 2\theta + \tau\cos 2\theta \quad 3.4$$

This gives the corresponding shear stress,

$$\tan 2\phi = -2\tau/(\sigma_x-\sigma_y) \quad 3.5$$

This gives the directions of the principal stress planes derived from the new stresses σ_x, σ_y, τ and

$$\sigma_1 = 0.5(\sigma_x+\sigma_y)+0.5[(\sigma_x-\sigma_y)^2 + 4\tau^2]^{0.5} \quad 3.6(a)$$

$$\sigma_1 = 0.5(\sigma_x+\sigma_y)-0.5[(\sigma_x-\sigma_y)^2 + 4\tau^2]^{0.5} \quad 3.6(b)$$

giving the actual values of the principal stresses.

Of course, the combined hoop stress is obtained by a simple addition of the hoop stresses due to A and B.

A computer program was written to combine the stresses in this way, using the above equations as the calculation algorithm. A full description of the workings of the program is given in Appendix I. (the same program was later used to combine the thermal and mechanical stresses for a bottom-joint analysis).

The mechanical stresses due to tightening torque and self-weight were then combined using the program, to produce a complete mechanical stress analysis for a top

joint.

3.10 Improved Mechanical Model-Results

Generally, in a given stress field, it is possible to experience a wide range of stresses - typically, in the present work, these will be separated by several orders of magnitude. With such a large range, the smaller stresses may be considered to be zero. More importantly, due to inaccuracies in the finite element program, the lower order stresses may even be incorrect in sign. Therefore, in considering stressed subregions of the electrode, it is necessary to define some arbitrary level of stress below which nodes will be considered as having zero stress. The level chosen depends, of course, on the peak stresses occurring over the whole of the region. For example, if we consider a subregion of tensile stresses where the peak stresses over the whole region are of the order of 10 MPa, then a stress state such as

σ_1= 0.1 MPa σ_2= 0.05 MPa σ_3= 0.11 MPa

could not reasonably be said to be triaxially tensile since rounding errors could be greater than the values of σ_2. This stress state would then be considered as effectively biaxial tension.

Fig. 3.9 shows the results of the analysis of the mechanical stresses calculated for the electrode top joint.

Regions A,B, and C exhibit a triaxial tensile stress state with all three principal stresses greater than 0.1 Mpa. Peak values of stresses are well below the material mean tensile failure strength (~10MPa). In region A, for example, the peak stress is at node 71, in the fillet radius:

σ_1= 2.5 MPa σ_2= 0.3 MPa σ_3= 0.7 MPa τ_m=1.1 MPa

Node 340, in a similar position in region B, has

σ_1= 2.6 MPa σ_2= 0.3 MPa σ_3= 0.8 MPa τ_m=1.1 MPa

and at the maximum radius of the nipple (region C) stresses peak at node 1314 with

σ_1= 4.7 MPa σ_2= 0.3 MPa σ_3= 0.8 MPa τ_m=2.2 MPa

These stress regions are as expected. The tightening of the electrode onto the nipple produces a pulling effect at the edge of the nipple. A slight splaying effect of the collar region as it is tightened, and the thread teeth slide, causes triaxial tension over regions A and B, and also results in the mildly triaxial compressive regions H and I. Regions D and E, which are not easily explainable by intuitive argument, turn out to have only two of the three principal stresses significantly compressive - for example node 1004, in the middle of region D

σ_1= -0.01MPa σ_2=-1.0 MPa σ_3=-1.0 MPa τ_m=0.5 MPa

Region F, near the socket counterbore, is sqeezed by the action of tightening, and here we see the largest stress peaks. Node 479, for example has

σ_1= -0.4MPa σ_2=-5.3 MPa σ_3=0.0 MPa τ_m=2.4 MPa

Region G is under in-plane compression, with hoop stress tensile. Over this region the hoop stress is relatively constant at about 0.5 MPa, but we find the value of σ_2 to decrease rapidly towards the surface of the electrode. Node 463, for example, near the socket, has

σ_1= -0.9MPa σ_2=-1.5 MPa σ_3=0.5 MPa τ_m=0.3 MPa

And node 476, near the surface

σ_1= 0.0MPa σ_2=0.0 MPa σ_3=0.5 MPa τ_m=0.0 MPa

Fig. 3.10 shows this in detail, being a plot of σ_2 against distance across the interface. Again, this is as would be expected, the splaying effect on the collar region causing greatest compression near the inside.

The result of the splaying effect may be seen most dramatically in Fig. 3.11(a) which shows the variation of hoop stress with axial distance from the end of the analysed section. As we approach the joint from below, the hoop stress becomes mildly compressive, the maximum compression corresponding roughly to region H in Fig. 3.9, becoming tensile as the interface is approached, and reaching a maximum of 0.5 MPa across the interface. An almost identical variation occurs when approaching the joint from the other direction. The maximum hoop tension

corresponds to very small in-plane compressive stresses of

σ_1= 0.0MPa σ_2=-0.001 MPa (node 269)

Fig. 3.11(b) shows the variation of hoop stress with axial distance from the centre along a line just below the socket base (line XY in Fig. 3.9). The effect of the fillet radius in raising the level of the stresses may be seen quite clearly as the hoop stress peaks at 0.25 MPa along this line. At the surface the hoop stress becomes mildly compressive as previously explained.

The finite element results predict the formation of a very small gap (less than 0.01 mm) at the periphery of the electrode/electrode interface due to the action of mechanical loads. This 'gap' of course assumes a perfectly flat finish to the ends of the electrode sections, and can in no way be regarded as measurable.

It is interesting to consider the likely effect of these mechanical stresses on the electrode material, although a fuller failure analysis is discussed in a later chapter. The absolute maximum tensile stress value occurring is 4.9 MPa, at the surface of the nipple near the interface (node 1305 & 1328) which has

σ_1= 4.9MPa σ_2= 0.2 MPa σ_3=0.9 MPa

Close examination of the stresses within this region shows that this stress decreases rapidly with distance. Node 1298, for example, only 1 cm from this point, exhibits a

stress state of

σ_1= 2.1MPa σ_2=-0.4 MPa σ_3=0.0 MPa

Thus, there is a localised triaxial tensile stress amounting to half the mean failure stress of the material (10 MPa), rapidly decreasing to well below this value. Failure of the electrode or nipple would thus not be expected under normal tightening conditions. A significant overload torque (a factor of 2, for example) may well take this region into risk of failure however.

The other regions of peak tensile stress (A & B in Fig. 3.9) have absolute maxima of 2.5 MPa (nodes 71 & 340). Again, these decrease rapidly with distance so that failure here due to normal tightening stresses is unlikely. The same comment as before applies to an overtightened electrode however.

Peak compressive stresses of 5 MPa occur in region F. The crushing strength of electrode graphite is about 25 MPa, however, and these compressive stresses are unlikely to cause failure even under overload conditions.

The model of mechanical stresses has thus identified two regions of interest in the electrode structure:

(i) A region of triaxial tensile stress near the fillet radius at the base of the socket. The magnitude of the stresses in this region may be up to one half of the tensile strength of the material.

(ii) A region of high compressive stress at the entrance to the socket.

During a later part of the work in which the thermal stresses were modelled, the mechanical stresses were evaluated separately using a much more complicated mesh and more accurate loading assumptions. Although discussed in more detail in Chapter V it is noted here that the results from the more complex model reinforced the general observations made in this chapter.

3.11 SUMMARY

The determination of mechanical stresses in a graphite electrode by a Finite Element method involves several simplifying assumptions. However, a simple model of the mechanical forces on the top joint of a graphite electrode has been developed and has shown that no regions are critically stressed before thermal stresses are added. Peak stresses occur in the fillet radius, at the entrance to the socket and at the edge of the nipple. Overtightening of the electrode joint in order to achieve better electrical contact would appear to be undesirable, however, since these regions may be brought into danger of failure.

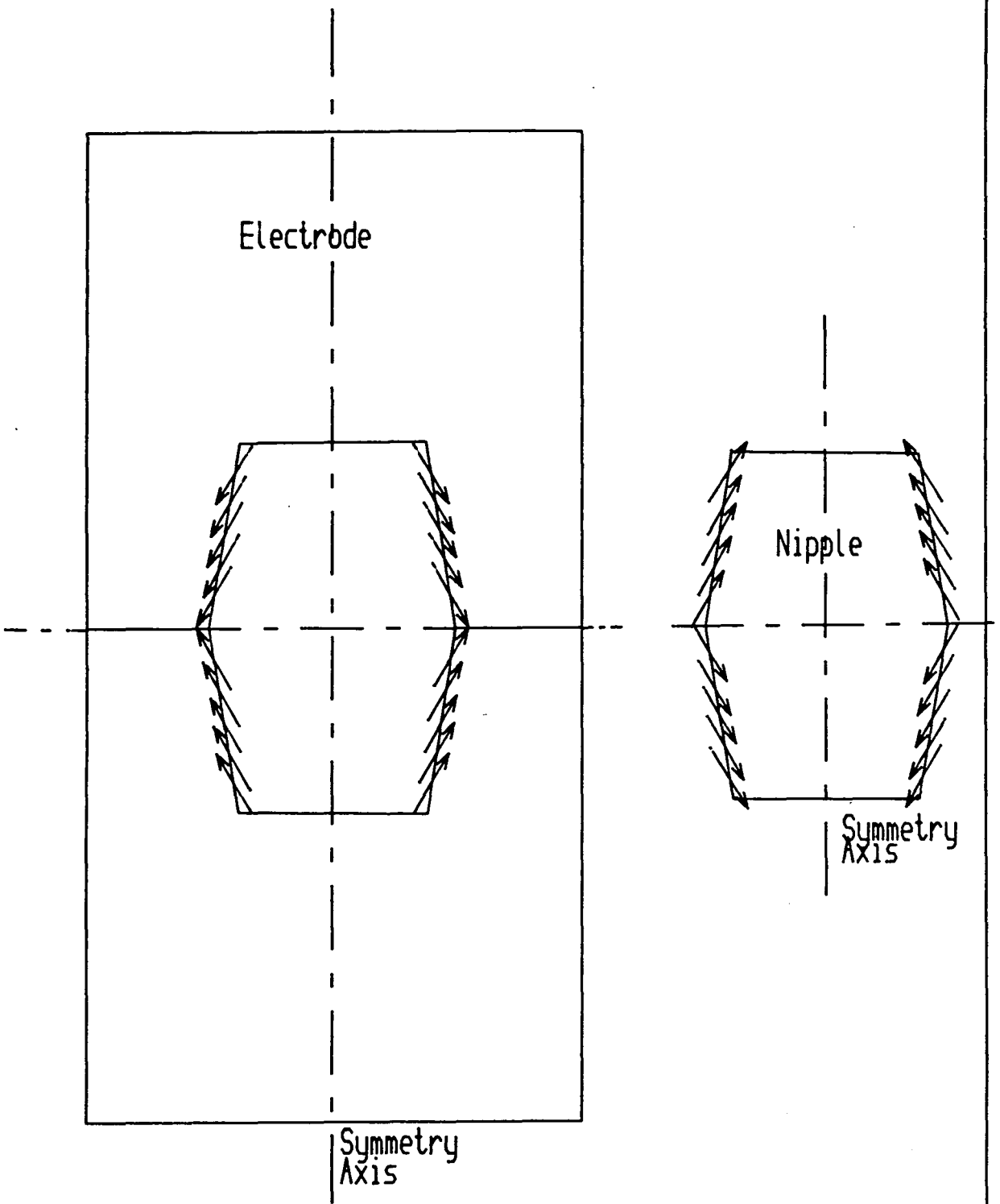

Fig. 3.1 Equilibrium force distribution in electrode.

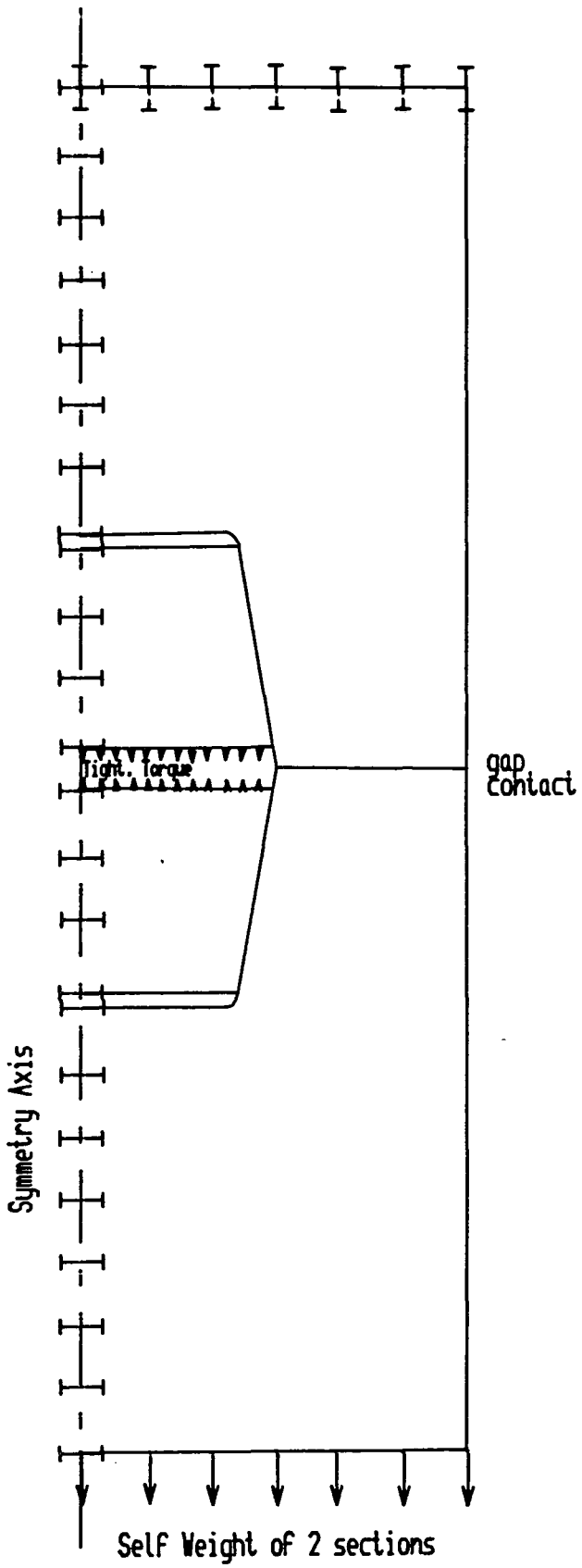

Fig. 3.2 A possible method of mechanical load application.

Fig 3.3 Variation of axial force with μ

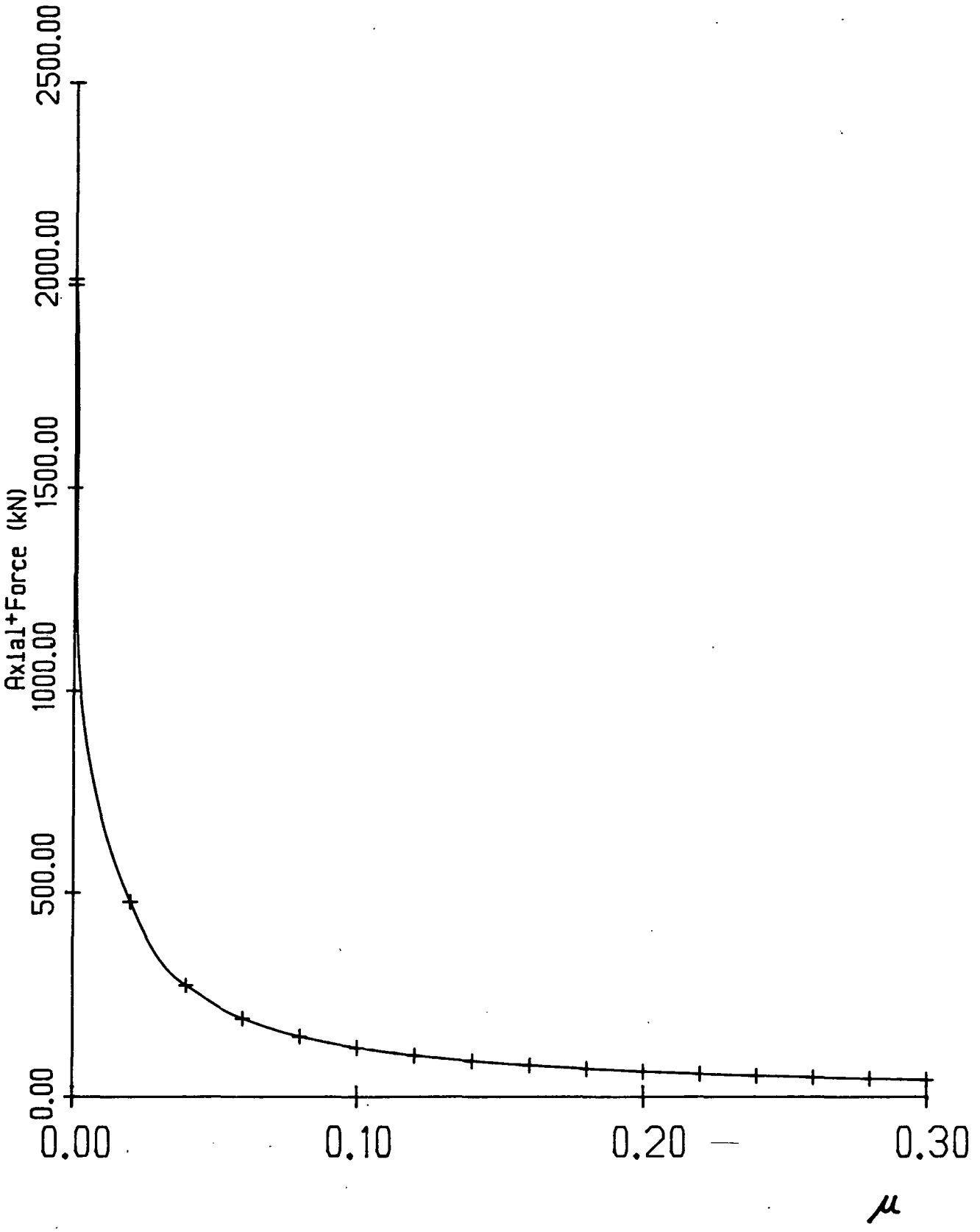

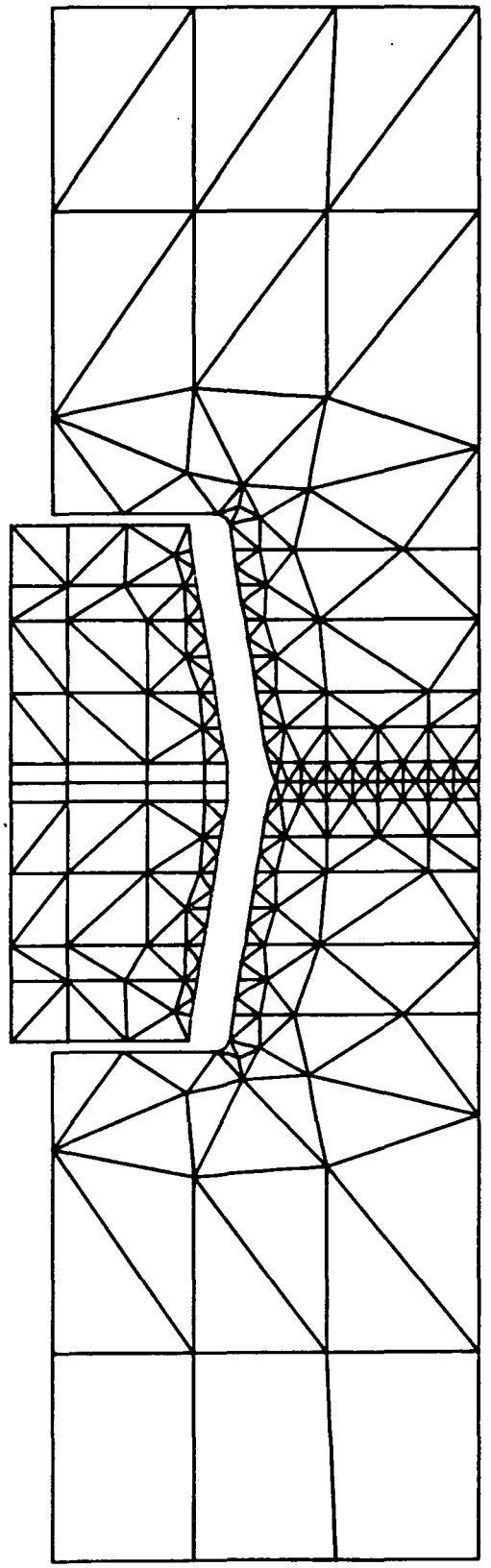

Fig. 3.4 E8 Finite Element Mesh.

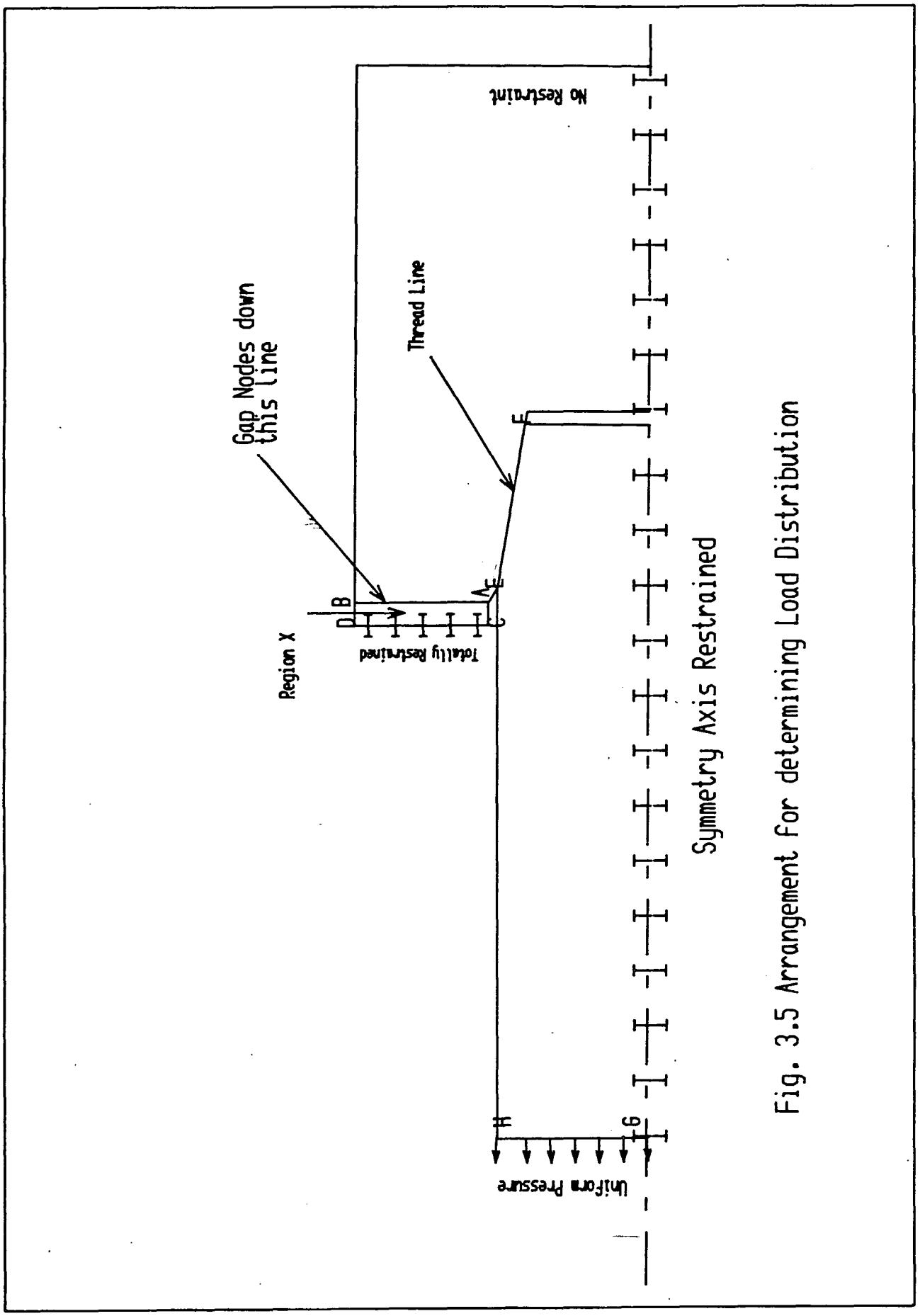

Fig. 3.5 Arrangement For determining Load Distribution

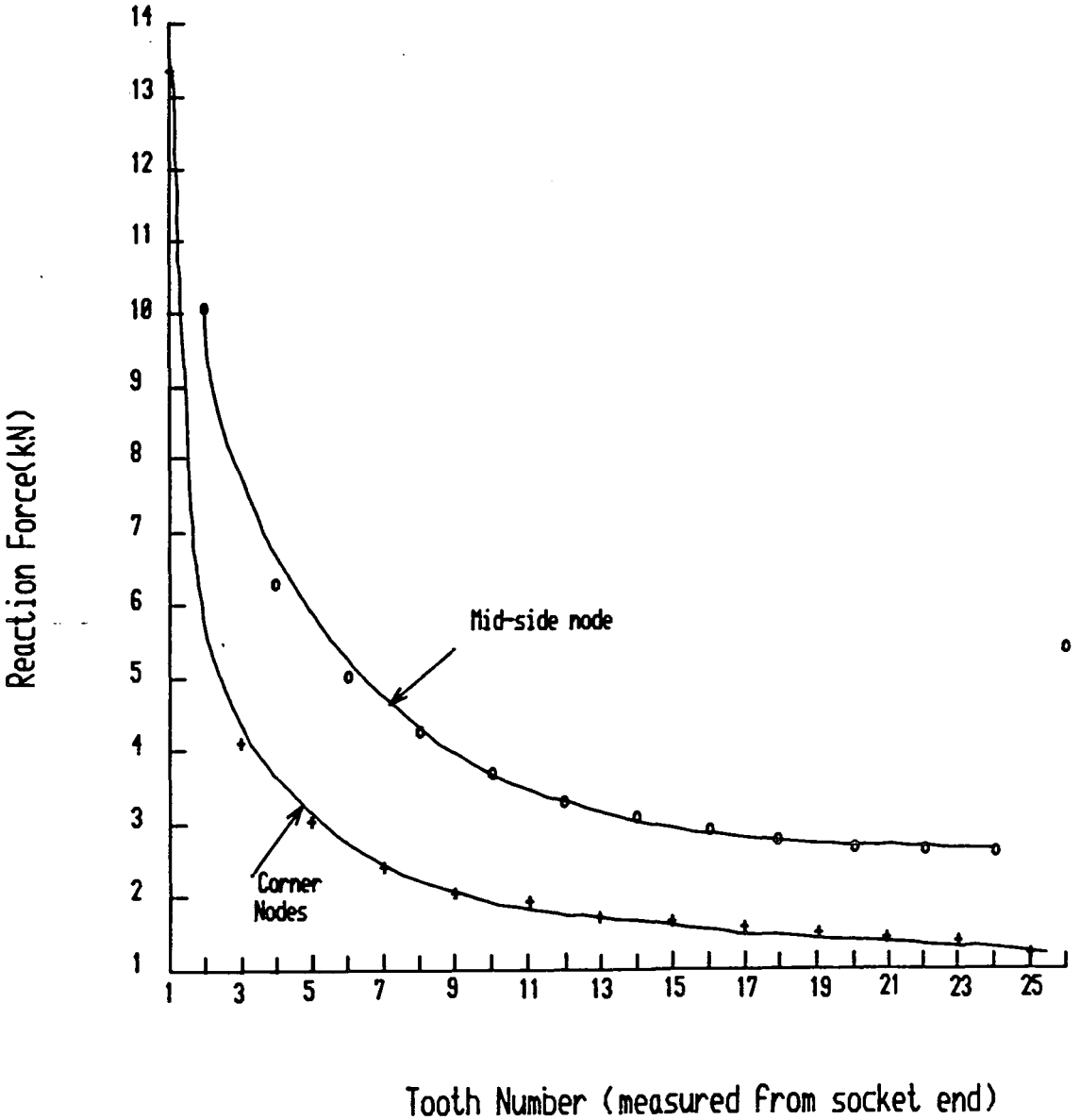

Fig. 3.6 Reactions down thread teeth
(E8 mesh, mechanical forces.)

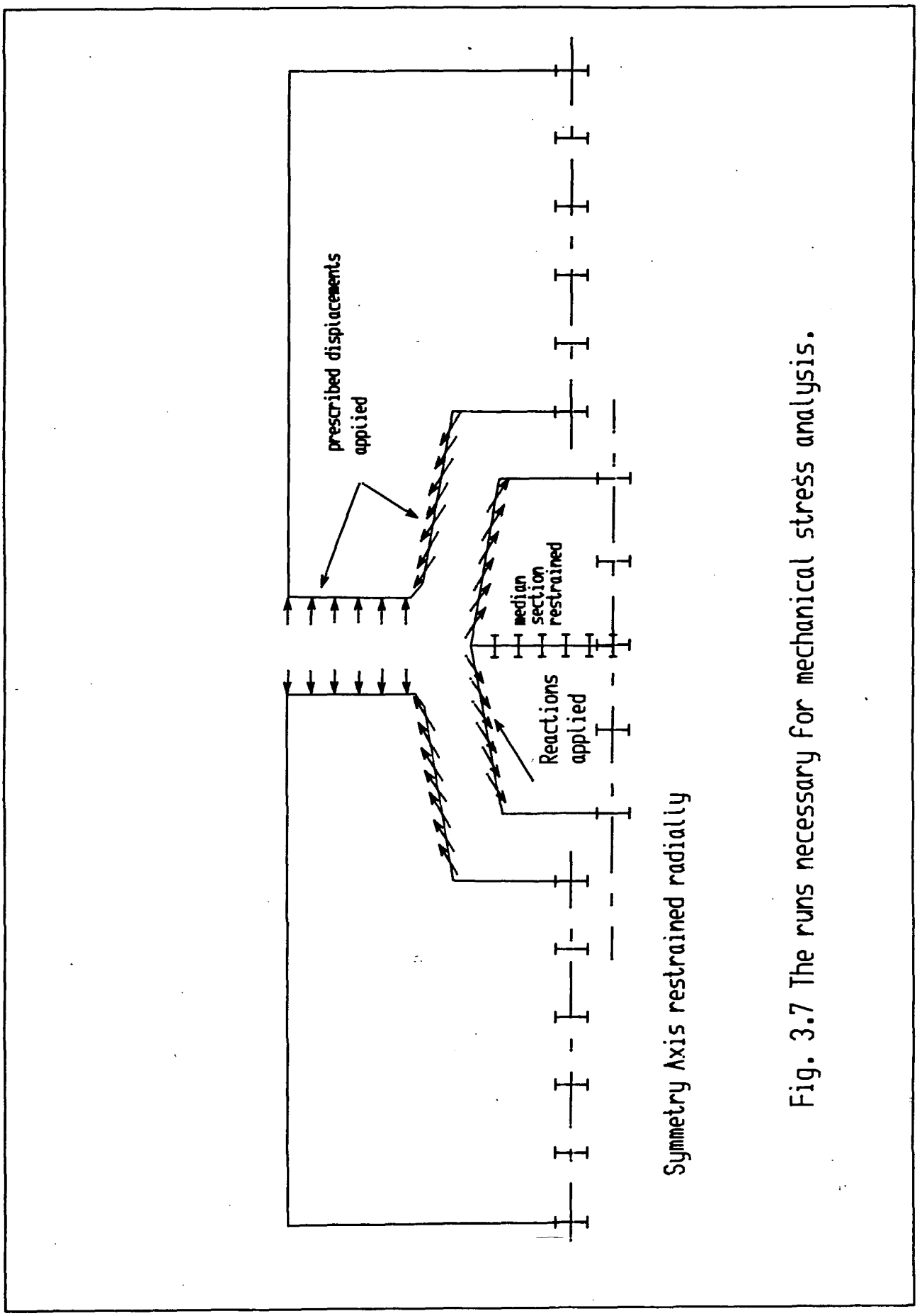

Fig. 3.7 The runs necessary for mechanical stress analysis.

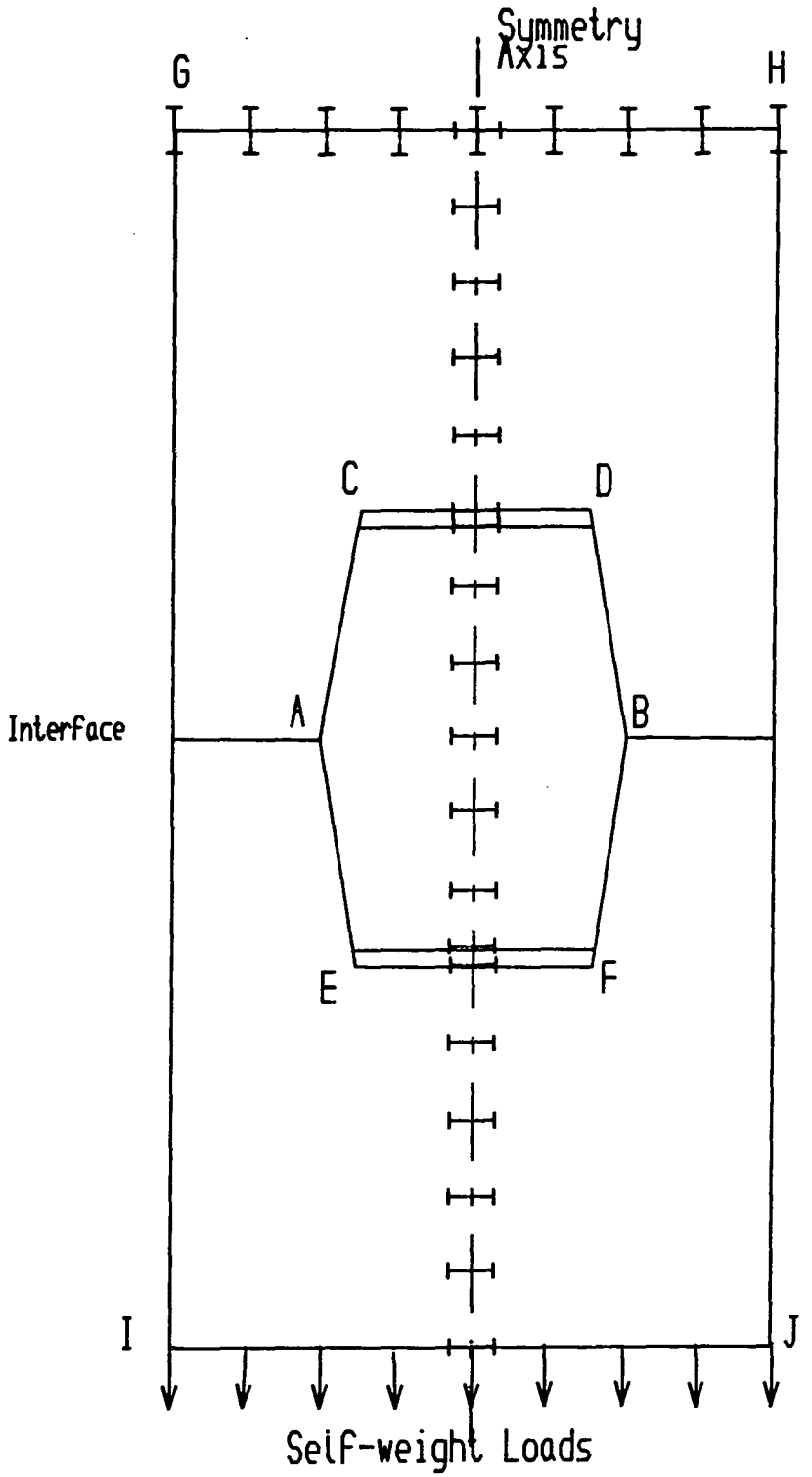

Fig. 3.8 Arrangement for self-weight
Stress Analysis.

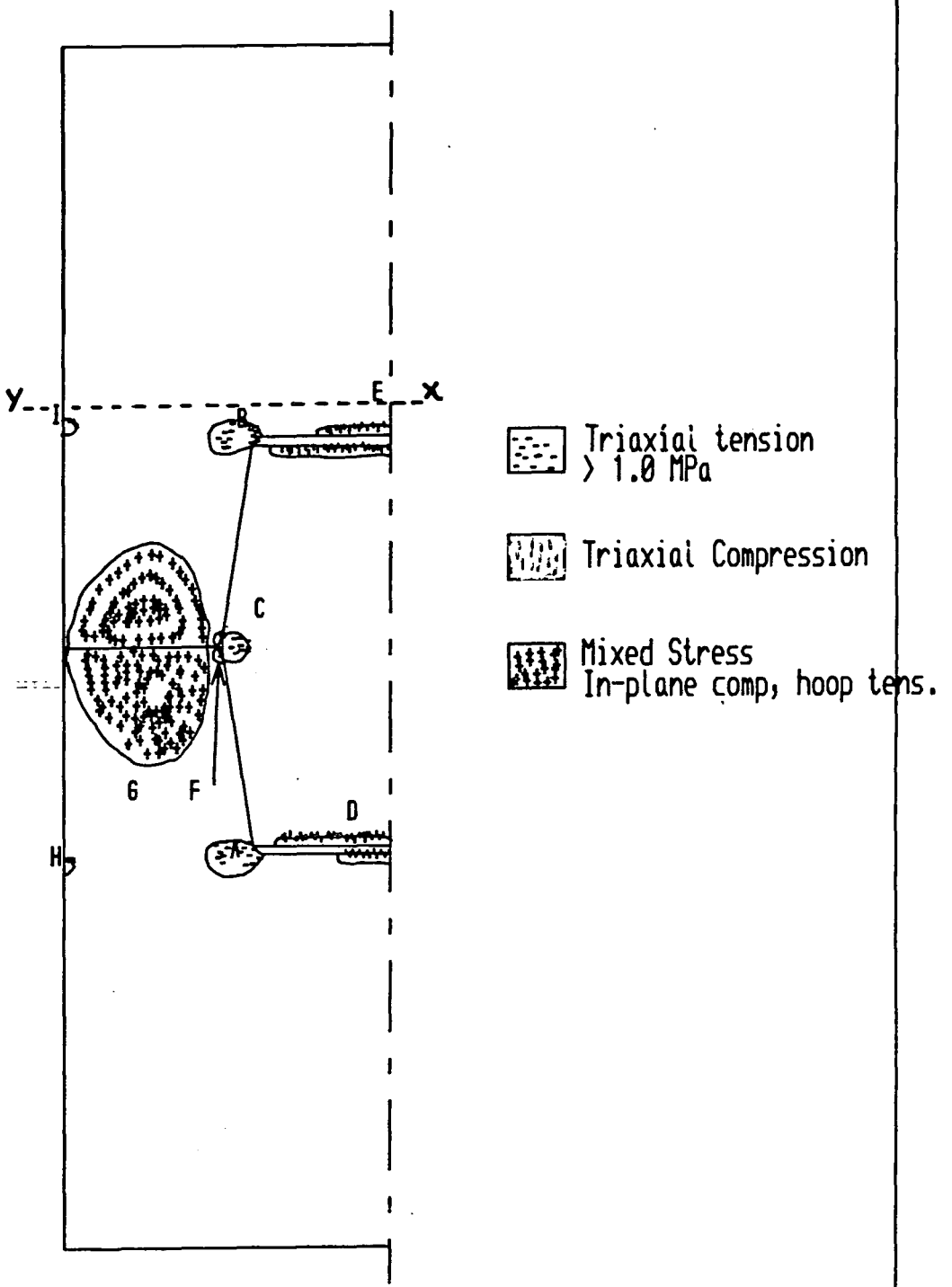

Fig. 3.9 Mechanically stressed regions of an electrode

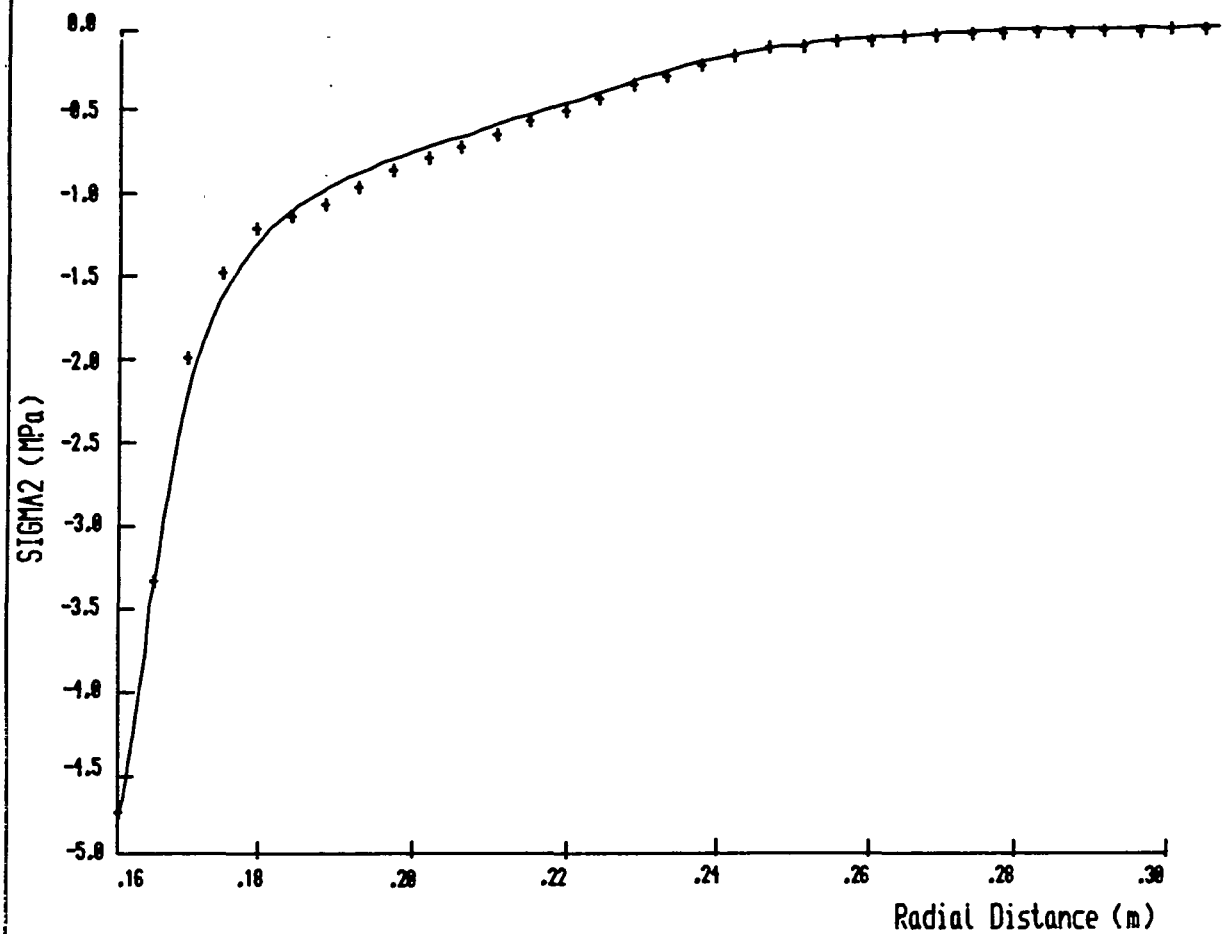

Fig. 3.10 Compressive principal stress across interface (E8)

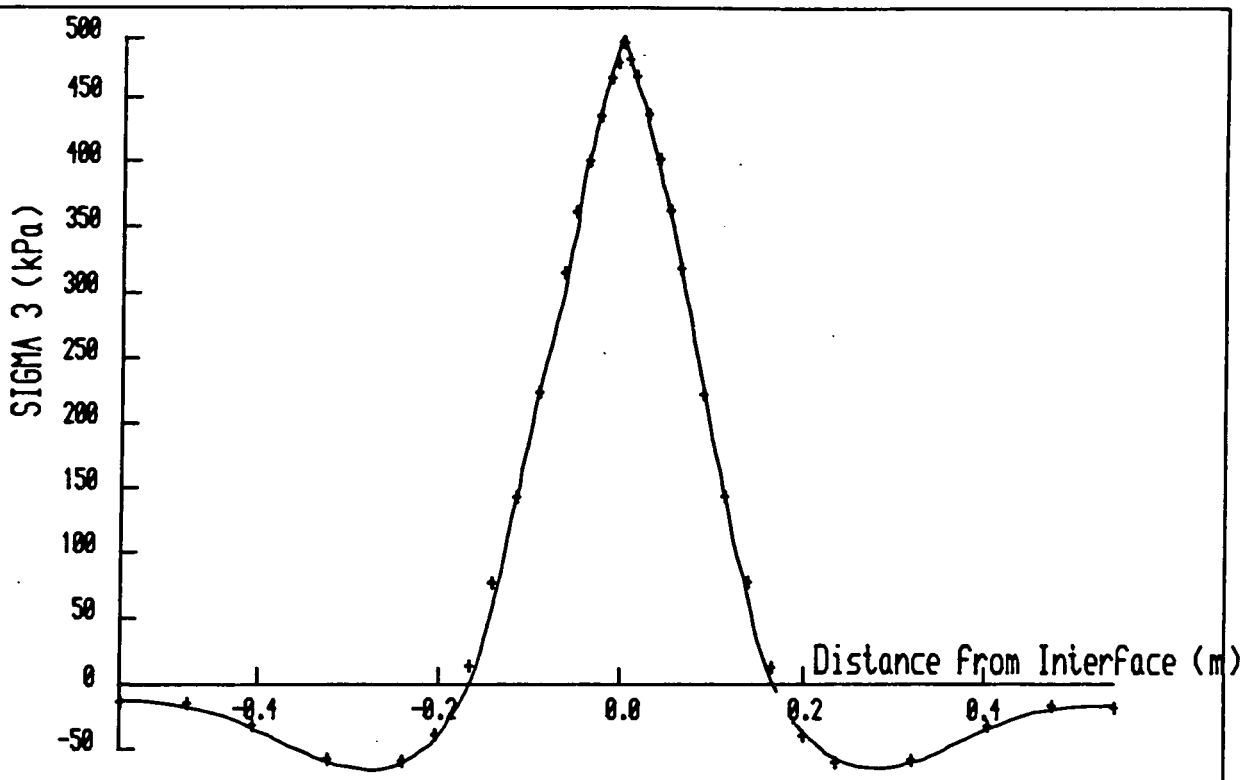

Fig. 3.11(a) Surface hoopstress vs dist. from Tip

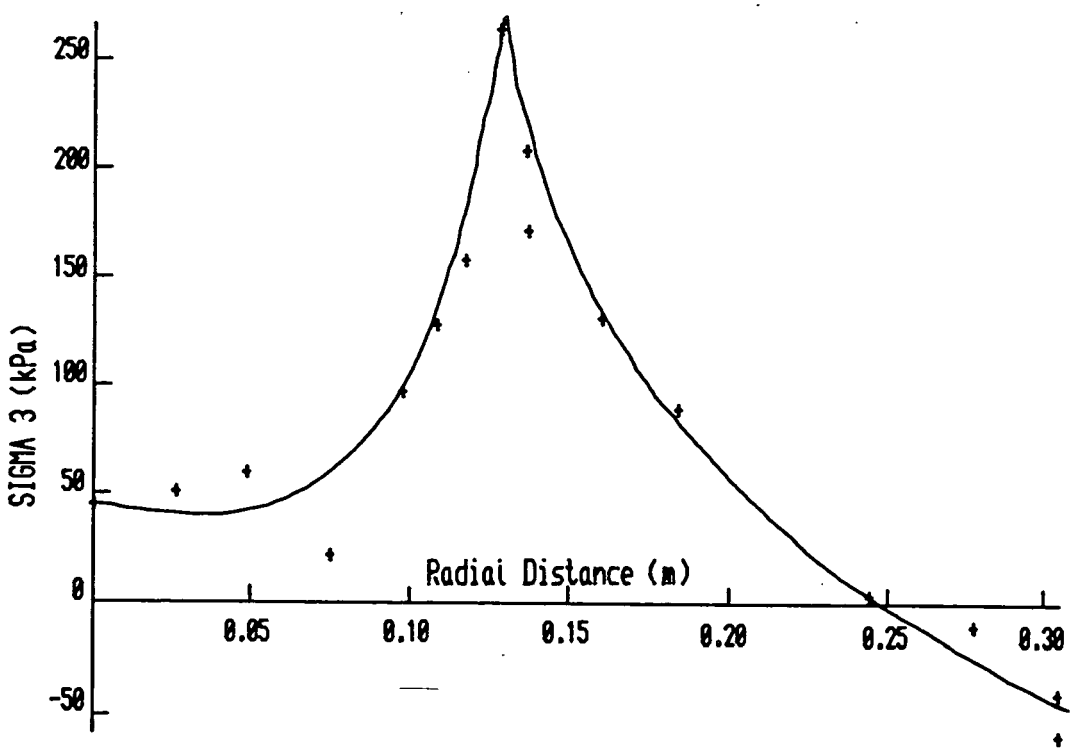

Fig. 3.11(b) Hoop Stress on Socket Base Nodes.

CHAPTER 4

THE ANALYSIS OF THERMAL STRESSES

4.1 Thermal Shock Effects

The electrode experiences thermal shock effects both on initial warm-up and on removal from the furnace for recharging. Initial warm-up from cold occurs only when the furnace has been shut down for some time. Removal of a hot electrode, on the other hand, occurs frequently during the manufacturing process, and because of the large temperature difference between the electrode and surroundings, the surface cooling and, therefore, hoop stresses, are much more severe. The thermal shock analysis was therefore confined to the removal of the electrode from the furnace.

In order to perform a thermal shock stress analysis, it is necessary to obtain a description of the variation of the temperature fields within the electrode with time. Facilities exist within PAFEC for the calculation of transient temperature fields. However, these are inappropriate for the present problem because of the method provided for defining heat-transfer coefficients. In PAFEC, only linear heat transfer is catered for i.e. those situations in which the rate of energy transfer is proportional to the temperature difference.

The present problem has a fourth-power dependency of heat loss on absolute temperature due to the predominantly radiative heat loss, so that, if the temperatures are to be evaluated using PAFEC, this would

involve the calculation of an effective heat-transfer coefficient at each nodal point on the surface, depending on its temperature. Since, after a small timestep, all the nodal temperatures change, the effective coefficients would all need to be recalculated before the next timestep, and so on until the required analysis time is reached. This is a very tedious and error-prone procedure, and another course of action was sought.

4.2 The Finite Difference Approach

Montgomery et al. (1979) outlined a set of Finite Difference equations suitable for calculating the temperature distribution in an axisymmetric body at a time $t+\Delta t$, given the distribution at time t. Despite lack of detail in the derivation and some errors in the equations, the ideas were used to form the basis of a major computer program for temperature calculation. By a series of applications of a basic set of finite difference equations, the program predicts the temperature field at any time t, given the field at time t=0. A further program displays the results graphically as a series of temperature contours. Because a regular mesh was used for the Finite Difference procedure, an interpolation program is required to assign temperatures to the Finite Element nodes, which will not normally coincide with the Finite Difference nodes. In this way, thermal stresses may be calculated using finite elements.

On removal from the furnace, an electrode loses heat in two ways. Convection currents in the air surrounding the electrode carry away heat at a rate depending on the excess temperature of the electrode over its surroundings, and radiation from the white-hot surface is responsible for heat flow at a rate proportional to the fourth power of the absolute temperature excess. At these temperatures, radiation is by far the most important mechanism for heat loss from the electrode. As a first approximation, therefore, the following assumptions were embodied in the Finite Difference program:

(i) The electrode is a semi-infinite cylinder of uniform properties i.e. no tapering has taken place; end effects are only important at the electrode tip; the thermal properties of the nipple are identical to those of the electrode.

(ii) Axial heat flow ceases at distances from the electrode tip greater than three times the electrode radius (Weng, 1977). This is an important assumption, whose validity was checked in a later stage of the work by carrying out an equivalent analysis using four electrode radii as the critical distance for zero axial heat flow. The corresponding increase in computing time was not justified by the small difference in results. The heat

flows implied by this assumption are shown in Fig. 4.1.

(iii) The electrode radiates as a perfect black-body, and most of the heat loss is by radiation. The rate of convective heat loss is proportional to the difference in temperature between the electrode and its surroundings.

(iv) The electrode reaches a steady-state temperature distribution in the furnace before being instantaneously removed into the ambient workshop temperature. Whether or not this occurs in practice is open to some question, but the assumption is forced due to lack of reliable information to the contrary. If steady-state is not reached, then the initial temperature field could be different each time the electrode is removed.

(v) The material of the electrode is isotropic and homogenous and its mechanical and thermal properties are independent of the temperature.

(vi) The temperature distribution in the electrode is at all times axisymmetric. Previous work (Elliott, 1969) has shown this to be a valid assumption.

4.3 Finite Difference Theory

The problem of finding the temperature distribution on removal from the furnace is that of solving the basic heat conduction equation assuming no heat generation (Timoshenko, 1951)

$$D\nabla^2\theta = \frac{\partial\theta}{\partial t} \qquad (4.1)$$

where θ is the temperature and D the Thermal Diffusivity of the material. Rewriting this in cylindrical coordinates we obtain

$$D\left\{\frac{\partial^2\theta}{\partial r^2} + \frac{1}{r}\frac{\partial\theta}{\partial r} + \frac{\partial^2\theta}{\partial z^2}\right\} = \frac{\partial\theta}{\partial t} \qquad (4.2)$$

where r and z are the radial and axial coordinates respectively. This is the appropriate equation to solve in the present problem.

In order to transform this equation into computer algorithms, the double and single partial differentials must be rewritten as expressions involving the appropriate finite differences.

Assuming a radial temperature variation, the quantity $(\partial\theta/\partial r)$ may be evaluated approximately at the point (r,z) by the following expression.

$$\left(\frac{\partial\theta}{\partial r}\right)_{r,z,t} = \frac{\theta_{r+\Delta r,z,t} - \theta_{r-\Delta r,z,t}}{2\Delta r}$$

where Δr is a small increment in the radial direction.

Similarly, at the points (r-Δr) and (r+Δr) we may write

$$\left(\frac{\partial\theta}{\partial r}\right)_{r-\Delta r,z,t} = \frac{\theta_{r,z,t} - \theta_{r-\Delta r,z,t}}{\Delta r}$$

and

$$\left(\frac{\partial\theta}{\partial r}\right)_{r+\Delta r,z,t} = \frac{\theta_{r+\Delta r,z,t} - \theta_{r,z,t}}{\Delta r}$$

The expression $(\partial^2\theta/\partial r^2)$ is therefore approximately represented by

$$\left(\frac{\partial^2\theta}{\partial r^2}\right)_{r,z,t} = \frac{(\theta_{r+\Delta r,z,t} + \theta_{r-\Delta r,z,t} - 2\theta_{r,z,t})}{(\Delta r)^2}$$

Similarly, we may write an expression for the axial derivative

$$\left(\frac{\partial^2\theta}{\partial z^2}\right)_{r,z,t} = \frac{(\theta_{r,z+\Delta z,t} + \theta_{r,z-\Delta z,t} - 2\theta_{r,z,t})}{(\Delta z)^2}$$

where Δz is a small increment in the axial direction.

Using these finite difference representaions we can rewrite equation 4.2 as

$$\theta_{r,z,t+\Delta t} = \theta_{r,z,t} +$$

$$\frac{D\Delta t[(2r+\Delta r)\theta_{r+\Delta r,z,t} + (2r-\Delta r)\theta_{r-\Delta r,z,t} - 4r\theta_{r,z,t}}{2r(\Delta r)^2}$$

$$+ \quad \frac{\theta_{r,z+\Delta z,t} + \theta_{r,z-\Delta z,t} - 2\theta_{r,z,t}]}{(\Delta z)^2} \qquad (4.3)$$

using the fact that

$$\frac{\partial\theta}{\partial t} \approx \frac{\theta_{r,z,t+\Delta t} - \theta_{r,z,t}}{\Delta t}$$

Equation 4.3 is an extremely useful relationship, enabling the temperature at any point (r,z) to be evaluated after a time interval Δt, given the initial temperature field. The temperature at the point at time $t+\Delta t$ is evaluated from the temperatures at the neighbouring points at time t. Equation 4.3 was used as the basic algorithm for the Finite Difference computer program. The following points about equation 4.3 should be noted:

(i) It cannot be used for points lying on the axis of the electrode, since a value cannot be assigned to the temperature $\theta_{r-\Delta r}$.

(ii) It cannot be used for a point lying on the sidewall or end surfaces of the electrode because in this case values cannot be assigned to the temperatures $\theta_{r+\Delta r}$ and $\theta_{z-\Delta z}$ respectively.

(iii) It makes no mention of radiative or convective heat loss from the surface of the electrode.

While equation 4.3 can be used for temperature calculations in any part of the electrode body, it requires modification for points on the axis or surface of the electrode. Fig. 4.2 shows the particular regions which require special consderation.

(A) THE CENTRAL AXIS (r=0, 0 < z < 3R)

It can be shown (Smith, 1965) that, if the problem is symmetrical about the origin

$$\lim_{r \to 0} \frac{1}{r} \frac{\partial}{\partial r} = \frac{\partial^2}{\partial r^2}$$

Substituting in eq 4.3 we obtain

$$\theta_{r,z,t+\Delta t} = \theta_{r,z,t} + \frac{(\theta_{r,z+\Delta z,t} + \theta_{r,z-\Delta z,t} - 2\theta_{r,z,t})}{(\Delta r)^2}$$

$$+ \frac{2(\theta_{r+\Delta r,z,t} + \theta_{r-\Delta r,z,t} - 2\theta_{r,z,t})}{(\Delta z)^2}$$

Since, at r=0, $\theta_{r+\Delta r} = \theta_{r-\Delta r}$ for axisymmetry

$$\theta_{0,z,t+\Delta t} = \theta_{0,z,t} + \frac{4D\Delta t(\theta_{0+\Delta r,z,t} + \theta_{0,z,t})}{(\Delta r)^2}$$

$$+ \frac{D\Delta t(\theta_{0,z+\Delta z,t} + \theta_{0,z-\Delta z,t} - 2\theta_{0,z,t})}{(\Delta z)^2} \qquad (4.4)$$

and this is the equation applicable to this region

(B) THE SIDEWALL SURFACE (r=R, 0 < Z < 3R)

Let θ'_R represent the quantity $(\partial\theta/\partial r)_R$ where R is the electrode radius. Then

$$\theta_{R+\Delta r} = \theta_R + \Delta r \theta'_R \qquad (4.5)$$

Consider the expression (extracted from equation 4.3)

$$\frac{(2r+\Delta r)\theta_{r+\Delta r,z,t} + (2r-\Delta r)\theta_{r-\Delta\theta,z,t} - 4r\theta_{r,z,t}}{2r(\Delta r)^2}$$

Evaluating this at r=R and substituting 4.5 we obtain

$$\frac{(2r+\Delta r)(\theta_{R,z,t} + \Delta r\theta'_{R,z,t}) + (2R-\Delta r)\theta_{R-\Delta r,z,t} - 4R\theta_{R,z,t}}{2r(\Delta r)^2}$$

which simplifies to

$$\frac{2(\theta_{R-\Delta r,z,t} - \theta_{R,z,t})}{(\Delta r)^2} + \frac{(2R+\Delta r)\theta'_{R,z,t}}{R\Delta r}$$

Now, at the surface

$$\frac{dq}{dt} = \frac{-kd\theta}{dr} = -k\theta'_{R,z,t} \qquad (4.6)$$

for unit area, where k=thermal conductivity and dq/dt = rate of heat loss

Since, at the surface we also have

$$(dq/dt)_R = S[(\theta_R+273)^4 - (\theta_A+273)^4] + h(\theta_R - \theta_A) \qquad (4.7)$$

(where S = Stephan's constant, θ_R = sidewall temperature

θ_A = workshop ambient temperature, h = convection coefficient)

then the equivalent form for equation 4.3 at the sidewall surface becomes

$$\theta_{R,z,t+\Delta t} = \theta_{R,z,t}$$

$$+ D\Delta t\left[\frac{2(\theta_{R-\Delta r,z,t} - \theta_{R,z,t})}{(\Delta r)^2}\right.$$

$$\frac{-(2R+\Delta r)\{S[(\theta_{R,z,t}+273)^4 - (\theta_A+273)^4] + h(\theta_{R,z,t} - \theta_A)\}}{R\Delta rk}$$

$$\left. + \frac{\theta_{R,z+\Delta z,t} + \theta_{R,z-\Delta z,t} - 2\theta_{R,z,t}}{(\Delta z)^2}\right] \qquad (4.8)$$

(C) THE BOUNDARY OF THE AXIAL FLOW SECTION (Z=3R, 0 < r <R)

In this region there is no z-dependence of the temperature field so the axial terms in equation 4.3 may be disregarded. The equation applicable to this region is therefore

$$\theta_{r,3R,t+\Delta t} = \theta_{r,3R,t} + D\Delta t\left[\frac{(2r+\Delta r)\theta_{r+\Delta r,3R,t} + (2r-\Delta r)\theta_{r-\Delta r,3R,t} - 4r\theta_{r,3R,t}}{2r(\Delta r)^2}\right] \quad (4.9)$$

(D) THE END FACE OF THE ELECTRODE (0 < r < R, Z=0)

Clearly, the conditions here are similar to those in (B), and the equivalent form for the equation (paying due regard to sign) is:

$$\theta_{r,0,t+\Delta t} = \theta_{r,0,t} + D\Delta t\left[\frac{(2r+\Delta r)\theta_{r+\Delta r,0,t} + (2r-\Delta r)\theta_{r-\Delta r,0,t} - 4r\theta_{r,0,t}}{2r(\Delta r)^2} - \frac{2\{S[(\theta_{r,0,t}+273)^4 - (\theta_A+273)^4] + h(\theta_{r,0,t}-\theta_A)\}}{k\Delta z} + \frac{2(\theta_{r,0+\Delta z,t} - \theta_{r,0,t})}{(\Delta z)^2}\right] \quad (4.10)$$

(E) THE END FACE, AT THE CENTRE (r=0, Z=0)

Using the fact that

$$\lim_{r\to 0} \frac{1}{r}\frac{\partial}{\partial r} = \frac{\partial^2}{\partial r^2}$$

we obtain

$$\theta_{0,0,t+\Delta t} = \theta_{0,0,t}$$

$$+ D\Delta t\left[\frac{4(\theta_{0+\Delta r,0,t}-\theta_{0,0,t})}{(\Delta r)^2}\right.$$

$$\left.+\frac{2(\theta_{0,0+\Delta z,t}-\theta_{0,0,t})}{(\Delta z)^2}\right.$$

$$\left.-\frac{2[S[(\theta_{0,0,t}+273)^4-(\theta_A+273)^4]+h(\theta_{0,0,t}-\theta_A)]}{k\Delta z}\right]$$

(4.11)

(F) THE BOTTOM CORNER OF THE ELECTRODE (Z=0, r=R).

Here, cooling takes place from the bottom and side surfaces. We may therefore combine the ideas in sections (B) and (D) to obtain

$$\theta_{R,0,t+\Delta t} = \theta_{R,0,t}$$

$$+ D\Delta t\left[\frac{2(\theta_{R-\Delta r,0,t}-\theta_{R,0,t})}{(\Delta r)^2}\right.$$

$$\left.+\frac{2(\theta_{R,0+\Delta z,t}-\theta_{R,0,t})}{(\Delta z)^2}\right.-$$

$$\frac{[\Delta z(2R+\Delta r)+2(R\Delta r)]\{S[(\theta_{R,0,t}+273)^4-(\theta_A+273)^4]+h(\theta_{R,0,t}-\theta_A)\}]}{R\Delta rk\Delta z}$$

(4.12)

as the equation applicable to this region.

(G) ON THE AXIS AT THE BOUNDARY OF AXIAL FLOW (Z=3R, r=0)

Assuming no z- dependence and using

$$\lim_{r\to 0} \frac{1}{r}\frac{\partial}{\partial r} = \frac{\partial^2}{\partial r^2}$$

we obtain

$$\theta_{0,3R,t+\Delta t} = \theta_{0,3R,t} + 4D\Delta t\left[\frac{\theta_{0+\Delta r,3R,t} - \theta_{0,3R,t}}{(\Delta r)^2}\right] \qquad (4.13)$$

(H) ON THE SURFACE, AT THE BOUNDARY OF AXIAL FLOW. (z=3R, r=R

Assuming no z-dependence we obtain from equation (4.8)

$$\theta_{R,3R,t+\Delta t} = \theta_{R,3R,t} + D\Delta t\left[\frac{2(\theta_{R-\Delta r,3R,t} - \theta_{R,3R,t})}{(\Delta r)^2} - \frac{(2R+\Delta r)\{S[(\theta_{R,3R,t}+273)^4 - (\theta_A+273)^4] + h(\theta_{R,3R,t} - \theta_A)\}}{r\Delta rk}\right] \qquad (4.14)$$

Equations 4.3, 4.4 and 4.8-4.14 thus provide a complete transient analysis of the temperatures in the electrode. The Finite Difference process can be seen as a series of successive solutions of these equations. If an initial temperature field is defined, the temperature at any time, t, afterwards may be found by successive applications of the Finite Difference equations. This set of equations was used to construct a computer program capable of predicting the temperature at any time after

removal from the furnace, given an initial temperature field defined by (Montgomery, 1979):

$$\theta_{r,z} = 1650 + 200(1-[r^2/R^2]) + 250\exp(-z/r) + 1650\exp(-3[z+r]/R) \quad (4.15)$$

4.4 The Computer Implementation

Overall Philosophies

(i) The program was written so that modifications and improvements could be easily made at a later date.

(ii) Several of the parameters used to run the program were placed under user control to increase flexibility and must therefore be entered as the program is run. The user is prompted to enter the required numbers in free format.

(iii) The program was organised so that no confusion would arise in interpretation of the output. Each temperature field is therefore output into a separate magnetic disc file which is automatically created and identified by the program with a unique filename. This filename is the analysed elapsed time in seconds.

(iv) The starting point for the program may be an internally generated field as used by Montgomery et.al. (1979), or an externally produced field which is read from a disc file.

(v) The temperature fields were written by the program in such a way as to be readable by the interpolation program (see later), without further processing, thus preserving the identity of the temperature fields.

A full description of the Finite Difference program, and explanatory flow-diagrams, will be found in Appendix II.

Before using the Finite Difference scheme it was thoroughly tested using a range of mesh sizes and timesteps. Several different initial temperature fields were tried, including uniform temperature, and linearly varying temperatures (in both axial and radial directions). By using such simple fields as these, it is easy to ensure that there are no anomalies in the temperature predictions. Thorough investigation showed only one discrepancy, which occurred when the timestep was varied. This was done in order to verify that the program would arrive at the same temperature field after a given analysis time, using various timestep values. It was found that, for timestep values above about 5-6 seconds, instability occured at certain nodes, whose temperature began to oscillate wildly.

The computer formulation of the Finite Difference equations was carefully checked and found to be correct, so the problem was assumed to lie in the Finite Difference equations themselves. Reference to standard works on Finite Difference methods (Smith, 1978) revealed that it was not possible to obtain the stability and convergence conditions for equations such as these. From examination of the form of the finite difference equations, however, it is obvious that the stability conditions depend on a compromise between the (fixed) diffusivity, the timestep and the mesh spacing (Δr) It had to be accepted therefore that the scheme could only be operated on a relatively small timestep (4 seconds was chosen as an acceptable compromise).

A post-processing program was also written to read the output files from the finite difference program and present the results graphically. This was a short program consisting almost entirely of calls to subroutines in the commercial GINO subroutine library, and will not be described here.

4.5 The Need For Interpolation

There are two main disadvantages in using a combination of the Finite Difference and Finite Element approaches

(i) The Finite Difference formulation places limitations upon the complexity of geometry which can be considered. The formulation just

described limits the outer boundary to being a straight-sided cylinder. Tapering of the electrode may not easily be simulated with this formulation. Irregular Finite Difference meshes may be used, but operating conditions of the electrode are so variable that the boundary conditions for the model are in any case poorly defined. For example, during use the electrode develops not only a taper, but also a variable amount of rounding, cracking and formation of holes at the tip. The results from any overall model of such a complex shape may only be given general interpretation, and so the extra complexity involved in the computer modelling of the geometry changes was not considered worthwile.

(iii) The finite element nodal points are not, in general, coincident with those on the regular Finite Difference mesh. (Fig. 4.3 shows the problem more clearly). An interpolation program is therefore required which, given the temperatures at the Finite Difference nodes, will assign a temperature to each of the Finite Element nodes.

An interpolation program was therefore written (Appendix II) to read directly the output files written by

the Finite Difference program, assigning temperatures to the Finite Element nodal points.

4.6 The Interpolation program

General Philosophies

(i) The program must be adaptable i.e. not specific to one particular Finite Element Mesh.

(ii) The input data format must be simple.

(iii) There must be no confusion over identification of the output. The program therefore must label the output file and write into it comments which positively identify the sources of all the input information.

(iv) The continuity of the interpolation at the boundaries of a Finite Difference cell must be satisfactory.

(v) The temperature contours produced by the interpolated temperatures must be practically identical to the original Finite Difference contours.

(vi) The output from the interpolation program must be a file which is directly readable by PAFEC. Module headers and a title must therefore automatically be written by the program, as well as suitable comment cards.

The program produced to satisfy these requirements centres on a bicubic spline interpolation subroutine in the commercial NAG library. Briefly, a spline is a set of piecewise continuous polynomials which may be used to approximate a function over a given interval. Simplifying, for the present, the two-dimensional temperature distribution by a radial-only variation, we may consider the Finite Difference temperatures as particular values of some unknown but complicated function which represents the radial variation. By choosing a set of polynomials to represent the variation between pairs of nodes, ensuring that the end-point temperatures are correctly predicted, interpolation between nodes is possible. Cubics are normally chosen for the polynomials since the first and second derivatives exist at the end points of the approximation interval.

The NAG bicubic spline interpolation subroutine enables 2-dimensional interpolation to be performed by using the above procedure in two orthogonal directions over the temperature field. By averaging the interpolated values (which in practice are almost identical) in the two directions a unique temperature can be assigned to any point within the grid, provided the coordinates of the point are known. A full description of the interpolation program is to be found in Appendix III. Before use the interpolation program was carefully tested as follows.

(i) A copy of the program was made and modified to enable 'single shot' interpolation to be performed. A pair of coordinates typed in would thus produce a single result which could then be carefully examined. Using one of the Finite Difference fields, a particular cell of four temperatures was chosen, and interpolation performed along several selected lines through the cell. Fig. 4.4 shows the results. The smoothness of the line of inerpolated values and the good continuity at the boundaries suggests that the program is satisfactory. Note that the interpolated temperature at a point on one of the lines may be greater than the two end-point temperatures.

(ii) A PAFEC run was carried out for a particular timestep using temperature distribution elements rather than stress elements, the input data being the interpolated temperatures calculated by the program. PAFEC was programmed to calculate temperatures and plot the results as a series of contours. Since, in this case, all the temperatures are 'known', the resultant contours will represent the interpolated temperature field. Careful comparison with the original Finite

Difference field showed the differences to be negligible, and this was regarded as adequate proof of the accuracy of the interpolated field.

4.7 Temperature Distribution and Thermal Stress Results

An analysis of the thermal shock stresses produced when an electrode is removed from the furnace was now posssible. The analysis consists of the following steps:

(i) Run the Finite Difference program with suitable input data to obtain the temperature distributions at various times after removal.

(ii) Examine the resultant temperature fields using the graphics output program.

(iii) Set up a file containing the Finite Element coordinates.

(iv) For each timestep, run the interpolation program to read from the numbered temperature files and assign temperatures to the Finite Element nodes.

(v) For each timestep, attach the file of interpolated temperatures to a previously-prepared PAFEC 'base' file containing all the information for the stressing run apart from the interpolated temperatures.

(vi) Run PAFEC to calculate the stresses.

A finite Difference run was therefore performed using 19 radial nodes and a timestep value of 4.0 seconds, assuming a works ambient temperature of 30°C.

The results were then processed by the graphical conversion program and the resultant contours for two timestep values are shown in Fig. 4.5 (note that this diagram is not quite to scale - the space provided for plotting contours is constant, regardless of the length of electrode analysed). The important points to note about the temperature fields are:

(i) The time t=0 (initial temperature field) has a 'hot spot' at the end of the electrode, on the axis. This is at 3500°C and represents the point where the arc makes contact with the electrode. The surface temperature gradients are small. Of course, this temperature field is only a graphical representation of the equation used to describe it (equation 4.15) and is simply a starting-point for the program. It is only one of a large number of equally valid starting fields, but does represent approximately a correspondence with the temperatures measured by Nedopil & Storzer (1967).

(ii) The fields representing the 'cooled' electrode show the most severe temperature gradients to be near the sidewall and end surfaces. The internal temperature field varies relatively slowly. This is to be expected since the surface of the electrode is cooling at a rate proportional to the fourth power of the temperature difference between the surface of the electrode and the surroundings, whereas the conduction rate is directly proportional to the temperature difference. At such high temperatures, the difference in rate of heat flow due to the two mechanisms is considerable. The temperature field prediction is borne out by examination of a newly-failed electrode, the brightness of the surface layers being considerably less than that of the interior layers. High hoop stresses may therefore be expected as the outer layers contract onto the inner ones. Because of this rapid heat loss at the surface, the importance of the conduction mechanism is greatly reduced, and the magnitude of the surface hoop stresses are unlikely to be heavily dependent on the exact form of the initial internal temperature distribution. They will, however,

depend very much on the surface temperature. Fig 4.6 shows some graphs of the temperature distribution along selected lines in the electrode.

4.8 Thermal shock Stresses-Results

For an electrode bottom joint the stress field is due to a combination of mechanical and thermal stresses. The combined stresses are discussed in detail later in the chapter. The following points, however, emerge from an examination of the thermal-only stresses.

(i) there is a rapidly increasing hoop stress near the surface of the electrode, high enough to cause certain failure in the region for much of the time an electrode is out of the furnace.

(ii) High compressive stresses are induced near the socket entrance; these may be expected to be increased by mechanical loading, which also causes peak compressive stresses in this region.

(iii) Fairly high compressive stresses are induced at the base of the socket. A possible explanation for these is given later in the chapter, but it is noted here that these may be expected to 'swamp' the tensile stresses occurring in this region due to mechanical loading.

4.9 Combined Stresses

The thermal stresses obtained by the means described above were combined with the mechanical stresses calculated as described in Chapter III by the stress combination program, described in Appendix I. Table 4.1 shows some selected nodal points with their associated stress values. The row marked M.O. represents stresses due to mechanical loading under normal tightening torque. It is readily apparent that these are in all cases negligible in comparison to the thermal stress field. In discussing the combined stress field due to thermal and mechanical loading, the effects of the mechanical forces are very small and may be for most purposes neglected.

Significant triaxial tension (all three direct stresses > 1 MPa) exists on all surface nodes for a large proportion of the time analysed, the first 'easing' of this situation appearing at the 320 sec timestep at surface points near the bottom corner and the interface. Examination of the actual stresses at these points (nodes 7,21,269,428 in Table 4.1, for example) shows the tensile stresses occurring here to be well in excess of the material failure strength, a peak of 25.5 MPa appearing in the hoop stress at node 7. Stresses on surface nodes fall below the material failure strength only after an elapsed time of 1200 seconds.

The reason for these high stresses lies in the

rapid radiative cooling occurring at the surface when the electrode is removed from the furnace. Rapid contraction occurs both radially and longitudinally. The longitudinal component of contraction causes high values of σ_1 (most positive principal stress), parallel to the electrode axis (note the low values of β at nodes 21 and 428). At 'corner' nodes, of course, σ_1 does not act in the longitudinal direction.

Fig. 4.7 shows the variation of hoop stress along the length of the electrode for various times after removal from the furnace. From this we can see that the surface hoop stress peaks at the 320 second timestep, only becoming less than the mean failure stress after 1200 sec. These stresses may be considered to be purely thermal, the mechanical stresses in this region being several orders of magnitude smaller. The 'dips' in the line near the interface and the ends of the electrode may be attributed to the freedom of movement at the nearby corner. Thus, if the electrode/electrode interface were modelled as a continuum, the longitudinal and hoop stresses would have been expected to be constant over the interface. Modelling the interface with 'gaps' allows it to separate slightly on cooling, allowing some strain energy redistribution in the nearby region, and hence a perturbation in the stresses.

The high tensile hoop stresses at the surface of the electrode take the material well past its mean failure strength. However, it is worth noting that this is a fairly

localised effect. If we look, for example, at nodes 19 and 20 in Table 4.1 (these are just below the surface node 21) we see that the hoop stress reduces from 18 MPa to 5 MPa over a radial distance of only 5 cm.

The high tensile hoop stresses also have an effect at points within the electrode. Fig. 4.8, for example, shows, for the 640 second timestep, regions in triaxial compression (of magnitude > 1 MPa). In the general body of the electrode, these compressive stresses can be attributed to the 'sqeezing' effect caused by the difference in temperature between the body and the surface. The fillet radius acts as a stress concentrator. See node 75, in Table 4.1, for example, which has a peak compressive stress of around 20 MPa. Again, these stresses are almost entirely thermal. The severity of these stresses is worsened by the sliding action modelled across the thread teeth, which allows quite large radial displacements to be accomodated on the thread tooth line. Thus, had the thread tooth line been modelled by rigidly connected nodes, the radial contraction of the electrode would have been resisted by the nipple. With the sliding allowed, much greater radial displacements may be accommodated, raising the stress level at the fillet radius.

The change from compressive to tensile hoop stress is clearly shown in Fig. 4.9 which is a plot of hoop stress vs radial distance from the electrode axis, taken along a line of nodes just below the socket base (line XY in Fig.

3.9). This line passes through the compressive region around the socket base, but is some distance away from the really high stress concentration produced by the corner. Peak hoop stresses around the 640 second timestep are also clearly shown by this graph. An interesting point is that the lines all pass through a point corresponding to 1/3 of the electrode radius below the surface (node 319), this point enjoying almost zero thermal hoop stress.

A region under compressive in-plane stresses occurs near the socket entrance. Fig. 4.8 shows this region for the 640 second timestep. The presence of this region may be explained by the action of the screw thread under cooling. A larger coefficient of thermal expansion was used for the nipple than for the electrode. In a temperature field in which the inner regions are hotter than the outer regions, there will be a 'wedging' effect as the nipple teeth slide over the electrode teeth, causing high compressive stresses as the electrodes are forced together, and placing the nipple under tension in this region (see node 1314) at its edge. Node 480 shows this effect, with peak compressive stresses of around 15 MPa, again at the 640 second timestep. The size of this region varies only slightly over the time period analysed, showing that it is due to effects changing only slowly with time, i.e. the temperature of the inner regions of the electrode (see the temperature contour plots of Fig. 4.5).

It is worth noting that this is the only region in which the mechanical stresses provide any significant contribution to the stress field. As an example, node 273, on the inner region of the interface, suffers a peak total compressive stress of 27 MPa over the time period analysed (just in excess of the mean compressive failure strength). At this point the mechanical stress is about 4.7 MPa. Of course, as the thermal stresses in the region decrease (albeit slowly) as a function of time and distance, the mechanical stresses become a greater percentage of the total stress field. They are never sufficiently high, however, to significantly increase the failure probability.

Correspondingly, node 1314, on the nipple, has peak tensile stress of 15 MPa over the period analysed, at a point at which the mechanical stresses are 3.8 MPa.

Node 45 is in the quality control sampling region, at the end of the socket. This is in a state of generally low compressive stress throughout the time analysed. Although the removal of a core sample may well change the geometry sufficiently to cause high stress concentrations, it is fair to say that, given the necessity to take such samples, this is a reasonable region from which to take them.

Although this chapter has discussed the peak stresses occurring over the electrode, it should be noted that, for the majority of the time analysed, a good proportion of the electrode is in a 'safe' stress

situation, i.e. with all three stresses being of smaller magnitude than 5.0 MPa. Fig. 4.10 shows the extent of such regions for three representative timesteps of 80, 640, and 2400 seconds. This point is of significance in Chapter VI, when the failure of the electrode is discussed.

4.10 SUMMMARY

A complete thermal shock stress analysis for the removal of the electrode from the furnace has been achieved. Using a finite element and finite difference model of the electrode assembly, the thermally induced stresses have been shown to be sufficient acting alone to cause surface splitting. While such splits may in themselves not propagate to cause catastrophic failure, the reduction in structural strength caused increases the risk of failure by other mechanisms.

In some regions thermal loads may be expected to reduce the severity of the mechanical stresses, whereas elsewhere the opposite effect is likely to occur, but in every case the thermal stresses are much larger than the mechanical stresses.

7

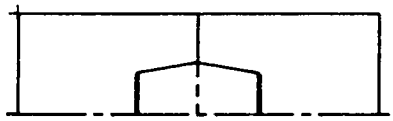

	β	σ_1	σ_2	σ_3	τ_m
M.O.	-2.5	0.0	0.0	0.0	0.0
0 s	89.7	-0.6	-1.2	7.8	0.3
80 s	24.0	13.0	2.7	25.5	5.2
320 s	18.6	5.4	0.3	19.2	2.6
640 s	14.0	2.2	-0.2	14.1	1.2
1200 s	10.9	0.8	-0.2	9.6	0.5
2400 s	12.5	0.3	-0.1	5.2	0.2
3600 s	16.7	0.2	-0.1	3.4	0.1

10

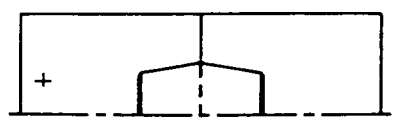

	β	σ_1	σ_2	σ_3	τ_m
M.O.	-19.7	0.0	0.0	0.0	0.0
0 s	-3.6	2.7	-4.8	-0.3	3.8
80 s	22.9	-9.5	-13.7	-11.5	2.1
320 s	48.5	-4.5	-9.5	-6.2	2.5
640 s	52.5	-1.7	-7.3	-3.1	2.8
1200 s	52.9	-0.5	-5.0	-1.4	2.3
2400 s	51.8	-0.1	-2.5	-0.6	1.2
3600 s	50.2	-0.1	-1.5	-0.4	0.7

19

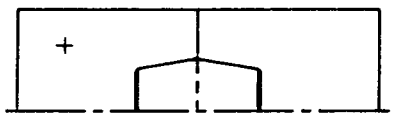

	β	σ_1	σ_2	σ_3	τ_m
M.O.	-39.2	0.0	-0.1	0.0	0.1
0 s	11.9	0.1	-0.9	1.6	0.5
80 s	43.5	2.3	-2.0	-1.0	2.1
320 s	34.5	0.6	-7.9	-3.3	4.2
640 s	35.0	1.5	-8.1	-1.6	4.8
1200 s	36.2	1.6	-6.2	-0.3	3.9
2400 s	37.3	0.9	-3.3	0.0	2.1
3600 s	37.4	0.5	-2.0	0.0	1.3

20

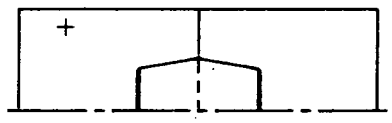

	β	σ_1	σ_2	σ_3	τ_m
M.O.	-57.3	0.0	0.0	0.0	0.0
0 s	67.2	-0.6	-1.1	2.3	0.3
80 s	4.4	2.5	-4.3	2.2	3.4
320 s	14.5	5.4	-4.9	4.6	5.1
640 s	18.5	5.5	-4.2	5.1	4.9
1200 s	20.9	4.2	-3.0	4.2	3.6
2400 s	22.2	2.2	-1.6	2.4	1.9
3600 s	22.3	1.3	-1.0	1.5	1.1

able 4.1 Combined Stresses at various times.

21

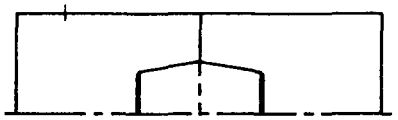

	β	σ_1	σ_2	σ_3	τ_m
M.O.	-88.9	0.0	-0.1	0.0	0.0
0 s	82.4	0.1	-1.6	3.6	0.8
80 s	-1.4	21.3	7.1	21.2	7.1
320 s	2.9	18.8	2.7	17.9	8.0
640 s	5.1	14.4	1.2	14.1	6.6
1200 s	6.5	9.6	0.5	9.7	4.5
2400 s	7.3	4.9	0.2	5.2	2.3
3600 s	7.4	3.0	0.2	3.3	1.4

45

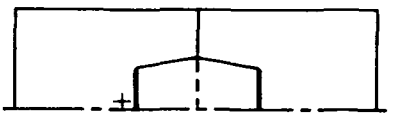

	β	σ_1	σ_2	σ_3	τ_m
M.O.	-89.5	0.1	0.0	0.1	0.0
0 s	-4.7	-0.3	-2.5	-2.2	1.1
80 s	-4.1	-0.6	-3.3	-3.3	1.4
320 s	-4.7	-1.2	-6.3	-6.4	2.6
640 s	-5.6	-1.7	-8.5	-8.5	3.4
1200 s	-5.3	-1.6	-8.4	-8.3	3.4
2400 s	-4.7	-0.9	-5.3	-5.2	2.2
3600 s	-4.4	-0.5	-3.3	-3.2	1.4

48

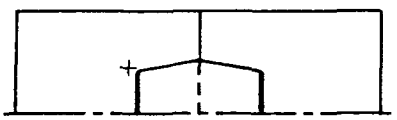

	β	σ_1	σ_2	σ_3	τ_m
M.O.	-3.0	0.4	0.0	0.1	0.2
0 s	6.6	1.0	-1.6	-1.0	1.3
80 s	-45.9	-1.7	-4.8	-3.2	1.5
320 s	-58.0	-3.5	-11.3	-6.5	3.9
640 s	-57.9	-4.4	-13.4	-7.2	4.5
1200 s	-56.1	-4.2	-11.6	-6.4	3.7
2400 s	-53.5	-2.6	-6.6	-3.9	2.0
3600 s	-51.2	-1.6	-4.0	-2.5	1.2

69

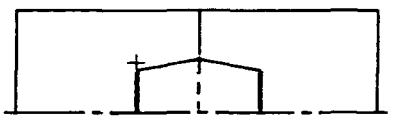

	β	σ_1	σ_2	σ_3	τ_m
M.O.	-19.2	0.3	0.2	0.2	0.1
0 s	-7.3	1.1	-0.7	-0.9	0.9
80 s	-38.6	-0.8	-5.1	-3.1	2.1
320 s	-44.5	-3.0	-11.7	-6.0	4.4
640 s	-43.5	-3.7	-13.9	-6.4	5.1
1200 s	-41.8	-3.3	-12.2	-5.6	4.5
2400 s	-40.3	-1.8	-7.2	-3.5	2.7
3600 s	-39.5	-1.0	-4.4	-2.2	1.7

)le 4.1 (cont.) Combined Stresses at various times.

75

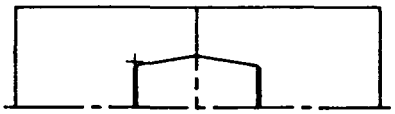

	β	σ_1	σ_2	σ_3	τ_m
M.O.	7.5	0.6	0.2	0.3	0.2
0 s	-3.4	1.3	-0.4	-0.9	0.9
80 s	-47.1	-0.7	-6.1	-3.5	2.7
320 s	-52.9	-2.7	-15.5	-7.4	6.4
640 s	-52.9	-3.4	-19.1	-8.3	7.8
1200 s	-52.1	-3.0	-16.9	-7.4	6.9
2400 s	-51.0	-1.7	-9.7	-4.5	4.0
3600 s	-49.9	-0.9	-5.8	-2.8	2.4

237

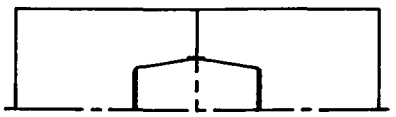

	β	σ_1	σ_2	σ_3	τ_m
M.O.	-83.7	-0.3	-4.7	-0.3	2.2
0 s	-83.5	-1.0	-22.4	-3.5	10.7
80 s	-85.6	-0.8	-21.2	-0.6	10.2
320 s	88.6	0.4	-23.4	0.8	11.9
640 s	85.6	2.0	-27.7	0.6	14.8
1200 s	-90.0	0.0	-23.3	0.7	11.6
2400 s	-88.3	-0.4	-18.4	0.0	9.0
3600 s	-86.8	-0.5	-15.1	-0.4	7.3

269

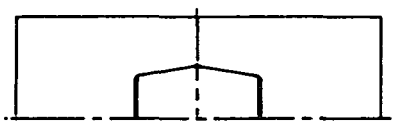

	β	σ_1	σ_2	σ_3	τ_m
M.O.	56.1	0.0	0.0	0.4	0.0
0 s	79.2	0.0	-0.1	3.4	0.0
80 s	59.1	0.0	-0.2	16.0	0.1
320 s	62.9	0.0	-0.1	17.6	0.1
640 s	66.2	0.0	-0.1	16.1	0.0
1200 s	66.4	0.0	-0.1	13.2	0.0
2400 s	70.3	0.0	-0.1	8.3	0.0
3600 s	64.0	0.0	0.0	5.6	0.0

319

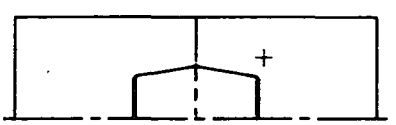

	β	σ_1	σ_2	σ_3	τ_m
M.O.	46.8	0.2	0.0	0.1	0.1
0 s	37.9	0.0	-2.0	-0.2	1.0
80 s	51.1	0.3	-4.3	-1.8	2.3
320 s	45.6	-1.5	-7.7	-2.7	3.1
640 s	40.2	-1.8	-8.2	-1.8	3.2
1200 s	37.3	-1.5	-7.0	-1.0	2.8
2400 s	36.9	-0.9	-4.5	-0.6	1.8
3600 s	37.5	-0.5	-2.9	-0.4	1.2

ble 4.1 (cont.) Combined Stresses at various times.

428

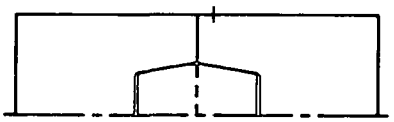

	β	σ_1	σ_2	σ_3	τ_m
M.Q.	-79.1	0.0	0.0	0.3	0.0
0 a	6.4	0.2	0.0	3.6	0.1
80 a	4.5	4.8	0.6	14.9	2.1
320 a	4.9	2.5	0.1	14.9	1.2
640 a	5.1	1.6	0.0	13.2	0.8
1200 a	5.1	1.1	0.0	10.6	0.5
2400 a	4.7	0.6	0.0	6.7	0.3
3600 a	5.7	0.4	0.0	4.6	0.2

1082

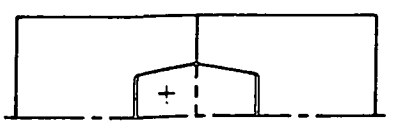

	β	σ_1	σ_2	σ_3	τ_m
M.Q.	-12.4	0.4	-0.3	-0.2	0.4
0 a	-8.7	0.3	-1.3	-0.9	0.8
80 a	-6.9	0.2	-1.0	-0.7	0.6
320 a	-2.1	-0.1	-1.3	-0.9	0.6
640 a	7.3	-0.8	-2.0	-1.3	0.6
1200 a	11.4	-0.9	-2.4	-1.5	0.8
2400 a	7.9	-0.5	-1.7	-1.1	0.6
3600 a	2.5	-0.3	-1.2	-0.9	0.5

1314

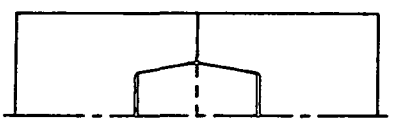

	β	σ_1	σ_2	σ_3	τ_m
M.Q.	0.0	3.8	0.3	0.7	1.8
0 a	-0.1	18.4	1.7	4.9	8.4
80 a	-0.1	12.8	1.1	3.6	5.8
320 a	0.0	12.6	1.0	4.6	5.8
640 a	-0.1	14.3	1.0	6.4	6.6
1200 a	0.0	14.7	1.0	6.6	6.8
2400 a	0.1	12.3	0.9	4.9	5.7
3600 a	0.1	10.4	0.8	3.6	4.8

1328

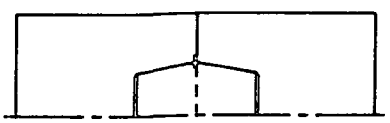

	β	σ_1	σ_2	σ_3	τ_m
M.Q.	-3.7	4.0	0.2	0.8	1.9
0 a	-5.0	19.8	1.2	5.0	9.3
80 a	-4.8	13.7	0.8	3.7	6.4
320 a	-4.0	13.4	0.7	4.7	6.3
640 a	-3.8	15.3	0.8	6.5	7.3
1200 a	-3.6	15.4	0.8	6.7	7.3
2400 a	-3.7	12.9	0.7	4.9	6.1
3600 a	-4.0	11.0	0.6	3.7	5.2

ble 4.1 (cont.) Combined Stresses at various times.

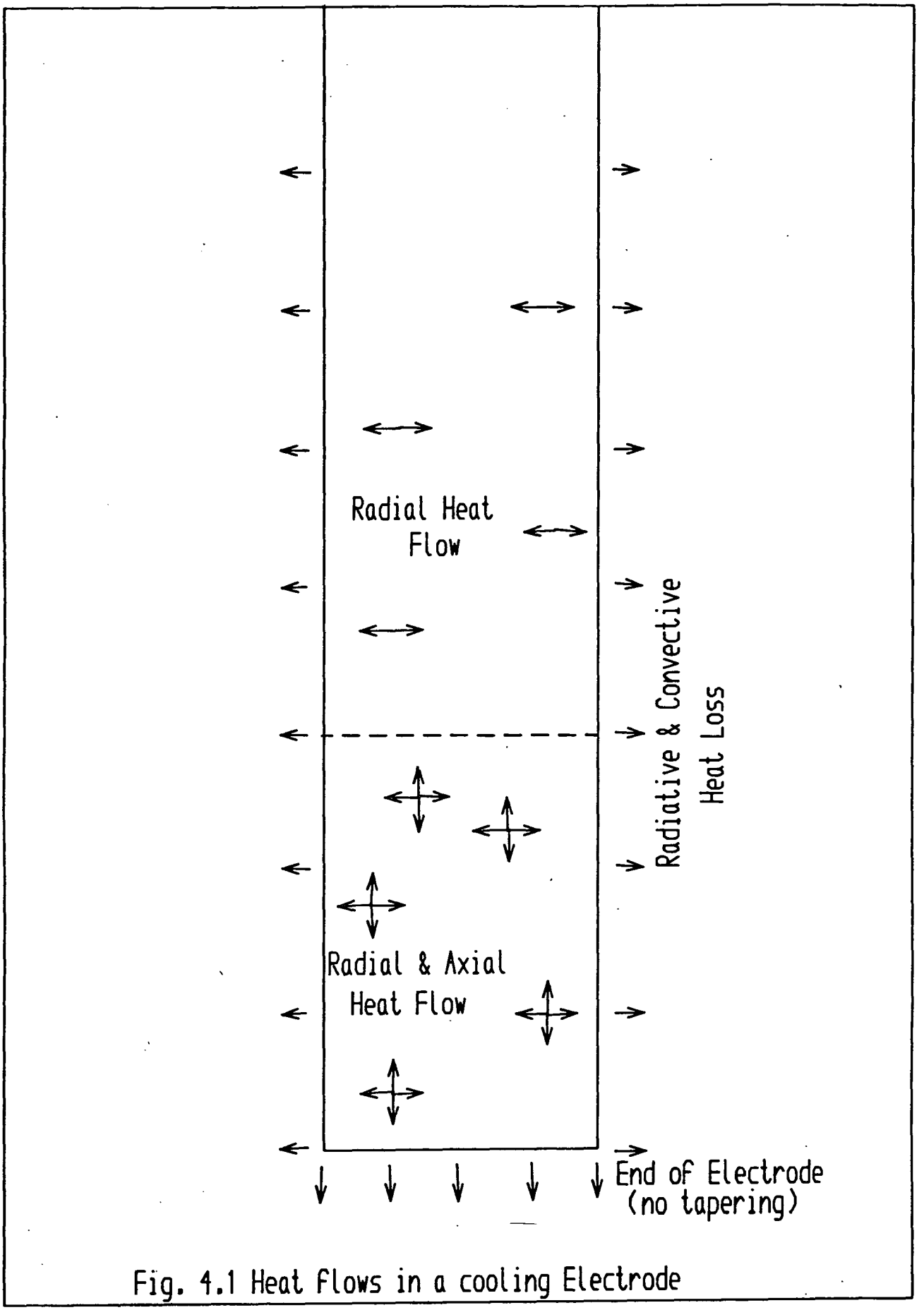

Fig. 4.1 Heat Flows in a cooling Electrode

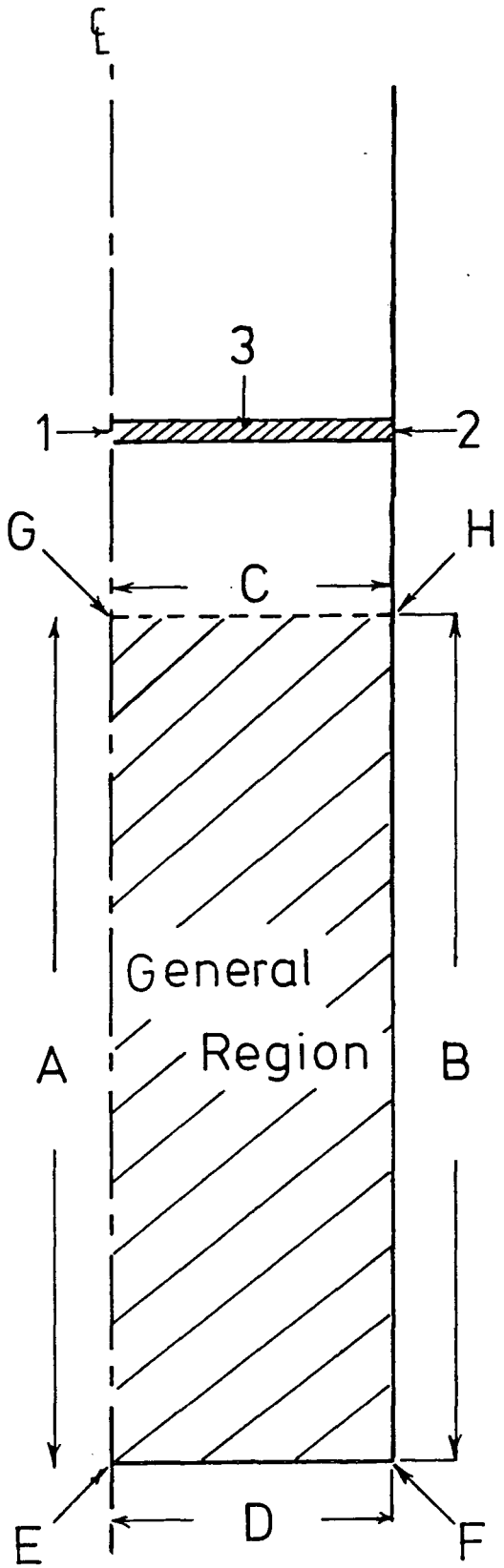

Fig 4.2 The Regions considered separately in the Finite Difference Program

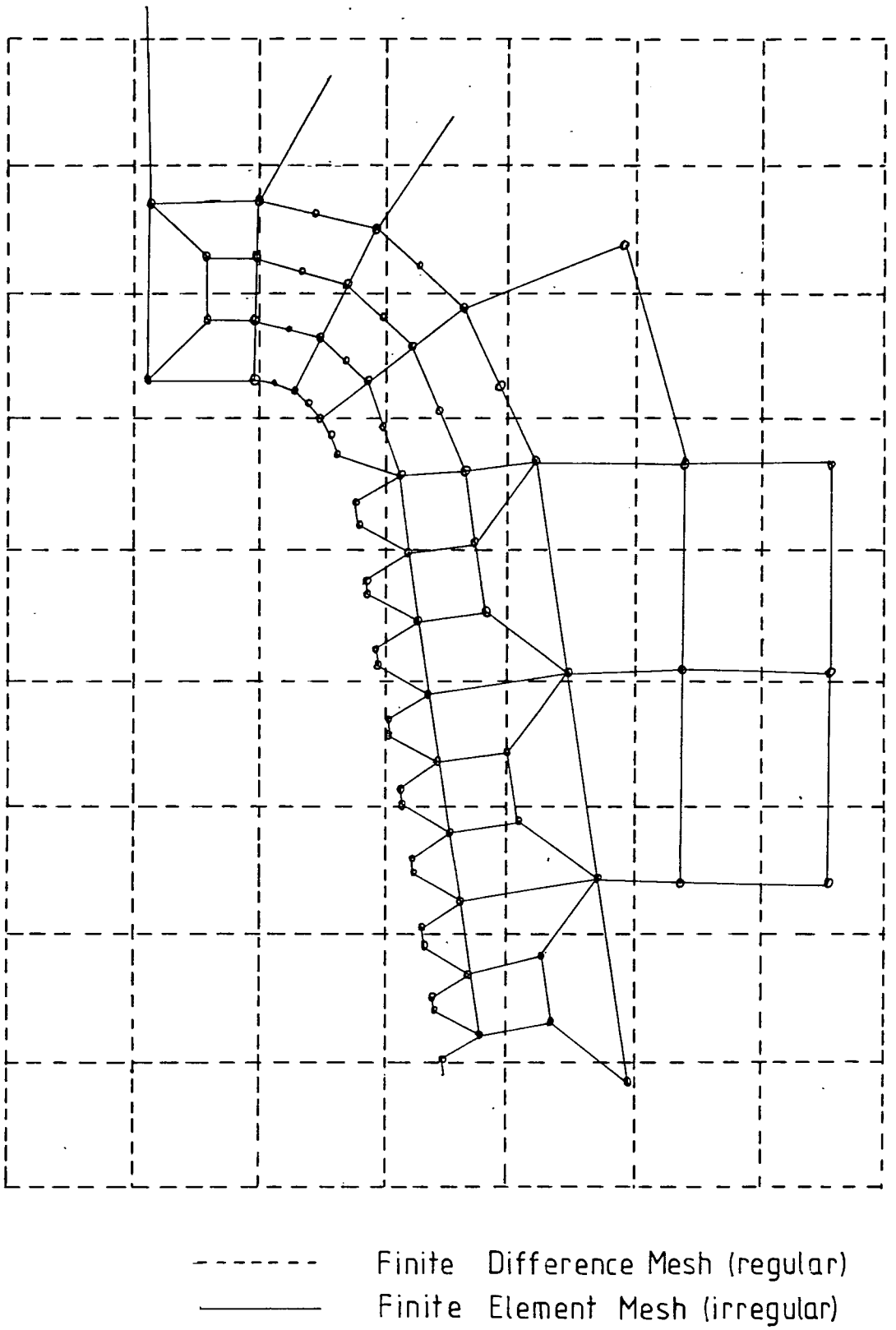

Fig 4.3 The Need for Interpolation

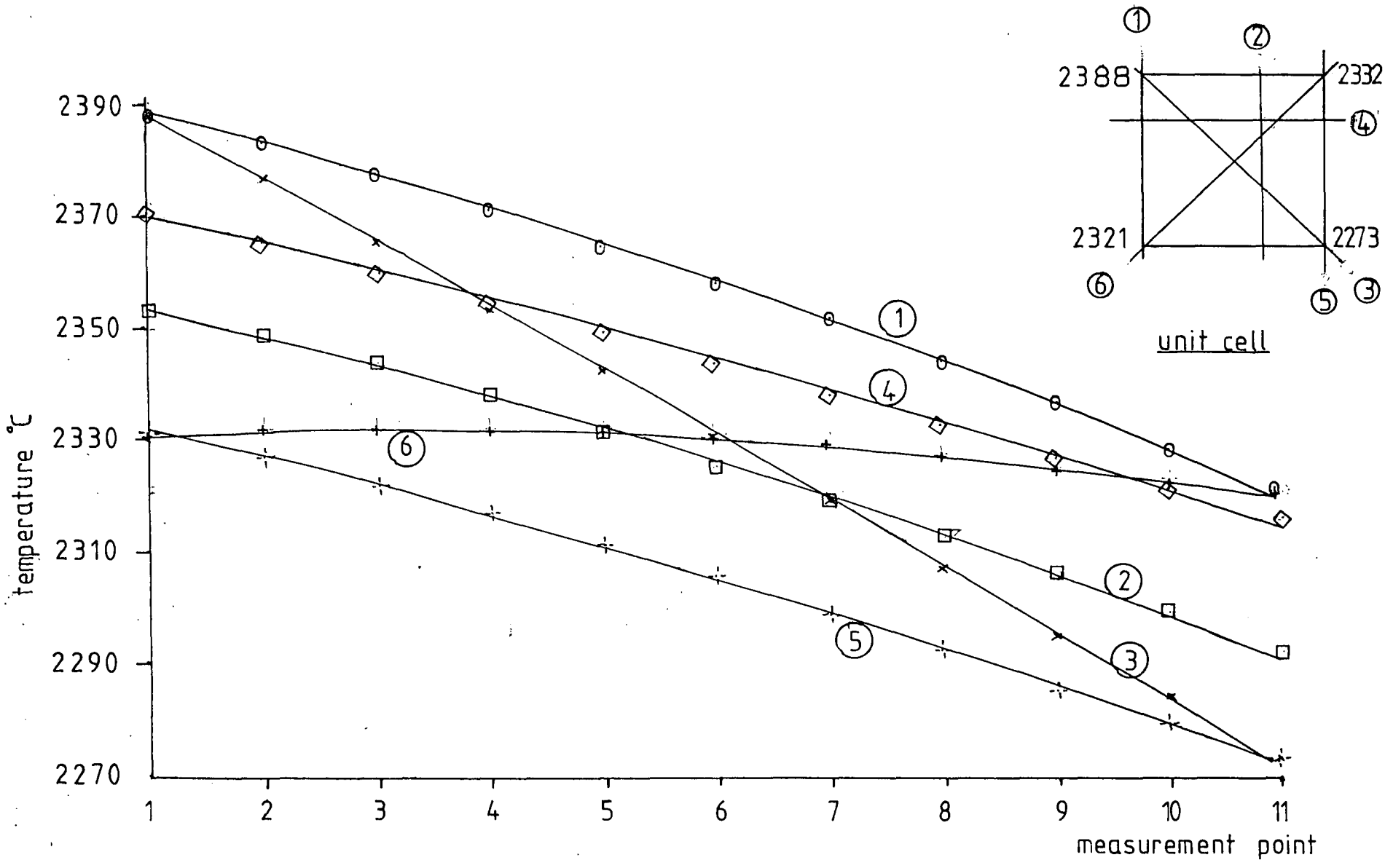

Fig 4.4 Continuity of Interpolation

Isotropic Finite Difference Program Immediate Removal From Furnace.Last update A

Timestep Value 4.0 seconds, 19 Radial Nodes, 71 Axial Nodes,

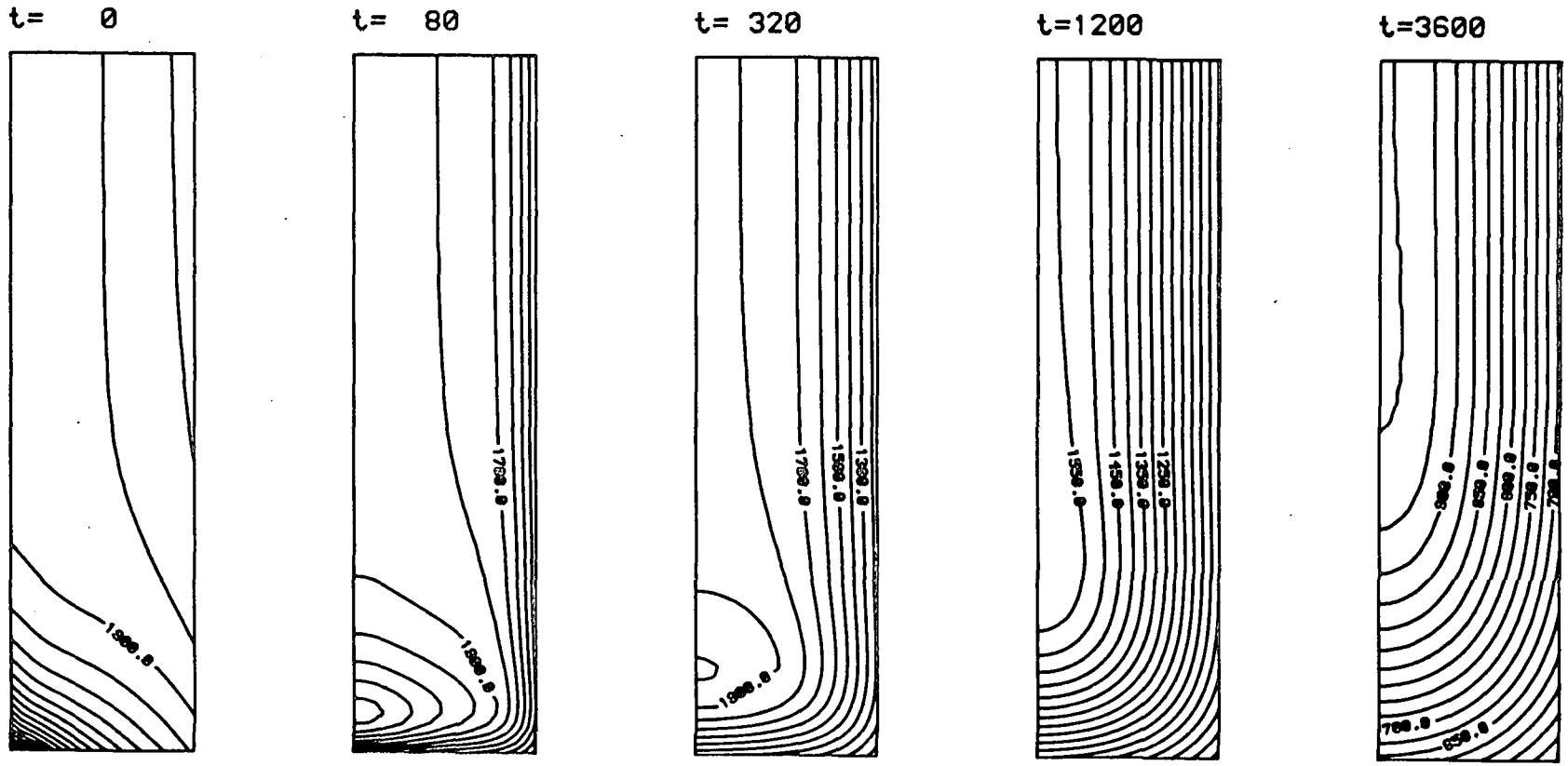

Fig 4.6 Finite Difference Temperature Fields

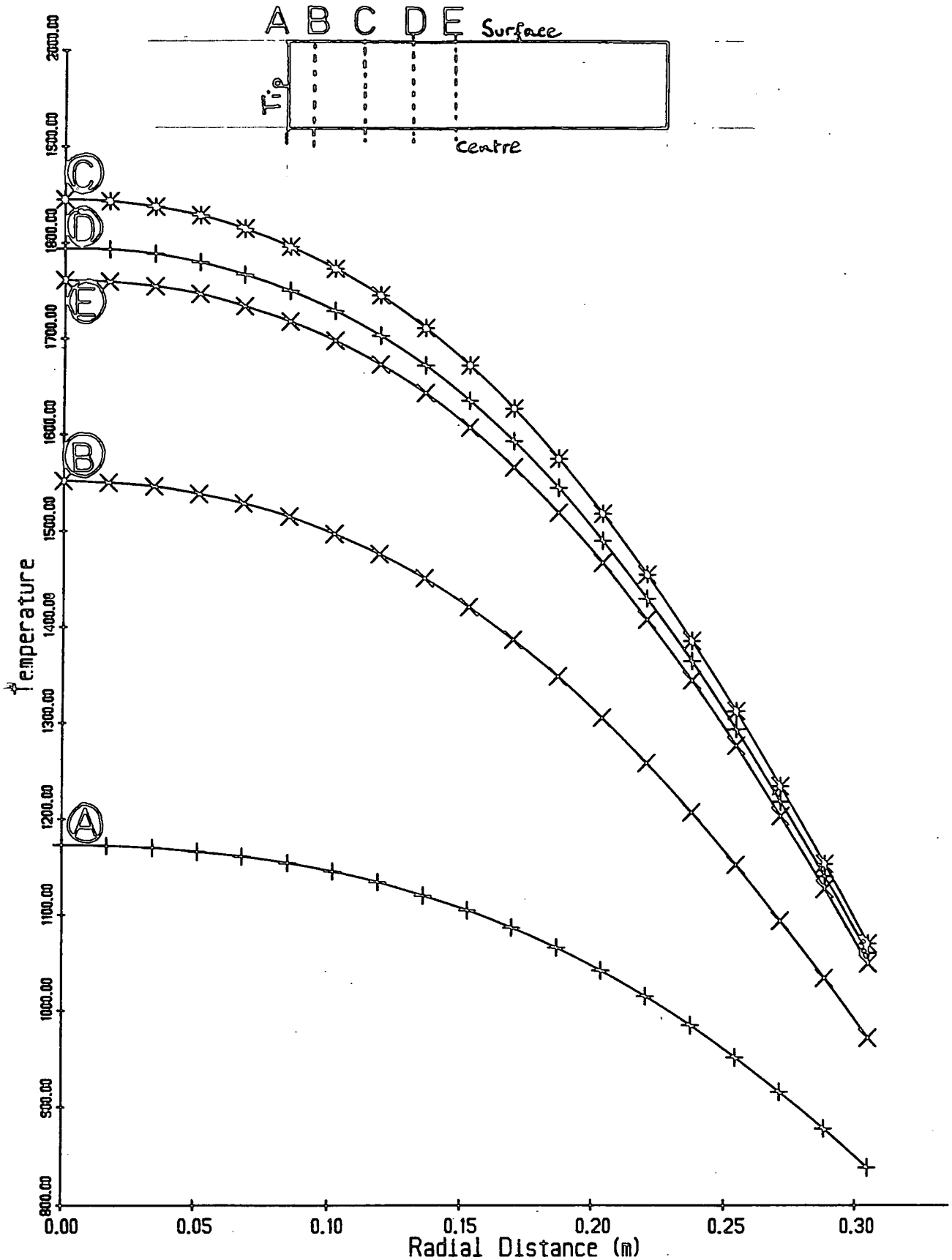

Fig 46(a) Radial variation of Temperature (640

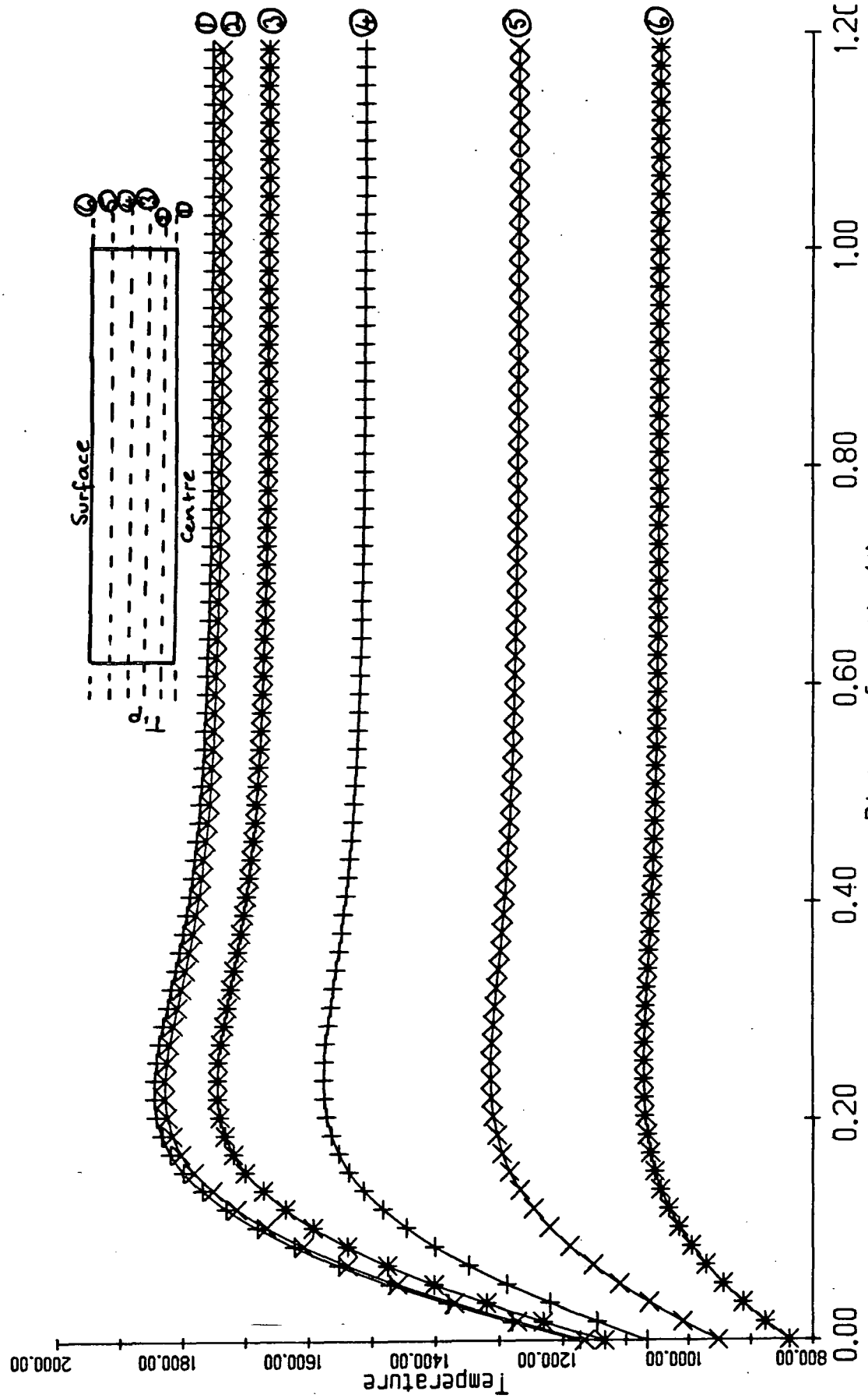

Fig 46(b) Longitudinal variation of Temperature (640s)

Fig 47 Total hoop stress (surface) vs distance from tip

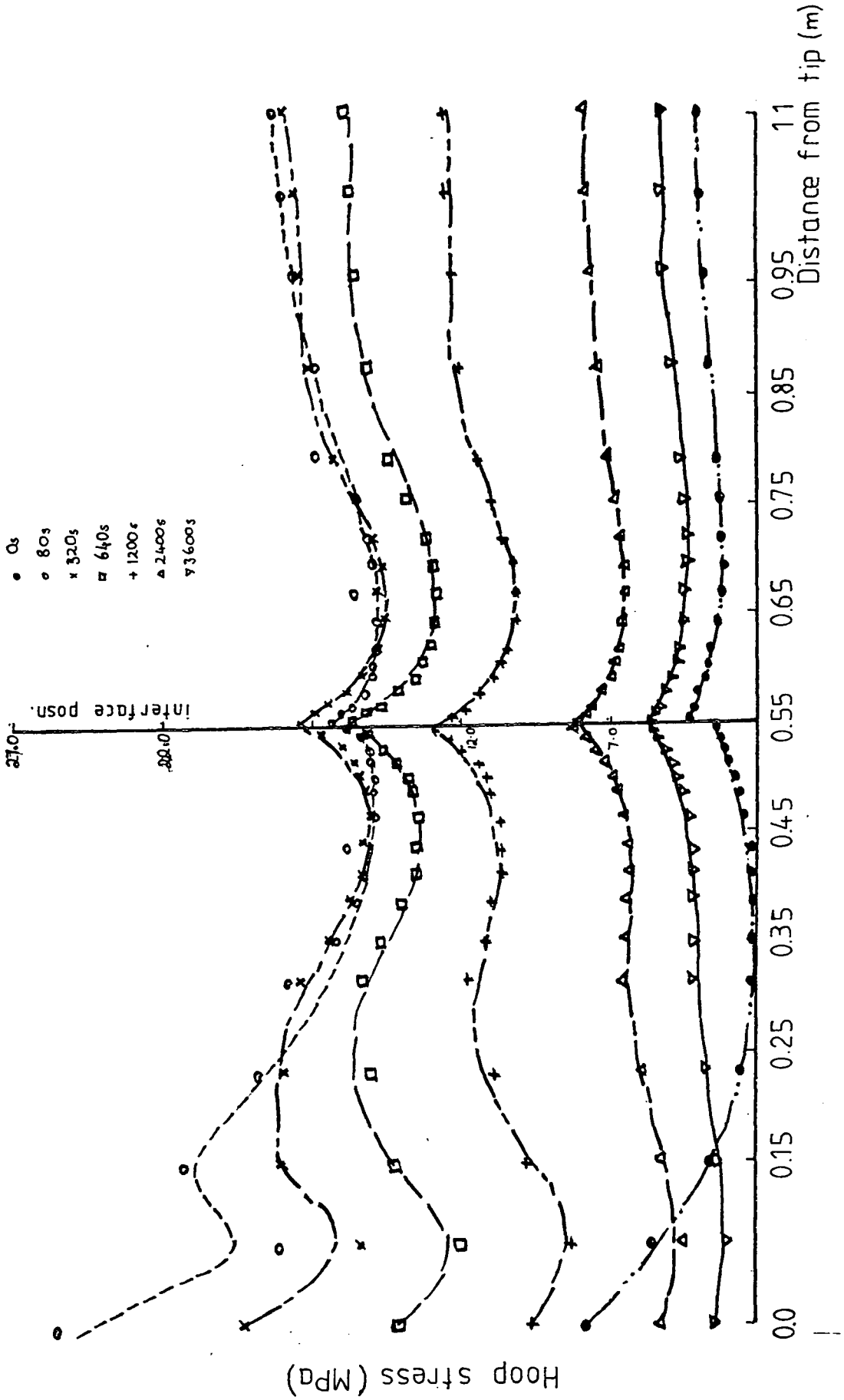

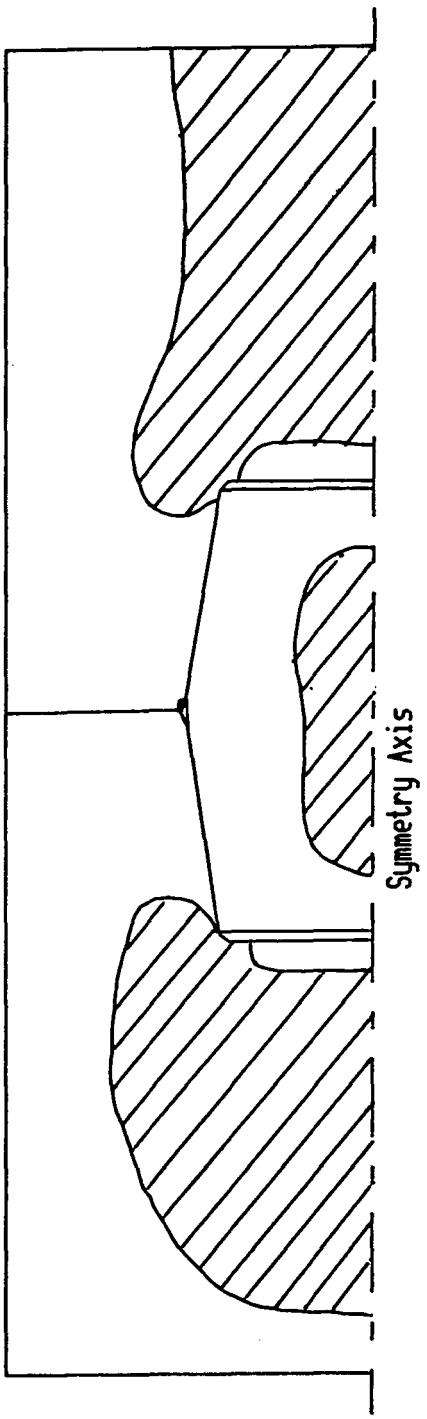

Fig. 4.8 E8 mesh Triaxial compressive regions at 640 sec

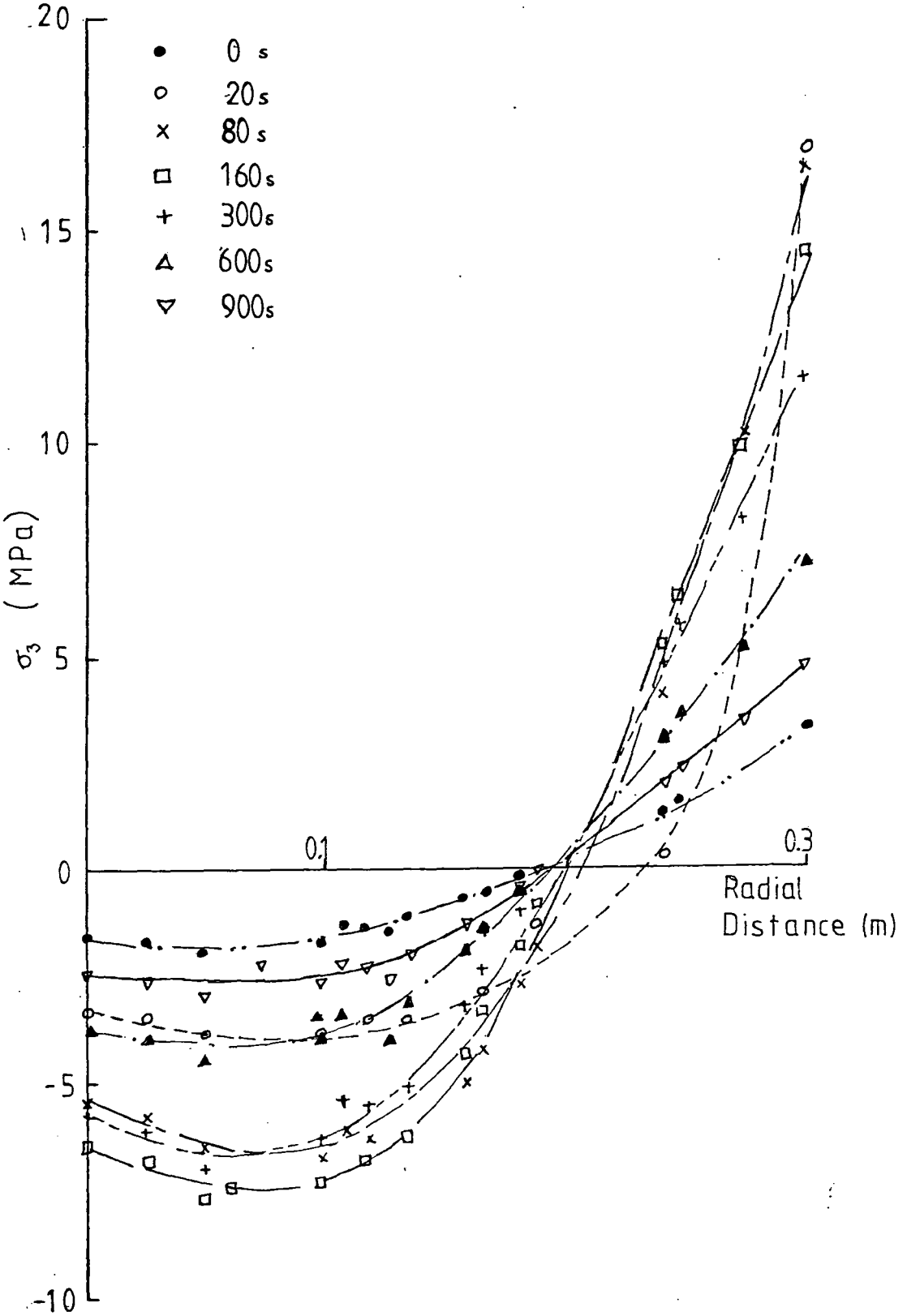

Fig 4.9 Hoop stress vs radial distance

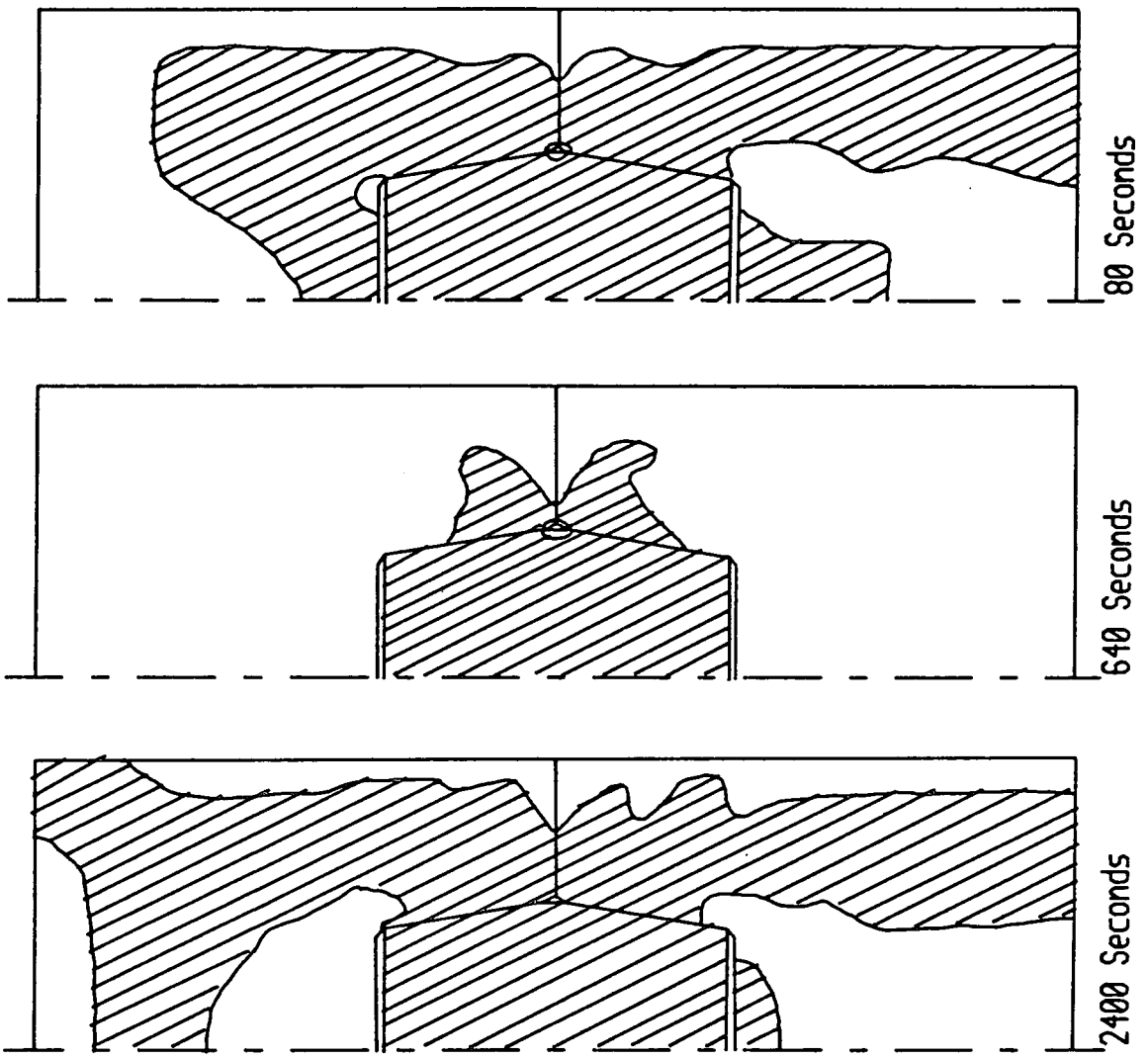

Fig. 4.10 Relatively low stressed regions (< 5 MPa)
in Cooling Electrode

CHAPTER 5

IMPROVING THE MODEL

5.1 General Observations

Since the original Finite Element mesh was primarily designed for the evaluation of mechanical stresses, with a view to a relatively small CPU time for execution, the design needed to be changed to improve its performance for thermal stresses. In particular, experience with the simpler mesh had shown that peak stresses are likely to appear on or near the surface of the electrode, and that the boundaries of regions suffering peak stresses may not be stationary in time. The improved mesh (serial number E14) was therefore designed to include the following considerations.

(i) Improved accuracy by using a larger number of elements with higher order displacement polynomial.

(ii) more uniform distribution of elements near the surface.

(iii) A larger number of elements to be used, allowing direct modelling of the thread teeth, including the gap/sliding effect.

(iv) Improved modelling of the fillet radius, which had proved to be a critical area.

5.2 Gap Contact between Graphite Surfaces

The method of allowing for gap contact in the PAFEC scheme dictates the element order for the thread teeth. In particular, gap contact is only allowed between coincident nodes. An examination of the thread geometry (Fig. 1.5) shows that thread tooth penetration into the mating thread is approximately 2/3 of the thread depth. Elements available in the PAFEC scheme have 0, 1 or 2 'midside' nodes, the corresponding number of nodes per element being 4, 8 or 12 respectively. Obviously, to accommodate the geometry of the thread teeth, 2 midside nodes are necessary (Fig. 5.1), since elements with only one midside node would allow only half - meshing of the teeth. The 12 noded isoparametric element was therefore used. Ideally, these very-high-order elements would have been used to model only the thread teeth, and 8-noded elements would have been used for the rest of the mesh. Unfortunately, the combination of element types available does not permit a transition from 12 noded to 8-noded elements, so 12-noded elements had to be used throughout.

5.3 The improved Finite Element mesh

Because the element field was very large, the organisation of element and node numbers became a major problem. Because the areas of maximum stress were known from previous results, the mesh was numbered completely 'by hand' so that areas of interest could have similar node numbers and would therefore appear close to each other in

the computer printout.

Production of the mesh was begun by defining a single element to represent a thread tooth. Because this is geometrically the most difficult area this single element mesh was scaled up to preserve accuracy. A further element was then added to represent the mating of two thread teeth (Fig. 5.1). Not until these two elements were exactly correct in both size and orientation was the geometrical form scaled down to actual size. The two meshing elements were then reproduced 28 times, with the appropriate coordinate transformations, to represent the complete thread form. The numbering of the nodes was carefully arranged so that corresponding points on adjacent thread teeth had identical last digits in their node numbers, to facilitate interpretation of results. The remaining elements were then added, particular care being taken at the fillet radius in the socket base to make sure the geometry was properly represented. The final mesh consisted of 1200 elements and 7,300 nodes, and is shown in Fig. 5.2.

Nominal mechanical loads were applied to this mesh for testing purposes, but the initial runs indicated that excessive computing resources were required. This possibility had been anticipated, so the save/restart facilities in PAFEC were tested on the trial job. Unfortunately, these proved to be unsatisfactory, having not at the time been fully developed and tested. It was

therefore decided that the mesh would need to be simplified so that a job could run from start to finish within a reasonable computing time.

5.4 Simplification of the Improved Model

As explained earlier, the geometry of the meshing teeth dictates the number of midside nodes (2) on the mating sides of the elements. This was the initial reason for using 12-noded isoparametric elements. An 8-noded element does exist, however, with two midside nodes on one pair of opposite sides and none on the other (see Fig. 5.3(a)). The thread teeth could thus be modelled using these elements correctly oriented. Unfortunately, these elements are compatible only with 4-noded quadrilateral elements, forcing the choice of these elements for most of the rest of the mesh. The difficulties involved are shown in Fig. 5.3(b). An additional problem produced by the choice of 4-noded quadrilateral elements is in the modelling of the fillet radius at the socket base. Curved element sides can only be defined using elements with at least one midside node. A six-noded quadrilateral element was therefore used for this purpose.

The mesh was reconstructed using the mixture of elements described, including appropriate triangular elements where necessary. Thus, the job was reduced to manageable proportions, and progress was resumed using the simplified mesh.

The ideas outlined in Chapter III were first used

in the determination of mechanical stresses using the simplified version of the improved mesh.

Thus, a construction of similar form to that shown in Fig. 3.5, was created using the E14 mesh. Gap nodes were defined between corresponding thread teeth on the electrode and nipple, with a coefficient of sliding friction of 0.15 between mating surfaces. Unfortunately, the CPU time required for stressing this mesh was still unacceptable, so further simplification was sought.

A trial run with the GAPS module removed from the data file, i.e., defining all mating surfaces to be rigidly connected, showed that the main reason for the unacceptable CPU time was the iterative process used by PAFEC for this facility. Several methods for circumventing the problem were considered:

(i) Since the thread pitch line on the E14 mesh was designed to correspond as exactly as possible to the E8 mesh, it was decided to attempt to use displacements from the E8 mesh down the thread teeth (which of course had used the GAPS facility, and therefore carried the necessary information about the gap status) as prescribed displacements on the E14 mesh. The displacements at individual nodes corresponding to thread teeth on the E8 mesh were therefore retrieved from the PAFEC output to the E8 mechanical stressing runs. The E14 mesh was then divided into three parts: the electrode

section below the joint, the electrode section above the joint, and the nipple. These three regions were then stressed in separate runs. The electrode sections were loaded with prescribed displacements along the thread tooth nodes corresponding to the E8 equivalents, the interface nodal displacements being interpolated from the E8 calculated displacements (again containing information on the gap status). The nipple section was loaded with the reactions corresponding to the prescribed displacements along the thread teeth. By this method the benefit of the GAPS calculation was carried over between the meshes, without the disadvantages of the excessive CPU time required for execution.

The results obtained from this technique were, however, unsatisfactory. Although it was not to be expected that stress values should be identical between the two meshes, particularly in the region of the thread teeth, the stress values predicted were in some cases an order of magnitude different. This discrepancy is thought to be due to a lack of precision in the displacement values output by PAFEC, a small absolute error in displacement being sufficient to produce a large error in the induced stress.

(ii) Since PAFEC calculates reactions across gap nodes, a similar procedure to (i) was considered using these calculated reactions (which of course are zero for 'opened' gaps) instead of the displacements. However, this procedure turned out to be unworkable due to the particular form of mesh which had been used for the E8 runs. In the E8 mesh, the thread pitch line was constructed so that one node corresponded to each thread tooth. To save on element numbers, thread teeth were represented alternately by mid-side and corner nodes in the E8 mesh. When plotting the reaction at the thread teeth against distance down the thread form, a family of two distinct curves was obtained (similar to that shown in Fig. 3.6 for mechanical stresses), one corresponding to the corner nodes, the other to the mid-side nodes. This phenomenon is due to the particular form of the displacement polynomial used in the element, which produces a nonlinear set of reactions over the element edge. The reactions calculated are in fact those which do an equivalent amount of work on the structure to the calculated displacements. This phenomenon makes it impossible meaningfully to transfer reactions from the E8 mesh to the E14 mesh since the E14 mesh uses one element to represent each thread tooth. It is not clear how

to redistribute the calculated reactions between the teeth to obtain an equivalent situation.

(iii) There is, within PAFEC, a similar, but not identical, module to the GAPS module, called the HINGES.AND.SLIDES module (hereafter referred to as the SLIDES module). While the GAPS module allows the user to specify that two nodes are to interact only if there is a compressive normal reaction between them, the SLIDES module allows two nodes to slide over one another with zero friction. An important difference between this and the GAPS module is that, when tensile reactions occur between pairs of nodes, the connection is not released; they remain constrained to slide (with zero friction) in the specified direction. Thus, if it is known in advance which pairs of nodes remain in contact, and these are specified as SLIDES, the only difference between GAPS and SLIDES is that the frictional coefficient is zero in the latter case. Since this module is much less heavy on CPU time than the GAPS module, it was decided to use this approach. The E8 mesh output was examined to ascertain which thread teeth remain in contact under mechanical loading. The equivalent E14 nodes were then specified in a HINGES module, using an extended E14 mesh as in

Fig. 3.5. Those teeth which did not remain in contact were given total freedom of movement.

This method makes the minimum of connections between the two Finite Element meshes - no numerical data is passed between them, simply information on boundary conditions. Progress was resumed using the E14 equivalent of the mesh shown in Fig. 3.5, with the relevant GAP nodes redefined as HINGE nodes (in the case of mechanical stresses, all thread teeth turned to to be in contact). The mechanical stresses for the other electrode sections were obtained as described in Chapter III.

5.5 Mechanical Stresses - Results (Bottom joint)

In this case, the analysis was carried out purely for a bottom joint, so self-weight effects were neglected. the areas of interest are shown in Fig. 5.4, with a sample of the computed stresses in Table 5.1 (the line marked M.O.). The results were noted to be symmetric about the interface. Generally, the regions are similar to those obtained with the coarser, E8 mesh.

Peak tensile stresses occur at the fillet radius (see node 5234, for example) with mechanical stresses

σ_1 = 1.0 MPa, σ_2 = 0.1 MPa, σ_3 = 0.3 MPa, τ_m = 1.0 MPa

These are slightly lower than the E8 equivalent, probably due to the more accurate fillet radius representation in this mesh. Peak tensile stresses also occurr, as before, at the maximum nipple radius (node 7250), with stress values

σ_1 = 3.9 MPa, σ_2 = 0.4 MPa, σ_3 = 0.8 MPa

These are very close to the E8 equivalent (node 1328) which has

σ_1 = 4.0 MPa, σ_2 = 0.2 MPa, σ_3 = 0.8 MPa

Peak compressive stresses occur, as before, on the interface and surrounding nodes. Node 2628, for example, has

σ_1 =-1.3 MPa, σ_2 =-5.2 MPa, σ_3 =-0.7 MPa

The corrsesponding E8 node (237) has

σ_1 =-0.3 MPa, σ_2 =-4.7 MPa, σ_3 =-0.3 MPa

This shows good agreement in σ_2, the most compressive in-plane stress, but poor agreement in σ_1, and only moderate agreement in σ_3. This is most probably due to the difference between the GAPS and SLIDES modelling assumptions, which would be expected to have more effect at this point. Comparisons between the meshes have not been drawn for nodes on or near to the thread teeth. This is beacause the geometry is different in this region for the E8 mesh and the E14 mesh. The stresses in such regions

would not therefore be expected to be directly comparable.

Elsewhere in the electrode, agreement between the two meshes is good. Nodes 2812, in the 'body' of the nipple, for example, has

σ_1 = 0.4 MPa, σ_2 =-0.3 MPa, σ_3 =-0.2 MPa

This compares well with the corresponding E8 node (1082), which has

σ_1 = 0.4 MPa, σ_2 =-0.3 MPa, σ_3 =-0.2 MPa

Node 1813, a small distance into the electrode from the fillet radius, has

σ_1 = 0.3 MPa, σ_2 =-0.1 MPa, σ_3 = 0.2 MPa

The corresponding E8 node (69) has

σ_1 = 0.3 MPa, σ_2 = 0.2 MPa, σ_3 = 0.2 MPa

As would be expected, the major differences in the stresses calculated by the two meshes are in the regions where there is a geometry difference.

Plotting the stressed regions of the electrode (Fig. 5.4) we see a similar distribution between the two meshes (see Fig. 3.9 for the E8 version). Again, various regions may be identified. Regions A and B, for example, are triaxially tensile, though peak stresses in this region

are slightly smaller than before due to the better model of the fillet radius curvature. region C, the triaxial stresses on the nipple, is slightly smaller than before.

Triaxial compression occurs in regions D and E, also as before, but this time the corresponding regions in the electrode have disappeared. Close examination of the computer printout, however, shows that in this region the stress magnitudes are small (typically < 0.05 MPa in magnitude). The triaxial compression regions H and I have apparently spread from being only a single node in extent to over 10 in this mesh. Close examination of the mesh in this region however shows that there is a much greater nodal mesh density than before, so this increase in size is probably due to an improvement in the modelling accuracy.

Region F is also triaxially compressive, showing peak stresses due to tightening torque similar to those obtained with the E8 mesh. Additionally, a region J, of triaxial compression, has appeared. The magnitudes of the stresses within this region are, however, quite small (typically < 0.5 MPa).

The shape of region G, the mixed stress region with in-plane compression, hoop tension, is slightly different from before. This is thought to be due to the slightly different boundary conditions at the interface (free sliding, instead of frictional contact) and due to the smaller element density in this region on the E14 mesh.

In addition to the regions shown in Fig. 5.4, some of the nodal points on the thread teeth showed stress combinations corresponding to those previously discussed. These showed no coherent pattern, however, and it is likely that the stresses in this region are not adequately modelled with either Finite Element mesh. In particular, the thread root radii are modelled simply as 60° corners, rather than the small radius actually existing in practice. Discussion of stresses in these regions is therefore excluded here (although some further remarks will be made in Chapter VI, on failure considerations).

Fig. 5.5(a) shows the variation of mechanical hoop stress at the surface along the length of the electrode. Again, there is a maximum near the interface due to the splaying of the collar region by the applied forces coupled with the sliding movement over the thread teeth, the hoop stress becoming peak negative at points just beyond the axial position of the fillet radius. The peak tensile value reached is 0.4 MPa, whereas previously it was 0.5 MPa. This reduction is again thought to be due to the increased freedom over the interface.

Fig. 5.5(b) shows the hoop stress variation along a radial line just below the socket base. This has the same shape as the corresponding E8 graph (Fig. 3.11(b)). The difference in absolute values is explained in this case since the E14 diagram corresponds to a line rather deeper below the socket base. This choice was necessitated by the

fact that the disposition of elements did not allow the selection of an identically-placed line.

5.6 Thermal/Mechanical Stress Analysis-Results.

Having checked the compatibility of the E14 mesh with the previous results from mechanical stresses, the thermal analysis was performed. As before, this involves running the finite difference program to calculate the temperature field, interpolating to the Finite Difference points, and then entering the thermal loads for a PAFEC stressing run.

This phase of the work was extremely heavy on computing resources - some of the resources required for the jobs are listed below

(i) Finite Difference run - 300 seconds of C.P.U. time.

(ii) Interpolation for each timestep - 600 seconds C.P.U. time.

(iii) PAFEC stressing run for each timestep - 800 seconds C.P.U. time.

(iv) Production of one frame of graphical output - 300 seconds C.P.U. time.

(v) Storage requirements for stopping & starting job for one graphical output frame - 1200 pages.

(vi) Printout for each job 700 pages.

(vii) Total storage space requirement - 4000 pages.

It was originally intended to produce thermal stressing runs for timesteps identical to those produced for the E8 mesh. However, examination of the thermal stress results for the E8 mesh showed that the GAPS iteration process had not completely converged for most of the timesteps; the convergence was only badly incomplete for a small number of timesteps. The number of thread teeth engaged for such timesteps therefore became indeterminate, making it impossible to define a meaningful number of SLIDES in the corresponding E14 stressing runs. The thermal analysis for the E14 mesh was therefore confined to timesteps 0, 20, 80, 300, and 900, corresponding to 0, 80, 320, 1200, and 3600 seconds after removal. Even so, the amount of graphic output available was very small, and much of the analysis of the results had to be done by inspection of the digital printout.

The numerical results which produced the temperature fields in Fig. 4.5 were interpolated to the E14 Finite Element mesh points as before.

The interaction between the thread teeth, and across the electrode/electrode interface, was represented by defining those nodes which the E8 mesh had calculated as being in contact (for the appropriate timestep) as SLIDES, and giving the other corresponding pairs complete freedom of movement (i.e. an analagous process to that used for mechanical stresses). The mechanical stresses were then combined using the combination program of Chapter III, and

the results examined. There was a minor difference in the applied restraints between the E8 runs and the E14 runs. This difference was at the top of the analysed section. In the E8 thermal runs this edge was restrained from moving in the axial direction. In the E14 thermal runs this edge was unrestrained. This would not be expected to make any appreciable difference to the stresses, except in regions very close to the restraint, although of course the absolute values of displacements would be expected to be quite different. This assumption is borne out by the results. In fact neither of the two conditions is a truly accurate representation of the real situation (see Chapter VIII, on Further Work). The similarity of the results between the two meshes indicates that they are not particularly sensitive to this condition.

Table 5.1 shows some results from areas of particular interest. The approximate location of each node is represented pictorially at the top of each column. Several of these regions deserve close inspection;

(i) The region of the fillet radius at the socket base (nodes 1813, 1973). During cooling the predominant in-plane stress moves from tension to compression, the mechanical stresses at this point are swamped by both the steady-state and thermal shock loads. The hoop stress in this region varies from being mildly tensile under mechanical stresses to considerably compressive (7.5 MPa) after cooling

for about 20 minutes. Examination of the thermal stress output shows that, as expected, the thermal stresses in this region are highly compressive. the mild triaxial tension existing under mechanical loading is thus swamped by these heavily compressive thermal stresses. These may be explained, as before, by the surface cooling of the electrode sqeezing the central regions, the fillet radius acting as a stress concentrator. These triaxial compressive stresses are below the crushing strength of the material and are therefore unlikely to cause failure. It is therefore to be expected that collar-type failures are less likely to occur when thermal stresses are added, i.e. on the bottom joint.

(ii) The electrode walls and end surfaces. Nodes 114, 504 and 2604 all lie on the electrode surface. The tensile hoop stress developed on the surface as a result of cooling clearly exceeds the tensile strength values (see Chapter II) at some stages of the cooling process. Although the stress-time curves at these points all exhibit maxima, these sometimes occur at different times during the cooling cycle. Nodes 504,2604, and node 114 (the corner node) have reached maximum stress levels by 80 seconds, although the hoop stress on node 2604 does not reach its maxi mum until 320 seconds

after removal. The stress field here after 320 s (node 504) is:

σ_1 =15.7 MPa, σ_2 = 3.2 MPa, σ_3 =17.1 MPa,

τ_m = 6.2MPa

These stresses exceed the tensile strength values in two directions. The possibility of longitudinal cracking on the surface of the electrode is therefore very great, especially since the strength of brittle materials such as graphite is least under triaxial tensile stresses (Brocklehurst, 1977). Note that node 2604, on the corner of the interface, has

σ_1 = 2.5 MPa, σ_2 = 0.4 MPa, σ_3 =18.3 MPa

The reduction in σ_1 and σ_2 is due to the freedom allowed to these nodes to contract away from the interface due to the SLIDES model.

(iii) Points near the axis at the base of the socket (e.g. nodes 1326, 1914, 6455). The stresses in this region are predominantly compressive, and reach absolute maximum values of 10.0 MPa; in general they are very much lower than this. This is of interest because cylindrical samples are frequently taken from this region for quality control analysis. Removal of a cylindrical specimen involves a considerable change in geometry of the electrode. If the sample were to

be taken from a highly-stressed region this may cause an unacceptable perturbation in the stress field, with possible increase in the failure risk. The results show that this region is an acceptable compromise for quality control sampling.

(iv) A point on the interface of the electrodes, near the inside of the socket. As mentioned earlier, nodes neighbouring 2628 are in danger of local crushing under mechanical stresses. Examination of the results shows that this danger is increased by the action of cooling . A compressive stress of 5.5 MPa is increased to 14.2 MPa by cooling. The existence of this region may be explained, as before, by the wedging action of the (relatively) expanding nipple, pressing the two electrode halves together.

The variation of surface hoop stress along the electrode length for various times is shown in Fig. 5.6. The surface hoop stress has reached a maximum after 80 seconds, when the value near the tip begins to fall again. This is essentially as predicted by the previous model.

Fig. 5.7 shows the variation of hoop stress along the line XY (Fig. 5.4) with time, showing a compressive value near the fillet radius at the socket base. This diagram also shows the radial extent of the tensile hoop stresses during the time the electrode is out of the

furnace. The critical hoop stresses appearing at the surface can be clearly seen, as also can the compressive hoop stress around the area which under purely mechanical loads is in a state of critical triaxial tensile stress.

Examination of the complete digital printout over the whole of the analysed region shows the following general trends:

(i) Tensile stresses on and near the electrode surface. On the surface itself stresses are triaxially tensile, and the high (> mean failure stress) hoop stresses penetrate to a maximum of about 1/5 of an electrode radius over the timesteps analysed.

(ii) A central 'core' of triaxial compressive stress, broken by the changes in geometry, which varies in size as cooling progresses. Fig. 5.8 shows this region for the 320 second timestep. This includes the fillet radius region, and the localised interface crushing.

(iii) In between regions (i) and (ii) mentioned above, a region of mixed stress whose size varies depending on the stage of cooling, with stress values generally below the mean failure strength.

5.7 CONCLUSIONS

(1) Mechanical stresses in an electrode column joint are not critical. The stresses due to tightening torque and electrode self-weight are not sufficient in themselves to cause failure.

(2) There are compressive stresses at the socket entrance which will not cause crushing under mechanical stresses alone. Thermal stresses increase the likelihood of this, however.

(3) Thermal stresses swamp the tensile stresses in the collar region. Longitudinal cracking is promoted by thermal stresses, as is crushing at the socket entrance.

(4) Sampling for quality control purposes at the base of the socket, on the axis, is reasonable.

5.8 SUMMARY

By improving the Finite Element model, a complete thermal and mechanical stress analysis of a thermally shocked electrode has been obtained, embodying the minimum of simplifying assumptions. Results agree well with previous determinations using a simpler mesh. Although the probable effect of these stresses on the material has been briefly mentioned, a detailed discussion of the failure of electrodes under these stress fields is left to the next chapter.

114

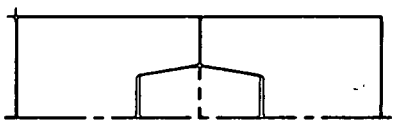

	β	σ_1	σ_2	σ_3	τ_m
M.O.	-70.8	0.0	0.0	0.0	0.0
0 s	79.2	0.4	-0.6	8.2	0.5
80 s	30.2	11.0	3.1	25.7	4.0
320 s	29.5	5.6	1.0	19.4	2.3
1200 s	29.3	2.3	0.3	10.0	1.0
3600 s	29.8	0.9	0.1	3.6	0.4

296

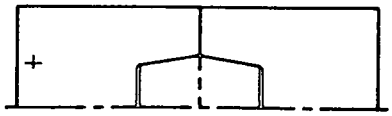

	β	σ_1	σ_2	σ_3	τ_m
M.O.	-24.1	0.0	0.0	0.0	0.0
0 s	-5.0	0.8	-4.4	0.3	2.6
80 s	19.9	-1.6	-8.2	-4.6	3.3
320 s	49.7	1.6	-5.5	0.6	3.6
1200 s	52.7	2.1	-3.4	2.0	2.8
3600 s	50.4	0.6	-1.1	0.6	0.8

504

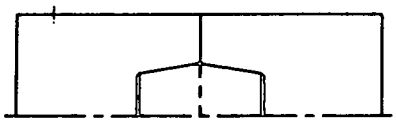

	β	σ_1	σ_2	σ_3	τ_m
M.O.	-79.5	0.0	0.0	0.0	0.0
0 s	-85.2	0.4	-1.6	4.5	1.0
80 s	0.8	18.6	5.9	20.2	6.3
320 s	4.4	15.7	3.2	17.1	6.2
1200 s	7.2	7.1	1.2	9.1	3.0
3600 s	8.8	2.1	0.4	3.1	0.9

513

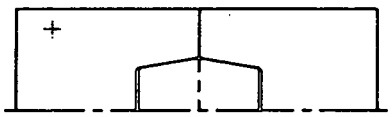

	β	σ_1	σ_2	σ_3	τ_m
M.O.	-51.4	0.0	0.0	0.0	0.0
0 s	-28.3	0.1	-0.9	3.1	0.5
80 s	31.6	-1.6	-5.7	-0.6	2.0
320 s	29.5	2.4	-7.0	2.6	4.7
1200 s	30.5	2.8	-3.8	3.5	3.3
3600 s	30.5	0.9	-1.2	1.3	1.0

ble 5.1 Stresses at various times (imp. model).

1326

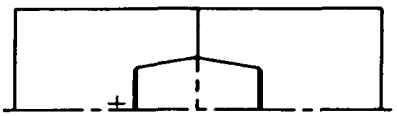

	β	σ_1	σ_2	σ_3	τ_m
M.O.	76.5	0.1	0 0	0.1	0.0
0 s	-2.8	-0.4	-2.3	-2.1	1.0
80 s	-6.0	-0.9	-3.9	-3.9	1.5
320 s	-6.7	-1.6	-7.6	-7.5	3.0
1200 s	-6.4	-2.2	-9.9	-9.6	3.8
3600 s	-5.7	-0.8	-3.7	-3.6	1.5

1813

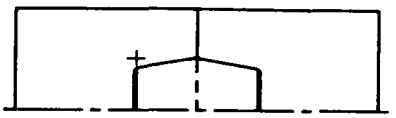

	β	σ_1	σ_2	σ_3	τ_m
M.O.	-8.1	0.3	0.1	0.2	0.1
0 s	-3.3	0.8	-0.6	-0.8	0.7
80 s	-41.4	-0.6	-4.9	-3.1	2.1
320 s	-47.8	-2.4	-11.3	-5.5	4.4
1200 s	-45.9	-2.6	-11.6	-4.9	4.5
3600 s	-43.5	-0.8	-4.1	-1.9	1.6

1914

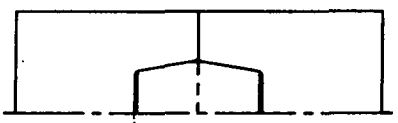

	β	σ_1	σ_2	σ_3	τ_m
M.O.	84.6	0.0	0.0	0.0	0.0
0 s	-1.9	-0.2	-2.7	-2.7	1.3
80 s	-5.8	0.3	-1.7	-1.6	1.0
320 s	-13.7	0.8	-1.6	-1.4	1.2
1200 s	-15.0	0.9	-2.4	-2.2	1.7
3600 s	-12.3	0.2	-1.4	-1.3	0.8

1973

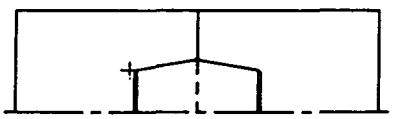

	β	σ_1	σ_2	σ_3	τ_m
M.O.	18.0	0.4	0.1	0.2	0.2
0 s	9.5	0.8	-1.6	-1.1	1.2
80 s	-38.6	-1.8	-5.5	-3.6	1.8
320 s	-49.3	-3.8	-13.3	-7.3	4.8
1200 s	-47.4	-4.7	-14.5	-7.5	4.9
3600 s	-43.6	-1.8	-5.1	-2.9	1.6

ble 5.1 (cont.) Stresses at various times (imp. model).

2604

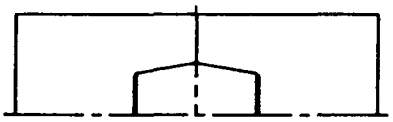

	β	σ_1	σ_2	σ_3	τ_m
M.O.	-6.9	0.0	0.0	0.3	0.0
0 s	-68.4	0.4	0.1	3.5	0.2
80 s	-74.0	4.5	1.0	17.3	1.7
320 s	-70.7	2.5	0.4	18.3	1.0
1200 s	-67.6	1.2	0.2	13.5	0.5
3600 s	-67.1	0.5	0.1	5.8	0.2

2625

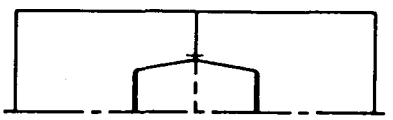

	β	σ_1	σ_2	σ_3	τ_m
M.O.	73.1	-0.5	-1.5	0.4	0.5
0 s	59.7	-1.2	-5.8	0.7	2.3
80 s	17.3	3.3	-1.0	5.5	2.2
320 s	10.0	7.8	-0.1	8.7	3.9
1200 s	12.3	6.3	-0.7	8.4	3.5
3600 s	20.0	1.8	-1.1	3.8	1.5

2628

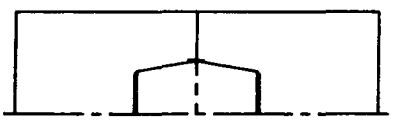

	β	σ_1	σ_2	σ_3	τ_m
M.O.	-88.0	-1.3	-5.2	-0.7	1.9
0 s	-88.2	-7.1	-26.6	-6.1	9.7
80 s	86.5	-4.7	-25.6	-2.7	10.4
320 s	84.3	-4.5	-30.6	-2.4	13.1
1200 s	85.2	-5.1	-29.9	-2.3	12.4
3600 s	87.1	-3.7	-18.4	-2.1	7.4

2812

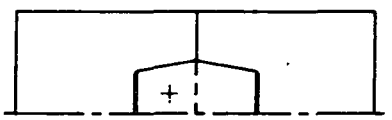

	β	σ_1	σ_2	σ_3	τ_m
M.O.	-11.7	0.4	-0.3	-0.2	0.3
0 s	-7.4	0.3	-1.4	-1.1	0.9
80 s	-6.6	0.2	-1.1	-0.9	0.6
320 s	-2.2	-0.2	-1.4	-1.2	0.6
1200 s	10.5	-1.2	-2.6	-2.0	0.7
3600 s	2.1	-0.4	-1.4	-1.1	0.5

ble 5.1 (cont.) Stresses at various times (imp. model).

4457

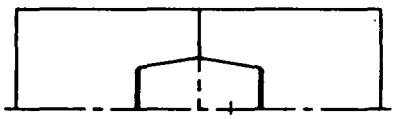

	β	σ_1	σ_2	σ_3	τ_m
M.O.	4.3	0.2	-0.3	-0.3	0.2
0 s	-0.9	-0.2	-1.4	-1.4	0.6
80 s	-1.0	-0.2	-1.2	-1.2	0.5
320 s	-2.6	-0.4	-1.4	-1.4	0.5
1200 s	-8.2	-1.6	-2.8	-2.7	0.6
3600 s	-5.2	-0.7	-1.4	-1.4	0.4

5212

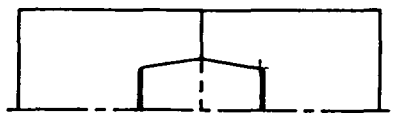

	β	σ_1	σ_2	σ_3	τ_m
M.O.	-11.0	1.6	0.2	0.5	0.7
0 s	63.7	-0.5	-4.2	-2.0	1.9
80 s	65.4	-1.2	-9.4	-5.6	4.1
320 s	68.2	-2.6	-20.9	-10.7	9.2
1200 s	68.5	-2.9	-23.7	-10.2	10.4
3600 s	67.3	-1.1	-8.9	-3.9	3.9

ble 5.1 (cont.) Stresses at various times (imp. model).

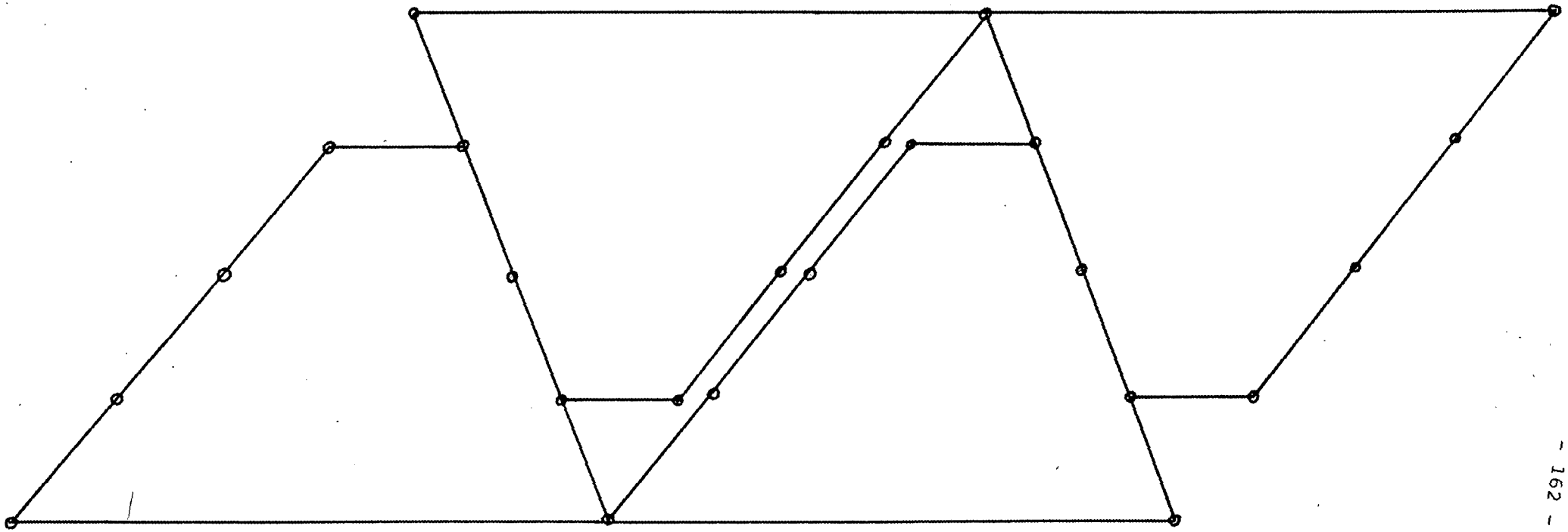

Fig 5.1 Meshing of Thread Tool

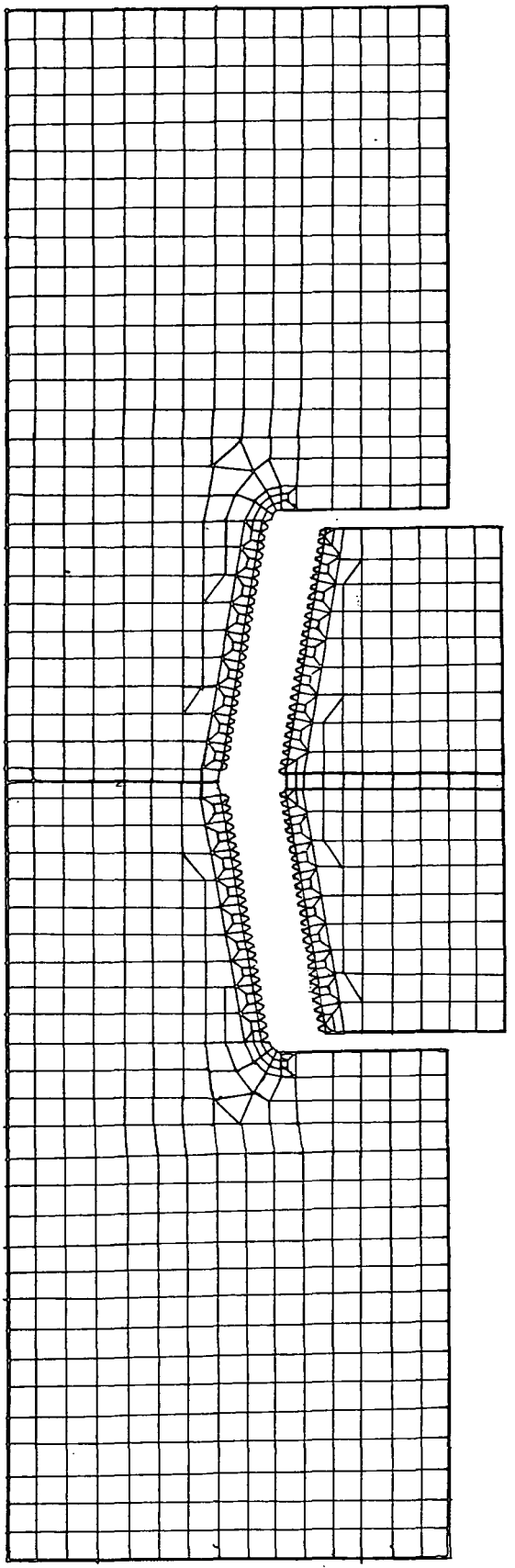

Fig 5.2 Finite Element Mesh No.E14.

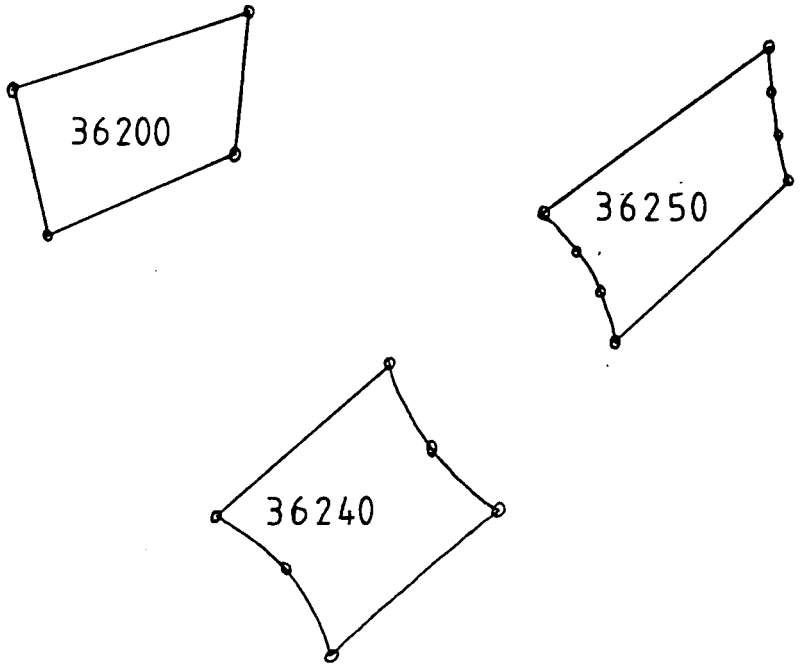

Fig 5.3(a) Elements selected from the PAFEC Library

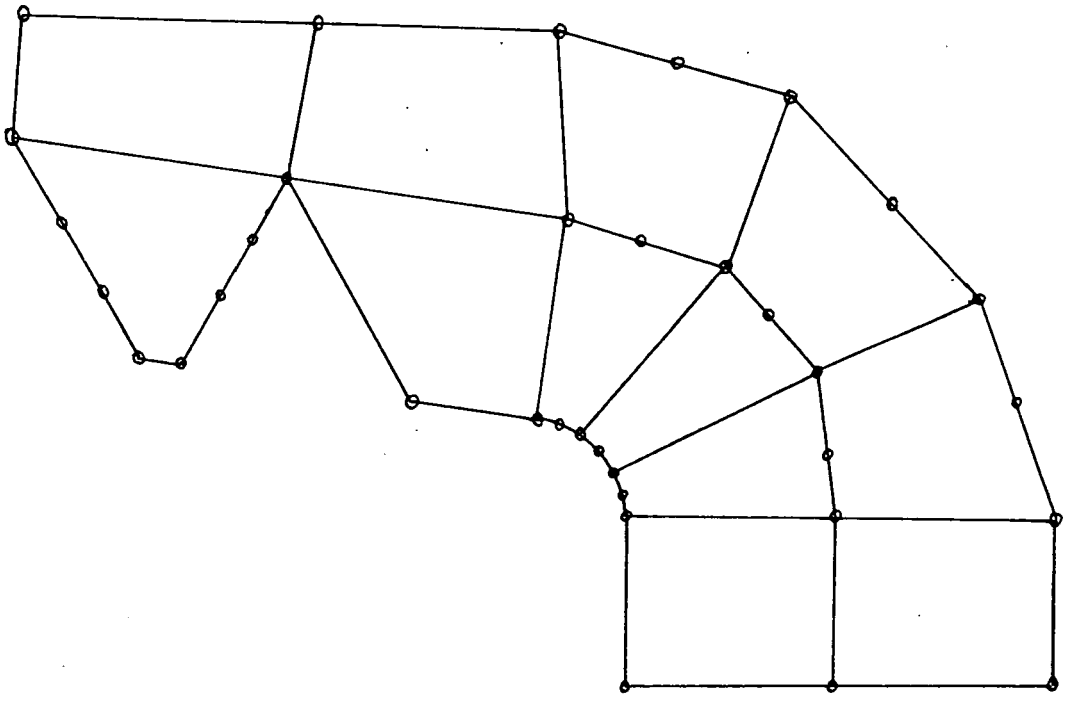

Fig 5.3(b) Combining the Elements in a Mesh

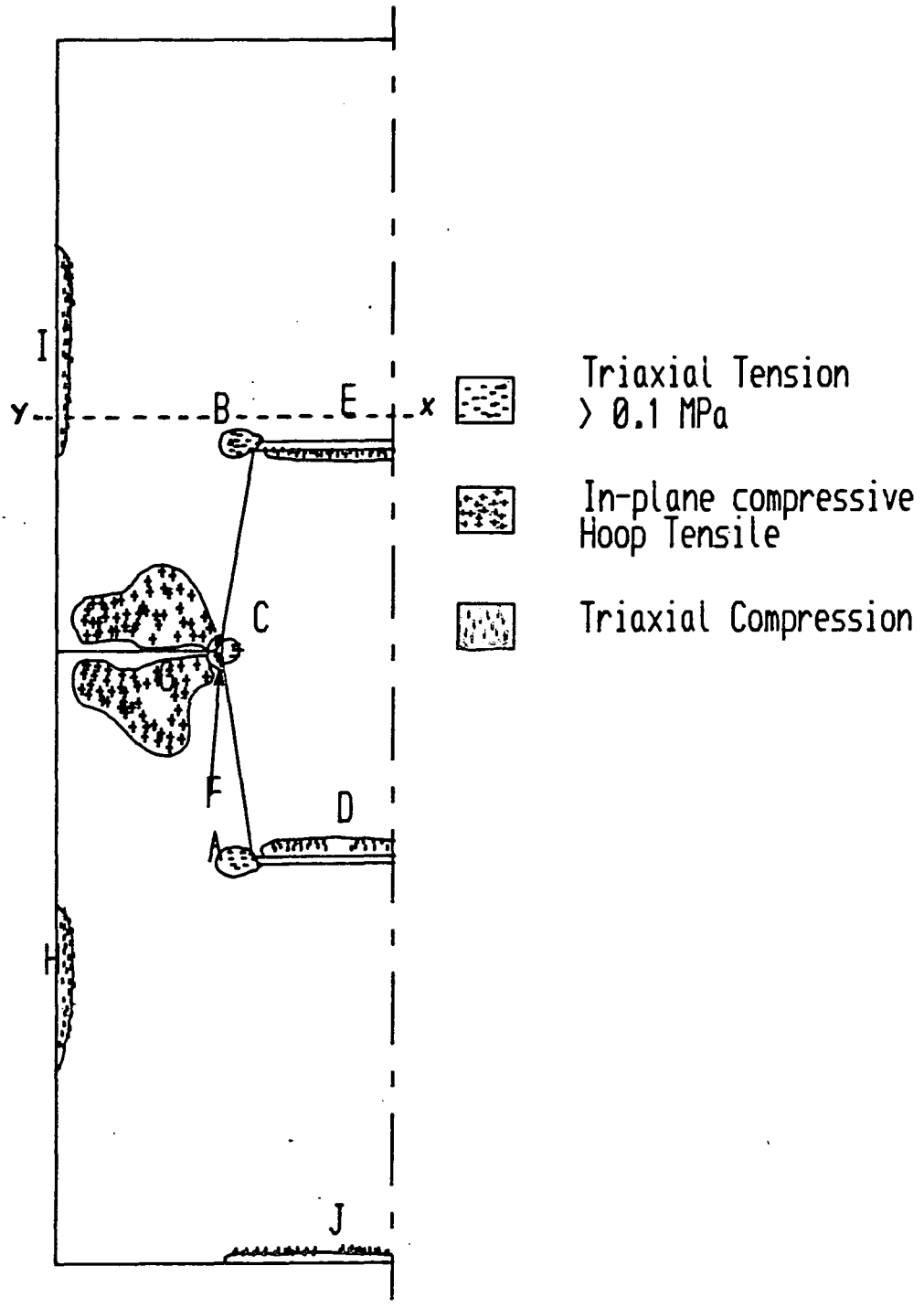

Fig. 5.4 Torque only E14 mesh stress regions.

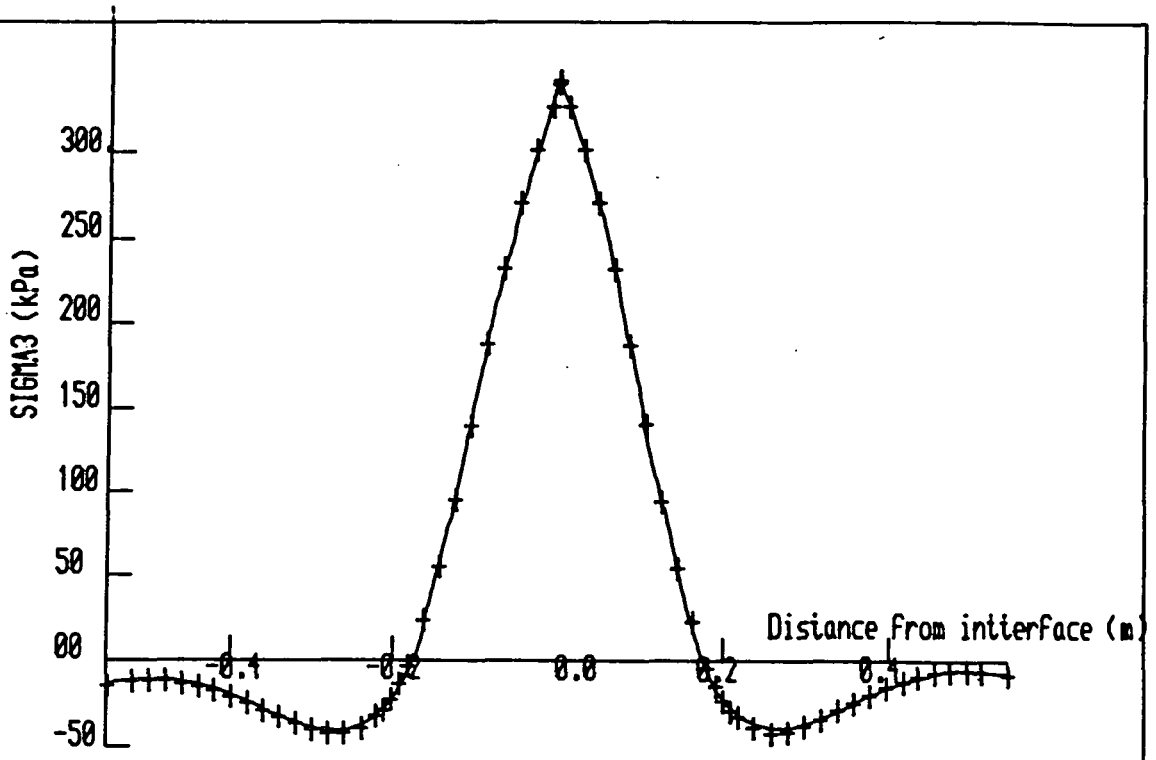

Fig. 5.5(a) Mechanical Surface Hoop Stress vs. distance.

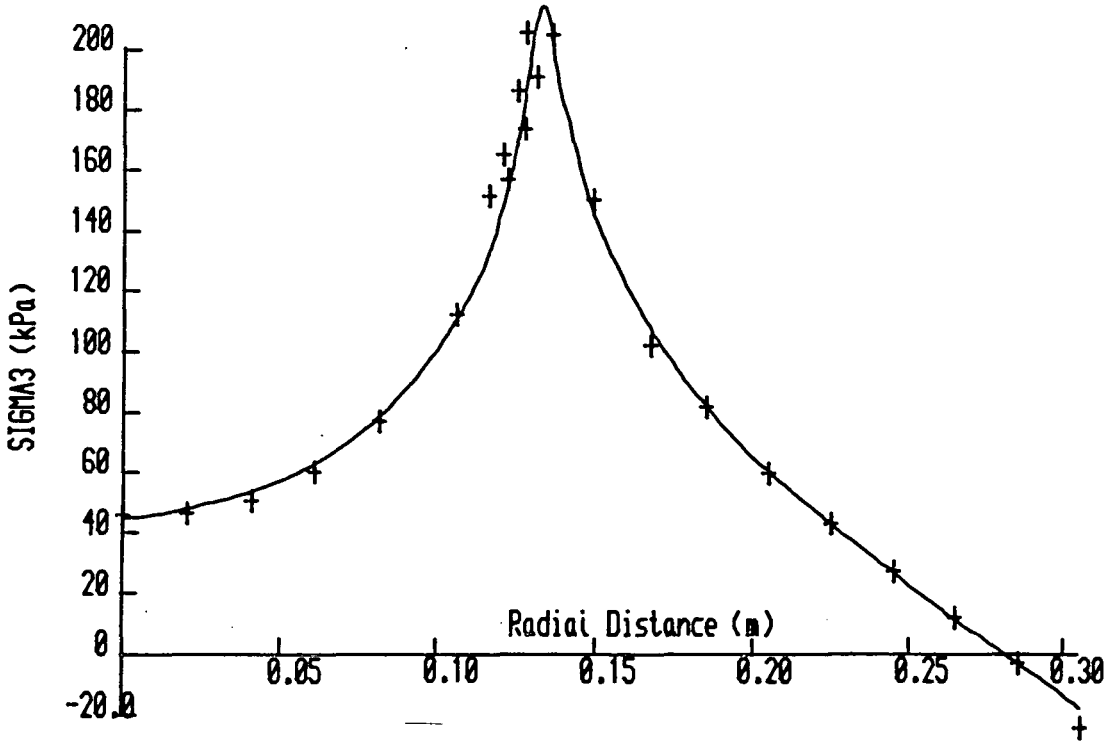

Fig. 5.5(b) Radial Variation of Mechanical Hoop Stress.

Fig 5.6 Surface thermal hoop stress vs distance from tip.

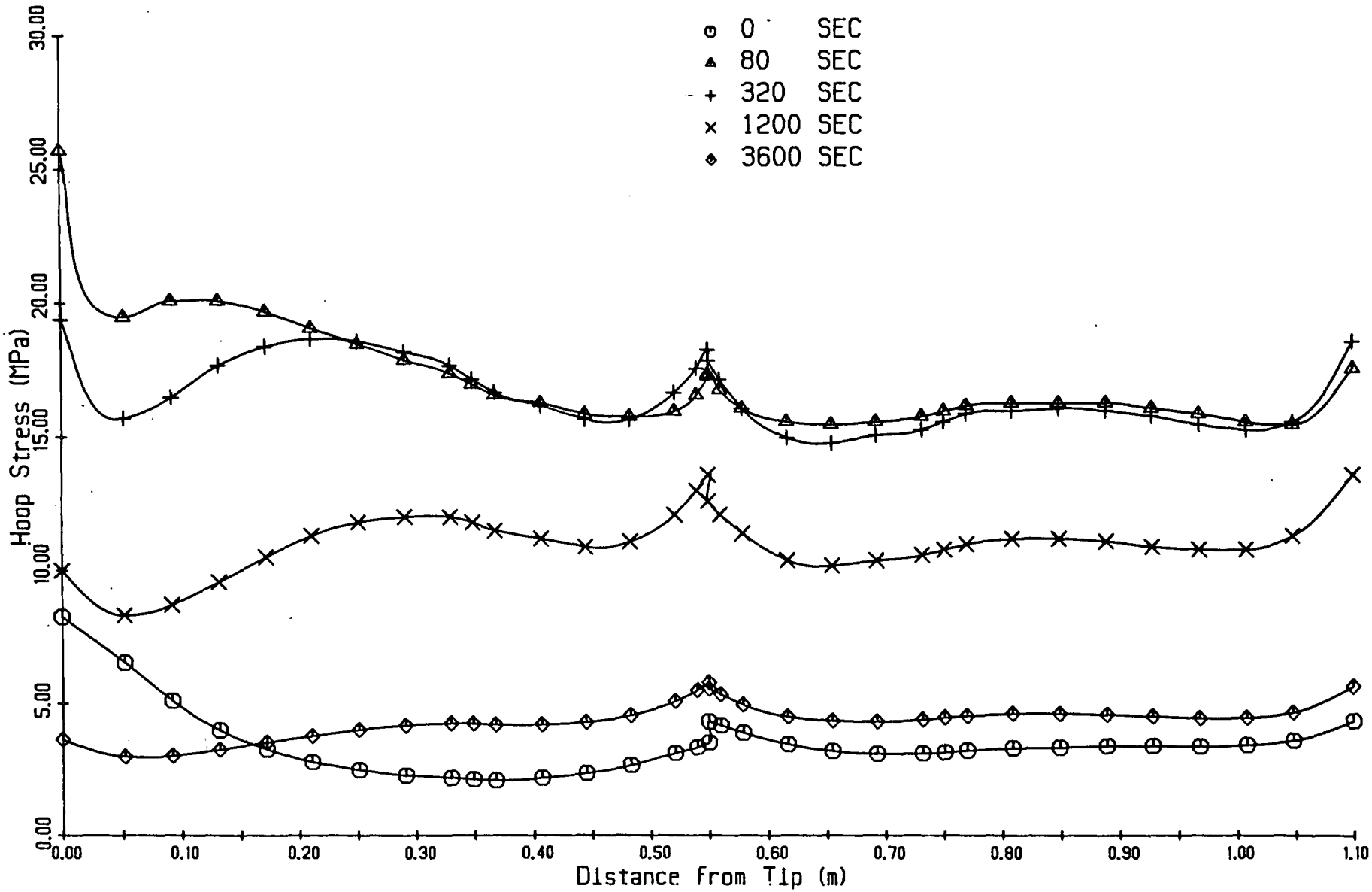

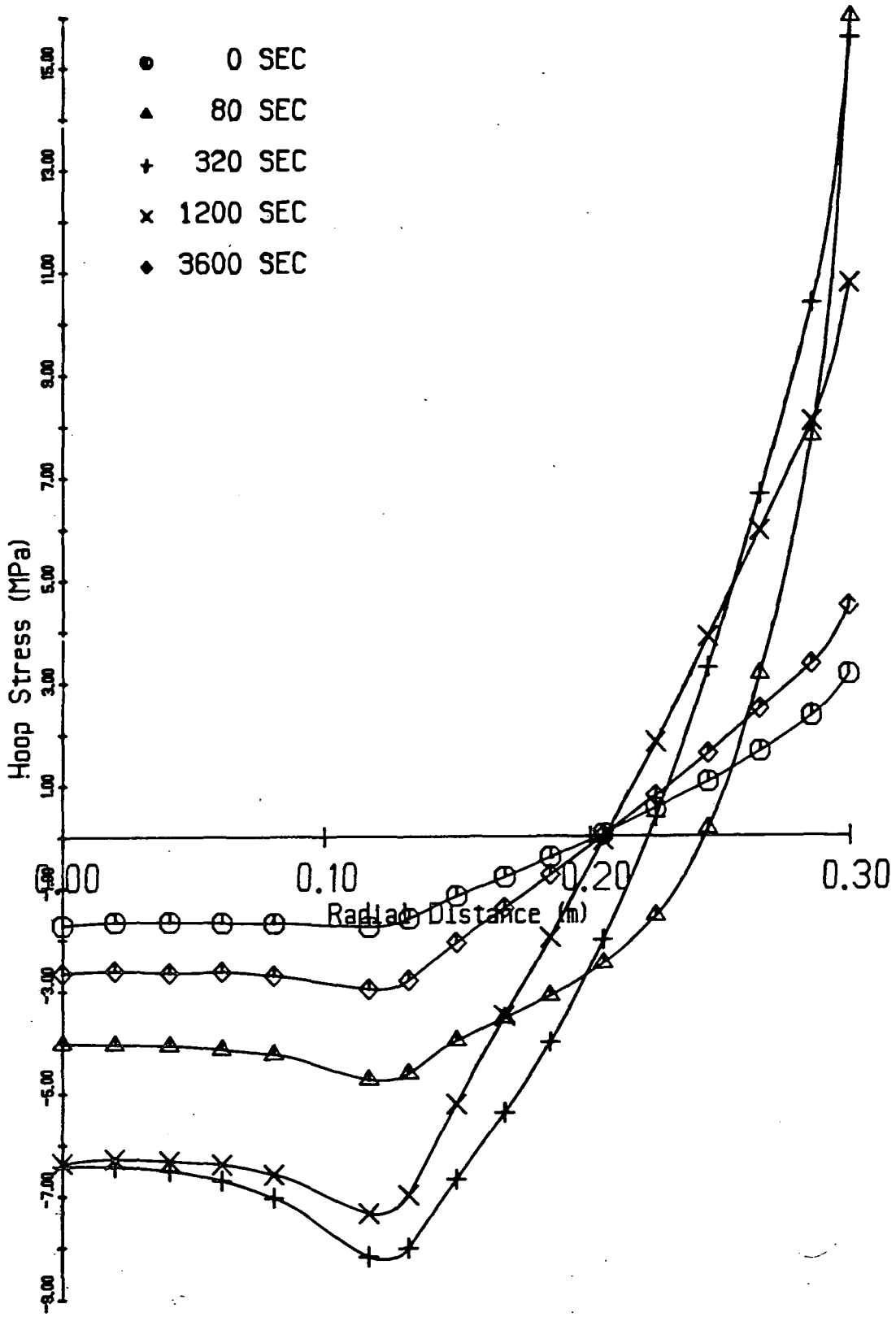

Fig 5.7 Radial variation of thermal hoop stress.

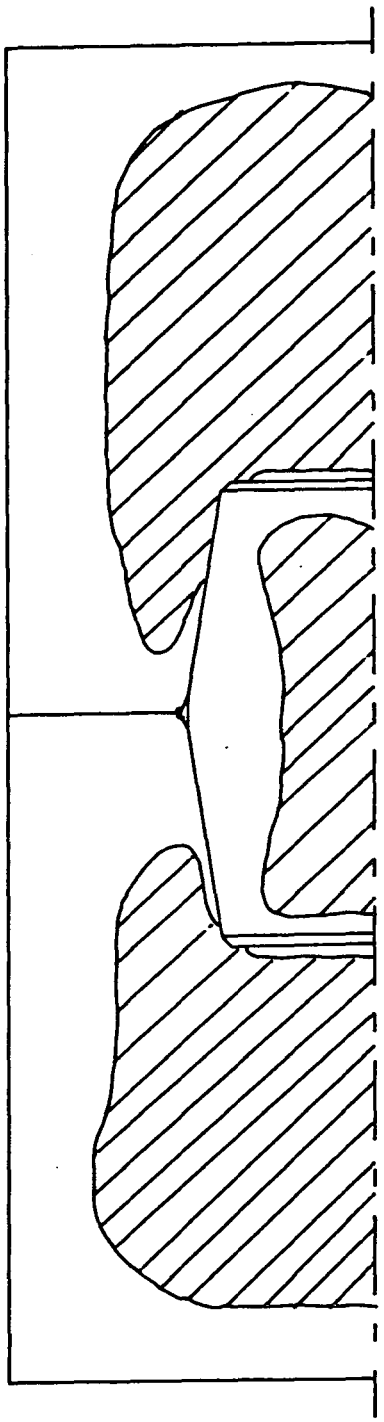

Fig. 5.8 Central core of triaxial compression
(E14 mesh 320 seconds after removal)

CHAPTER 6

FAILURE ANALYSIS

6.1 Possible Approaches

The mechanical and thermal stress analysis discussed in the previous chapters, while highlighting the areas of maximum stress, give little help in the evaluation of the effects of any efforts to reduce failure probability. Such efforts may consist of a total redesign of the electrode joint, improvements in material properties, or the use of a reflective shield around the electrode, as discussed later. The object of a failure analysis is to establish the effects of the calculated stresses on the material at the appropriate temperature. Three approaches are possible

(i) Failure envelope

(ii) Fracture Mechanics

(iii) Statistical analysis combined with (i)

The choice of approach depends upon the type of material (i.e. brittle or ductile) and upon the degree of complexity of the stress field. The three possible approaches are now considered in more detail.

6.2 Failure Envelope

The 'failure envelope' approach is by far the simplest method of assessing whether or not a component will fail under given loading conditions. Basically, the stressses in the component are analysed either experimentally (e.g. by photoelasticity) or theoretically

by analytical or Finite Element techniques. An appropriate failure criterion is then selected - for example, the 'maximum principal tensile stress' criterion, which states that the material will fail if the tensile stress exceeds a particular value (the 'tensile strength'). By comparing the maximum stresses with the strengths, the material may be classified as 'safe', 'critical' or 'failed'. With a ductile material this is a perfectly satisfactory procedure, and this is in fact the traditional approach to engineering design, using a determined stress field and a yield criterion. However, with brittle materials tensile testing has major problems due to misalignment effects, which with a ductile material would be accommodated quite easily by plastic deformation. The standard 'tensile test' for a brittle material is thus a three-point bend test which avoids the problems of misalignment. However, even this test shows a considerable scatter in results due to the variable probability of finding a flaw within a critical region of the specimen. The stress-concentrations produced at such flaws initiate fracture in a brittle material but are largely absorbed by plastic flow in a ductile material. This variable probability also produces a 'size effect', so that the 'tensile strength' of a small specimen is greater than that for a similarly-shaped large specimen.

There have been many attempts to take all these factors into account to produce an average strength

prediction under multiaxial stresses, a so-called 'failure envelope'.

The most generally adopted criterion at the moment is the 'maximum principal stress' approach mentioned above, but this fails to give an accurate prediction in the Tension-Tension (T-T) quadrant, where most brittle materials show a strength reduction under near-equal biaxial tension. (Jortner (1971) has shown this reduction in strength to be 15% for graphite).

Coulomb (see, for example Timoshenko, 1953) proposed that failure occurred when the shearing stress reached the cohesive stress of the material in shear, and Stassi d' Alia (1959) has proposed using the limiting octahedral shear stress.

Griffiths (1920) attempted to take into account the existence of flaws in the material. He developed a theory of brittle fracture based on the hypothesis that the presence of inherent crack-like defects caused stress concentrations in the material, resulting in fracture.

In his original paper, Griffith gave the uniaxial failure stress, σ_f, for a body containing sharp cracks of length 2c, as

$$\sigma_f = \left(\frac{2E\gamma}{\pi c}\right)^{1/2}$$

where γ is the effective surface energy per unit area, and E is the eleastic modulus. This was later modified for a

biaxial stress state with cracks of uniform size randomly oriented in the principal stress plane, leading to an effective 'failure envelope' given by

$$\sigma_1 = \sigma_t \qquad (6.1)$$

for $3\sigma_1 + \sigma_2 > 0$

$$(\sigma_1 - \sigma_2)^2 + 8\sigma_t(\sigma_1 + \sigma_2) = 0 \qquad (6.2)$$

for $\sigma_1 - \sigma_2 > 0$ and $3\sigma_1 + \sigma_2 < 0$

where σ_1, σ_2 are the principal stresses and the uniaxial tensile strength is σ_t.

The Griffith theory predicts that the uniaxial compressive strength of a brittle material containing sharp cracks is eight times its uniaxial tensile strength, but a modification of the theory by Babel and Sines (1968) allowed defects of different shapes to be considered, predicting a variation in the ratio of compressive/ tensile strength of 3 to 8. For graphite this ratio is 3, according to data published in a review by Brocklehurst (1977).

Fig. 6.1 (by Brocklehurst, 1977) shows the comparison between the experimental data and the effective failure envelopes produced by some of the above theories. It is obvious that the theories discussed so far are not satisfactory in explaining the observed failure envelope. In view of this, various empirical theories have been proposed. One of these is due to Ely (1968), who suggested a modification to the maximum strain energy theory, leading to the following failure envelope

$$\xi = \frac{\sigma_1^2}{\sigma_t} - \frac{2\nu\sigma_1\sigma_2}{\sigma_t\sigma_c} + \frac{\sigma_2^2}{\sigma_c} = 1 \qquad (6.3)$$

where σ_1, σ_2 are the principal stresses and the corresponding failure strengths are σ_t and σ_c.

This equation gives a reasonably good description of much of the experimental data in the T-T and C-T quadrants, and posssibly also in the C-C quadrant (although this is less certain due to the unreliability of the data in these regions).

A difficulty exists in the interpretation of this failure envelope in that the uniaxial tensile strengths determined for the electrode material used in this investigation are not very reliable. Several investigators have determined modulus of rupture values for the graphite but these may be up to a factor of 2 in excess of the uniaxial tensile strength values. The actual value of this ratio is uncertain for the material in question, but a value of 1.5 has been suggested by Brocklehurst (1977). As indicated in Chapter II , a value of 10 MPa was chosen for the mean uniaxial tensile strength and 25 MPa for the mean compressive strength were used in this project.

An additional difficulty arises in that the stress field is fully three-dimensional (although axisymmetry was assumed in the Finite Element analysis, the stress field is fully three-dimensional as far as the material is concerned). Equation 6.3 expresses the failure envelope in terms of only two stresses. The effect of the

third stress must therefore be ignored. We may, however, obtain some general predictions for the highly-stressed areas by evaluating the left-hand-side of equation 6.3, a value of 1 corresponding to failure in that region.

A computer program was written which takes each set of nodal values and evaluates the parameter ξ (equation 6.3) for all possible combinations of two stresses taken from the three principal stresses. The highest value is chosen and this is compared to unity to determine the failure (or otherwise) of that node. Since the Ely equation makes no predictions for the C-C quadrant, a maximum principal stress criterion was used for this region. Thus, in all cases, the most severe pair of stresses was chosen for the evaluation. Since the third component of the stress will often be quite small in comparison to the other two, the accuracy of the failure prediction will be quite good in such cases.

Running the program on the mechanical stress fields shows that there are no nodes in failure under the Ely criterion using $\nu = 0.25$, $\sigma_t = 10$ MPa, $\sigma_c = 25$ MPa. This observation is applicable to both Finite Element meshes.

On the electrode surface (nodes 504, 114 on E14 mesh), the mechanical stresses are insufficient to cause any danger of failure, but under the action of the thermal stresses, surface nodes have reached failure stresses by 80s. Fig. 6.2 shows the nodes failed under the Ely Criterion for the 320 second timestep (E14 mesh used). It

is interesting to note that the fillet radius nodes have failed under compression. This is a very localised failure, however, and because the surrounding stresses are compressive, is unlikely to cause a catastrophic failure by crack propagation. Similarly, the inner interface nodes have failed in compression,

The failure of the outside nipple nodes is more serious since these are in triaxial tension. The stress concentration is highly localised however, and a crack formed may not propagate sufficiently for the nipple to actually break. As mentioned in Chapter IV, however, this tension is largely thermal, and a result of the unequal expansion coefficients of the nipple and electrode. In the sensitivity analysis (Chapter VII), it is shown that, for equal expansion coefficients between electrode and nipple, these stresses are much reduced.

These observations must, however, be carefully interpreted. In many cases the values of the stresses decrease quite rapidly as the distance from the critical node increases. These 'dangerous' stresses are often very localised, and failure of a very small region may not be sufficient to cause a complete failure of the whole assembly. In other words, the 'failure envelope' approach does not give any indication as to whether a crack, once initiated, will propagate under these applied stresses. Furthermore, the finite element method is not necessarily sufficiently accurate to predict highly localised stresses

(virtually stress-concentrations) with confidence.

6.3 Fracture Mechanics

The point raised at the end of the previous section is normally handled using a Fracture Mechanics approach. This approach assumes that brittle fractures always originate at cracks or crack-like flaws, and makes use of the stress analysis of a cracked part to define the conditions under which such a crack will propagate and cause catastrophic failure. A basic concept of fracture mechanics is that of the 'stress intensity factor', K, which can be defined for the three basic crack-opening modes I, II, and III. K is a measure of the stress-intensification due to the crack, and enables the stresses around the crack tip to be calculated from the standard equation (crack opening mode I)

$$\sigma_n = \frac{K_I f(\theta)}{\sqrt{2\pi r}}$$

where $f(\theta)$ is an angular function specific to the particular stress component required, and r is the distance from the crack tip.

K_I is a function of the specimen dimensions, loading conditions, and crack geometry, and in general it is proportional to

$$(\text{gross stress}) \times (\text{crack length})^{1/2}$$

For example, in an infinite plate with remote stress σ and crack length 2a, K_I is given by

$$K_I = \sigma(\pi a)^{1/2}$$

It is found that under increasing load a crack will start to grow as long as the loading conditions are such that

$$K_I > K_{IC}$$

where K_{IC} is the critical value of K_I.

K_{IC} is normally referred to as the fracture toughness, and is a property of the material under certain conditions.

For a crack to grow under static loading two conditions are necessary;

(i) There must be a high enough stress present to operate a suitable fracture mechanism.

(ii) The strain energy released by an increment of crack growth must equal or exceed the energy required to form the new crack surfaces.

Given an expression for K_I, and an experimentally determined value for K_{IC}, it is thus possible find a crack length for a given loading situation, above which catastrophic failure may be expected to occur. The actual existence of such cracks may then be confirmed or discounted using non-destructive testing (N.D.T.) techniques.

Unfortunately, the determination of values for the stress intensity factor has not progressed beyond relatively simple conditions of load and geometry.

Moreover, in a complex three-dimensional stress field, fracture mechanics concepts are of little use, since fracture toughness is usually measured in Mode I (plane Stress).

6.4 Statistical Approach

Although the failure criterion of Ely is a good description of the mean strength envelope of the graphite, it gives no indication of the statistical variations in failure stress which are of importance to the engineer. This problem is normally handled using Weibull Statistics, which predict the probability of survival, S, of a body under a uniform stress σ as

$$S = \exp(-\sigma/\sigma_o)^m$$

where σ_o is a constant which may be obtained from experimental data by 'best fit' methods. The probability of failure P_f under uniform stress σ is thus given by

$$P_f = 1 - \exp(-\sigma/\sigma_o)^m \qquad (6.4)$$

In conducting a Weibull analysis of fracture data the failure stresses are first arranged in ascending order (ranked). Each failure stress is then assigned a 'rank value', F_j which is the statistical probability of failure below the j-th stress value. These values may be obtained from tables, or calculated from the expression

$$F_j = \frac{j - 0.3}{n + 0.4}$$

where j is the rank number and n the total number of observations.

By taking logs on both sides of equation 6.4 it may be shown that a plot of $\log.\log[1/(1-P_f)]$ against $\log\sigma$ is a straight line of slope m. The quantity m is known as the Weibull Modulus, and is a measure of the scatter on the results, a low value indicating a high variability of fracture stress (a value of $m = \infty$ in the above equation gives $P_f = 1$ for $\sigma > \sigma_o$ and $P_f = 0$ for $\sigma < \sigma_o$, i.e. the situation existing with ductile materials).

It may also be shown (see, for example, Braiden (1980)) that, for specimens of different volumes V_1 and V_2 with failure stresses σ_1 and σ_2 respectively

$$\left(\frac{\sigma_1}{\sigma_2}\right) = \left(\frac{V_2}{V_1}\right)^{1/m}$$

which allows the failure stress to be predicted for any specimen, provided results are available for specimens of a given volume. Amesz et al. (1973), have shown that this equation gives pessimistic results for failure strength of graphites when extrapolating experimental results to higher volumes - thus a greater dependence of strength on volume is predicted than is observed in practice. It has been shown, however, (Price & Cobb, 1972) that the Weibull theory predicts the observed fracture envelope in the T-T quadrant, the reduction in equibiaxial strength of 0.85 being achieved with a Weibull modulus of about 12.

The original Weibull theory assumes uniform stress, a situation not often encountered in practice, and this makes application of the theory difficult in most real

situations.

This problem has been circumvented by Stanley et al. (1973) who consider an assembly of N elements, each subjected to a uniform stress, combining the failure probabilities of each individual element to obtain an overall failure probability of the complete assembly.

The following assumptions are fundamental to the above work

(i) The failure probability of an element due to one principal stress is independent of the presence of the other principal stresses. The survival probability of an element subjected to three principal stresses is the product of the survival probabilities obtained by subjecting the element to each of the three principal stresses in turn.

(ii) The survival probability of the whole structure is equal to the product of the survival probabilities of the elements.

(iii) A crack, once initiated will always propagate. Thus failure of a single element implies failure of the whole structure.

By applying Weibull statistics to the individual elements (and assuming the strength characteristics of the material to be isotropic), the probability of failure of the assembly is shown to be

$$P_{f\,tot} = 1-\exp\left\{-\left[\left(\frac{1}{m}!\right)^m\left(\frac{\sigma_{nom}}{\sigma_{fv}}\right)^m\left(\frac{V}{v}\right)\sum\right]\right\} \quad (6.5a)$$

where m is the Weibull Modulus, σ_{nom} is a nominal stress value, σ_{fv} the tensile failure stress of unit volume and V is the volume of the structure. $\sum$ is the Stress Volume Integral (S.V.I.) given by

$$\sum = \int_V \left[\left(\frac{\sigma_1}{\sigma_{nom}\,H(\sigma_1)}\right)^m + \left(\frac{\sigma_2}{\sigma_{nom}\,H(\sigma_2)}\right)^m + \left(\frac{\sigma_3}{\sigma_{nom}\,H(\sigma_3)}\right)^m\right]\frac{dV}{v} \quad (6.5b)$$

where H is the Heaviside Unit Operator such that

$H(\sigma) = 1$ for σ positive (tensile)

$H(\sigma) = -\alpha$ for σ negative (compressive)

and α is the modulus of the ratio of compressive to tensile strengths.

The problem of calculating the failure probability is thus reduced to the calculation of the following quantities

(i) $[(1/m)!]^m$ - the material consistency factor, which is a function of the Weibull Modulus only.

(ii) $[\sigma_{nom}/\sigma_{fv}]^m$ - the load strength factor. σ_{nom} is any convenient nominal stress value. If an analysis is performed for several magnitudes of load, with an identical distribution, σ_{nom} is normally chosen to be proportional to this load value, thus making $\sum$ independent of the

load magnitude.

(iii) V/v - the component size factor (v is the unit volume)

(iv) Σ - the Stress Volume Integral. This is a function of the distribution of stresses throughout the material, and is independent of the magnitude of the loads.

This analysis has been extended by Stanley et al. (1977) to cover the case of orthotropic material properties, but the extended analysis requires knowledge of the anisotropic behaviour of not only the strength values, but also of the Weibull Modulus. Such determinations were not available so only the isotropic case is considered here.

The method seems ideal for analysing the failure probability in the present problem using the finite element mesh as the element subdivisional system. It does, however, have some disadvantages when applied in this context.

(i) As the author of the original work shows, the value finally assigned to the stress volume integral depends upon the number and size of the element subdivisions. For a given element size, the stress volume integral converges to a limit as the number of elements is increased. A value for the stress volume integral which is independent of the number of elements occurs only when the element size is sufficiently small. The most

accurate value of the stress volume integral was found by Stanley to occur when the smallest elements were used in highly-stressed areas.

In the present analysis, the number and size of the elements may be varied only at considerable expense of computing time. Stanley was able to vary the element size easily to obtain the best convergence, having considered only analytic solutions to the stress analysis. It is difficult, therefore, to check the convergence of the solution for this problem.

(ii) The theory is based on the assumption that failure of one element results in complete failure of the whole body. In the case of the electrode, this is not a justifiable assumption. Examination of an electode which has undergone service shows that many parts have 'failed' in the strict sense, but the structure as a whole is still intact. Care must therefore be taken in interpreting results from this probability calculation.

(iii) The elemental stress values were obtained by averaging the nodal stress values output by PAFEC. In regions where the stresses vary rapidly with position this is not an accurate method.

(iv) The theory applies only to steady-state stresses. Transient stresses have recently been considered by Stanley (1982), but this work requires a

considerably greater computing commitment than the equivalent steady-state analysis. In any case, it is obvious from the magnitudes of the stresses involved, in comparison to the unit volume failure strength of 2 MPa (see next section), that a failure probability of 1 is going to be predicted for most of the time analysed. Thus the Stanley analysis will only give meaningful results in this problem for the mechanical stresses. However, out of interest it was decided to investigate more fully the effect of varying unit volume failure strength on thermal stress fields. Additionally, the field at 3600 seconds was used for an investigation into the additional effects of a change in Weibull modulus.

6.5 Calculation of Failure Probability

The theory was implemented as three separate computer programs (Appendix V).

The program SA1 is a preprocessing program which takes as its input two pieces of output from a PAFEC run: the list of nodal coordinates and the list of element topologies. The list of nodal coordinates is read into a program array, and a line of topology is then read in. Each node number is located from the node list, and the topology information is converted into a set of coordinate pairs, representing the corner positions of the element. The process is repeated until the whole of the topology list

has been converted to coordinate pairs.

SA2 reads the new topology list written by SA1 and calculates the fractional volume (dV/V) of the complete structure that each element occupies.

SA3 reads the nodal average stress values from a PAFEC run and assigns an average stress to each element. This stress is then associated with the correct element fractional volume from the list produced by SA2 and the stress integral is evaluated using an assumed value for the Weibull modulus. Finally, SA4 calculates the failure probability using equations 6.5.

6.6 Calculation of Failure Probability - Results

Reliable strength data for the graphite in question has been difficult to find, but a limited amount of data was obtained from B.S.C. This consisted of the results of Modulus of Rupture (M.O.R.) tests on specimens 1" x 1" x 6" taken from nine premium grade electrodes (one sample from each end) at an unspecified temperature. Twenty 'pseudo traction' tensile strength results were also included - these are the results of a diametral compression test on a cylinder 50mm dia. x 25mm thick. Some doubts were cast on the validity of this method, however, so these results were not used.

With this limited data, values for the Weibull Modulus, m, and σ_{fv}, the unit-volume (1 m^3) uniaxial tensile strength were obtained from a Weibull plot of the experimental data. Stanley (1973) has shown that, if the

compressive and shear stresses in a three-point bend specimen are negligible, equation (6.5) may be evaluated as follows

$$P_f = 1 - \exp\{-[(1/m)!]^m(\sigma_{max}/\sigma_{fv})^m(V/v)/2(m+1)^2\} \quad (6.6)$$

The failure probability, P_f, may be determined as a function of σ_{max} from ranked test data (as described in the previous section, and a plot of log.log $[(1/1-P_f)]$ against $\log\sigma_{max}$ is thus a straight line with slope m and intercept given by

$$\log\{-[(1.m)!]^m(1/\sigma_{fv})^m(V/v)/2(m+1)^2\} + \log.\log e$$

Since m and V are known, σ_{fv} may be calculated.

The determination of these quantities for the sample available is given in Appendix IV, where it is shown that $\sigma_{fv} \simeq 2$ MPa and m=10. As noted in section 6.4, however, there is some evidence that the volume dependence from the Weibuill analysis underestimates the unit volume tensile strength at large volumes. The unit volume used in this formulation of the analysis was 1 m^3, and this is four orders of magnitude greater than the test specimen size. It is likely, therefore, that this figure is too low. Furthermore, the temperature of the specimens in the tests producing the results in Appendix IV was not stated;

Montgomery (1979) has shown that the strength increases with temperature. The value for σ_{fv} is thus somewhat indeterminate. The analysis has therefore been performed for a range of σ_{fv} from 2 to 9 MPa and the results are shown in Table 6.1, presented graphically in Fig. 6.3. These are results applying to stresses obtained from the E8 mesh only.

From Table 6.1, it can be seen that, for tightening torque only, the failure probability for σ_{fv} = 2 MPa is 0.002. Thus, fracture under normal tightening torque only should be expected in only 2 in 1000 cases. For all higher values of σ_{fv} investigated, the failure probability is zero to the accuracy of the program.

Table 6.1 shows the failure probability for each of the stress fields calculated, for a unit volume failure strength varying from 2 MPa to 10 MPa. the thermal stresses are such that the material always fails, even for much higher values of σ_{fv}.

This does not imply a 100% practical failure rate, however, since the failure of one element defines complete failure in the Stanley analysis. By examination, we can see that many stresses exceed 2 MN/m^2 so on the above failure criterion a 100% failure rate is reasonable. However, examination of used electrodes shows a multitude of cracks and splits. Every electrode thus 'fails' in the Stanley sense, but evidently a crack, once initiated, does not necessarily propagate - a direct indication that graphite

is not a perfectly brittle material (see Chapter II). Table 6.2 shows, for the 3600 second timestep, the effect of variation in Weibull modulus.

The method of failure probability prediction proposed by Stanley has been shown in this chapter to produce consistent results. Two factors make it difficult to use in the present context.

(i) The unit volume failure stress is rather indeterminate - the Weibull estimate is probably too pessimistic.

(ii) A crack, once initiated, does not necessarily propagate catastrophically, as examination of a used electrode shows. Thus, a 100% probability of crack formation does not imply a 100% catastrophic failure rate.

6.7 SUMMARY

Three methods of evaluating the effects of the calculated thermal/mechanical stresses on the electrode have been examined.

The 'failure envelope' approach gives a good indication of which areas are critically stressed but does not give a 'failure prediction'. No accurate failure envelope has been suggested for graphite at room temperature or elevated temperatures.

Fracture mechanics is not yet sufficiently advanced to analyse such a complicated load/geometry/time situation.

The statistical analysis suggested by Stanley produces a 'failure probability' figure, but because of the assumptions inherent in the work, this figure is unrealistic for this problem.

		TOTAL FAILURE PROB FOR STATED STRENGTH (MPa)								
TIME (s)	S.V.I.	2.0	3.0	4.0	5.0	6.0	7.0	8.0	9.0	10
0	0.1821E-22	1.000	1.000	0.966	0.305	0.057	0.013	0.003	0.001	0.0
80	0.3601E-18	1.000	1.000	1.000	1.000	1.000	1.000	1.000	1.000	0.9
160	0.1495E-18	1.000	1.000	1.000	1.000	1.000	1.000	1.000	1.000	0.9
320	0.3581E-19	1.000	1.000	1.000	1.000	1.000	1.000	0.999	0.884	0.5
640	0.8775E-20	1.000	1.000	1.000	1.000	1.000	0.998	0.797	0.388	0.1
1200	0.9639E-21	1.000	1.000	1.000	1.000	0.955	0.486	0.161	0.053	0.0
2400	0.9692E-37	1.000	1.000	0.836	0.176	0.031	0.007	0.002	0.001	0.0
3600	.2903E-24	1.000	0.617	0.053	0.006	0.001	0.000	0.000	0.000	0.0
Tight. only.	0.9324E-29	0.002	0.000	0.000	0.000	0.000	0.000	0.000	0.000	0.0

S.V.I. = Stress Volume Integral

Table 6.1 Failure predictions for Various Tensile Strengths

		MEAN UNIT VOLUME FAILURE STRENGTH (MPa)								
m	S.V.I.	2.0	3.0	4.0	5.0	6.0	7.0	8.0	9.0	10.0
8	0.1319E-19	1.000	0.329	0.039	0.007	0.002	0.001	0.000	0.000	0.000
9	0.6016E-22	1.000	0.452	0.044	0.006	0.001	0.000	0.000	0.000	0.000
10	0.2903E-24	1.000	0.617	0.053	0.006	0.001	0.000	0.000	0.000	0.000
11	0.1472E-26	1.000	0.800	0.066	0.006	0.001	0.000	0.000	0.000	0.000
12	0.7798E-29	1.000	0.941	0.086	0.006	0.001	0.000	0.000	0.000	0.000
13	0.4280E-31	1.000	0.994	0.115	0.007	0.001	0.000	0.000	0.000	0.000

m=Weibull Modulus

Table 6.2 Failure probability at 3600 sec for various Weibull Moduli and Failure Strengths.

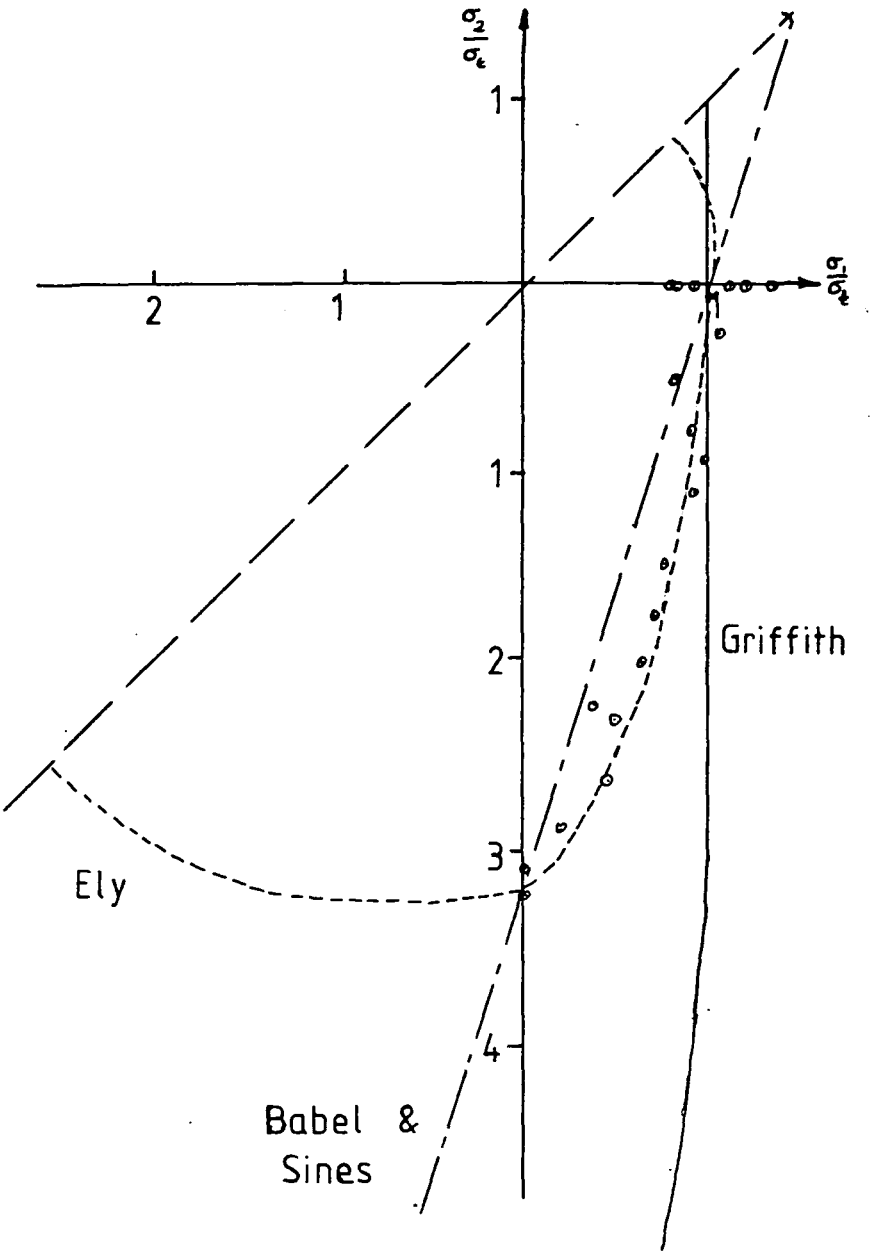

Fig 6.1 Possible Failure Envelopes for Graphite

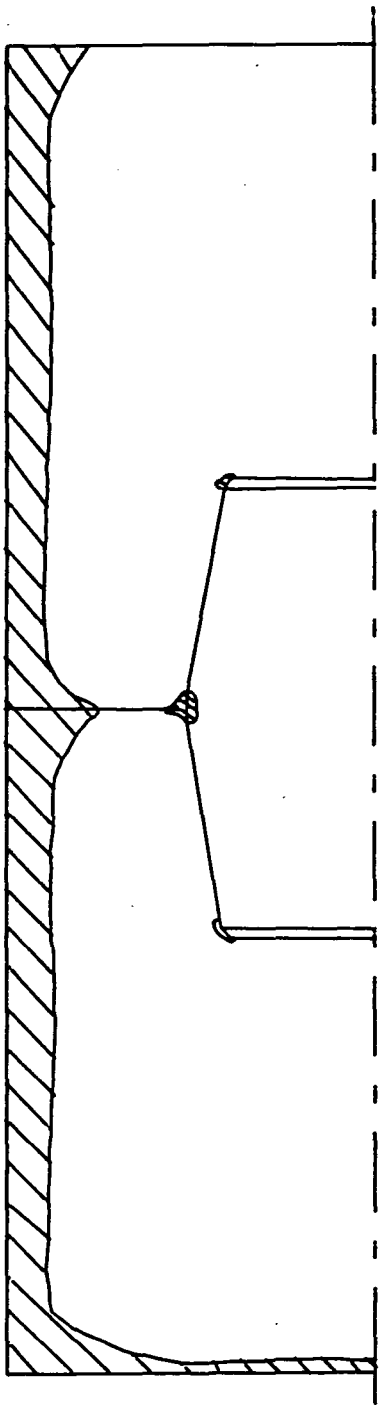

Fig. 6.2 Nodes failed under Ely crit at 320s (E14 mesh).

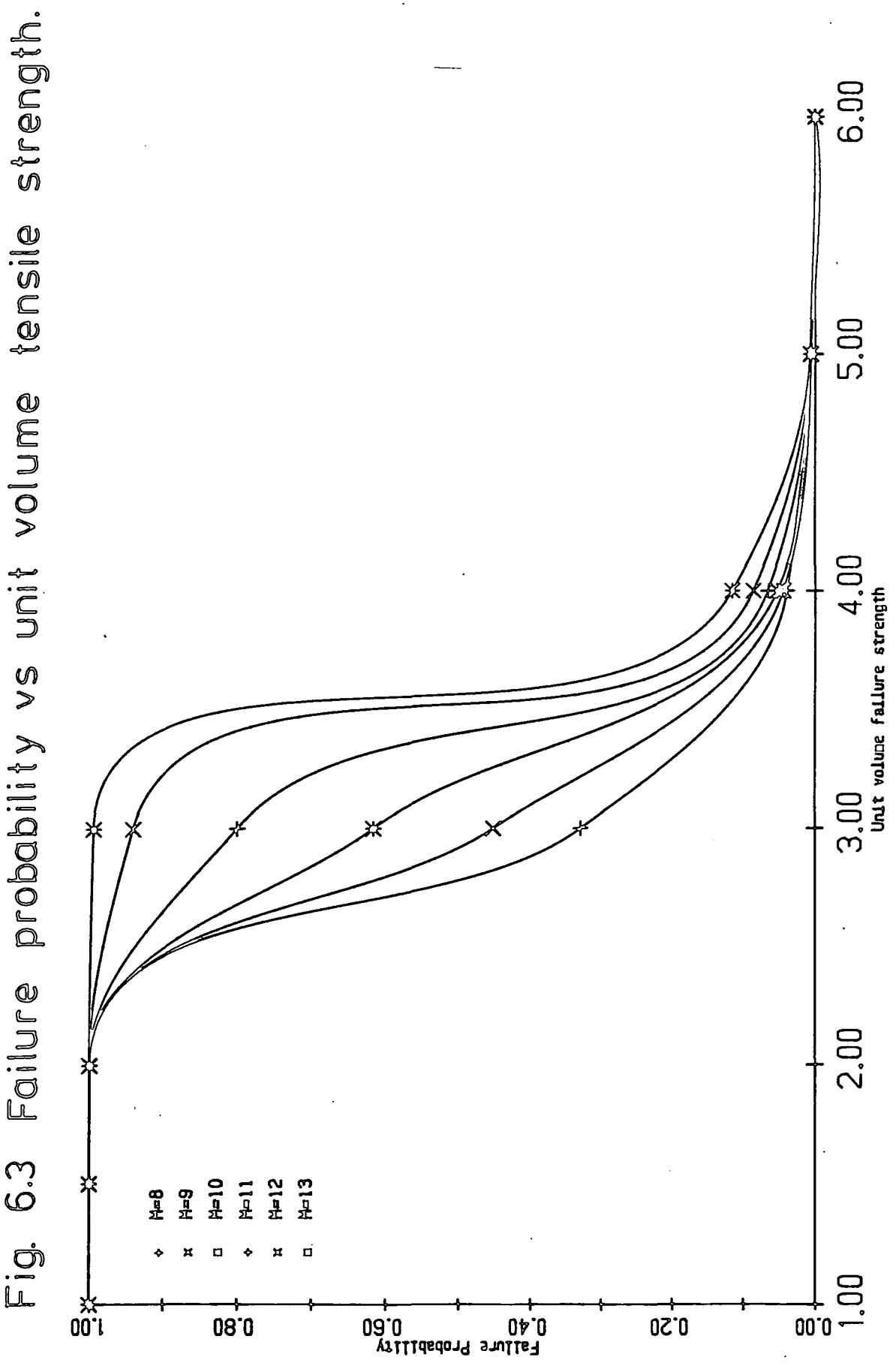

Fig. 6.3 Failure probability vs unit volume tensile strength.

CHAPTER 7

SENSITIVITY ANALYSIS

7.1 Introduction

The Finite Difference and Finite Element schemes presented in the previous chapters were arrived at by a judicious balance between complexity and the need to obtain answers within a reasonable C.P.U. time.

Thus, material properties were considered to be isotropic and homogenous. The electrode was considered to be unworn, and removed instantaneously from the furnace. This chapter is intended to provide some justification for the use of a relatively simple Finite Difference model, by showing some of the additional refinements that were considered, and the results of some trial runs using different basic assumptions. The chapter may be considered in two parts. The first part (sections 7.2 to 7.5) outline the possible improvements to the Finite Difference scheme and some results of these improvements. The second part of the chapter (sections 7.6 to 7.8) is concerned with the sensitivity of the thermal analysis to changes in material properties.

7.2 Possible ways of improving the Model

The following areas were considered appropriate for development.

(i) Inclusion of the effects of orthotropy in the material thermal properties.

(ii) Consideration of non-black-body radiation effects from the surface of the electrode.

(iii) Allowance for axial heat flow at distances greater than three electrode radii from the tip.

(iv) Consideration of the effects of the temperature-dependent thermal conductivity of graphite.

(v) Consideration of the effect of placing a reflective shield around the electrode while it is out of the furnace. This was mentioned by the sponsors of the project as a possible method of reducing thermal shock stresses.

The implementation of these improvements involved considerable modifications to the Finite Difference model. A rigorous extension of the analysis to the case of a generally isotropic material, with material properties also dependent upon position and temperature, would require modifications to the Finite Difference scheme which could not be justified in view of the poor accuracy and reliability of the available property determinations. On the other hand, some information on the anisotropy and temperature-dependence of graphite material properties was available, and the Finite Difference scheme was therefore modified in such a way as to make use of this extra information as simply as possible.

7.2.1 Effect of Orthotropy in Material Thermal Properties

By assuming the graphite to be orthotropic and homogenous, the thermal conduction properties of the material may be represented by k_r, k_z, k_θ, the principal thermal conductivities in the radial, axial and circumferential directions respectively - these may be temperature-dependent Assuming that the spatial derivatives of the thermal conductivities are everywhere zero, and that there is no circumferential temperature variation, the heat conduction equation for orthotropic media then becomes (Carslaw & Jaeger, 1959).

$$D_r\left(\frac{\partial^2\theta}{\partial r^2} + \frac{\partial\theta}{r\partial r}\right) + D_z\frac{\partial^2\theta}{\partial z^2} = \frac{\partial\theta}{\partial t} \qquad (7.1)$$

where $D_r=k_r/\rho c$ and $D_z=k_z/\rho c$ (ρ, c are assumed independent of temperature).

The Finite Difference equation for a general point inside the electrode body then becomes

$$\theta_{r,z,t+\Delta t} = \theta_{r,z,t} + \frac{D_r\Delta t[(2r+\Delta r)\theta_{r+\Delta r,z,t} + (2r-\Delta r)\theta_{r-\Delta r,z,t} - 4r\theta_{r,z,t}]}{2r(\Delta r)^2}$$

$$+ \frac{D_z\Delta t[\theta_{r,z+\Delta z,t} + \theta_{r,z-\Delta z,t} - 2\theta_{r,z,t}]}{(\Delta z)^2} \qquad (7.2)$$

Corresponding modifications may be made to the equations applying to particular areas of the electrode, i.e. the radiating surfaces and the central axis. The relevant terms in the Finite Difference program were therefore rewritten in order to incorporate these

modifications, producing a set of equations equivalent to 4.3,4.4 & 4.8-4.14 and the program was thoroughly tested using trial values for the thermal diffusivities, plotting the results using the graphical output program as before.

7.2.2 Differences in electrode and nipple material properties.

By dividing the electrode joint into regions in which thermal conductivity is independent of position, the corresponding spatial derivatives of thermal conductivity are zero everywhere except on the boundaries of these regions. Thus equation 7.2 is applicable to the regions shown in Fig. 7.1 (which is a simplified representation of a joint) if the spatial derivatives on the boundaries are ignored. Since the thread form is not modelled in this Finite Difference scheme the above inaccuracy is considered relativly insignificant in comparison to the real perturbations of the heat flow across the electrode/nipple boundaries due to variable thread tooth contact. The spatial variation of material properties was thus handled by simply modifying the Finite Difference program in such a way as to use the correct material properties for the point under consideration, by calling a subroutine DECIDE immediately before each Finite Difference calculation. The purpose of this subroutine is to ascertain which material properties are relevant to the point in question. The full flow-diagram of the subroutine DECIDE is shown in Appendix II.

The finite difference program was again thoroughly tested using suitable values for the diffusivity of electrode graphite, nipple graphite and air. However, instability occurred in the equations, after several timesteps, in the region of the air gap. Despite thorough checking of the implementation the problem remained and it was concluded that the instability was caused by the relatively large value of the diffusivity of the air in comparison to that of the graphite material (see comments on stability in Chapter IV). The air gap at the top of the nipple was therefore removed by defining the properties of air to be identical to those of the nipple graphite. This was more convenient than rewriting the subroutine to ignore the air-gap, and simply means that the electrode socket is completely filled by nipple graphite as far as the Finite Difference program is concerned.

7.2.3 Variation of Thermal Conductivity with Temperature.

The thermal conductivity of graphite decreases with temperature. Reliable determinations of the thermal conductivity of electrode graphite are scarce in the open literature but the Graphite Engineering Handbook presents, graphically, data collected from various sources representing the temperature variation of thermal conductivity of several types of extruded graphite. Most of the determinations have been made over a very limited temperature range and show considerable scatter but it is possible to obtain a single line representing the

variation by averaging the observations at each temperature. When this is done, and the necessary unit conversions are made, the result is as shown in Fig. 2.4. For electrode and nipple graphite. Accurate thermal conductivity values for the two principal directions were not available even at room temperature. It is, however, possible to show that the curve in Fig. 2.4 corresponds quite well with the known values of thermal conductivity of electrode graphite, by the following method.

(i) A third-order polynomial was fitted to the curve in Fig. 2.4 by the method of least squares. This yields the following equation representing the experimental data:

$$K_\theta = A_0 (1 + A_1\theta + A_2\theta^2 + A_3\theta^3) \qquad (7.3(a))$$

where $A_0 = 162.6$, $A_1 = -9.11 \times 10^{-4}$, $A_2 = 3.01 \times 10^{-7}$, $A_3 = -3.3 \times 10^{-11}$

The room-temperature (25°C) value of thermal conductivity from this equation is 159.0 W/mK.

(ii) Information supplied by A.G.L.(U.K.) Ltd. (1979) shows that the room-temperature specific electrical resistance of electrode graphite (in $\mu\Omega$-cm) measured parallel to the extrusion direction is as follows:

Electrode (600mm)	Nipple (350mm)
800	560

Using the fact that (A.G.L., 1979)

$K(cal/s\ cm\ °C) = 0.00031\ \sigma\ (mho/cm)$

where σ is the electrical conductuvity and K the thermal conductivity. The predicted room-temperature values for the thermal conductivities (in W/mK) are therefore:

Electrode	Nipple
162.8	232.5

The electrode room-temperature thermal conductivity parallel to the extrusion direction is very close to that predicted by the polynomial. The polynomial was thus taken to represent the axial thermal conductivity of the electrode material.

For a full temperature-dependent analysis, two curves are required, representing the variation of thermal conductivity with temperature for electrode and nipple. The variation for the nipple material was represented by:

$$K_\theta = B_0(1 + B_1\theta + B_2\theta^2 + B_3\theta^3) \qquad (7.3(b))$$

the form of the variation for the nipple material is thus assured to be identical to that of the electrode material. A value of 233 is assigned to B_0 to produce the correct room-temperature value.

Using the fact (Elliott, 1969) that the anisotropy ratio for thermal conductivity $K_R/K_A = 1.25$ the radial conductivity for any given temperature may also be obtained

for nipple and electrode material. Appendix II gives details of how the Finite Difference program was modified to take account of this.

7.2.4 Allowance for Non-Black-Body Radiation.

The original Finite Difference formulation assumed black-body radiation from the electrode surface. Elliott (1969) suggested a value of 0.8 for the emissivity of graphite at the temperatures involved, and Mantell (1968) argued for a temperature-dependent emissivity but gave no details of the proposed variation. The terms involving radiation were therefore identified in the computer program and multiplied by an extra factor 'EMS', the emissivity of the material surface, which for all subsequent runs was defined as 0.8 (this process also sets the absorptivity of the material equal to 0.8 - a reasonable assumption).

7.2.5 The effect of placing a Reflective Shield around the Electrode.

One possible method of reducing the thermal shock transients is to enclose the electrode in a reflective shield while sections are being replaced. This would reduce the radiative heat loss by re-radiating a large proportion of the heat back into the electrode.

Since, in the Finite Difference scheme, the rate of heat loss at the surface was calculated as

$$(dq/dt)_R = \varepsilon S[(\theta_R+273)^4-(\theta_A+273)^4] + h(\theta_R-\theta_A)$$

where ε is the emissivity of the surface, h is the convection coefficient and S is Stephan's Constant of radiation, we can simulate the effect of a reflective shield by assuming a proportion α of this heat to be radiated back (α may be identified as the reflectivity of the shield). Then

$$(dq/dt)_R = S\varepsilon[(\theta_R+273)^4-(\theta_A+273)^4]-\varepsilon S\alpha[(\theta_R+273)^4-(\theta_A+273)^4]$$
$$+h(\theta_R-\theta_A)$$
$$=(1-\alpha)\varepsilon S[(\theta_R+273)^4-(\theta_A+273)^4]+h(\theta_R-\theta_A)$$

at the surface, assuming perfect absorption of the heat radiated back to the electrode (we might also assume that, due to confinement of the electrode, convection would be reduced and hence the value of h would be vastly decreased).

In the computer model, the effect of a reflective shield can thus be simulated by arranging for the radiative terms to be multiplied by the factor (1-ALPHA). The value of the parameter ALPHA is input by the user on prompting by the program. The effects of this modification are discussed later in the Chapter.

7.2.6 Allowance for Axial Heatflow at any distance from the electrode tip

Previously, the finite difference program had been set up in such a way that the full 'two-dimensional' heat flow was only applied at distances from the electrode tip of up to three electrode radii. At greater distances than this, a one-dimensional version of the equations was

used to allow only radial heat flow. This is done to save computing time. In the modified version, axial heat flow is permitted to a distance defined by the user.

7.3 The improved Finite Difference Program

The modified version of the Finite Difference program is thus capable of taking into account;

(i) anisotropy of material properties

(ii) non-black-body radiation

(iii) variable extent of axial heat flow

(iv) different material properties of electrode and nipple

(v) temperature dependence of thermal conductivity.

7.4 Stress Calculations from the improved program

As mentioned in Chaper V, the GAPS module in PAFEC was found not to fully converge for certain timesteps. This makes the task of ascertaining the effects of changes to the Finite Difference program more difficult, since there is no guarantee that, for a given timestep, the GAPS iteration process will fully converge for all variations considered. There are several possible ways of circumventing this problem, none of which is entirely satisfactory. The method to be described represents what was considered to be the best compromise.

(i) Choose one particular timestep value for the comparisons. This timestep must be one for which the GAPS process was convergent (or nearly so),

and one which represents a typical 'out of furnace' time. The step number chosen was 80, corresponding to 320 seconds after removal.

(ii) From the previous full GAPS run, note which thread tooth and interface nodes are in contact for this timestep.

(iii) Set up PAFEC runs for the temperature fields from the improved Finite Difference program, and connect those nodes which are in contact in the full runs together using PAFEC's GENERALISED CONSTRAINTS module. This allows the displacement at a node to be specified as a linear combination of the displacements at another node. The module was used in such a way as to simulate SLIDING (no friction) at the contact nodes. All other thread node pairs were free to take up the positions they choose. In order to provide a firm basis for comparison, the original timestep 80 stresses were recalculated using this method.

The main inaccuracy in this method, of course, is that changing the Finite Difference program complexity or material properies will, in general, change the number of contacting thread teeth or interface nodes for the timestep considered. Thus a full GAPS run should be performed for each comparison.As mentioned earlier, however, there is no guarantee that convergence would be obtained with a full GAPS run on each problem. Such a course was therefore

considered to be a waste of computing resources.

A further inaccuracy occurs due to the fact that friction is not simulated between contacting nodes. Since the whole purpose of this chapter is to provide comparisons, however, these inaccuracies were not considered serious.

7.5 Results of the Finite Difference Improvements

Using the 320 second interpolated temperature field from the original Finite Difference program, the stress run was executed using the GENERALISED CONSTRAINTS concepts described earlier. All other parameters were identical for this initial run. Some typical results are shown in Table 7.1 , under the line headed "Std Set". By comparing these results with those for the 320 second time step in Table 4.1 the effect of turning the GAPS analysis into a GENERALISED CONSTRAINTS analysis may be seen.

The line in Table 7.1 marked "Std Ort" represents the stresses calculated from the improved Finite Difference program It should be noted that this is not directly comparable to the line marked "Std Set" because, as well as anisotropy, temperature dependent material thermal properties and reduced emissivity are incorporated. Even so, the consistency between these runs is quite good, the biggest difference occuring at node 10 where the compressive stresses are increased considerably in the orthotropic run. Elsewhere, however, the differences are fairly small.

The effect of increasing the axial analysis to 4 electrode radii is shown in the line marked "4 Radii". Comparing this with the "Std Orth" line we see that this has a totally negligible effect on the stresses in the region of interest.

As previously mentioned, the emissivity for these orthotropic runs was set at 0.8. The lines in Table 7.1 marked "0.6 Ems" and "1.0 Ems" represent the effects of changing the emissivity of the electrode surface to 0.6 and 1.0 respectively. We would expect that decreasing the emissivity, which would decrease the rate of radiative heat loss at the surface, should allow better equalisation of the temperatures in the outer layers, and hence lower the stresses in this region. In the interior regions, the effect would be expected to be less marked. Examination of Table 7.1 shows that this is indeed the case. Node 20, for example, on the surface, has a hoop stress of 21 MPa reduced to 19 MPa and increased to 22 MPa on decreasing and increasing respectively the emissivity between these limits. At node 20, just below the surface, the effect is much less marked.

The effect of enclosing the electrode by a reflective shield immediately on removal from the furnace, is simulated in the lines marked "0.4 Shd" and "0.7 Shd" in Table 7.1. These refer to shields of reflectivity 0.4 and 0.7 respectively. The stresses induced at the surface would be expected to be reduced by the 0.4 reflectivity shield,

and further reduced by the 0.7 reflectivity shield, since the heat reflected back will cause a partial equalisation of the near-surface temperatures.

Node 21, for example, with an original stress state of

$$\sigma_1 = 21.0\ \text{MPa} \sigma_2 = 4.4\ \text{MPa} \sigma_3 = 20.8\ \text{MPa} \tau_m = 8.3\ \text{MPa}$$

becomes, with the 0.4 reflectivity shield

$$\sigma_1 = 18.1\ \text{MPa} \sigma_2 = 4.1\ \text{MPa} \sigma_3 = 18.1\ \text{MPa} \tau_m = 7.0\ \text{MPa}$$

and with the 0.7 reflectivity shield

$$\sigma_1 = 14.0\ \text{MPa} \sigma_2 = 3.4\ \text{MPa} \sigma_3 = 14.6\ \text{MPa} \tau_m = 5.3\ \text{MPa}$$

The effect is less marked at points remote from the surface. Node 75, for example, near the fillet radius, has initial stress state

$$\sigma_1 = -2.0\ \text{MPa} \sigma_2 = -11.2\ \text{MPa} \sigma_3 = -6.1\ \text{MPa} \tau_m = 4.6\ \text{MPa}$$

which with the 0.4 reflectivity shield becomes

$$\sigma_1 = -1.6\ \text{MPa} \sigma_2 = -9.2\ \text{MPa} \sigma_3 = -5.0\ \text{MPa} \tau_m = 3.8\ \text{MPa}$$

and for the 0.7 reflectivity shield

$$\sigma_1 = -1.2\ \text{MPa} \sigma_2 = -6.8\ \text{MPa} \sigma_3 = -3.7\ \text{MPa} \tau_m = 2.8\ \text{MPa}$$

The provision of such a shield is thus seen to be beneficial in reducing surface stresses, but does little to improve matters in the interior of the electrode.

7.6 Materials Sensitivity Analysis

Six material properties were varied with a view to investigating the effects on thermal stresses. These were as follows:

k	(thermal conductivity)	=	50 W/m K	(+25%)
k		=	30 W/m K	(-25%)
c	(spec. heat cap.)	=	2300 J/kg K	(+15%)
c		=	1700 J/kg K	(-15%)
h	(convection coeff.)	=	18.8 W/m^2 K	(+50%)
h		=	6.3 W/m^2 K	(-50%)
E_e	(Elec. Youngs mod.)	=	16.25 GPa	(+25%)
E_n	(Nipple Youngs mod)	=	17.5 GPa	(+25%)
E_e	(Elec. Youngs mod.)	=	9.55 GPa	(-25%)
E_n	(Nipple Youngs mod)	=	10.5 GPa	(-25%)
ν	(Poisson Ratio)	=	0.35	(+40%)
ν		=	0.15	(-40%)
α_e	(C.T.E. Electrode)	=	2.5 $\mu\varepsilon$/K	
α_n	(C.T.E. Nipple)	=	2.5 $\mu\varepsilon$/K (equal values for nipple & electrode)	
α_e	= α_n	=	3.0 $\mu\varepsilon$/K	(+25%)
α_e	= α_n	=	2.0 $\mu\varepsilon$/K	(-25%)

Of these, the variation in k, c and h required the Finite Difference program to be modified, and consequent re-interpolation of the temperature field to the Finite

Element points. The variation in E, ν, α did not require modification to the Finite Difference program. The original interpolated temperature field for this time step could therefore be used with a modified Finite Element model. The effects of these variations are now discussed individually.

7.7 Sensitivity to Finite Difference parameters

7.7.1 Thermal Conductivity

The effect of varying the thermal conductivity of the graphite material by 25% on either side of the standard value may be seen by examination of the lines marked "K red" and "K inc" in Table 7.2.

Points on the electrode surface (nodes 7,21), which suffer large tensile hoop stresses, may be seen to experience a reduction in tensile stresses when the thermal conductivity of the material is increased. This is easily explained when one considers that the surface suffers extreme radiative heat loss. The heat conduction within the electrode is unable to equalise the temperature gradient at the surface, hence the high hoop stresses. An increase in thermal conductivity, however, will allow better equalisation of the surface temperature gradient, reducing the surface hoop stress. The magnitude of the effect is greatly reduced at points within the body of the electrode (node 319, for example).

7.7.2 Specific Heat Capacity

The effect of changing the specific heat capacity of the electrode material will generally be expected to change the stresses in the opposite direction to that of a change in the thermal conductivity. This is because an increase in the specific heat capacity causes a decrease in the overall diffusivity of the material.

The effect of changing the specific heat capacity by 15% on either side of the standard set is shown in the lines marked "SHC red" and "SHC inc" in Table 7.2. Thus, at nodes 7 & 21, for example, the surface stresses are increased when the specific heat capacity is increased. Again, interior nodes (20, 75, 319, for example) show a much less marked effect.

7.7.3 Convection Coefficient

The effect of varying the convection coefficient by 50% on either side of the standard set is shown in the lines marked "CC red" and "CC inc" in Table 7.2. The greatest effect is at the surface nodes (· 7, 21, for example). Even here, the effect is negligible, but we may observe that increasing the convection coefficient increases the rate of surface heat loss, and hence the surface stresses. We may conclude from this that convective heat loss from the electrode is negligible, and in fact the Finite Difference equations of Chapter IV would have been equally valid without including allowance for convection.

7.8 Sensitivity to Finite Element parameters

7.8.1Young's Modulus

The effect of varying the modulus of the material by 25% on either side of the standard set is shown in the lines marked "E red" and "E inc" in Table 7.3.

In this case, a marked effect on the thermal stresses may be observed over all regions of the electrode/nipple combination. An increase in the value of the modulus increases the magnitude of the thermal stresses. This is the effect to be expected - the electrode attempts to take up the same displaced shape as before, but larger forces are required to cause this to happen.

7.8.2 Poisson's Ratio

The effect of varying Poisson's Ratio for graphite by 40% on either side of the standard set is shown in the lines marked "NU red" and "NU inc" in Table 7.3.

In this case there is no general trend for the stress change with change of ν, the direction and magnitude of the change depending upon the stress at the point and at neighbouring points. At most of the points chosen (nodes 20, 75, 319, for example) an increase in ν causes an increase in the magnitude of the three principle stresses. However, at node 19, we see that σ_3 is decreased in magnitude by an increase in ν, and that σ_1 and σ_2 are decreased in magnitude. Node 237, however, has the value of σ_2 decreasing in magnitude and σ_1 and σ_3 increasing in magnitude when ν is increased.

7.8.3 Thermal Expansion Coefficient (C.T.E.)

The investigation into the effect of changing the C.T.E. was slightly different from the other investigations. In Chapter IV, it was asserted that the large compressive stresses at the socket entrance, and the large tensile stresses at the edge of the nipple could be attributed to the difference in expansion coefficients between electrode and nipple. For the investigation into the effect of C.T.E. the coefficients for the electrode and nipple were set equal. Three runs were carried out:

(i) Coefficient for nipple set equal to standard value for electrode (see line marked "CTE =" in Table 7.3)

(ii) Coefficients equal and reduced by 25% from standard (line "CTE red").

(iii) Coefficients equal and increased by 25% over standard (line "CTE inc").

At points away from the electrode/nipple interface (nodes 7,19,45 for example), making the C.T.E.'s equal makes little difference to the induced stresses. Reducing the expansion coefficient shows, however, as would be expected, a sizeable decrease in the magnitudes of the principal stresses.

Close to the electrode/nipple interface (nodes 237, 1314) the magnitude of the stresses is reduced considerably by making the C.T.E.'s equal, and further reduced by a reduction in the absolute values. Nodes 1082

and 470 show this effect to a lesser extent. This reinforces the explanation in Chapter IV, for the existence of high stresses in this region in the first place.

7.9 CONCLUSIONS

The effects of various changes in the analysis have been investigated. The results indicate that significant reduction in thermal stresses may be obtained by

(i) Decreasing the emisssivity of the electrode surface.

(ii) Providing a reflective shield to enclose the electrode while it is out of the furnace.

(iii) Decreasing the values of specific heat capacity, Young's Modulus, Poisson's Ratio, expansion coefficient.

(iv) Increasing the value of the material thermal conductivity.

(v) Making the thermal expansion coefficients of the electrode and nipple more nearly equal.

7

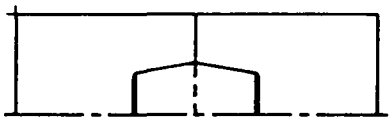

	β	σ_1	σ_2	σ_3	τ_m
Std Set	18.6	5.4	0.3	19.2	2.5
Std Ort	21.3	7.5	0.3	22.3	3.6
4 Radii	21.3	7.5	0.3	22.3	3.6
0.6 Ems	21.5	7.4	0.4	21.5	3.5
1.0 Ems	21.0	7.5	0.1	23.0	3.7
0.4 Shd	21.7	7.4	0.6	20.8	3.4
0.7 Shd	22.1	7.0	0.9	18.5	3.0

10

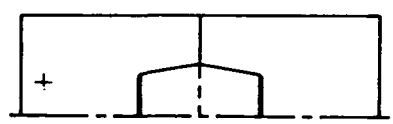

	β	σ_1	σ_2	σ_3	τ_m
Std Set	48.7	-4.5	-9.5	-6.2	2.5
Std Ort	33.1	-8.5	-13.1	-10.3	2.3
4 Radii	33.1	-8.5	-13.1	-10.3	2.3
0.6 Ems	31.0	-8.1	-12.5	-9.9	2.2
1.0 Ems	34.5	-8.8	-13.6	-10.6	2.4
0.4 Shd	29.5	-7.8	-12.1	-9.5	2.1
0.7 Shd	24.4	-6.7	-10.8	-8.5	2.0

19

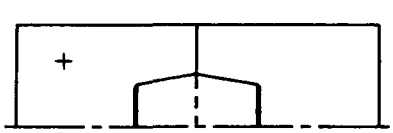

	β	σ_1	σ_2	σ_3	τ_m
Std Set	34.7	0.6	-7.9	-3.3	4.3
Std Ort	36.8	0.2	-5.8	-3.5	3.0
4 Radii	36.8	0.2	-5.8	-3.5	3.0
0.6 Ems	36.1	0.3	-5.2	-3.0	2.7
1.0 Ems	37.2	0.1	-6.4	-4.0	3.3
0.4 Shd	35.5	0.4	-4.7	-2.6	2.5
0.7 Shd	32.1	0.5	-3.3	-1.5	1.9

20

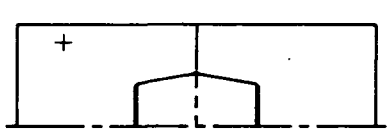

	β	σ_1	σ_2	σ_3	τ_m
Std Set	14.6	5.4	-4.9	4.6	5.2
Std Ort	9.9	4.0	-5.1	3.6	4.6
4 Radii	9.9	4.0	-5.1	3.6	4.6
0.6 Ems	9.3	3.7	-4.6	3.4	4.2
1.0 Ems	10.3	4.4	-5.4	3.9	4.9
0.4 Shd	8.8	3.4	-4.3	3.3	3.9
0.7 Shd	7.1	2.7	-3.3	2.9	3.0

able 7.1 Results from Improved F.D. Program.

21

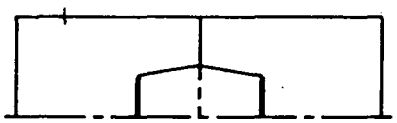

	β	σ_1	σ_2	σ_3	τ_m
Std Set	2.9	18.8	2.7	17.9	8.1
Std Ort	0.9	21.0	4.4	20.8	8.3
4 Radii	0.9	21.0	4.4	20.8	8.3
0.6 Ems	0.7	19.3	4.1	19.2	7.6
1.0 Ems	1.0	22.2	4.4	21.8	8.9
0.4 Shd	0.5	18.1	4.1	18.1	7.0
0.7 Shd	-0.2	14.0	3.4	14.6	5.3

45

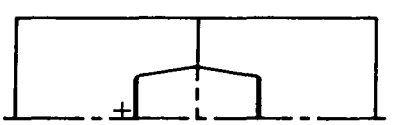

	β	σ_1	σ_2	σ_3	τ_m
Std Set	-4.7	-1.2	-6.4	-6.4	2.6
Std Ort	-3.6	-0.8	-4.9	-4.9	2.0
4 Radii	-3.6	-0.8	-4.9	-4.9	2.0
0.6 Ems	-3.7	-0.7	-4.5	-4.5	1.9
1.0 Ems	-3.5	-0.9	-5.3	-5.3	2.2
0.4 Shd	-3.8	-0.7	-4.1	-4.1	1.7
0.7 Shd	-4.0	-0.5	-3.2	-3.2	1.3

48

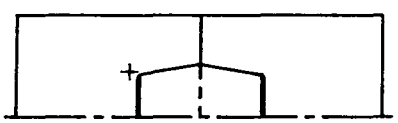

	β	σ_1	σ_2	σ_3	τ_m
Std Set	-59.2	-3.6	-11.5	-6.6	4.0
Std Ort	-56.0	-2.8	-8.2	-5.3	2.7
4 Radii	-56.0	-2.8	-8.2	-5.3	2.7
0.6 Ems	-55.5	-2.6	-7.4	-4.8	2.4
1.0 Ems	-56.3	-3.1	-8.9	-5.8	2.9
0.4 Shd	-55.0	-2.4	-6.8	-4.3	2.2
0.7 Shd	-52.8	-1.8	-5.0	-3.2	1.6

69

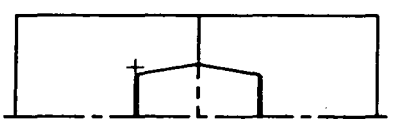

	β	σ_1	σ_2	σ_3	τ_m
Std Set	-45.0	-3.3	-11.9	-6.2	4.3
Std Ort	-43.6	-2.3	-8.7	-5.3	3.2
4 Radii	-43.6	-2.3	-8.7	-5.3	3.2
0.6 Ems	-43.1	-2.0	-7.9	-4.7	2.9
1.0 Ems	-43.8	-2.5	-9.4	-5.7	3.5
0.4 Shd	-42.6	-1.8	-7.1	-4.3	2.7
0.7 Shd	-40.8	-1.2	-5.3	-3.1	2.0

ble 7.1 (cont.) Results from Improved F.D. Program.

75

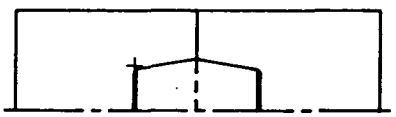

	β	σ_1	σ_2	σ_3	τ_m
Std Set	-53.7	-3.0	-16.0	-7.7	6.5
Std Ort	-52.1	-2.0	-11.2	-6.1	4.6
4 Radii	-52.1	-2.0	-11.2	-6.1	4.6
0.6 Ems	-51.8	-1.8	-10.0	-5.5	4.1
1.0 Ems	-52.3	-2.2	-12.1	-6.7	5.0
0.4 Shd	-51.6	-1.6	-9.2	-5.0	3.8
0.7 Shd	-50.4	-1.2	-6.8	-3.7	2.8

237

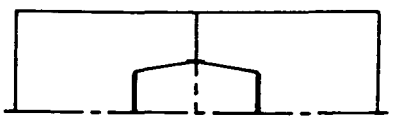

	β	σ_1	σ_2	σ_3	τ_m
Std Set	87.0	0.8	-18.8	1.0	9.8
Std Ort	87.9	0.5	-17.0	0.6	8.7
4 Radii	87.9	0.5	-17.0	0.6	8.7
0.6 Ems	89.6	0.1	-17.1	0.2	8.6
1.0 Ems	86.6	0.8	-17.0	1.0	8.9
0.4 Shd	-89.1	-0.2	-17.2	-0.2	8.5
0.7 Shd	-85.0	-0.7	-17.8	-1.2	8.5

269

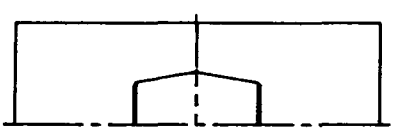

	β	σ_1	σ_2	σ_3	τ_m
Std Set	54.3	0.0	-0.1	17.2	0.0
Std Ort	54.8	0.0	-0.1	17.2	0.1
4 Radii	55.0	0.0	-0.1	17.2	0.1
0.6 Ems	54.7	0.0	-0.1	15.7	0.0
1.0 Ems	54.5	0.0	-0.1	18.4	0.1
0.4 Shd	54.7	0.0	-0.1	14.5	0.0
0.7 Shd	55.2	0.0	-0.1	11.2	0.0

319

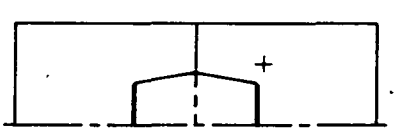

	β	σ_1	σ_2	σ_3	τ_m
Std Set	45.7	-1.7	-7.7	-2.8	3.0
Std Ort	50.3	-1.1	-6.8	-3.1	2.8
4 Radii	50.3	-1.1	-6.8	-3.1	2.8
0.6 Ems	49.9	-1.0	-6.1	-2.8	2.6
1.0 Ems	50.6	-1.3	-7.3	-3.4	3.0
0.4 Shd	49.6	-0.9	-5.7	-2.5	2.4
0.7 Shd	48.0	-0.6	-4.3	-1.7	1.9

ble 7.1 (cont.) Results from Improved F.D. Program.

428

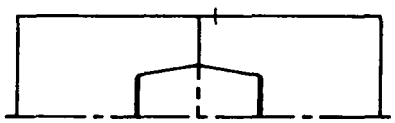

	β	σ_1	σ_2	σ_3	τ_m
Std Set	4.8	2.5	0.1	14.6	1.2
Std Ort	4.6	3.1	0.1	15.0	1.5
4 Radii	4.6	3.1	0.1	15.0	1.5
0.6 Ems	4.6	2.8	0.1	13.8	1.4
1.0 Ems	4.7	3.2	0.1	16.0	1.6
0.4 Shd	4.6	2.7	0.1	12.8	1.3
0.7 Shd	4.7	2.1	0.1	10.0	1.0

1082

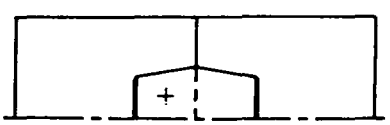

	β	σ_1	σ_2	σ_3	τ_m
Std Set	12.5	-0.5	-1.0	-0.7	0.3
Std Ort	1.2	-0.2	-0.6	-0.4	0.2
4 Radii	1.2	-0.2	-0.6	-0.4	0.2
0.6 Ems	0.0	-0.2	-0.6	-0.4	0.2
1.0 Ems	3.0	-0.2	-0.6	-0.4	0.2
0.4 Shd	-1.0	-0.1	-0.6	-0.4	0.2
0.7 Shd	-3.6	-0.1	-0.7	-0.5	0.3

1314

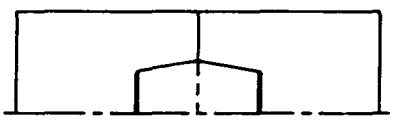

	β	σ_1	σ_2	σ_3	τ_m
Std Set	0.0	8.8	0.7	3.9	4.0
Std Ort	0.0	7.6	0.7	2.7	3.5
4 Radii	0.0	7.6	0.7	2.7	3.5
0.6 Ems	-0.1	8.3	0.8	2.8	3.8
1.0 Ems	0.0	7.1	0.6	2.6	3.2
0.4 Shd	0.0	8.8	0.8	2.9	4.0
0.7 Shd	0.0	10.3	1.0	3.2	4.6

1328

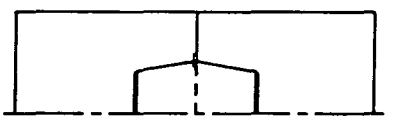

	β	σ_1	σ_2	σ_3	τ_m
Std Set	-4.2	9.3	0.6	3.9	4.4
Std Ort	-4.9	8.2	0.5	2.7	3.8
4 Radii	-4.9	8.2	0.5	2.7	3.8
0.6 Ems	-5.0	8.9	0.6	2.9	4.2
1.0 Ems	-4.8	7.6	0.5	2.6	3.6
0.4 Shd	-5.1	9.5	0.6	3.0	4.4
0.7 Shd	-5.2	11.1	0.7	3.3	5.2

ble 7.1 (cont.) Results from Improved F.D. Program.

7

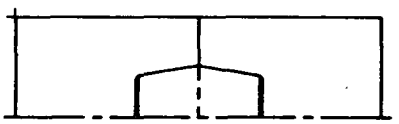

	β	σ_1	σ_2	σ_3	τ_m
Std Set	18.6	5.4	0.3	19.2	2.5
K red	19.9	7.2	0.5	22.1	3.3
K Inc	17.8	4.3	0.2	17.1	2.0
SHC red	17.7	4.5	0.2	18.1	2.2
SHC Inc	19.4	6.2	0.5	20.1	2.9
CC red	18.6	5.4	0.3	19.0	2.5
CC Inc	19.4	6.2	0.5	20.1	2.9

10

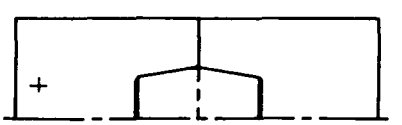

	β	σ_1	σ_2	σ_3	τ_m
Std Set	48.7	-4.5	-9.5	-6.2	2.5
K red	46.3	-6.1	-11.1	-8.0	2.5
K Inc	49.8	-3.4	-8.3	-5.0	2.5
SHC red	50.3	-3.7	-9.0	-5.4	2.6
SHC Inc	46.8	-5.1	-9.9	-6.9	2.4
CC red	48.6	-4.4	-9.4	-6.1	2.5
CC Inc	46.8	-5.1	-9.9	-6.9	2.4

19

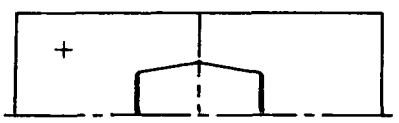

	β	σ_1	σ_2	σ_3	τ_m
Std Set	34.7	0.6	-7.9	-3.3	4.3
K red	35.8	0.5	-7.9	-4.0	4.2
K Inc	34.3	0.9	-7.6	-2.6	4.3
SHC red	34.6	0.8	-8.2	-3.0	4.5
SHC Inc	34.9	0.5	-7.5	-3.4	4.0
CC red	34.6	0.6	-7.8	-3.3	4.2
CC Inc	34.9	0.5	-7.5	-3.4	4.0

20

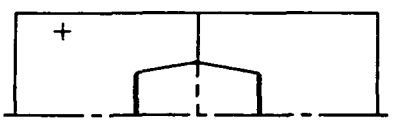

	β	σ_1	σ_2	σ_3	τ_m
Std Set	14.6	5.4	-4.9	4.6	5.2
K red	13.0	5.4	-5.5	4.5	5.4
K Inc	15.7	5.2	-4.5	4.6	4.8
SHC red	15.7	5.6	-4.8	4.9	5.2
SHC Inc	13.6	5.2	-4.9	4.4	5.1
CC red	14.5	5.3	-4.9	4.6	5.1
CC Inc	13.6	5.2	-4.9	4.4	5.1

able 7.2 Sensitivity Analysis - F.D. Parameters.

21

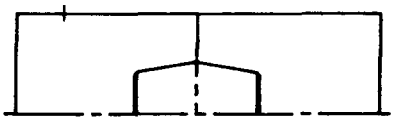

	β	σ_1	σ_2	σ_3	τ_m
Std Set	2.9	18.8	2.7	17.9	8.1
K red	2.0	21.9	3.7	20.9	9.1
K Inc	3.5	16.5	2.0	15.8	7.2
SHC red	3.4	18.0	2.3	17.1	7.9
SHC Inc	2.3	19.4	3.0	18.5	8.2
CC red	2.8	18.6	2.6	17.8	8.0
CC Inc	2.3	19.4	3.0	18.5	8.2

45

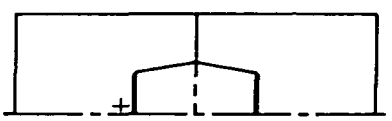

	β	σ_1	σ_2	σ_3	τ_m
Std Set	-4.7	-1.2	-6.4	-6.4	2.6
K red	-4.1	-1.1	-6.2	-6.3	2.5
K Inc	-5.3	-1.3	-6.5	-6.5	2.6
SHC red	-5.0	-1.3	-6.9	-7.0	2.8
SHC Inc	-4.5	-1.1	-6.0	-6.0	2.4
CC red	-4.7	-1.2	-6.3	-6.4	2.6
CC Inc	-4.5	-1.1	-6.0	-6.0	2.4

48

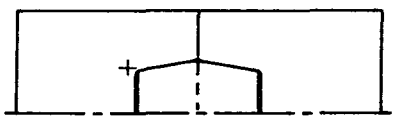

	β	σ_1	σ_2	σ_3	τ_m
Std Set	-59.2	-3.6	-11.5	-6.6	4.0
K red	-58.7	-3.6	-11.2	-6.8	3.8
K Inc	-59.4	-3.5	-11.5	-6.3	4.0
SHC red	-59.4	-3.8	-12.3	-6.9	4.2
SHC Inc	-58.9	-3.4	-10.8	-6.3	3.7
CC red	-59.2	-3.5	-11.4	-6.5	3.9
CC Inc	-58.9	-3.4	-10.8	-6.3	3.7

69

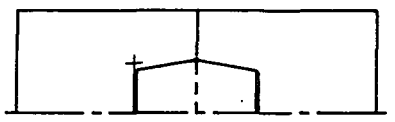

	β	σ_1	σ_2	σ_3	τ_m
Std Set	-45.0	-3.3	-11.9	-6.2	4.3
K red	-45.1	-3.2	-11.7	-6.5	4.2
K Inc	-44.8	-3.3	-11.8	-5.9	4.3
SHC red	-44.9	-3.5	-12.7	-6.4	4.6
SHC Inc	-45.0	-3.0	-11.2	-6.0	4.1
CC red	-45.0	-3.3	-11.8	-6.2	4.3
CC Inc	-45.0	-3.0	-11.2	-6.0	4.1

able 7.2 (cont.) Sensitivity Analysis - F.D. Parameters.

75

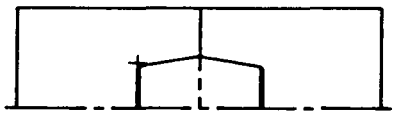

	β	σ_1	σ_2	σ_3	τ_m
Std Set	-53.7	-3.0	-16.0	-7.7	6.5
K red	-53.4	-2.8	-15.4	-7.8	6.3
K Inc	-53.7	-3.0	-16.1	-7.4	6.5
SHC red	-53.8	-3.2	-17.2	-8.0	7.0
SHC Inc	-53.5	-2.8	-14.9	-7.3	6.1
CC red	-53.6	-2.9	-15.8	-7.6	6.4
CC Inc	-53.5	-2.8	-14.9	-7.3	6.1

237

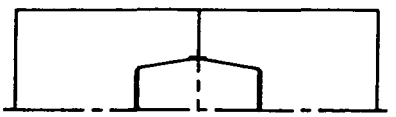

	β	σ_1	σ_2	σ_3	τ_m
Std Set	87.0	0.8	-18.8	1.0	9.8
K red	85.5	1.2	-18.0	1.5	9.6
K Inc	88.2	0.4	-19.3	0.7	9.8
SHC red	87.0	0.8	-19.4	1.1	10.1
SHC Inc	87.1	0.7	-18.3	1.0	9.5
CC red	87.1	0.7	-18.8	1.0	9.8
CC Inc	87.1	0.7	-18.3	1.0	9.5

269

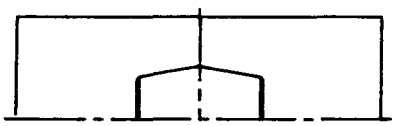

	β	σ_1	σ_2	σ_3	τ_m
Std Set	54.3	0.0	-0.1	17.2	0.0
K red	54.6	0.0	-0.1	19.2	0.1
K Inc	53.6	0.0	-0.1	15.6	0.0
SHC red	53.9	0.0	-0.1	17.0	0.0
SHC Inc	54.7	0.0	-0.1	17.3	0.0
CC red	55.2	0.0	-0.1	17.0	0.0
CC Inc	54.7	0.0	-0.1	17.3	0.0

319

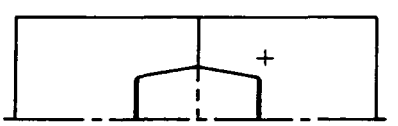

	β	σ_1	σ_2	σ_3	τ_m
Std Set	45.7	-1.7	-7.7	-2.8	3.0
K red	48.2	-1.6	-8.0	-3.4	3.2
K Inc	43.6	-1.7	-7.4	-2.4	2.8
SHC red	44.2	-1.9	-8.0	-2.7	3.1
SHC Inc	46.8	-1.6	-7.4	-2.9	2.9
CC red	45.6	-1.7	-7.6	-2.8	3.0
CC Inc	46.8	-1.6	-7.4	-2.9	2.9

ble 7.2 (cont.) Sensitivity Analysis - F.D. Parameters.

428

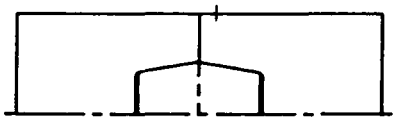

	β	σ_1	σ_2	σ_3	τ_m
Std Set	4.8	2.5	0.1	14.6	1.2
K red	4.7	3.2	0.1	16.5	1.6
K inc	4.9	2.0	0.0	13.1	1.0
SHC red	4.7	2.3	0.1	14.3	1.1
SHC inc	4.7	2.7	0.1	14.8	1.3
CC red	4.7	2.5	0.1	14.5	1.2
CC inc	4.7	2.7	0.1	14.8	1.3

1082

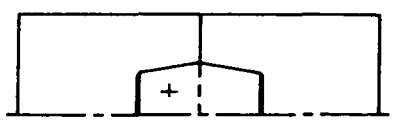

	β	σ_1	σ_2	σ_3	τ_m
Std Set	12.5	-0.5	-1.0	-0.7	0.3
K red	9.8	-0.3	-0.8	-0.5	0.2
K inc	14.9	-0.6	-1.2	-0.8	0.3
SHC red	15.7	-0.6	-1.2	-0.8	0.3
SHC inc	9.7	-0.4	-0.8	-0.6	0.2
CC red	12.5	-0.5	-1.0	-0.7	0.3
CC inc	9.7	-0.4	-0.8	-0.6	0.2

1314

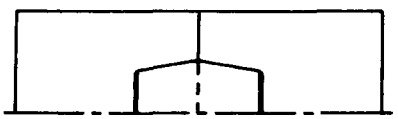

	β	σ_1	σ_2	σ_3	τ_m
Std Set	0.0	8.8	0.7	3.9	4.0
K red	0.0	7.5	0.6	3.2	3.4
K inc	0.1	9.8	0.8	4.4	4.5
SHC red	0.0	9.3	0.7	4.3	4.3
SHC inc	0.0	8.5	0.7	3.6	3.9
CC red	0.0	8.9	0.7	3.9	4.1
CC inc	0.0	8.5	0.7	3.6	3.9

1328

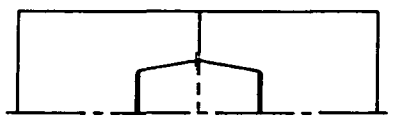

	β	σ_1	σ_2	σ_3	τ_m
Std Set	-4.2	9.3	0.6	3.9	4.4
K red	-4.3	7.9	0.5	3.3	3.7
K inc	-4.1	10.4	0.6	4.4	4.9
SHC red	-4.0	9.8	0.6	4.4	4.6
SHC inc	-4.3	9.0	0.5	3.6	4.2
CC red	-4.2	9.4	0.6	3.9	4.4
CC inc	-4.3	9.0	0.5	3.6	4.2

ble 7.2 (cont.) Sensitivity Analysis - F.D. Parameters.

7

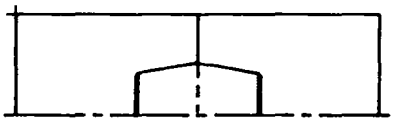

	β	σ_1	σ_2	σ_3	τ_m
Std Set	18.6	5.4	0.3	19.2	2.5
CTE =	18.7	5.4	0.3	19.2	2.5
CTE red	18.7	4.3	0.3	15.4	2.0
CTE Inc	18.7	6.5	0.4	23.1	3.0
E red	18.6	4.1	0.2	14.4	1.9
E Inc	18.6	6.8	0.4	24.0	3.2
NU red	18.8	4.3	-0.2	18.5	2.3
NU Inc	19.4	7.8	1.5	20.8	3.2

10

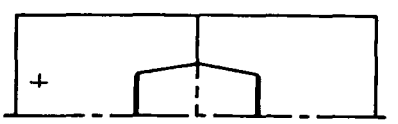

	β	σ_1	σ_2	σ_3	τ_m
Std Set	48.7	-4.5	-9.5	-6.2	2.5
CTE =	48.9	-4.4	-9.5	-6.2	2.5
CTE red	48.9	-3.6	-7.6	-4.9	2.0
CTE Inc	48.9	-5.3	-11.4	-7.4	3.0
E red	48.7	-3.4	-7.1	-4.6	1.9
E Inc	48.7	-5.6	-11.8	-7.7	3.1
NU red	45.2	-3.4	-7.8	-5.1	2.2
NU Inc	52.6	-7.0	-13.0	-8.9	3.0

19

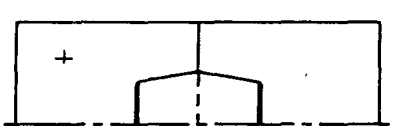

	β	σ_1	σ_2	σ_3	τ_m
Std Set	34.7	0.6	-7.9	-3.3	4.3
CTE =	34.9	0.7	-8.0	-3.3	4.3
CTE red	34.9	0.5	-6.4	-2.6	3.5
CTE Inc	34.9	0.8	-9.6	-3.9	5.2
E red	34.7	0.5	-5.9	-2.5	3.2
E Inc	34.7	0.8	-9.9	-4.1	5.3
NU red	34.8	0.0	-7.8	-3.5	3.9
NU Inc	34.3	2.4	-6.9	-2.0	4.7

20

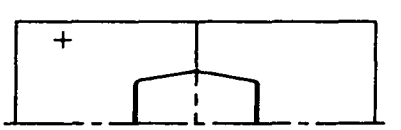

	β	σ_1	σ_2	σ_3	τ_m
Std Set	14.6	5.4	-4.9	4.6	5.2
CTE =	14.7	5.4	-4.9	4.7	5.2
CTE red	14.7	4.3	-3.9	3.8	4.1
CTE Inc	14.7	6.5	-5.9	5.6	6.2
E red	14.6	4.0	-3.7	3.5	3.9
E Inc	14.6	6.7	-6.1	5.8	6.4
NU red	15.0	4.7	-4.6	4.0	4.6
NU Inc	13.7	6.4	-5.1	5.6	5.8

ble 7.3 Sensitivity Analysis - F.E. Parameters

21

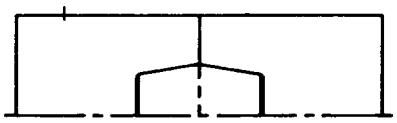

	β	σ_1	σ_2	σ_3	τ_m
Std Set	2.9	18.8	2.7	17.9	8.1
CTE =	2.8	18.8	2.6	17.9	8.1
CTE red	2.8	15.1	2.1	14.3	6.5
CTE Inc	2.8	22.6	3.2	21.5	9.7
E red	2.9	14.1	2.0	13.4	6.0
E Inc	2.9	23.5	3.3	22.4	10.1
NU red	3.2	16.3	1.9	15.3	7.2
NU Inc	2.3	22.8	4.4	22.0	9.2

45

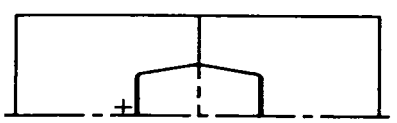

	β	σ_1	σ_2	σ_3	τ_m
Std Set	-4.7	-1.2	-6.4	-6.4	2.6
CTE =	-4.7	-1.2	-6.4	-6.5	2.6
CTE red	-4.7	-1.0	-5.1	-5.2	2.1
CTE Inc	-4.7	-1.5	-7.7	-7.8	3.1
E red	-4.7	-0.9	-4.8	-4.8	1.9
E Inc	-4.7	-1.5	-8.0	-8.0	3.3
NU red	-4.6	-1.0	-6.1	-6.2	2.6
NU Inc	-4.6	-1.6	-6.9	-6.9	2.6

48

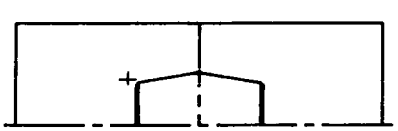

	β	σ_1	σ_2	σ_3	τ_m
Std Set	-59.2	-3.6	-11.5	-6.6	4.0
CTE =	-60.2	-3.7	-11.8	-6.7	4.1
CTE red	-60.2	-2.9	-9.4	-5.4	3.3
CTE Inc	-60.2	-4.4	-14.2	-8.1	4.9
E red	-59.2	-2.7	-8.6	-4.9	3.0
E Inc	-59.2	-4.5	-14.4	-8.3	5.0
NU red	-58.6	-3.4	-10.4	-5.6	3.5
NU Inc	-59.8	-3.6	-12.8	-7.7	4.6

69

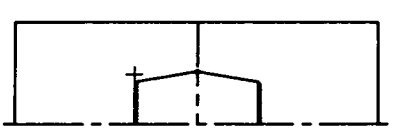

	β	σ_1	σ_2	σ_3	τ_m
Std Set	-45.0	-3.3	-11.9	-6.2	4.3
CTE =	-45.9	-3.5	-12.2	-6.4	4.3
CTE red	-45.9	-2.8	-9.7	-5.1	3.5
CTE Inc	-45.9	-4.2	-14.6	-7.6	5.2
E red	-45.0	-2.4	-8.9	-4.6	3.2
E Inc	-45.0	-4.1	-14.9	-7.7	5.4
NU red	-44.1	-2.8	-10.7	-5.2	3.9
NU Inc	-46.3	-3.8	-13.3	-7.5	4.8

able 7.3 (cont.) Material Sensitivity Analysis - F.E.

75

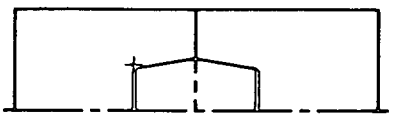

	β	σ_1	σ_2	σ_3	τ_{max}
Std Sol	-53.7	-3.0	-16.0	-7.7	6.5
CTE □	-54.2	-3.2	-16.5	-7.9	6.7
CTE rod	-54.2	-2.5	-13.2	-6.3	5.3
CTE Inc	-54.2	-3.8	-19.8	-9.5	8.0
E rod	-53.7	-2.2	-12.0	-5.7	4.9
E Inc	-53.7	-3.7	-20.0	-9.6	8.1
NU rod	-53.3	-2.6	-14.3	-6.1	5.8
NU Inc	-54.1	-3.4	-18.1	-9.6	7.4

237

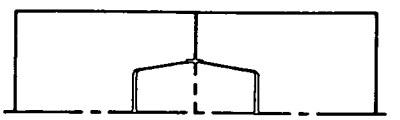

	β	σ_1	σ_2	σ_3	τ_{max}
Std Sol	87.0	0.8	-18.8	1.0	9.8
CTE □	70.8	6.1	-5.4	3.8	5.8
CTE rod	70.8	4.9	-4.3	3.0	4.6
CTE Inc	70.8	7.4	-6.4	4.5	6.9
E rod	87.0	0.6	-14.1	0.8	7.3
E Inc	87.0	1.0	-23.5	1.3	12.2
NU rod	-88.5	-0.4	-21.3	1.1	10.4
NU Inc	81.0	2.5	-16.1	2.2	9.3

269

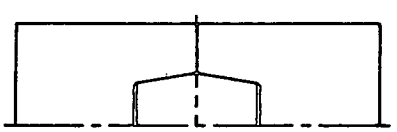

	β	σ_1	σ_2	σ_3	τ_{max}
Std Sol	54.3	0.0	-0.1	17.2	0.0
CTE □	55.2	0.0	-0.1	16.6	0.0
CTE rod	55.2	0.0	-0.1	13.3	0.0
CTE Inc	54.7	0.0	-0.1	19.9	0.0
E rod	53.9	0.0	-0.1	12.9	0.0
E Inc	54.3	0.0	-0.1	21.5	0.0
NU rod	53.2	0.0	-0.1	16.9	0.0
NU Inc	55.7	0.0	-0.1	17.5	0.0

319

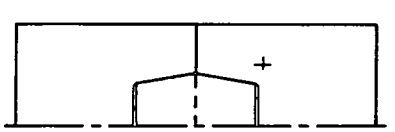

	β	σ_1	σ_2	σ_3	τ_{max}
Std Sol	45.7	-1.7	-7.7	-2.8	3.0
CTE □	46.4	-1.9	-7.7	-2.9	2.9
CTE rod	46.4	-1.5	-6.2	-2.3	2.3
CTE Inc	46.4	-2.3	-9.3	-3.4	3.5
E rod	45.7	-1.3	-5.8	-2.1	2.3
E Inc	45.7	-2.1	-9.7	-3.5	3.8
NU rod	44.6	-1.7	-7.0	-2.5	2.7
NU Inc	46.9	-1.5	-8.4	-2.9	3.4

able 7.3 (cont.) Material Sensitivity Analysis - F.E.

428

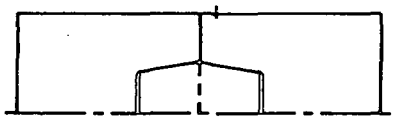

	β	σ_1	σ_2	σ_3	τ_m
Std Sol	4.8	2.5	0.1	14.6	1.2
CTE □	4.7	2.6	0.1	14.2	1.3
CTE rod	4.8	2.1	0.0	11.4	1.0
CTE Inc	4.7	3.2	0.1	17.0	1.5
E rod	4.8	1.9	0.1	10.9	0.9
E Inc	4.8	3.1	0.1	18.2	1.5
NU rod	4.9	2.1	0.0	14.1	1.0
NU Inc	5.0	3.0	0.2	15.2	1.4

1082

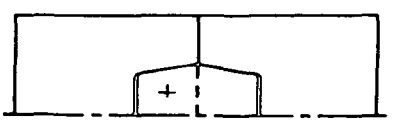

	β	σ_1	σ_2	σ_3	τ_m
Std Sol	12.5	-0.5	-1.0	-0.7	0.3
CTE □	48.0	-0.2	-0.8	-0.2	0.3
CTE rod	48.0	-0.2	-0.6	-0.2	0.2
CTE Inc	47.9	-0.3	-0.9	-0.3	0.3
E rod	12.5	-0.4	-0.7	-0.5	0.2
E Inc	12.6	-0.6	-1.2	-0.9	0.3
NU rod	1.1	-0.3	-1.0	-0.8	0.3
NU Inc	34.3	-0.6	-1.1	-0.6	0.2

1314

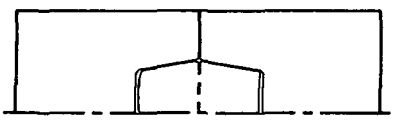

	β	σ_1	σ_2	σ_3	τ_m
Std Sol	0.0	8.8	0.7	3.9	4.0
CTE □	-89.9	-0.6	-3.9	0.7	1.7
CTE rod	-89.9	-0.5	-3.1	0.6	1.3
CTE Inc	-89.9	-0.7	-4.7	0.9	2.0
E rod	0.0	6.6	0.5	2.9	3.0
E Inc	0.0	11.0	0.9	4.9	5.0
NU rod	0.0	11.2	1.0	3.3	5.1
NU Inc	0.0	6.0	0.4	3.9	2.8

1328

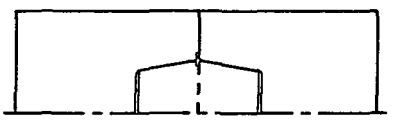

	β	σ_1	σ_2	σ_3	τ_m
Std Sol	-4.2	9.3	0.6	3.9	4.4
CTE □	81.0	-0.4	-4.5	0.7	2.0
CTE rod	81.0	-0.3	-3.6	0.5	1.6
CTE Inc	81.0	-0.5	-5.3	0.8	2.4
E rod	-4.2	7.0	0.4	2.9	3.3
E Inc	-4.2	11.7	0.7	4.9	5.5
NU rod	-4.2	11.7	0.3	3.2	5.7
NU Inc	-3.8	6.5	0.8	4.2	2.9

ble 7.3 (cont.) Material Sensitivity Analysis - F.E.

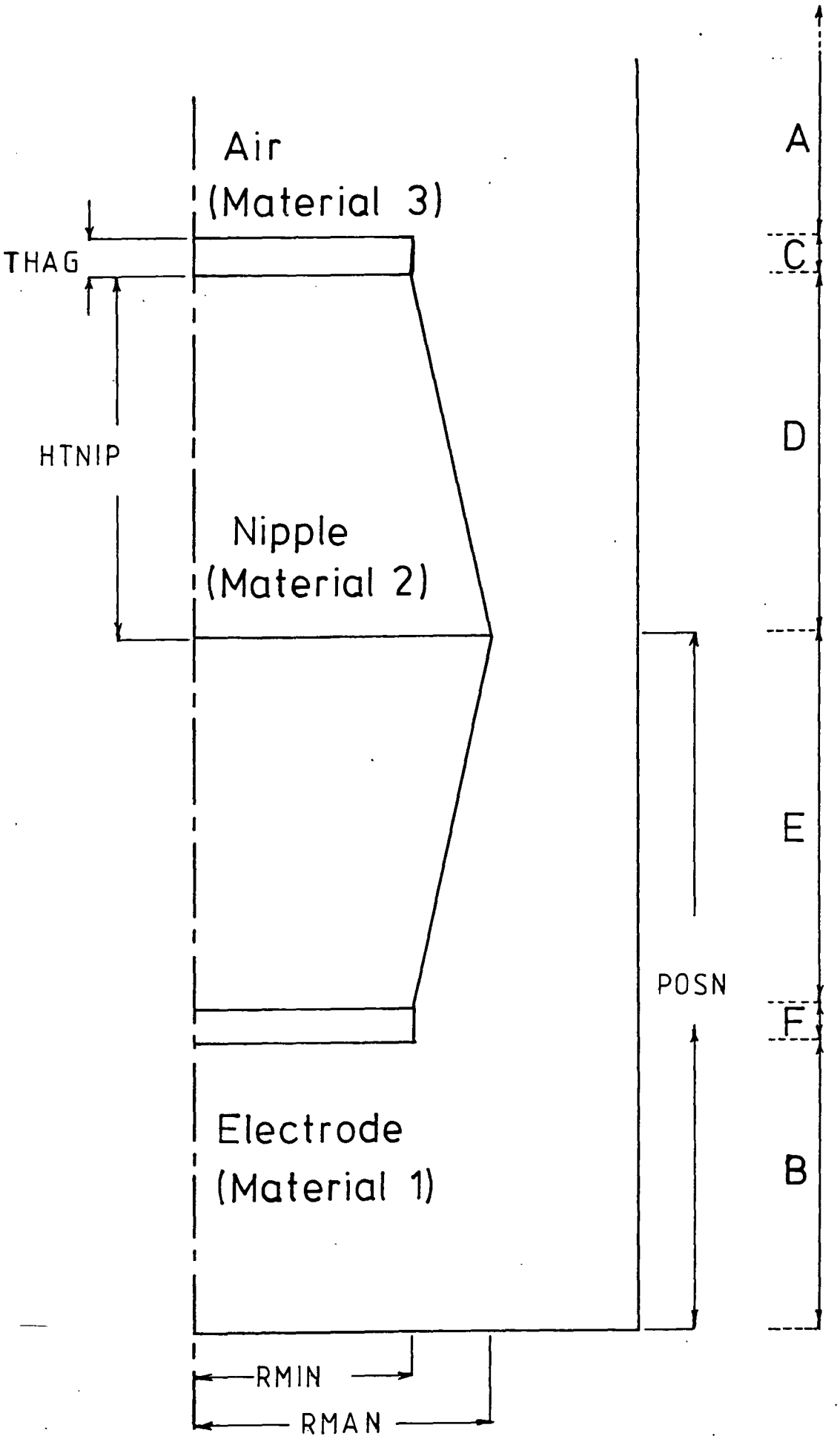
Air
(Material 3)
THAG
HTNIP
Nipple
(Material 2)
Electrode
(Material 1)
RMIN
RMAN
POSN
A
C
D
E
F
B

CHAPTER 8

SUGGESTIONS FOR FURTHER WORK

8.1 Consideration of Tapered/Chipped Electrodes

A limitation of the analysis described in previous chapters is that it considers only 'perfect' electrodes, i.e. those in which no tapering or chipping takes place. There are three possible ways of extending the analysis to consider tapered or chipped electrodes.

(i) Obtain a finite element program which allows for radiative heat transfer.

(ii) Write a more complex finite difference program which allows irregular meshes.

(iii) Write additional subroutines for PAFEC to allow radiative cooling.

8.2 Consideration of Dissimilar Electrode Sections

Sometimes, a premium-grade electrode section is used in a column containing regular grade sections. The implications of this in terms of failure probability could be evaluated by a further refinement of the finite difference program and the finite element formulation. The program for calculating failure probability would also need to be modified to use the appropriate values for failure strength.

8.3 Material Property Determinations

The lack of reliable material property data is a serious restriction on the accuracy of the present results. The parameters for which reliable data are required are,

strength (compressive and tensile), Young's modulus, thermal conductivity, expansion coefficient and fracture toughness. All need to be measured over a range of temperature, with due regard for anisotropy, and with values for Weibull Moduli where appropriate.

8.4 Provision for Orthotropy in Mechanical Properties

If the material property determinations mentioned in section 8.3 were performed, it would be worth extending the finite element model to include orthotropy. Facilities for this now exist within PAFEC, but the computing time will be increased.

8.5 Effect of a Different Initial Temperature Distribution

Many theoretical temperature fields are available in the literature but the choice of these is difficult without any real experimental verification, and an accurate steady-state temperature prediction would perhaps provide the greatest step forward from the present situation. Some progress in this direction has been made by the British Steel Corporation (Montgomery et al., 1979), using a colour video-recording technique.

The Finite Difference program described in the previous chapters is capable of dealing with any given axisymmetric temperature field without modification.

8.6 Photoelastic Analysis

Attempts to find mechanical stresses by two-dimensional photoelastic analysis were not carried to a conclusion. Appendix VI describes an unsuccessful attempt

to carry out a two-dimensional analysis. To do this properly, a three-dimensional approach is required.

This technique would unquestionably give a more accurate analysis of the mechanical stress field than the finite element technique, since the number of simplifying assumptions to be made is vastly reduced. For example, thread tooth contact will be determined by similar equilibrium conditions to those prevailing in an actual electrode; similarly, tightening torque may be applied correctly rather than as a series of discrete forces to individual thread teeth or as a uniform pressure over the nipple.

8.7 Non-Instantaneous Removal of Electrode From Furnace

The assumption of the Finite Different procedure described is that the electrode is instantaneously removed from the furnace. In fact the removal takes approximately 30 seconds. This could be incorporated into the Finite Difference model by allowing the program to calculate the ambient temperature θ_a from an equation of the form

$$\theta_a = 1600\, e^{-\beta t}$$

where β is a constant calculated such that $\theta_a = 30$ for $t = 30$. The value of θ_a would thus be calculated for each timestep less than 30 seconds, and set equal to 30 thereafter.

8.8 Non-Instantaneous Application of Reflective Shield

By arranging for the program to continuously monitor the elapsed time, the fact that any reflective

shield cannot be instantaneously applied may be accounted for. Thus, the reflectivity of the shield would be set equal to zero for $t < t_r$ and to 0.7 for $t \gg t_r$, where t_r is the time after extraction when the shield is applied.

8.9 Electromagnetic Loading and Resonance

In addition to the thermal and mechanical loads imposed on an electrode, the close proximity of three current-carrying conductors imposes electromagnetic loading on the joint structure.

A preliminary investigation into the effects of resonance, in which PAFEC was used to calculate the resonant frequency of an electrode considered as a simple cylinder with density variations due to the presence of the nipples, showed that the fundamental resonant frequency of an electrdode is about 80 Hz, fairly close to mains frequency. A more elaborate evaluation of the loads involved is given in Appendix VII. A full analysis of these effects was not possible due to time restrictions, but a more elaborate investigation into electromagnetic forces and resonance would be useful in any continuance of the work.

8.10 Improved Failure Probability Calculation

As noted in Chapter VI, it was not economically feasible to check the convergence of the stress volume integral for different mesh configurations. In the mesh configuration used, there are some marked variations in the stresses predicted by different elements at particular

nodes. Thus, an accurate failure probability analysis requires a systematic refinement of the mesh in these regions of high stress gradient.

Furthermore, Stanley (1982) has recently developed the previous work on failure probability under steady-state stresses to include failure probability calculations for transient thermal stresses. The failure probability calculations performed in Chapter VI may only be used as a very approximate indication as to the effects of any attempt to improve the failure situation.

In a transient stress field, the failure probability of a given element may increase then decrease with time. Since a steady-state analysis may be performed at a time after the maximum failure probability of such an element is reached, an erroneous failure probability will result. In other words, when assessing the total failure probability up to a given time instant in a transient analysis, the maximum failure probability attained by each element up to that point in time must be used. Clearly, this means that the failure probability may reach a steady value (of unity) before the stresses settle to steady-state values.

What is required is a 'time marching' technique in which the failure probability of each element at a given analysis time is compared with that at the previous time, the larger of the two values being used in the failure probability calculation. Clearly, the choice of timestep

value is important - too large a timestep, and failure probability maxima will be missed.

The cost of performing such an analysis for this problem would be prohibitive, and can therefore only be recommended as an extension to the work if large funds became available. Clearly, from the point of view of accuracy, however, this would be a desirable addition.

8.11 Improved structural Failure Criterion

One of the fundamental assumptions of the Stanley failure analysis is that the failure of one element implies failure of the whole body. Clearly, this is not true for a graphite electrode since many electrodes are perfectly useable and are not considered to have failed even when in a severely chipped or cracked state. This assumption leads to a predicted failure probability of 1, compared to a practical failure rate of less than 0.1. More work is needed on this aspect to establish exactly the criterion for an electrode having 'failed' in the catastrophic sense. If such a criterion can be established, it may be possible to modify the Stanley analysis to obtain a realistic failure probability calculation.

8.12 Non-vertical Electrodes.

In some cases, electrodes are tilted to an angle of 45° from the vertical, when the furnace is tapped. Clearly, the mechanical stresses in this case are greater than with the electrode hanging vertically. An axisymmetric analysis cannot cope with such off-axis forces but if the

analysis was extended to the fully three-dimensional case the extra stresses imposed in this situation could be evaluated.

CHAPTER 9

CONCLUSIONS

(1) Mechanical stresses in the top joint have been shown, by a 'failure envelope' approach, to be insufficient to cause appreciable risk of failure. There is a localised stress concentration at the fillet radius near the socket base which may increase the risk of catastrophic failure from collisions with pieces of scrap metal, general handling etc.

The magnitude of the stresses occurring around the socket base will be reduced by increasing the fillet radius left in this corner. A possible way of achieving this is shown in Fig. 9.1 (originally suggested by Sanders (1973)), in which the base of the socket is bored out into a hemispherical shape, removing the sharp corner causing the stress concentration. Of course, such a design will reduce the overall stiffness of the joint and it may be that problems will occur due to excessive deflections in region X (Fig 9.1). Before implementing such a change, an analysis would be necessary to investigate this possibility, and to determine the optimum radius of the bore.

(2) A further mechanical stress concentration occurs at the entrance to the socket. This has been shown to be insufficient to cause localised crushing.

(3) A statistical approach shows a very low probability of failure under mechanical stresses.

(4) The effect of overtightening a joint has not been investigated in detail. As mentioned in the chapters on mechanical stresses, however, the highly mechanically stressed regions could be taken past the mean failure stress if the joint is significantly overtightened. Bearing in mind that this investigation has not considered all the forces acting on the electrode, it is obvious that tightening torques should be closely controlled.

(5) There is no evidence of mechanical or thermal stresses producing an appreciable gap at the periphery of the electrode/ electrode interface, as has been suggested by other workers. Any gap which does develop is probably smaller than the machining tolerance of the electrode end face.

(6) The thermal shock produced when an electrode is removed from the furnace causes severe temperature gradients near the surface of the electrode. The interior temperature distribution varies only slowly while the surface temperature decreases rapidly due to the radiative cooling. The surface temperature gradients are therefore largely

independent of the internal temperature distribution, but heavily dependent on the initial surface temperature of the electrode.

(7) The thermal shock stresses on cooling act in such a way as to overpower the magnitude of the tensile mechanical stresses in the socket base. Because the bottom electrode joint is more susceptible to thermal shock than the other two, this indicates that a 'collar' type failure is less likely on a bottom joint.

The compressive stresses at the socket entrance are increased by the action of cooling, but remain unlikely to contribute significantly to the risk of catastrophic failure.

(8) The effect of the thermal shock at the surface of the electrode is to produce high tensile hoop stresses, in excess of the uniaxial tensile strength of the material. A 'failure envelope' approach shows that these surface regions will always fail under the conditions considered, probably by longitudinal splitting (the so-called 'clothes peg' fracture). A statistical analysis of the stresses at 3600s after removal from the furnace also predicts a 100% failure rate but it should be noted that even a slightly more optimistic estimate of the unit volume failure strength reduces this probability markedly.

Additionally, the type of analysis employed assumes a 'weakest link' criterion in which the failure of one element implies failure of the whole body. We must therefore interpret this high failure probability as indicating that cracks will always form under thermal stresses. This 'local failure' is the reason for the high failure probability predicted by the approach used. As indicated in Chapter VI however, the unit volume uniaxial tensile strength of the material is rather uncertain, and a lower estimate of this quantity would indicate a much lower failure probability, since the graph of failure probability vs tensile strength has a large negative slope. We may conclude that thermal and mechanical stresses acting together are always sufficient to cause cracking. Examination of a used electrode shows that this need not necessarily cause a catastrophic failure. Much more work is required to obtain a better insight into the implications, in terms of catastrophic failure, of crack formation in the graphite material. Clearly, the Stanley assumption that the failure of one element is sufficient to cause the failure of the whole structure is not applicable to the electrodes.

(9) The bottom corner of the electrode undergoes the most severe thermal shock stresses, and will rapidly become rounded in use.

(10) The provision of a reflective shield around the electrode while it is out of the furnace considerably reduces the overall stress level, and would be a worthwhile modification to the process specification.

(11) The region chosen for quality control sampling (a cylindrical region on the electrode axis at the base of the socket) is thermally and mechanically in a low state of stress. Removal of this region is therefore unlikely to cause any serious perturbation of the stress field, and may therefore be regarded as an adequate compromise.

(12) The resonant frequency of a suspended electrode column is close to mains frequency, and this should be investigated further.

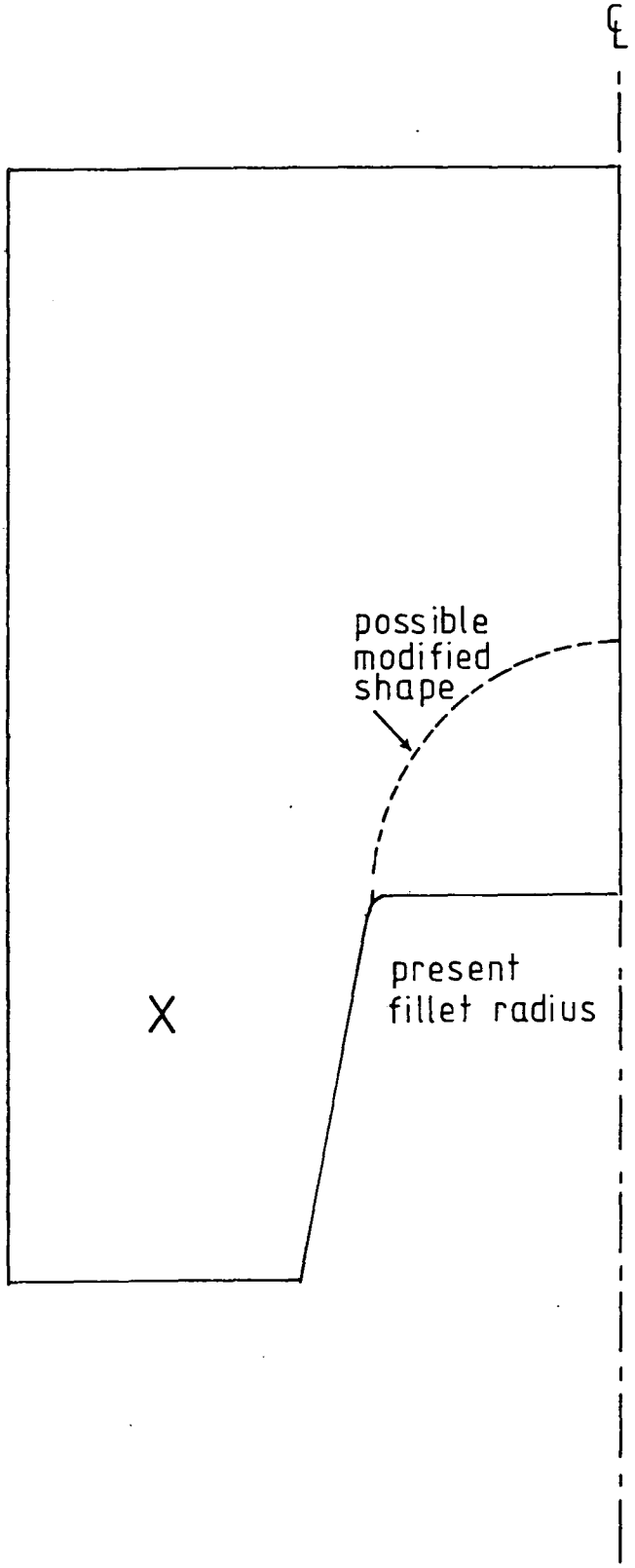

Fig 9.1 A possible way of reducing stress concentrations.

REFERENCES

ANGLO GREAT LAKES CORPORATION LTD, 1979, Private Communication.

J. AMESZ, J. DONEA, F. LANZA, 1973, "Extended abstracts.", 11th Biennial Conference on Carbon, Gatlinburg, 1973, CONF-73061, p221.

H. W. BABEL & G. SINES, 1968, "A biaxial fracture criterion for porous brittle materials.", Journal of Basic Engineering, p. 285, June, 1968.

R.E. BOLZ & G.L. TUVE, 1970, "Handbook of tables for applied engineering science", Chemical Rubber Co. 1970.

F.P. BOWDEN & D.TABOR, 1964 "Friction & lubrication of solids", Part I, Oxford University Press, 1964 edition.

P. M. BRAIDEN & R. AIREY, 1973, "A stress analysis of graphite electrode joints.", A.E.R.E. Report G-211, November, 1973.

P. M. BRAIDEN & R. AIREY, 1974, "Further work on the stress analysis of graphite electrode joints." , A.E.R.E. Report G-360, November, 1974.

P.M. BRAIDEN, 1980, "The development of rational design criteria for brittle materials.", Materials in Engineering, Vol. 2., no. 2., December 1980.

BRITISH STEEL CORPORATION (1), 1980 "Graphite Property Values", private communication, 1980.

BRITISH STEEL CORPORATION (3), 1980, "Summary of Electrode Properties", private communication, 1980.

J. E. BROCKLEHURST, 1977, "Fracture in polycrystalline graphite.", Chemistry and Physics of Carbon, Vol. 13., edited by P. L. Walker and P. A. Thrower, Dekker, 1977.

H. S. CARSLAW & J. C. JAEGER, 1959, "Conduction of heat in solids.", 2nd. edition, Oxford University Press, 1959, pp 9 - 46.

J.F. CORNWELL, 1981, "Some observations on friction in screw threads", Wear, 1981, vol 67, p329-339.

J. F. ELLIOTT & J. YAVORSKY, 1969, "Heat flow in an arc furnace electrode - a computer study.", Transactions of the American Foundrymen's Society, Vol. 77., p 447 - 454, 1969.

R. E. ELY, 1968, "Strength of magnesium silicate and graphite under biaxial stresses.", Bulletin of the American Ceramic Society, Vol. 47., no. 5., 1968.

J. M. FAIRCLOTH, I. W. GAZDA, C. A. SWITZER, O. T. SIGVALDSON, R. G. CHARLWOOD, 1976, "Finite element analysis of the thermally induced stresses in a 24-in diameter graphite electrode - nipple joint.", Electric Furnace Proceedings, 1976, p265 - 269.

A. A. GRIFFITH, 1920, " The phenomena of rupture and flow in solids.", Philosophic Transactions of the Royal Society, A, 221, 163, 1920.

G. W. GROVES & A. KELLY, 1963, "Independent slip systems in crystals.", Philosophical Magazine, Vol. 8, 1963, p877.

A. INCE, 1979, "Graphite electrodes.", Anglo Great Lakes Corporation Ltd., Internal Report, 23rd January, 1979.

J. JORTNER, 1971, "Multiaxial behaviour of ATJ-S Graphite." Technical Report AFML-TR-71-253, McDonnel-Douglas Astronautics Company, Santa Monica, California, December 1971.

J.N. KIRK(1), 1979, "Some Information on C.T.E. & Conductivity", private communication, 1979.

J.N. KIRK(2), 1979, "Some Information on Crushing Strength", private communication, 1979.

R.C. LINCOLN and R.C. HECKMAN, 1975, "Negative Pulse thermal diffusivity measurements of ATJ - s graphit to 3500 K", High Temperatures, High Pressures, 1975, v7, p71-77.

C. L. MANTELL, 1968, "Carbon and graphite handbook.", Interscience, New York, 1968.

R. W. MONTGOMERY, G. PAYNE, J. N. KIRK, 1979, "The basic properties of high - intensity arcs used in steelmaking.", Commission of European Communities E.C.S.C. Sponsored Research Project. Draft final report, 1979.

E. NEDOPIL & H. STORZER, 1967, "Measurement of the temperature distribution in electrode columns on introduction into the electric arc furnace.", Stahl und Eisen, Vol. 87., no. 7., p368 - 373, 1967.

A. NICHOLSON, J. WOODHOUSE, G. R. JORDAN, 1976, "Quality control of arc furnace electrodes.", Iron and Steel Making, no. 6., 1976

G. PAYNE(1), 1981, "Graphite Property Values", Private Communication, 1981.

G. PAYNE,(2) 1980, "Some results of graphite material property determinations at the British Steel Corp.", Private Communication, 1980.

R. J. PRICE & H. R. W. COBB, 1972, "Application of Weibull statistical theory to the strength of reactor graphite.", Proceedings of the Conference on Continuum aspects of Graphite Design, edoited by W. L. Greenstreet & G. C. Battle, U.S.A.E.C. Report CONF-701105, p514, February 1972.

W. N. REYNOLDS, 1965, "The mechanical properties of reactor graphite.", Philosophical Magazine, Vol. 11., 1965, p357.

L. M. SANDERS, 1973, "The calculation of tewmperature distribution and thermal stress in an arc furnace electrode nipple during arcing.", British Steel Corporation Internal Report PP/6245/3/73/D, 1973.

S. SATO, K. SATO, M. NIKAIDO, 1974, "An analysis of thermal stress fracture in a graphite electrode used in an arc steel making furnace.", Carbon, Vol. 12., 1974, p555 - 571.

W. E. SCHWABE, 1972, "The mechanics of consumption of graphite electrodes in electric steel furnaces.", Journal of Metals, 1972, p65-71.

J. SEMMLER, 1967, "Dependence of various graphite properties on temperature.", Stahl und Eisen, Vol. 87., no. 7., 1967.

G. D. SMITH, 1965, "Numerical solution of partial differential equations.", Oxford Mathematical Handbooks, Oxford, 1965.

G. D. SMITH, 1978, "Numerical solution of partial differential equations. Finite difference methods.", 2nd edition, Oxford Applied Mathematics and Computing Science Series, Oxford, 1978.

M. C. SMITH, 1970, "The deformation and fracture mechanism in polycrystalline graphite.", Proceedings of the conference on continuum aspects of graphite design, Gatlinburg, U.S.A.E.C. Report CONF-701105, 1972, p475.

J.E. SNYDER, 1976, "Guidelines for the selection and use of electric furnace electrodes and connecting pins", Electric Furnace Proceedings, 1976, p279-285.

D.G. SOPWITH, 1949, "The distribution of load in screw threads", Proc. I. Mech. Eng, vol 160, 1949

P. STANLEY, H. FESSLER, A. D. SIVILL, 1973, "An engineer's approach to the prediction of failure probability of brittle components.", Proceedings of the British Ceramic Society no. 22., June 1973, p453.

P. STANLEY, J. MARGETSON, 1977, "Failure probability analysis of an elastic orthotropic brittle cylinder subjected to axisymmetric theraml and pressure loading.", International Journal of Fracture, Vol. 13, No. 6, Dec., 1977.

P. STANLEY & F. S. CHAU, 1982, "Failure probability calculations for brittle components subjected to transient thermal stresses.", Proceedings of the British Ceramic Society, 1982, p119 - 132.

F. STASSI D'ALIA, 1959, "Limiting conditions of yielding of thick-walled cylinders and spherical shells". U.S. Army research Office, Frankfurt, Germany, no. 9851., 1959.

S. TIMOSHENKO & J. N. GOODIER, 1951, "Theory of elasticity.", McGraw-Hill, New York, 1951.

S. TIMOSHENKO & D.H. YOUNG, 1968, "Elements of Strength of Materials", 5th Edition, Van Nostrand Co. Inc. 1968, p58-64.

S. TIMOSHENKO, 1953, "History of strength of materials.", McGraw-Hill, New York, 1953.

UNION CARBIDE CO., 1959, "The industrial graphite engineering handbook", Union Carbide Co. 1959.

R. VON MISES, 1928, "Mechanik der plastischen Fermanderung von Kristallen.", Angewandte Math. Mech. no. 8., 1928, p168.

T. L. WENG & E. J. SELDIN, 1977, "Calculation of steady-state temperatures in graphite electrodes in an electric arc steel furnace.", Carbon, Vol. 15., 1977, p391 - 398.

APPENDIX I

STRESS COMBINATION PROGRAM

Program Description

After setting up the input and output file assignments, a line of data is read in corresponding to a node in stress field 'A', followed by a node from stress field 'B'. Next, the angle through which stresses 'B' must be rotated in order to correspond to the orientation of stresses 'A' is calculated (DTHETA). The subroutine ROTATE is now called to find the stress components of node 'B' at angles DTHETA to the principal directions, giving the stress components (SIGMAX, SIGMAY and TAU) OF 'B' in the principal directions OF 'A'. The subroutine 'ROTATE' uses equation 3.3 and 3.4 to perform these calculations. The new values of the total stress components due to 'A' and 'B' are now found by adding these calculated components to the original components of 'A', with whose orientation they now correspond.

The variables NSIGX, NSIGY, NSIGH, NTAU represent the in-plane, hoop and shear stresses of the new combined stress field at this point. The program now calculates the new principal stresses NSIG1, NSIG2, NSIG3, NTAUM corresponding to these components. This is done by calling the subroutine PRISTR which uses equation 3.6 to calculate the new principal stress values, and equation 3.5 to calculate the angle of the new principal stress planes to the orientation of stresses 'A'. the orientation to the

global x-axis (angle NBETA) is calculated by adding this angle to the original inclination of the most positive principal stress due to 'A'.

One further operation remains. Equations 3.5 and 3.6 give the angles of the new principal stress planes and the principal stresses respectively. They do not, however, associate the values of σ_1 and σ_2 with the correct choice of the two orthogonal solutions to equation 3.5. This association is done in the program by rotating the new combined stresses by the angle calculated by PRISTR, using the subroutine ROTATE, to ascertain which of the angles (NBETA or NBETA + 90°) corresponds to the most positive principal stress.

Finally, the combined principal stresses and their orientation is printed out, and the program passes to the calculation of the combined stress field at the next node.

```
      LOGICAL*1 FMT(1) /'*'/
      LOGICAL*1 NAME1(20), NAME2(20), NAME3(20), OUTNAM(20)
      COMMON /VARS/ PI
      REAL NSIGX, NSIGY, NSIGH, NTAU, DELBET, NSIG1, NSIG2, NSIG3,
     1     NTAUM, NBETA, NSIG12
      WRITE (6,10)
   10 FORMAT (' ', 'Program for combining stresses using the', /,
     1        'equation ser and ideas from Timoshenko & Young', /,
     2        '"Elements of strength of materials"')
      WRITE (6,20)
   20 FORMAT (' ', 'Enter name of file containing stresses "A"')
      READ (5,30) NAME1
   30 FORMAT (20A1)
      CALL FTNCMD('ASSIGN 1=?;', 0, NAME1)
      WRITE (6,40)
   40 FORMAT (' ','Enter name of file containing stresses "B"')
      READ (5,30) NAME2
      CALL FTNCMD('ASSIGN 2=?;', 0, NAME2)
      WRITE (6,60)
   60 FORMAT (' ', 'Enter name of output file')
      READ (5,30) OUTNAM
      CALL FTNCMD('ASSIGN 7=?;', 0, OUTNAM)
      PI = ARCOS(-1.0)
      DO 120 I = 1, 10000
   70   READ (1,FMT,END=130) NODEA, ID1A, XA, YA, ZA, ABETA, ASIG1,
     1  ASIG2, ASIG3, ASIG12, ATAUMX, ID2A
        READ (2,FMT,END=130) NODEB, ID1B, XB, YB, ZB, BBETA, BSIG1,
     1  BSIG2, BSIG3, BSIG12, BTAUMX, ID2B
        IF(NODEA.NE.NODEB) STOP 500
        BTAU = 0.0
C....
C....   by definition....
C
C....  calculate the rotation angle
C .... convention in this prog is always to rotate stresses B onto
C..... stresses A
C
        DTHETA = ABETA - BBETA
C
C ...  calculate values of direct and shear stress when rotating B
C ..   through  angle DTHETA degrees.
C .... the rotated stress state is represented by sigmax, sigmay,
C ....
        CALL ROTATE(BSIG1, BSIG2, BSIG3, BTAU, DTHETA, SIGMAX, SIGMAY,
     1       TAU, SIGMAH)
C
C....  NSIGX, NSIGY, NSIGH are the new direct stresses at this
C....  orientation (i.e. the rotated b stresses plus the original
C....  a stresses. of course the only contribution to shear stress
C....  at this orientation is from  the rotated b stresses.
C
        NSIGX = ASIG1 + SIGMAX
        NSIGY = ASIG2 + SIGMAY
        NSIGH = ASIG3 + SIGMAH
```

```
C
C...   just for tidiness!
C
         NTAU = TAU
C
C...   now calculate the new principal stresses NSIG1, NSIG2, NSIG3,
C...   and their angular displacement DELBET from the original
C...   orientation af the A stresses. Note this is not the angle to
C...   the global x- axis.
C
         CALL PRISTR(NSIGX, NSIGY, NSIGH, NTAU, DELBET, NSIG1, NSIG2,
     1         NSIG3, NTAUM)
C.
C...    NSIGX ------› NTAU  are the total stress components at the
C...    orientatiion of stresses "A"
C...    NSIG1 ------› NTAUM are the new principal stresses, and
C...    delbet is the angle to be turned through to reach them.
C.
         CALL RADDEG(DELBET, DEGS)
C..
C..     Rotate the new stress situation back through the angle calculated
C..     by PRISTR. If CSIGX is now the *least* positive, flip the angle
C..     BETA by 90 degrees.
C..
         NBETA = ABETA + DEGS
         CALL ROTATE(NSIGX, NSIGY, NSIGH, NTAU, DEGS, CSIGX, CSIGY, CTAU,
     1         CSIGH)
         IF (CSIGY .GT. CSIGX) NBETA = NBETA + 90.0
         IF (NBETA .GT. 90.0) NBETA = NBETA - 180.0
         IF (NBETA .LT. - 90.0) NBETA = 180 + NBETA
C...
C... a dummy variable  -  we didn't calculate it!
C... my TAUMAX appears to be what PAFEC calls sigma12
C... ie half the difference between the principal stresses
C..  pafec's taumax is usually the same as its sigma12 but
C... not always.
C...
         PFTAUM = 111111.1
         WRITE (7,100) NODEA, ID1A, XA, YA, ZA, NBETA, NSIG1, NSIG2,
     1   NSIG3, NTAUM, PFTAUM, ID2A
  100    FORMAT (' ', I5, 2X, I2, 3(2X,F7.4), 2X, F5.1, 5(2X,E10.4), 2X,
     1          I5)
  120 CONTINUE
  130 STOP
      END
C
C
C
C
      SUBROUTINE ROTATE(OSIGX, OSIGY, OSIGH, OTAU, DTHETA, RSIGX, RSIGY,
     1            RTAU, RSIGH)
C...   OSIGX -----› OTAU are the stresses fed to the subroutine.
C...   RSIGX -----› RTAU are the stresses on rotating by an angle
C...   'DEGS' degrees.
C
      COMMON /VARS/ PI
```

```
C
C.... RSIGX, RSIGY, RSIGH, RTAU, are the stress components of
C.... stress field b after rotation by angle DTHETA degrees.
C
      SEMSUM = (OSIGY + OSIGX) / 2.0
      SEMDIF = (OSIGX - OSIGY) / 2.0
      CALL DEGRAD(DTHETA, RADS)
C
C.... find direct stress at DTHETA degrees from original OSIGX
C
      RSIGX = SEMSUM + (SEMDIF*COS(2.0*RADS)) - (OTAU*SIN(2.0*RADS))
C
C.... and the shear stress
C
      RTAU = SEMDIF * SIN(2.0*RADS) + (OTAU*COS(2.0*RADS))
C
C.... now rotate through a further right angle
C
      RADS = RADS + (PI/2.0)
C
C.... and find the direct stress value
C
      RSIGY = SEMSUM + (SEMDIF*COS(2.0*RADS)) - (OTAU*SIN(2.0*RADS))
C
C.....the hoop stress is unchanged by the rotation
C
      RSIGH = OSIGH
      RETURN
      END
C
C
C
C
      SUBROUTINE PRISTR(SIGX, SIGY, SIGH, TAU, DELBET, SIG1, SIG2, SIG3,
     1            TAUM)
C
C.... calculates the new principal stresses and their angular
C.... displacement from the original directions of the 'A'
C.... principal stresses.
C.... SIGX ------> TAU is the stress state handed to the routine.
C.... SIG1 ------> TAUM are the new pronc stresses & max shear.
C
      COMMON /VARS/ PI
      REAL SIGX, SIGY, SIGH, TAU, DELBET, SIG1, SIG2, SIG3, TAUM, NBETA
      SEMSUM = (SIGX + SIGY) / 2.0
      DIFSQ = (ABS(SIGX - SIGY)) ** 2.0
      TERM = ((DIFSQ/4.0) + ((ABS(TAU))**2.0)) ** 0.50
C
C.... these are the new principal stresses
C
      SIG1 = SEMSUM + TERM
      SIG2 = SEMSUM - TERM
C
C...   hoop stress is unchanged by the rotation to principal
C...   stress directions
C
      SIG3 = SIGH
```

```
C
C...   and the angle
C
       DELBET = -0.5 * (ATAN(2.0*TAU/(SIGX - SIGY)))
C...   lastly the maximum shear stress
C
       TAUM = 0.5 * (SIG1 - SIG2)
       RETURN
       END
C
C
C
C
       SUBROUTINE DEGRAD(DTHETA, RADS)
C
C.... converts degrees to radians
C
       COMMON /VARS/ PI
       RADS = DTHETA * PI / 180.0
       RETURN
       END
C
C
C
C
       SUBROUTINE RADDEG(RADS, DEGRS)
C
C....  converts radians to degrees
C
       COMMON /VARS/ PI
       DEGRS = RADS * 360.0 / (2.0*PI)
       RETURN
       END
```

APPENDIX II

THE FINITE DIFFERENCE PROGRAM

The computer program was developed to solve the finite difference equations 4.3, 4.4 & 4.8-4.14 using assumptions similar to those used by Montgomery (1979). Modifications to these equations described in Chapter V required improvements to the program, and consequent increase in complexity. A qualitative description of the modifications required is given later in this section.

The purpose of the program is to calculate the temperature field after time t, given the field at time t=0. This is done by a series of solutions, each one giving the field after time Δt. Initially the starting temperature field is set up in the array TEMP. This is a three-dimensional array holding the value for the temperature at node LR, LZ after time interval number LT. Thus LT=1 corresponds to the initial field (time t=0), the radial position LR=1 corresponds to the electrode central axis and LZ=1 to the electrode endface. The third dimension of the array TEMP is '2'. The program is arranged so that the temperature of node LR, LZ is first read from TEMP(LR,LZ,1) and the temperature after time interval Δt written to TEMP(LR,LZ,2). On the next loop through the timesteps the temperature of the node is read from TEMP(LR,LZ,2) and written to TEMP(LR,LZ,1). Thus, storage space is reduced.

First, the initial data is set up in the correct units; next, the file-writing facility is set up. The

program is arranged to create files of the form XXXXYYYY where XXXX is a user-defined character string and YYYY is an integer representing the number of the timestep being calculated. Next, the temperature array is initialised, and, after performing various checks to make sure the program arrays have not overflowed, the mesh spacing is calculated. A check is performed to make sure that the length of electrode being analysed is greater than three times the electrode radius.

The initial temperature field is now calculated according to the relationship

$$\theta_{r,z} = 1650 + 200(1-[r^2/R^2]) + 250\exp(-z/r) + 1650\exp(-3[z+r]/R)$$

and written into the array TEMP for LT=1. This temperature field is then output into the file 0000, along with X and Y arrays and other information required by the interpolation program.

The Finite Difference temperature calculations begin next, the results being written into the array TEMP after each timestep. The evaluation of the temperatures on the boundaries is performed first, and the regions mentioned in the program correspond to those in Fig 4.2. Thus 1,2,E,F,G and H are single-point calculations, while 'DO' loops in LR only and LZ only are needed for C,D and A,B respectively. The general region requires a loop of LR nested within an LZ loop.

```
C Finite Difference program  to solve the equations given in the
C ECSC report from British Steel Corporation.
C Radial and Axial analysis is performed for a distance
C of z=3R from the tip,and an axial-only  analysis is performed
C for distances greater then 3R from the tip
C
C
      DIMENSION TEMP(20,80,2), X(80), Y(20), ILIST(15)
C..
C.. ILIST is the list of timesteps that will be written.
C..
      REAL K
C..
C.. (thermal conductivity)
C..
      DATA K, ROE, VWFAC, STEPH /40.0, 1650.0, 1.0, 5.6686E-8/
C..
C..(Thermal Conductivity (W/mK), Density (kg/m**3), View Factor,
C.. Stephan Constant (W/m**2K**4))
C..
      DATA H, C /12.5, 2.0E03/
C..
C.. Convection Coefficient (W/m**2K), Specific Heat Cap. (J/kg)
C..
      DATA DELTIM, TA, NTIMST, NODES /4.0, 30.0, 900, 19/
C..
C.. Timestep (sec), ambient temp (deg C), no of steps, no of radial
C.. nodes.
C..
      DATA R, TOTLEN /0.3048, 1.2/
C..
C.. Electrode Radius(m), length to be analysed (m)
C..
      DATA ILIST /5, 10, 20, 40, 80, 160, 300, 600, 900/
      DATA NUMLST /9/
C..
C.. NUMLST is the number of elements in 'list'.
C..
      LOGICAL*1 FMT(1) /'*'/
C..
C.. Set up the facility for output file identification
C..
      LOGICAL*1 NAME1(20)
      LOGICAL*1 PROG(85)
      LOGICAL*1 LASS(18), CREFIL(16), PREF(4)
      CALL MOVEC(10, 'ASSIGN 12=', LASS(1))
      CALL MOVEC(8, '    0000', LASS(11))
      CALL MOVEC(8, '$CREATE ', CREFIL(1))
      CALL MOVEC(4, '____', PREF(1))
      CALL MOVEC(35, 'Isotropic Finite Difference Program', PROG(1))
      CALL MOVEC(32, ' Immediate Removal From FurnaCe.', PROG(36))
      CALL MOVEC(18, 'Last update Aug 83', PROG(68))
      CALL FTNCMD('ASSIGN 11=*SINK*;')
C..
C..initialise the temperature arrays
C..
```

```
      DO 30 IT = 1, 2
        DO 20 IZ = 1, 80
          DO 10 IR = 1, 20
            TEMP(IR,IZ,IT) = 0.0
   10     CONTINUE
   20   CONTINUE
   30 CONTINUE
      DO 40 IX = 1, 80
        X(IX) = 0.0
   40 CONTINUE
      DO 50 IY = 1, 20
        Y(IY) = 0.0
   50 CONTINUE
      WRITE (6,60)
   60 FORMAT (' ', 'Arrays initialised')
      CALL FTNCMD('ASSIGN 15=*SOURCE*;')
   70 WRITE (11,80)
   80 FORMAT ('1', 14X, 'Finite Difference Program, BSC equations', /,
     1        24X, 'K.G.Middleton')
      WRITE (11,90) PROG
   90 FORMAT (' ', 'Program Identification line is', //, 85A1)
      IF (NODES .GT. 20) STOP 25
C.. so that we don't overflow the arrays.
      WRITE (11,100)
  100 FORMAT (' ', 'Enter up to 4 chars for filename prefix')
      READ (15,110) PREF
  110 FORMAT (4A1)
      CALL MOVEC(4, PREF, LASS(11))
      CALL MOVEC(4, PREF, CREFIL(9))
C..
      WRITE (11,120) DELTIM, TA, NTIMST, NODES
  120 FORMAT (' ', /, 'Using a time step of ', F4.1, ' seconds', /,
     1        'Shop ambient temp of ', F5.1, 'deg centigrade', /,
     2        'Calculating ', I7, 'timesteps', /, 'using', I7,
     3        '  radial nodes')
C..
C work out the number of nodes in the region z=0 to z=3R
C assuming DELR=DELZ
C..
C..
      NODEZ = (3*NODES) - 2
      NNODZ = NODEZ - 1
      NNODS = NODES - 1
      R3 = 3.0 * R
      IF (TOTLEN .LT. R3) WRITE (11,130)
  130 FORMAT ('1', '*****WARNING, LENGTH OF ELECTRODE SECTION TOO SMALL
     1***')
C..
C work out the mesh spacings in the radial and axial directions
C..
      DELR = R / ((NODES) - 1)
C..
C the mesh points are to be kept reasonably square, but with provision
C for changing the sides ratio if required
C..
      DELZ = (3.0*R) / (NODEZ - 1)
```

```
C..
C because the 2-d analysis extends to a distance of 3R from the
C tip,a 1-d (radial only) analysis is performed at distances
C greater than this. the value of DELZ must of course be the
C same as that used in the 2-d analysis so when the total
C analysis length is stated,this is re-evaluated (TOT) to
C make it a multiple of the DELZ calculated for the 2D analysis
C NDRAD is the number of 'extra' x-nodes over and above those
C within the distance 3R of the tip
C..
      L = NTIMST + 1
      NDRAD = (TOTLEN - R3) / DELZ
      TOT = (NDRAD*DELZ) + R3
      NDZTOT = NODEZ + NDRAD
      NNDZTT = NDZTOT - 1
C..
C set up the arrays for the x and y finite difference coordinates
C..
      X(1) = 0
      DO 140 IB = 1, NNDZTT
        X(IB + 1) = DELZ * IB
  140 CONTINUE
      Y(1) = 0
      DO 150 IC = 1, NNODS
        Y(IC + 1) = DELR * IC
  150 CONTINUE
      WRITE (11,160)
  160 FORMAT (' ', 'Use Internally Generated Temp Field? (Y/N)')
      READ (15,170) INTNL
  170 FORMAT (A1)
      CALL COMC(1, 'N', INTNL, IDUM, &220, &220)
C..
C next the two dimensional initial temperature field is read in
C..
      WRITE (6,180)
  180 FORMAT (' ', 'Enter name of file containing initial temp field')
      READ (15,190) NAME1
  190 FORMAT (20A1)
      CALL FTNCMD('ASSIGN 3=?;', 0, NAME1)
      DO 210 JZ = 1, NDZTOT
        READ (3,200) (TEMP(JA,JZ,1),JA=1,NODES)
  200   FORMAT (200(1X,F5.0))
  210 CONTINUE
      GO TO 280
  220 WRITE (11,230)
  230 FORMAT (' ', 'Internal Field to be used')
C.. Fill the array with the initial temperature field
      DO 270 JG = 1, NDZTOT
        DO 260 IG = 1, NODES
          T1 = 200.0 * (1 - ((Y(IG)**2)/(R**2)))
          IF (Y(IG) .EQ. 0.0) GO TO 240
          T2 = 250 * EXP(-X(JG)/Y(IG))
          GO TO 250
  240     T2 = 0.0
  250     T3 = 1650 * EXP(-3*((X(JG)/R) + (Y(IG)/R)))
          TEMP(IG,JG,1) = 1650 + T1 + T2 + T3
  260   CONTINUE
  270 CONTINUE
```

```
C..
C the following constant coefficients are an aid to the evaluation
C of some of the terms
C..
  280 D = K / (ROE*C)
      COEFF1 = D * DELTIM
      COEFF2 = (DELR**2)
      COEFF3 = DELZ ** 2
      COEFF4 = 2.0 / (K*DELZ)
      COEFF5 = (2.0*R + DELR) / (R*K*DELR)
C ..
C the following do loop is the overall time step do loop into which
C several other loops are nested.
C..
      DO 550 LT = 1, NTIMST
C..
C  decide which array layer to read from and write to
C..
  290   LRD = MOD(LT,2)
        IF (LRD .EQ. 0) LRD = 2
        LWRT = MOD(LT,2) + 1
C..
C print out the original temperature field into file 0000
C before the first timestep calculation
C..
        IF (LT .EQ. 1) GO TO 300
        GO TO 350
  300   CALL MOVEC(4,'0000',CREFIL(13))
        CALL CMD(CREFIL,16)
        CALL MOVEC(4,'0000',LASS(15))
        CALL FTNCMD(LASS,18)
        IDUMMY = LT - 1
        WRITE (12,450) PROG
        WRITE (12,470) NODES, NDZTOT, IDUMMY, DELTIM
        WRITE (12,460) DELR, DELZ
        DO 310 I = 1, NDZTOT
          WRITE (12,490) X(I)
  310   CONTINUE
        DO 320 I = 1, NODES
          WRITE (12,490) Y(I)
  320   CONTINUE
        WRITE (12,510) (Y(KV),KV=1,NODES)
        DO 330 JZ = 1, NDZTOT
          WRITE (12,520) X(JZ), (TEMP(JR,JZ,1),JR=1,NODES)
  330   CONTINUE
        WRITE (6,340)(LASS(JH),JH=11,18)
  340   FORMAT (' ', 'Original temp field  written to file      ',8A1)
```

```
C..
C radial only temperatures are to be worked out first, applicable
C to the region greater than 3R from the tip. The temps are
C evaluated for one value only of z then repeated
C the 1-dimensional region are labelled as follows
C                       1) r=0
C                       2) r=R  (outer edge of electrode )
C                       3) general equation for body of electrode
C
C let the first position in the temp array corresponding
C to a value of z greater than 3R be NFST
C..
  350   NSTART = NODEZ + 1
        DO 370 NFST = NSTART, NDZTOT
C..
C  first the boundary conditions at z=0
C..
C                           region '1'
C..
          TEMP(1,NFST,LWRT) = TEMP(1,NFST,LRD) + (4.0*COEFF1*(TEMP(2,
     1    NFST,LRD) - TEMP(1,NFST,LRD))) / COEFF2
C..
C                     then at z=R
C..
C                           region '2'
C..
          TERMR1 = 2.0 * (TEMP(NODES - 1,NFST,LRD) - TEMP(NODES,NFST,
     1    LRD)) / COEFF2
          RADR = (((TEMP(NODES,NFST,LRD) + 273.0)**4) - ((TA + 273.0)**
     1    4)) * STEPH * VWFAC
          CONVR = H * (TEMP(NODES,NFST,LRD) - TA)
          TEMP(NODES,NFST,LWRT) = TEMP(NODES,NFST,LRD) + COEFF1 * (
     1    TERMR1 - COEFF5*(RADR + CONVR))
C..
C then the general term is evaluated
C..
C                           region '3'
C..
          DO 360 LR = 2, NNODS
            RGEN1 = (((LR - 1)*DELR*2.0) + DELR) * TEMP(LR + 1,NFST,LRD
            RGEN2 = (((LR - 1)*DELR*2.0) - DELR) * TEMP(LR - 1,NFST,LRD
            RGEN4 = ((LR - 1)*DELR*4.0) * TEMP(LR,NFST,LRD)
            RGEN3 = ((LR - 1)*DELR*2.0) * (DELR**2)
            TEMP(LR,NFST,LWRT) = TEMP(LR,NFST,LRD) + COEFF1 * (RGEN1 +
     1      RGEN2 - RGEN4) / RGEN3
  360     CONTINUE
  370   CONTINUE
C..
C now the axial temperature calculations are performed.
C..
C The region at the corner points for the first time step must
C first be calculated.
C..
```

```
C                              region 'E'
          TERME1 = ((TEMP(2,1,LRD) - TEMP(1,1,LRD))*4.0) / COEFF2
          TERME2 = ((TEMP(1,2,LRD) - TEMP(1,1,LRD))*2.0) / COEFF3
          RADE = (((TEMP(1,1,LRD) + 273.0)**4) - ((TA + 273.0)**4)) *
     1    STEPH * VWFAC
          CONVE = H * (TEMP(1,1,LRD) - TA)
          TEMP(1,1,LWRT) = TEMP(1,1,LRD) + COEFF1 * (TERME1 + TERME2 - (
     1    COEFF4*(RADE + CONVE)))
C..
C                              region 'F'
C..
          TERMF1 = (TEMP((NODES - 1),1,LRD) - TEMP(NODES,1,LRD)) * 2.0 /
     1    COEFF2
          TERMF2 = (TEMP(NODES,2,LRD) - TEMP(NODES,1,LRD)) * 2.0 / COEFF3
          RADF = (((TEMP(NODES,1,LRD) + 273.0)**4) - ((TA + 273.0)**4)) *
     1    STEPH * VWFAC
          CONVF = H * (TEMP(NODES,1,LRD) - TA)
          TEMP(NODES,1,LWRT) = TEMP(NODES,1,LRD) + COEFF1 * (TERMF1 +
     1    TERMF2 - ((COEFF4 + COEFF5)*(RADF + CONVF)))
C
C                              region 'G'
C..
          TERMG1 = (TEMP(2,NODEZ,LRD) - (TEMP(1,NODEZ,LRD))) / COEFF2
          TEMP(1,NODEZ,LWRT) = TEMP(1,NODEZ,LRD) + 4.0 * (COEFF1*TERMG1)
C..
C                              region 'H'
C..
          TERMH1 = ((TEMP((NODES - 1),NODEZ,LRD) - TEMP(NODES,NODEZ,LRD))*
     1    2.0) / COEFF2
          RADH = (((TEMP(NODES,NODEZ,LRD) + 273.0)**4) - ((TA + 273.0)**4)
     1    ) * STEPH * VWFAC
          CONVH = H * (TEMP(NODES,NODEZ,LRD) - TA)
          TEMP(NODES,NODEZ,LWRT) = TEMP(NODES,NODEZ,LRD) + COEFF1 * (
     1    TERMH1 - COEFF5*(RADH + CONVH))
C..
C                              region 'A'
C..
C region A  for each time step the temps along the centre line must
C  be calculated. thus a do loop in LZ 2 to (NODEZ-1) must go in each
C time step. Similarly for region b,c,d
C
C
          DO 380 LZ = 2, NNODZ
            TERMA1 = (TEMP(2,LZ,LRD) - TEMP(1,LZ,LRD)) / COEFF2
            TERMA2 = (TEMP(1,LZ + 1,LRD) + TEMP(1,LZ - 1,LRD) - (2.0*TEMP(
     1      1,LZ,LRD))) / COEFF3
            TEMP(1,LZ,LWRT) = TEMP(1,LZ,LRD) + (4.0*COEFF1*TERMA1) + (
     1      COEFF1*TERMA2)
C..
C                              region 'B'
C region B for outer edge  also included in LZ do loop
C..
          TERMB1 = ((TEMP((NODES - 1),LZ,LRD) - TEMP(NODES,LZ,LRD))*2.0
     1     / COEFF2
          TERMB2 = (TEMP(NODES,LZ + 1,LRD) + TEMP(NODES,LZ - 1,LRD) - (
     1    2.0*TEMP(NODES,LZ,LRD))) / COEFF2
          RADB = (((TEMP(NODES,LZ,LRD) + 273.0)**4) - (((TA + 273.0))**
     1    4)) * STEPH * VWFAC
```

```
            CONVB = H * (TEMP(NODES,LZ,LRD) - TA)
            TEMP(NODES,LZ,LWRT) = TEMP(NODES,LZ,LRD) + COEFF1 * (TERMB1 +
     1      TERMB2 - COEFF5*(RADB + CONVB))
C end of this nested do loop
  380    CONTINUE
C
C..
C                              region 'C'
C region C requires LR do loop 2-nodes
C this part for top edge
C..
         DO 390 LR = 2, NNODS
C..
C term1 is so large it has been subdivided
C..
            SUB1 = ((((LR - 1)*DELR)*2.0) + DELR)
            SUB2 = ((((LR - 1)*DELR)*2.0) - DELR)
            SUB3 = (((LR - 1)*DELR)*2.0) * COEFF2
            SUB4 = (LR - 1) * DELR
            TERMC1 = ((SUB1*TEMP(LR + 1,NODEZ,LRD)) + (SUB2*(TEMP(LR - 1,
     1      NODEZ,LRD))) - ((4.0*SUB4)*TEMP(LR,NODEZ,LRD))) / SUB3
            TEMP(LR,NODEZ,LWRT) = TEMP(LR,NODEZ,LRD) + COEFF1 * TERMC1
C..
C                              region 'D'
C..
C region D  for bottom edge also included in nested loop
C..
            TERMD1 = ((SUB1*TEMP(LR + 1,1,LRD)) + (SUB2*TEMP(LR - 1,1,LRD)
     1      -(4.0*SUB4)*TEMP(LR,1,LRD))) / SUB3
            TERMD2 = 2.0 * (TEMP(LR,2,LRD) - TEMP(LR,1,LRD)) / COEFF3
            RADD = (((TEMP(LR,1,LRD) + 273.0)**4) - ((TA + 273.0)**4)) *
     1      STEPH * VWFAC
            CONVD = H * (TEMP(LR,1,LRD) - TA)
            TEMP(LR,1,LWRT) = TEMP(LR,1,LRD) + COEFF1 * (TERMD1 + TERMD2 -
     1       COEFF4*(RADD + CONVD))
C..
C end of nested do loop in LR
C..
  390    CONTINUE
C..
C now the general equation for the body. again term1 has been
C split up. this needs do loop of  LR 2 to nodes  embedded in LZ 2 to
C (NODEZ-1)
C                     region 'general body'
C..
         DO 410 LZ = 2, NNODZ
           DO 400 LR = 2, NNODS
              SBGEN1 = ((((LR - 1)*DELR)*2.0) + DELR)
              SBGEN2 = ((((LR - 1)*DELR)*2.0) - DELR)
              SBGEN3 = (((LR - 1)*DELR)*2.0) * (DELR**2)
              SBGEN4 = (LR - 1) * DELR
              TERMX1 = ((SBGEN1*TEMP(LR + 1,LZ,LRD)) + (SBGEN2*TEMP(LR -
     1        1,LZ,LRD)) - ((4.0*SBGEN4)*TEMP(LR,LZ,LRD))) / SBGEN3
              TERMX2 = (TEMP(LR,LZ + 1,LRD) + TEMP(LR,LZ - 1,LRD) - (2.0*
     1        TEMP(LR,LZ,LRD))) / COEFF3
```

```
            TEMP(LR,LZ,LWRT) = TEMP(LR,LZ,LRD) + COEFF1 * (TERMX1 +
     1      TERMX2)
  400     CONTINUE
  410   CONTINUE
C..
C arrange for the results from each time step to be written nto a
C different temporary file numbered -001,-002,-003 etc
C..
        WRITE (6,420) LT
  420   FORMAT (' ', 'CALCULATION COMPLETE FOR', I6, 4X, 'TIME STEPS')
        DO 430 I = 1, NUMLST
          IF (LT .NE. ILIST(I)) GO TO 430
          GO TO 440
  430   CONTINUE
        GO TO 550
  440   CALL BTD(LT, CREFIL(13), 4, IDIG, '0')
        CALL CMDNOE(CREFIL, 16)
        CALL BTD(LT, LASS(15), 4, IDIG, '0')
        CALL FTNCMD(LASS, 18)
        WRITE (12,450) PROG
  450   FORMAT (85A1)
        WRITE (12,470) NODES, NDZTOT, LT, DELTIM
        WRITE (12,460) DELR, DELZ
  460   FORMAT (' ', 2(E10.4,2X))
  470   FORMAT (' ', 2(I6), 3X, I6, F5.1)
        DO 480 I = 1, NDZTOT
          WRITE (12,490) X(I)
  480   CONTINUE
        DO 500 I = 1, NODES
          WRITE (12,490) Y(I)
  490     FORMAT (' ', 6(F7.4,2X))
  500   CONTINUE
        WRITE (12,510) (Y(KV),KV=1,NODES)
  510   FORMAT (' ', 8X, 25(F5.3,1X))
        DO 530 LZ = 1, NDZTOT
          WRITE (12,520) X(LZ), (TEMP(LR,LZ,LWRT),LR=1,NODES)
  520     FORMAT (' ', F6.4, 2X, 25(F5.0,1X))
  530   CONTINUE
        WRITE (6,540) LT
  540   FORMAT (' ', 'RESULTS WRITTEN TO  FILES FOR', I6, 4X,
     1          'TIME STEPS')
  550 CONTINUE
C..
C now the end of the main do loop
C..
```

```
C..
C & write out information
C..
      WRITE (6,560) TOT
  560 FORMAT (' ', 'Total length of electrode analysed=', F10.3)
  570 STOP
      END
```

Modifications necessary for Orthotropy & Temp - Dependant Material Properties

Before each calculation, the subroutines DECIDE, PROPS and COFFS are called to ascertain the material property set to be used, evaluate the properties at the appropriate temperature, and to calculate the values of temperature-dependent coefficients at this temperature. Finally, the appropriate temporary magnetic disc files are created, and the results are written into these files. A flow diagram is shown in Fig A2.1.

SUBROUTINE 'DECIDE'

The function of this subroutine is to decide which of the three materials (electrode graphite, nipple graphite or air) is appropriate to the calculation of temperatures at the point in question. The values LR, LZ, DELR and DELZ are the input parameters, from which the radial and axial coordinate of the point are calculated. A series of simple IF and GO TO statements using the variables mentioned in Fig 7.1 is used to assign a value of 1, 2 or 3 (electrode, nipple or air) to the variable IDEC, which is then passed back to the main program. The variable IDEC thus identifies to the subroutine PROPS the material set in question. A flow diagram of this subroutine is shown in Fig A2.2.

SUBROUTINE PROPS

Taking as input the value of the parameter IDEC and the value PTEMP (the temperature at the point after the previous timestep) the appropriate material set is selected, and the thermal conductivity of that material at temperature PTEMP is calculated according to equations 7.3(a) and 7.3(b). Values of both axial and radial conductivity are returned to the main program. For the model described, only thermal conductivity was assumed to have a temperature dependence. Most of the material properties are contained preprogrammed into this subroutine however, and are returned to the main program along with the thermal conducitivity. If extra data became available on the temperature variation of specific heat capacity for example, it would thus be very easy to incorprate by modification of this subroutine alone.

Subroutine COFFS

This subroutine is used to calculate values for various coefficients used in the program. Some of these are temperature-depenedent and must therefore be calculated for each timestep and position. For ease of reference, some non-temperature-dependent coefficients are also calculated here.

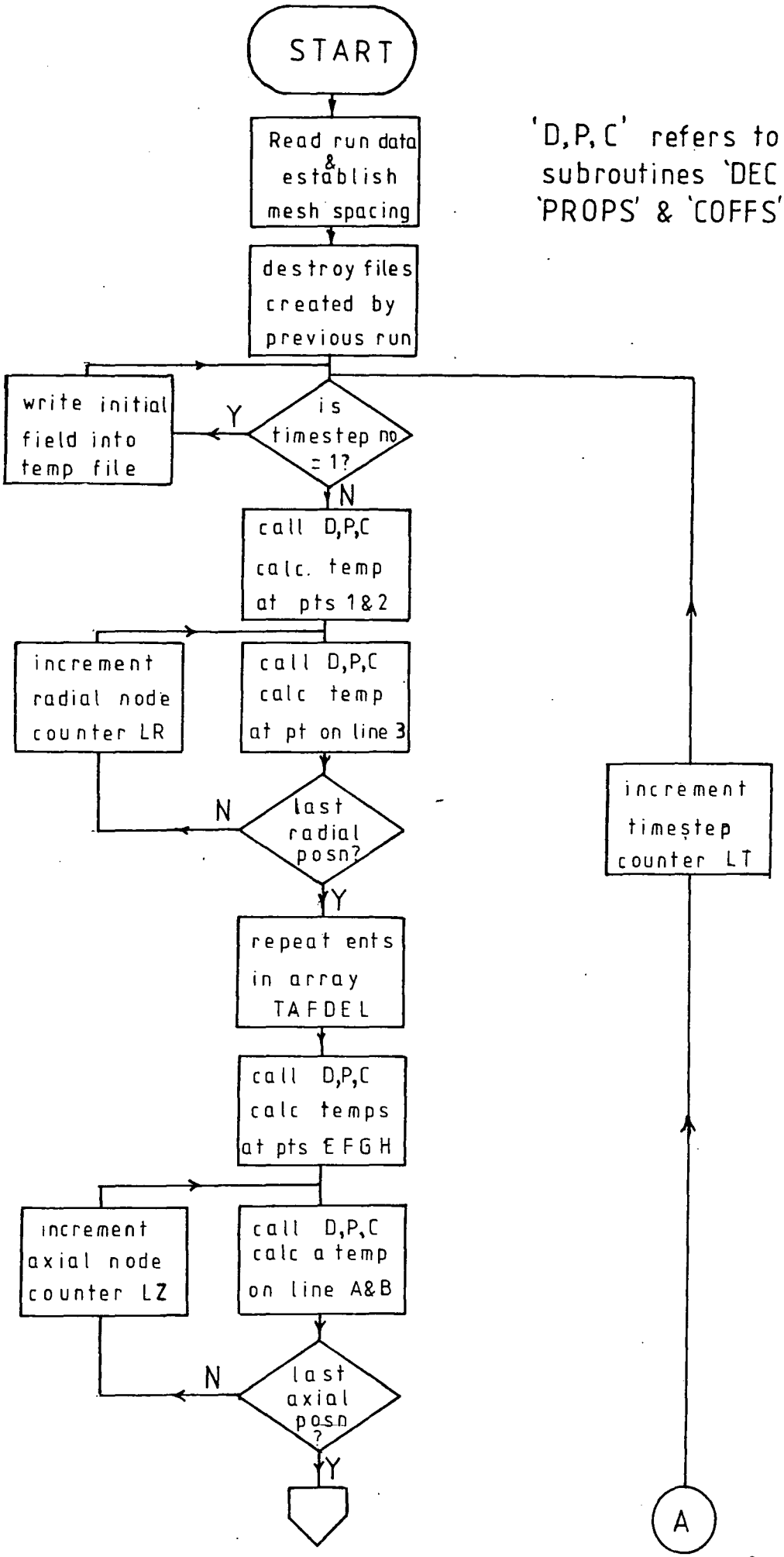

Fig A21(a) Simplified flow diagram for the improved Finite Difference Program 'FDPREM'

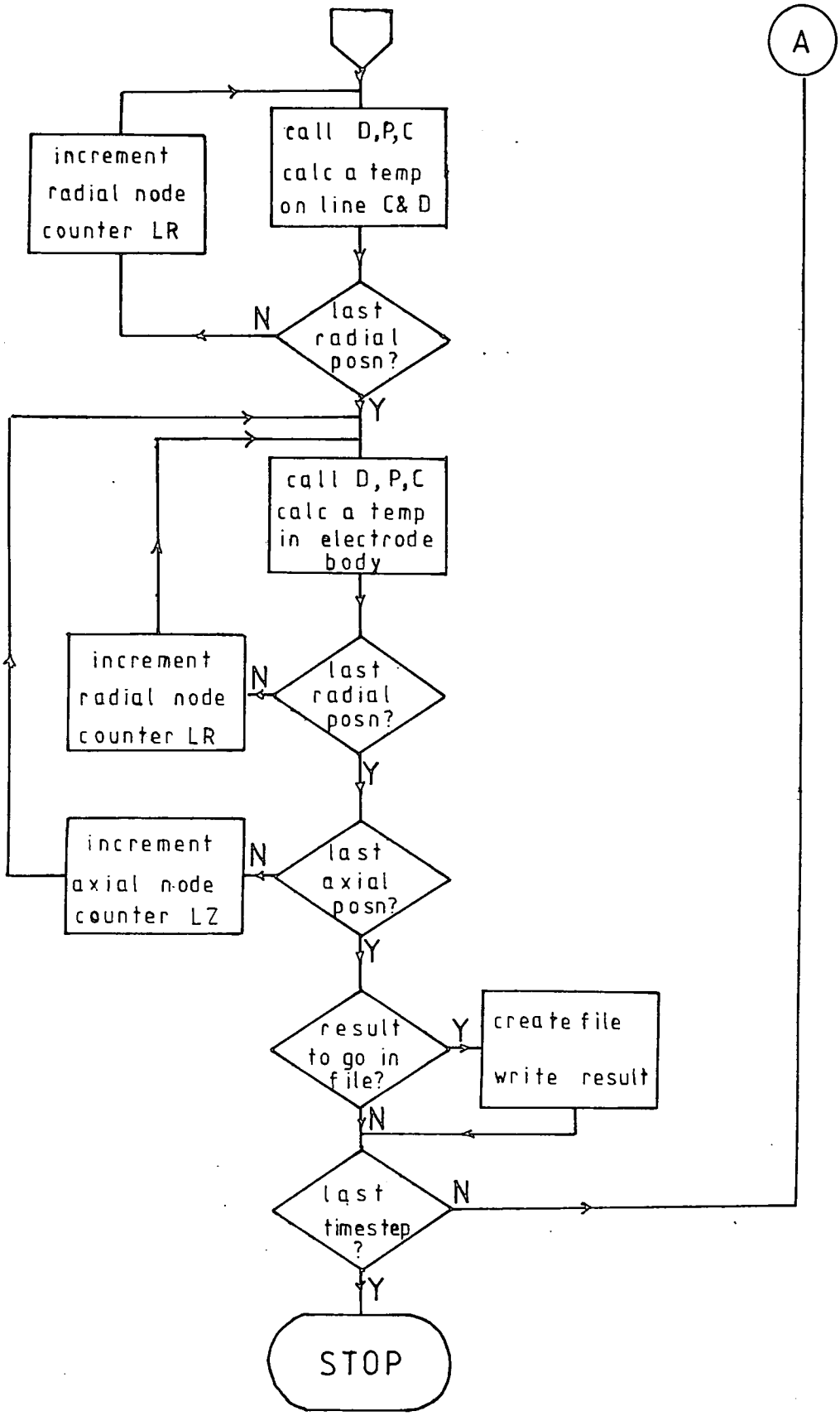

Fig A21(b) Simplified Flow Diagram for 'FDPREM' (cont.)

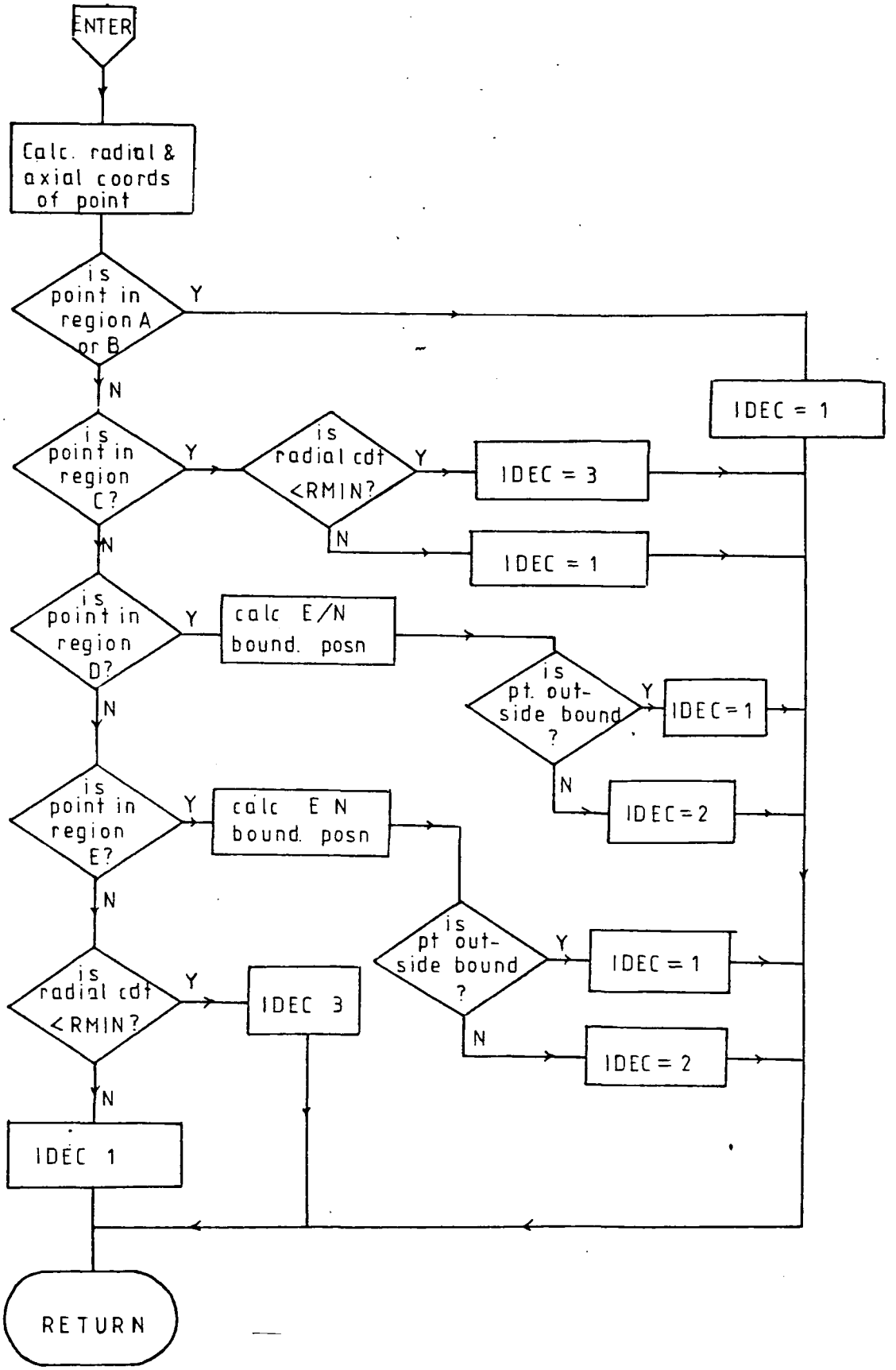

Fig A2.2 Flow Diagram for Subroutine DECIDE

APPENDIX III

THE INTERPOLATION PROGRAM

This program assigns temperatures to the Finite Element nodal coordinates, given the temperature field at the regularly spaced Finite Difference nodes. It is designed to read the temperature field straight from the files written by the Finite Difference program, complete with identifying information, and to output to automatically created disc files for each run. Additionally, each output file forms the first part of a PAFEC data file, complete with a title identifying the run, and comment cards giving additional information. All that is necessary to perform the mechanical/thermal stress analysis is thus to append to the output file a PAFEC 'base' file containing mesh information, mechanical loads and material properties. It is thus possible always to trace back to the original Finite Difference run a given PAFEC stress analysis.

The program is centred around a NAG interpolation subroutine. It was not possible to obtain the Fortran coding of this subroutine, so the use of it inevitably requires something of a 'black box' approach. In particular, workspace arrays must be defined purely from the documentation.

The use of NAG requires double precision throughout in the NUMAC implementation. The user is prompted to supply certain information as follows:-

(i) How far are the Finite Element coordinates to be moved. Since the origin of the Finite Element coorindate system is at the electrode/electrode interface, and that of the Finite Difference system is at the end of the electrode, a translation (DELTAX) is applied to each Finite Element coordinate.

(ii) The name of the file containing the temperature array - this is then assigned to input channel 5, and of course, contains all information about the Finite Difference run.

(iii) The name of the file containing the Finite Element coordinates. This is then assigned to read channel 7.

First, the Finite Difference meshing information is obtained from the temperature file..and a check is made to ensure that these will fit into the declared array sizes. Next the output file is assigned a number of the form '-INXXX', where XXX is a timestep, read from the temperature field file. All relevant information including a PAFEC title is read from this file, written to the output file and echoed on the screen. The arrays are dimensioned (see program 'comment' cards for the use of these arrays), and the Finite Element coordinates are read, one per pass, into the array FEC. A translation is added to ensure the correct origin. Such quantities as M1, N1, required by the program, were written into the temperature

file by the Finite Difference program and these, along with the scales of X and Y coordinates, are read in. The latter two are written into the arrays X and Y (note that 'X' corresponds to axial distance, and 'Y' to radial distance). The Finite Difference temperature field is now read into the array TEMP (the 'dummy' quantities read are also X and Y coordinates which were written into the file as a reference aid by the Finite Difference program). The variables required by the NAG subroutine which have not already been set up are now defined, and the subroutine (E01ACF) is called to perform the interpolation. The values of the interpolated temperature VAL, and VALL, represent the result obtained by interpolating in the X and Y directions. Since a single value is required, the mean of these two results is calculated and used as the interpolated temperature. Experience showed that VAL and VALL were invariably almost identical. The node number and corresponding interpolated temperature are now written to the output file and echoed on the screen.

```
C                    Interpolation  Program
C
C This program is centred around the NAG interpolation routine
C number   E01ACF
C
C                         Method of Use
C Use the finite diff program to  find the temp distribution
C on the rectangular mesh. This will output on both unit 6.and unit
C 7. The output from unit 7 is placed in a file which is read by this
C program.  this file will contain, without intervening text, the
C following arrays & variables
C X
C Y
C temp - the temperature array
C M1
C N1 -parameters relating to the array sizees.
C Note that The Finite Difference program  uses Z,R coordinates which in
C this  program  are  exchanged for X,Y.
C
C the array FEC contains a line of finite element coordinates.
C 1-D array subscript  vals  1=node number 2=axis number
C                            3=x-coord     4=y-coord
C
C for the NAG routines all variables must be in double precision.
C ..
      IMPLICIT REAL*8(A - H,O - Z)
      DIMENSION FEC(4), Y(19), X(71), XX(71), WORK(71), AM(71), D(71),
     1          TEMP(71,19)
      LOGICAL*1 FMT(1) /'*'/
      LOGICAL*1 NAME1(20), NAME2(20), NAME3(20), PROGLN(80)
      LOGICAL*1 LWRIT(20), CREFIL(18)
C..
C CREFIL is going to contain a character string to create a file.
C LWRIT  is going to caontain a character string to assign a
C channel to the created file. Set up the constant parts of these
C strings now.
C..
      CALL MOVEC(12,'ASSIGN 15=IN',LWRIT(1))
      CALL MOVEC(10,'$CREATE IN',CREFIL(1))
      CALL FTNCMD('ASSIGN 11=*SINK*;')
      CALL FTNCMD('ASSIGN 3=*SOURCE*;')
      WRITE (11,10)
   10 FORMAT ('1', 14X, 'Interpolation from F.D. to F.E.', //, 14X,
     1       'Originated 12 May 1980')
C
C obtain some information.....
C
      WRITE (11,20)
   20 FORMAT (' ', 'Enter name of file containing temperature array')
      READ (3,40) NAME1
C..
C Complete the next part of the create and assign strings with
C the first 4 characters of the temperature file name
C..
      CALL MOVEC(4,NAME1,CREFIL(11))
      CALL MOVEC(4,NAME1,LWRIT(13))
      CALL FTNCMD('ASSIGN 5=?;', 0, NAME1)
```

```
      WRITE (11,30)
   30 FORMAT (' ', 'Enter name of file containing Finite Element points'
     1       )
      READ (3,40) NAME2
      CALL FTNCMD('ASSIGN 7=?;', 0, NAME2)
   40 FORMAT (20A1)
      WRITE (11,50)
   50 FORMAT (' ', 'How far to move F.E. coords axially?')
      READ (3,FMT) DELTAX
C..
C   read in from the f.d. file the   identification line,
C   number of x&y nodal points  and the value of timestep and
C   timestep number
C..
      READ (5,60) PROGLN
   60 FORMAT (80A1)
C..
C Get preliminary information from the FD file.
C NTSTP is timestep number, VALSTP is value of step in secs
C..
      READ (5,FMT) M1, N1, NTSTP, VALSTP
C
C   safety device. the nag subroutine is sensitive to the
C   declared array sizes
C
      IF (M1 .NE. 19 .OR. N1 .NE. 71) GO TO 70
      GO TO 90
   70 WRITE (6,80)
   80 FORMAT (' ', '** Failure to start. Array overflow ** ')
      STOP 500
C
C  get the values of the f.d. mesh sizes from the f.d. file
C
   90 READ (5,FMT) DELR, DELZ
C..
C.. Turn the integers representing the timestep nos into characters
C.. and complete the create and assign character string.
C..
      CALL BTD(NTSTP,CREFIL(15),4,IDS,'0')
      CALL BTD(NTSTP,LWRIT(17),4,IDS,'0')
      CALL CMD(CREFIL,18)
      CALL FTNCMD(LWRIT,20)
      CALL EMPTYF(15)
C
C ETIM is the elapsed time in seconds
C
      ETIM = NTSTP * VALSTP
      WRITE (6,130) NTSTP, VALSTP
C
C write values back to terminal and to interpolation file
C
      WRITE (15,120) NTSTP, VALSTP, ETIM, NAME2
      WRITE (15,100)
      WRITE (6,100)
  100 FORMAT (' ', 'C  Simplified interp prog of April 1983')
      WRITE (15,110) PROGLN
      WRITE (6,110) PROGLN
```

```
  110 FORMAT (' ', 'C  Program Identification line (carried from FD)',
     1        , ' C    ', 80A1)
  120 FORMAT (' ', 'TITLE STEPNO ', I4, ' STEPVAL ', F4.1,
     1        ' ELAPSED TIME ', F6.1, ' COORD SOURCE ', 20A1)
      WRITE (15,130) NTSTP, VALSTP
  130 FORMAT (' ', 'C  Step Number  ', I4, '  of value  ', F4.1,
     1        '  seconds')
      WRITE (6,140) ETIM
      WRITE (15,140) ETIM
  140 FORMAT (' ', 'C  Total elapsed time is  ', F6.1, '  seconds')
      WRITE (6,150) M1, N1
      WRITE (15,150) M1, N1
  150 FORMAT (' ', 'C  Temperature array is', I5, '  by', I5)
      WRITE (15,160) NAME2
  160 FORMAT (' ', 'C  Finite element coords from file ', 20A1)
      WRITE (6,170) DELTAX
      WRITE (15,170) DELTAX
  170 FORMAT (' ', 'C  F.E. Coords moved by  ', F7.4)
      WRITE (15,180)
  180 FORMAT (' ', 'TEMPERATURE')
      WRITE (15,190)
  190 FORMAT (' ', 'TEMPERATURE  LIST.OF.NODES')
      DO 200 I = 1, N1
        READ (5,230) X(I)
  200 CONTINUE
      DO 210 I = 1, M1
        READ (5,230) Y(I)
  210 CONTINUE
  220 FORMAT (' ', I6)
  230 FORMAT (' ', 10(F7.4,2X))
      WRITE (6,240)
  240 FORMAT (' ', 'The X Finite Difference axis is as follows')
      WRITE (6,230) (X(I),I=1,N1)
      WRITE (6,250)
  250 FORMAT (' ', //, 'The Y Finite Difference Axis is as follows')
      WRITE (6,230) (Y(J),J=1,M1)
  260 FORMAT (I5)
C
C read in the temperature field
C
      READ (5,FMT) DUMMY
      DO 270 J = 1, N1
        READ (5,FMT) DUMMY, (TEMP(J,I),I=1,M1)
  270 CONTINUE
  280 READ (7,FMT,END=340) (FEC(II),II=1,4)
  290 FORMAT (' ', 20(F7.2,2X))
C
C shift the axial coords so that the FE & FD origins are
C the same
C
      FEC(3) = FEC(3) + DELTAX
C
C set up the variables required for the call to the NAG
C subroutine and call it
C
      VAL = 0
      VALL = 0
  300 IFAIL = 0
```

```
C
      CALL E01ACF(FEC(3), FEC(4), X, Y, TEMP, VAL, VALL, IFAIL, XX,
     1      WORK, AM, D, IG1, M1, N1)
C
C AVAL is the average of the two interpoloataed values
      NODE = IFIX(SNGL(FEC(1)))
      AVAL = (VAL + VALL) / 2.0
  310 WRITE (15,320) AVAL, NODE
  320 FORMAT (' ', F10.4, 6X, I6)
      GO TO 280
  340 STOP
      END
```

APPENDIX IV

DETERMINATION OF MATERIAL PROPERTIES

Two sets of Modulus of Rupture (M.O.R.) determinations from 3-point bend tests, and one set of 'Pseudo Traction' results were available for material property determination (Payne, 1981). The Pseudo Traction results were obtained from a diametral compression test on a cylinder 50mm in diameter by 25 mm thick. Some doubts have been cast on this method of obtaining tensile strengths, and indeed analysis of these results gave tensile strength values an order of magnitude smaller than those from M.O.R. determinations. The analysis of these results is therefore not included here, except to say that the predicted value of Weibull Modulus is 10, in accord with that obtained from the M.O.R. results.

The M.O.R. values were obtained by a three-point bend test on a specimen 6" x 1" x 1" (9.3×10^{-5} m^3).

Stanley (1973) has shown that, if compressive and shear forces make a negligible contribution to failure probability in a three-point bend test, then the probability of failure is given by

$$P_f = 1 - \exp\{[(1/m)!]^m (\sigma_{max}/\sigma_{fv})^m (V/v)/2(m+1)^2\}$$

$$= 1 - \exp\{[\sigma_{max}]^m (-Z)\} \qquad A4.1$$

where σ_{max} is the fracture stress of a particular specimen, and Z is given by

$$Z = \{[(1/m)!]^m (1/\sigma_{fv})^m (V/v)/2(m+1)^2\}$$

Taking logs on both sides of equation A3.1 we obtain

$$\log \log[1/1-P_f] = m \log \sigma_{max} + (\log Z + \log \log e)$$

A graph of $\log \log[1/1-P_f]$ against $\log \sigma_{max}$ is thus a straight line of slope m and intercept log Z + log log e. This analysis may thus now be used on the B.S.C. data to calculate values for the material properties.

(i) 'Y' - end. The raw data is ranked in increasing fracture stress σ_{max} and the quantities $\log \log[1/1-P_f]$ and $\log \sigma_{max}$ are evaluated. The results are presented below.

Rank	P_f(%)	$\log \log[1/1-P_f]$	σ_{max}	$\log \sigma_{max}$
1	7.4	-1.50	7.37	0.867
2	18.1	-1.06	7.49	0.874
3	28.7	-0.83	7.61	0.881
4	39.4	-0.66	7.74	0.888
5	50.0	-0.52	7.78	0.891
6	60.6	-0.39	7.86	0.897
7	71.2	-0.27	8.10	0.908
8	81.9	-0.13	9.20	0.964
9	92.5	0.05	11.80	1.072

These values are plotted in Fig. A4.1. The equation of the line representing these results is

$$\log \log[1/1-P_f] = 10.4 \log \sigma_{max} - 10.1$$

predicting a Weibull Modulus of about 10.

Thus

$$\{[(1/m)!]^m (1/\sigma_{fv})^m (V/v)/2(m+1)^2\} = 1.82 \times 10^{-10}$$

Since m = 10 this gives, for $V = 9.3 \times 10^{-5}$ m^3 and $v = 1m^3$

$$\sigma_{fv} = 2.04 \text{ MN/m}^2 \text{ for } 1m^3$$

(ii) 'AY' - end. Using the same procedure as before, we obtain

Rank	P_f(%)	log log[1/1-P_f]σ_{max}	logσ_{max}
1	8.3	-1.42	9.09	0.959
2	20.2	-1.01	9.09	0.959
3	32.1	-0.77	9.21	0.964
4	44.0	0.60	9.70	0.987
5	55.9	-0.45	10.07	1.003
6	67.8	-0.81	10.19	1.008
7	79.8	-0.16	11.54	1.062
8	91.7	0.03	12.89	1.110

These values are plotted in Fig A4.2. The equation of the line representing the points is

$$\log \log[1/1-P_f] = 7.93 \log \sigma_{max} - 8.54$$

predicting a Weibull Modulus of 8. Thus

$$\{[(1/m)!]^m (1/\sigma_{fv})^m (V/v)/2(m+1)^2\} = 6.61 \times 10^{-9}$$

For m = 8 this time, and V = 9.3×10^{-5} m^3, v = $1m^3$ as before

$$\sigma_{fv} = 1.7 \text{ MN/m}^2 \text{ for } 1m^3$$

The unit volume uniaxial tensile failure strength is thus 1.9 MN/m^2 per m^3 from the Weibull analysis, and the Weibull Modulus is 8-10. A value of 10 was used in the calculations since the slope of the Pseudeo Traction data was much more well-defined than that from tha M.O.R. data, and also predicted a value of 10 for the Weibull Modulus.

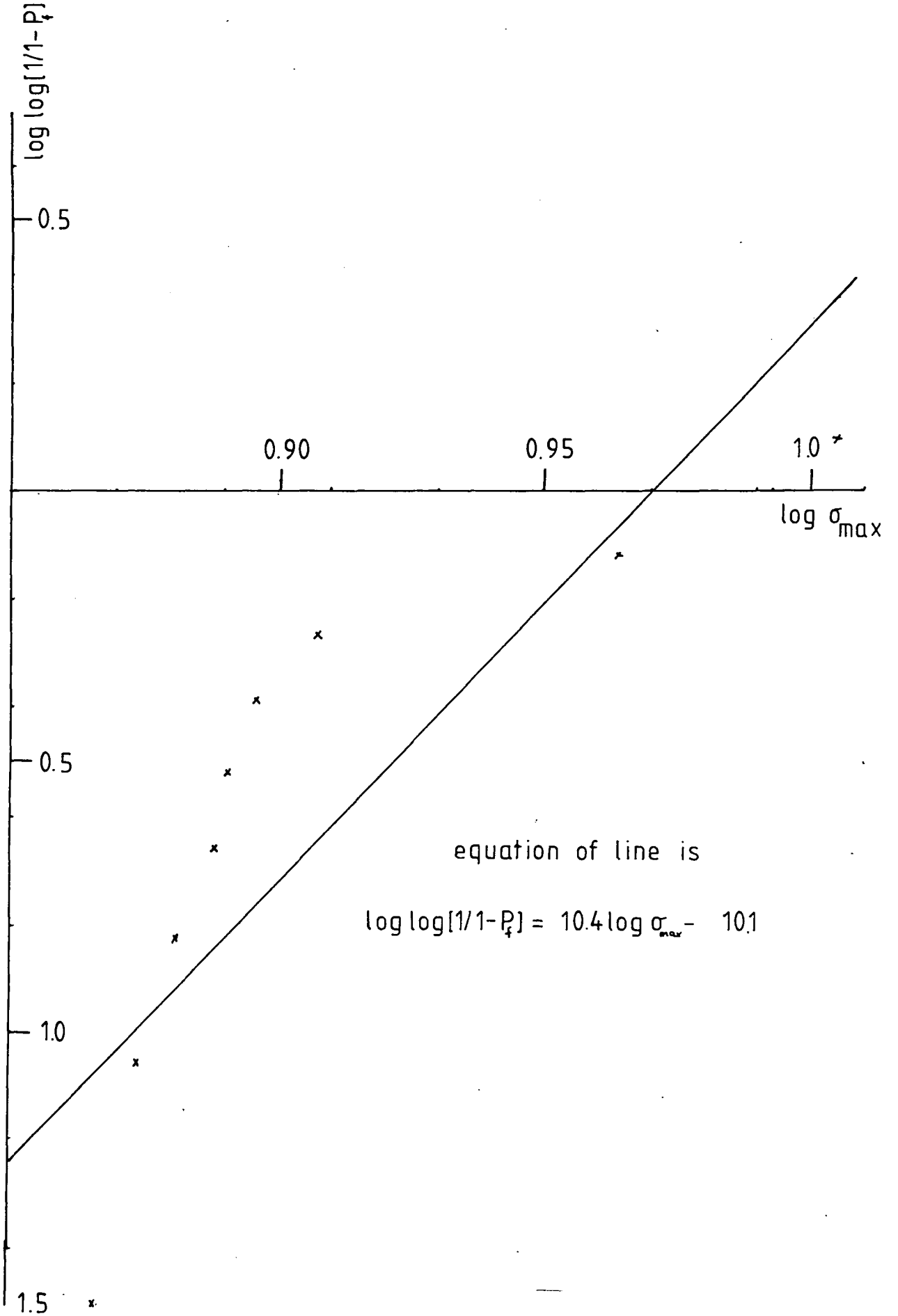

Fig A4.1 B.S.C. – M.O.R. Results – 'Y' end

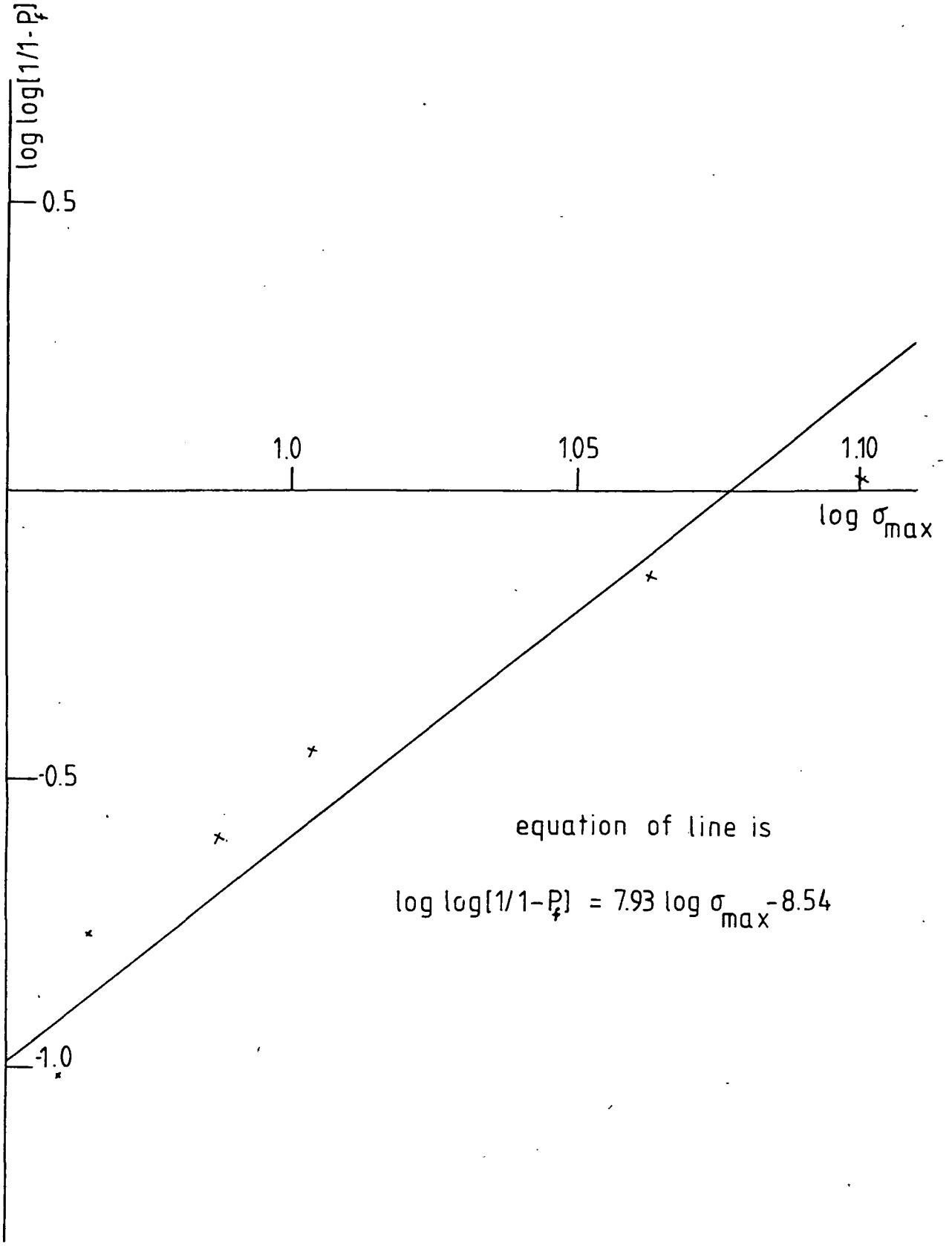

Fig A4.2 B.S.C. - M.O.R. Results - 'AY' end

APPENDIX V

STANLEY FAILURE ANALYSIS

This section describes a suite of programs; SA1, SA2, SA3, SA4, which collectively perform a Stanley Failure Analysis for a given stress field.

SA1

This program gathers together some information which is output in disjointed form by PAFEC. Two files are read by the program - the first contains all the nodal coordinates for the problem, the second contains, along with other information, the element topologies in terms of node numbers. The object of SA1 is to produce a file containing the coordinates of each corner of every element.

After first assigning the logical input/output channels, the nodal coordinates are read into the array COOR. Next a line of data is read in from the topology file. The element type is checked - if it is a triangular element the variable IN is set to 3, if quadrilateral IN is set to 4. The array COOR is now searched for each of the node numbers mentioned in the topolgy list, and when found, the relevant X and Y coordinates are noted in the arrays CX and CY respectively. If the node is not found, the run is aborted. Finally, the topolgy is written out as a set of coordinate pairs, before progressing to the next data line.

SA2

This program reads from the file produced by SA1. The cross - sectional area of each element is calculated from the nodal coordinates, and hence the fractional volume of the entire body which each each element represents is calculated.

As usual the logical input/output channels first assigned, and the total volume is calculated as a cylinder of user - defined radius and length. Three running totals are kept;

ACCUM - the accumulated fractional volume as each element is added.

ACCAR - the accumulated area as each element is added

ACCVOL -the accumulated volume as each element is added.

These three variables are first initialised. Next, a line of data is read from the file, and the element type is checked. For a triangular element, the following procedure is adopted:

(i) Call subroutine AREA to calculate the cross-sectional area of the element (XSAREA).

(ii) Call subroutine CENTRD to calculate the coordinates of the element centroid.

(iii) Add the area to ACCAR.

(iv) Calculate the volume of the element and accumulate ACCVOL.

(v) Calculate the fractional volume of the whole region and add to ACCUM.

(vi) Note the information in the array VOLEL.

(vii) When all elements done write out VOLEL.

If the element is quadrilateral, subroutine QUAD is called, which splits the element into two triangles and calls subroutine AREA and CENTRD twice each. The total area is found by addition, and the position of the centroid by taking moments. Steps (iii) to (vi) above are now performed Finally, the three running totals are printed out for checking purposes.

SA3

This program evaluates the Stress Volume Integral (S.V.I.). It reads the file producude by SA2, the element topology list and also the file containing nodal stresses. After setting up the required arrays and logical I/O assignments, the program prompts for the required information. This is saved in a file, to be read by SA4. The fractional volumes produced by SA2 are now read into the array ELFRAC. From the file containing the nodal stresses a list of nodes for the problem is read into the array LIST.

Next, an element and its type are read from the element topology file. The variable INODES is set to reflect whether it is triangular or quadrilateral. Subroutine FINDEL is now called to retrive the topology for that element, which it places in the array ITOP. ITOP is

now used in a call to FINDSR which copies the stresses for each of the nodes in ITOP to the array ELSTR. A small DO loop now calculates average values for the three principal stresses and writes them into the array AVSTR, with an element identifier. Three calls to subroutine EXPR now evaluate the individual contributions to the S.V.I. in equation 6.5(b) and these are added together before a call to PTSUM which now calculates the total contribution to the S.V.I. of the element being considered. The S.V.I. is now incremented and the program loops through the remaining elements, finally printing out the computed value for the S.V.I.

SA4

This program completes the failure probability calculation. After reading from the file produced by SA3 the information used for the S.V.I. calculation, the material consistency factor is calulated. If required, individual element failure probabilities are now calculated. Otherwise, the elemental information is skipped and the value of the S.V.I. calculated from SA3 is read and used to calculate the total failure probability using equation 6.5(a).

```
C                 SA1
C                 -------
C
C Program to take a file of coords, a file of element topologies
C and combine them to produce the equivalent topologies as a
C set of groups of coord pairs
C
      DIMENSION COOR(2500,4), CX(4), CY(4), N(4)
      LOGICAL*1 FMT(1) /'*'/
      LOGICAL*1 FILE1(20), FILE2(20), FILE3(20)
      WRITE (6,10)
   10 FORMAT (' ', 'Name of file containing coords?')
      READ (5,20) FILE1
   20 FORMAT (20A1)
      CALL FTNCMD('ASSIGN 2=?;', 0, FILE1)
      WRITE (6,30)
   30 FORMAT (' ', 'NAme of file containing topologies?')
      READ (5,20) FILE2
      CALL FTNCMD('ASSIGN 3=?;', 0, FILE2)
      WRITE (6,40)
   40 FORMAT (' ', 'Name of output file?')
      READ (5,20) FILE3
      CALL FTNCMD('ASSIGN 7=?;', 0, FILE3)
C
C.. Read in the coordinates.
C
      DO 50 I = 1, 2500
        READ (2,FMT,END=60) (COOR(I,J),J=1,4)
   50 CONTINUE
   60 IF(I.GT.2500) STOP 500
C
C.. Main seek loop
C
      DO 150 K = 1, 1200
C
C.. Read a topology set
C
        READ (3,FMT,END=180) INO, IGR, ITYPE, IPRO, (N(IN),IN=1,4)
C
C Set the node counter
C
        IF (ITYPE .NE. 36100 .AND. ITYPE .NE. 36110) GO TO 70
        GO TO 80
   70   IN = 4
        GO TO 90
   80   IN = 3
C
C.. This loop retrieves the coordinate pairs of each node in the
C.. topology list
C
   90   DO 120 L = 1, IN
          DO 110 KC = 1, 2069
            ICOUNT = 0
            IF (N(L) .EQ. IFIX(COOR(KC,1)))GO TO 100
            GO TO 110
  100       ICOUNT = ICOUNT + 1
```

```
C
C.. take a copy
C
              CX(L) = COOR(KC,3)
              CY(L) = COOR(KC,4)
              GO TO 120
  110       CONTINUE
C.. And if we didn't find any...
C
            IF (ICOUNT .EQ. 0) GO TO 160
  120     CONTINUE
C
C.. write out the results
C
          WRITE (7,140) INO, ITYPE, (CX(M),CY(M),M=1,IN)
          DO 130 JK = 1, IN
            CX(JK) = 0
            CY(JK) = 0
  130     CONTINUE
  140     FORMAT (' ', I4, 1X, I5, 1X, 8(1X,F7.4))
  150   CONTINUE
  160   WRITE (6,170)
  170   FORMAT (' ', ///, '***ERROR  NODE NOT FOUND IN LIST***')
  180   STOP
        END
```

```
C                        SA2
C                        -------
C  program to calculate the cross-sectional areas,
C  position of centroid and hence the fractional
C  volume of the axisymmetric finite elements.
C  Based on calculating the areas and centroid of a
C  basic triangular element,the quadrilateral
C  calculation is performed by splitting into two
C  triangular elements
      LOGICAL*1 FMT(1) /'*'/
      LOGICAL*1 FILE1(20), FILE2(20)
      DIMENSION VOLEL(2,1200)
C VOLEL is to contain the element nos and corresponding
C fractional volumes
      WRITE (6,10)
   10 FORMAT (' ', 'Name of file containing elements')
      READ (5,20) FILE1
   20 FORMAT (20A1)
      CALL FTNCMD('ASSIGN 3=?;', 0, FILE1)
      WRITE (6,30)
   30 FORMAT (' ', 'Name of output file?')
      READ (5,20) FILE2
      CALL FTNCMD('ASSIGN 7=?;', 0, FILE2)
      CALL FTNCMD('ASSIGN 8=*DUMMY*;')
      WRITE (6,40)
C
C  calculate the entire volume of the body using pi rsquared
C
   40 FORMAT (' ', /, 'Enter radius of electrode and length of region')
      READ (5,FMT) RADIUS, DLENTH
      TOTVOL = 3.14159 * (RADIUS**2.0) * DLENTH
C
C calculate the total area of mesh length x breadth
C for checking purposes
C
      TOTAR = RADIUS * DLENTH
C
C  keep a running total of areas and volume fractions as
C  they are calculated
C
      ACCUM = 0.0
      ACCAR = 0.0
      ACCVOL= 0.0
C
C read from file the element number,type ,and corner coords
C
      ICOUNT = 0
      DO 180 I = 1, 1200
        READ (3,FMT,END=190) INO, ITYPE, X1, Y1, X2, Y2, X3, Y3, X4, Y4
        ICOUNT = ICOUNT + 1
        WRITE (8,50) INO
   50   FORMAT (' ', 'ELEMENT NUMBER IS', I7)
```

```
C
C  if element is triangular type the area and centroid
C  are calculated directly by calling the appropriate
C  subroutines. Otherwise the subroutine 'QUAD' organises
C  the splitting into triangles and calls the relavent
C  subroutines
C
      IF (ITYPE .NE. 36100 .AND. ITYPE .NE. 36110) GO TO 60
      GO TO 70
 60   WRITE (8,80) X1, Y1, X2, Y2, X3, Y3, X4, Y4
      GO TO 90
 70   WRITE (8,80) X1, Y1, X2, Y2, X3, Y3
 80   FORMAT (' ', 'COORDS OF CORNERS ARE', 4('(',F7.4,',',F7.4,
     1         ')    '))
 90   IF (ITYPE .NE. 36100 .AND. ITYPE .NE. 36110) GO TO 100
      GO TO 110
100   CALL QUAD(X1, Y1, X2, Y2, X3, Y3, X4, Y4, XSAREA, XCENT, YCENT)
      GO TO 120
110   CALL AREA(X1, Y1, X2, Y2, X3, Y3, XSAREA)
      CALL CENTRD(X1, Y1, X2, Y2, X3, Y3, XCENT, YCENT)
120   WRITE (8,130) XSAREA
      ACCAR = ACCAR + XSAREA
130   FORMAT (' ', 'AREA OF CROSS SECTION=  ', 1PE11.4)
      WRITE (8,140) XCENT, YCENT
140   FORMAT (' ', 'COORDS OF CENTROID ARE ( ', F7.4, ', ', F7.4,
     1         ')  ')
      VOLUME = 2.0 * 3.14159 * YCENT * XSAREA
C
C  'FRACT' is the fractional volume of the element compared
C   to the volume of the body
C
      ACCVOL=ACCVOL+VOLUME
      FRACT = VOLUME / TOTVOL
      VOLEL(1,I) = INO
      VOLEL(2,I) = FRACT
C
C.. Write out the results.
C
      WRITE (8,160) VOLUME
      WRITE (8,150) FRACT
150   FORMAT (' ', /, 'Fraction of total volume is  ', 1PE11.4)
160   FORMAT (' ', 'Volume of toroid ', 1PE11.4)
      WRITE (8,170)
170   FORMAT (' ', 72('-'))
      ACCUM = ACCUM + FRACT
180 CONTINUE
190 WRITE (8,200) TOTVOL, ACCVOL
200 FORMAT (' ', 'Total vol direct=', F8.4, '  Accumulated=', F8.4)
    WRITE (7,210) TOTVOL
210 FORMAT (' ', F8.5)
    DO 230 K = 1, ICOUNT
      WRITE (7,220) (VOLEL(J,K),J=1,2)
220   FORMAT (' ', F5.0, 7X, 1PE11.4)
230 CONTINUE
    WRITE (8,240) TOTAR, ACCAR
240 FORMAT (' ', //, 'Total area direct=', F8.4, '  Accumulated=',
   1       F8.4)
    STOP
    END
```

```
      SUBROUTINE CENTRD(X1, Y1, X2, Y2, X3, Y3, XCENT, YCENT)
C
C calculate the position of the centroid of a triangular element
C
      XMED = (X2 + X3) / 2.0
      YMED = (Y2 + Y3) / 2.0
      XCENT = X1 + 2.0 * (XMED - X1) / 3.0
      YCENT = Y1 + 2.0 * (YMED - Y1) / 3.0
      RETURN
      END
      SUBROUTINE AREA(X1, Y1, X2, Y2, X3, Y3, TRIAR)
C
C  calculate the area of a triangular element by noting the
C  coords of the extremities and finding area of the
C  rectangle enclosing the triangle
C
      XMIN = AMIN1(X1,X2,X3)
      XMAX = AMAX1(X1,X2,X3)
      YMIN = AMIN1(Y1,Y2,Y3)
      YMAX = AMAX1(Y1,Y2,Y3)
      RECTAR = (YMAX - YMIN) * (XMAX - XMIN)
C
C  subtract off the triangular sub-elemental areas
C
      CALL SUB(X1, Y1, X2, Y2, SUB1)
      CALL SUB(X2, Y2, X3, Y3, SUB2)
      CALL SUB(X3, Y3, X1, Y1, SUB3)
      TRIAR = RECTAR - (SUB1 + SUB2 + SUB3)
      RETURN
      END
C
C
C
C
      SUBROUTINE SUB(XA, YA, XB, YB, SUBAR)
C
C  find the areas of the subsidiary triangles around the element
C
      SUBAR = ABS(0.5*((YB - YA)*(XB - XA)))
      RETURN
      END
C
C
C
      SUBROUTINE QUAD(X1, Y1, X2, Y2, X3, Y3, X4, Y4, ELAR, XBAH, YBAH)
      WRITE (8,10)
   10 FORMAT (' ', '** ELEMENT IS QUADRILATERAL TYPE**')
C
C  calculate area of two triangular porions of the element
C
      CALL AREA(X1, Y1, X2, Y2, X3, Y3, ARA)
      CALL AREA(X2, Y2, X3, Y3, X4, Y4, ARB)
```

```
C
C   calculate cross-sectional area of the element
C
      ELAR = ARA + ARB
C
C   calculate the positions of the centroids of the
C   two triangular parts of the element
C
      CALL CENTRD(X1, Y1, X2, Y2, X3, Y3, XABAH, YABAH)
      CALL CENTRD(X2, Y2, X3, Y3, X4, Y4, XBBAH, YBBAH)
C
C   calculate position of the centroid of the quadrilateral
C   element from the position of those of the triangles
C
      XBAH = ((ARA*XABAH) + (ARB*XBBAH)) / (ARA + ARB)
      YBAH = ((ARA*YABAH) + (ARB*YBBAH)) / (ARA + ARB)
      RETURN
      END
```

```
C                        SA3
C                       ------
      LOGICAL*1 FMT(1) /'*'/
      COMMON /PARMS/ WMOD, SIGFAL, CONSIS, SIGNOM
C
C Set up the program arrays
C   AVSTR holds the current value of the element av. stresses
C   ELFRAC holds element volumes expressed as a fraction
C          of the total volume totvol
C   ELSTR holds values of the current element stresses node
C         by node
C
      DIMENSION ELSTR(3,4), AVSTR(4), STFRAC(2,1200), ELFRAC(2,1200)
      DIMENSION ITOP(4), LIST(1200)
      LOGICAL*1 FILE1(20), FILE2(20), FILE3(20), FILE4(20)
      WRITE (6,10)
   10 FORMAT (' ', 'Name of file containing fractional volumes?')
      READ (5,20) FILE1
      CALL FTNCMD('ASSIGN 2=?;', 0, FILE1)
   20 FORMAT (20A1)
      WRITE (6,30)
   30 FORMAT (' ', 'Name of file containing element list?')
      READ (5,20) FILE2
      CALL FTNCMD('ASSIGN 3=?;', 0, FILE2)
      WRITE (6,40)
   40 FORMAT (' ', 'Name of file containing nodal stresses?')
      READ (5,20) FILE3
      CALL FTNCMD('ASSIGN 1=?;', 0, FILE3)
      WRITE (6,50)
   50 FORMAT (' ', 'Name of file for numerical output?')
      READ (5,20) FILE4
      CALL FTNCMD('ASSIGN 11=?;', 0, FILE4)
      CALL FTNCMD('ASSIGN 7=*SOURCE*;')
      WRITE (6,60)
   60 FORMAT (' ', /, 'Enter Compressive/Tensile strength ratio')
      READ (5,FMT) ALPHA
      WRITE (6,70)
   70 FORMAT (' ', /, 'Enter Nominal Stress')
      READ (5,FMT) SIGNOM
      WRITE (6,80)
   80 FORMAT (' ', /, 'Enter Weibull Modulus')
      READ (5,FMT) WMOD
C
C read in the fractional volumes node by node,counting the number
C and storing in IELCNT
C
      READ (2,FMT) TOTVOL
      DO 90 IELCNT = 1, 1201
        READ (2,FMT,END=100) (ELFRAC(J,IELCNT),J=1,2)
   90 CONTINUE
C
C Since it gets incremented before the read
C
  100 IELCNT = IELCNT - 1
      IF (IELCNT .GE. 1200) STOP 500
      WRITE (11,110) FILE3
  110 FORMAT (20A1)
```

```
      WRITE (11,120) IELCNT, TOTVOL, WMOD, SIGNOM, ALPHA
  120 FORMAT (' ', I6, 2X, F9.6, 2X, F4.1, 2X, E10.4, 2X, F4.1)
      WRITE (6,130)
      WRITE (6,120) IELCNT, TOTVOL, WMOD, SIGNOM, ALPHA
  130 FORMAT (' ', //, 'NUMELS   VOL   WEIBULL   NOMSTR   ALPHA')
C
C Get a list of the nodes in order from the nodes file
C
      DO 140 I = 1, 2000
        READ (1,FMT,END=150) LIST(I)
  140 CONTINUE
      REWIND 1
  150 IF (IELCNT .GE. 1200) STOP 500
  160 SVI = 0.0
  170 READ (3,FMT,END=220) IEL, IDUMMY, ITYPE
      BACKSPACE 3
      INODES = 3
      IF (ITYPE .NE. 36110 .AND. ITYPE .NE. 36100) INODES = 4
C
C Find the element and stresses
C
      CALL FINDEL(IEL, INODES, ITOP)
      CALL FINDSR(INODES, ITOP, ELSTR, LIST)
      AVSTR(1) = FLOAT(IEL)
      DO 190 K = 1, 3
        TOTAL = 0.0
        DO 180 ILINE = 1, INODES
          TOTAL = TOTAL + ELSTR(K,ILINE)
  180   CONTINUE
        AVSTR(K + 1) = TOTAL / INODES
  190 CONTINUE
C
C find averaged stresses over one element
C Now  evaluate the individual expressions in the integrand
C
      CALL EXPR(AVSTR(2), SIGNOM, WMOD, VALUE1, ALPHA)
      CALL EXPR(AVSTR(3), SIGNOM, WMOD, VALUE2, ALPHA)
      CALL EXPR(AVSTR(4), SIGNOM, WMOD, VALUE3, ALPHA)
C
C 'TERM' is the sum of the integrand contributions from the
C three principal stresses before multiplication by the
C fractional volume
C
      TERM = VALUE1 + VALUE2 + VALUE3
      CALL PTSUM(TERM, ELFRAC, PART, AVSTR, TOTVOL)
C
      DO 210 IE = 1, 4
        DO 200 IB = 1, 3
          ELSTR(IB,IE) = 0.0
  200   CONTINUE
  210 CONTINUE
C
C Accumulate the stress volume integral
C
      SVI = SVI + PART
C
C write out the results
C
      GO TO 170
```

```
  220 WRITE (7,240) SVI
      WRITE (11,230) SVI
  230 FORMAT (' ', E10.4)
  240 FORMAT (' ', ///, '***Stress Volume Integral=', E10.4, '***')
      STOP
      END



      SUBROUTINE EXPR(SIGMA, SIGNOM, WMOD, VALUE, RATIO)
C
C calculates the value of the individulal terms in the stress
C volume integral
C
      IF (SIGMA .LT. 0.0) GO TO 10
      GO TO 20
   10 H = -RATIO
      GO TO 30
   20 H = 1.0
   30 VALUE = (SIGMA/(SIGNOM*H)) ** WMOD
      RETURN
      END
C
C
C
C
      SUBROUTINE PTSUM(TERM, ELFRAC, PART, AVSTR, TOTVOL)
      COMMON /PARMS/ WMOD, SIGFAL, CONSIS, SIGNOM
C
C calculates the contribution to the stress volume integral
C of the element in question
C
      DIMENSION ELFRAC(2,1200), AVSTR(4)
      DO 10 I = 1, 1200
        IF (ELFRAC(1,I) .EQ. AVSTR(1)) GO TO 20
   10 CONTINUE
      WRITE(6,25)ELFRAC(1,I)
   25 FORMAT(1H ,'COULD NOT FIND ELEMENT  ',F8.1)
      STOP 500
   20 PART = TERM * ELFRAC(2,I)
      WRITE (11,30) ELFRAC(1,I), ELFRAC(2,I), PART
   30 FORMAT (' ', 2X, F6.0, 6X, E10.4, 6X, E10.4)
      RETURN
      END
C
C
C
C
      SUBROUTINE FINDEL(IEL, INODES, ITOP)
C
C retrieves the element topology for a given el. no. IEL
C
      DIMENSION ITOP(4)
      LOGICAL*1 FMT(1) /'*'/
   10 READ (3,FMT,END=20) ISAMP
      IF (ISAMP .NE. IEL) GO TO 10
```

```
      BACKSPACE 3
      READ (3,FMT) ISAMP, ID1, ID2, ID3, (ITOP(I),I=1,INODES)
   20 RETURN
      END
C
C
C
C
      SUBROUTINE FINDSR(INODES, ITOP, ELSTR, LIST)
C
C retrieves the stress values for nodes given in ITOP
C and places them in the array elstr
C
      DIMENSION ITOP(4), LIST(1200)
      LOGICAL*1 FMT(1) /'*'/
      DIMENSION ELSTR(3,4)
      ICALLS = 0
      DO 20 J = 1, 1201
C
C  (should be enough)
C
        DO 10 I = 1, INODES
          IF (LIST(J) .NE. ITOP(I)) GO TO 10
          ICALLS = ICALLS + 1
C
C J will contain the line number of the node in the file
C
          CALL COPYIT(J, ELSTR, I, ITOP(I))
          IF (ICALLS .LT. INODES) GO TO 20
          GO TO 30
   10   CONTINUE
   20 CONTINUE
   30 RETURN
   40 WRITE (6,50)
   50 FORMAT (' ', //, '********** ERRORIN FINDSR ********')
      STOP 500
      END
C
C
C
C
      SUBROUTINE COPYIT(J, ELSTR, I, NODE)
C
C copies the nodal stress into the right array entry
C J is the line in the file of the stress to copy
C I is the number of the node  on the copied element that we're
C
      LOGICAL*1 FMT(1) /'*'/
      DIMENSION ELSTR(3,4)
C
C direct access read
C
      JJJ = J * 1000
      READ (1'JJJ,FMT) IND, I2, D3, D4, D5, D6, (ELSTR(K,I),K=1,3)
      IF (IND .NE. NODE) GO TO 10
      RETURN
```

```
10 WRITE (6,20) NODE
20 FORMAT (' ', 'ERROR IN COPYIT, NODE', I7)
   RETURN
   END
```

```
C                                SA4
C                                ---
C Calculates the Failure Probabilities
C
      LOGICAL*1 FMT(1) /'*'/
      LOGICAL*1 FILE1(20), SFILE(20)
      WRITE (6,10)
   10 FORMAT (' ', 'File containing SVI.S?')
      READ (5,20) FILE1
   20 FORMAT (20A1)
      CALL FTNCMD('ASSIGN 3=?;', 0, FILE1)
      READ (3,30) SFILE
   30 FORMAT (20A1)
      READ (3,FMT) IELS, TOTVOL, WMOD, SIGNOM, ALPHA
      WRITE (6,40)
   40 FORMAT (' ', 'Unit Volume Failure Strength?')
      READ (5,FMT) SIGFAL
      GAM = GAMMA((1.0/WMOD) + 1)
      CONSIS = GAM ** WMOD
      WRITE (6,50) CONSIS
   50 FORMAT (' ', 'Material Consistency Factor', 2X, F6.3)
      SOVERS = (SIGNOM/SIGFAL) ** WMOD
      FACMUL = CONSIS * SOVERS * TOTVOL
      WRITE (6,60)
   60 FORMAT (' ', 'Element No.  Failure Prob')
      WRITE (6,70)
   70 FORMAT (' ', 'Calculate elemental failure probabilities(Y/N)')
      READ (5,80) ANS
   80 FORMAT (A1)
      CALL COMC(1, ANS, 'Y', IDIFF, &90, &90)
   90 DO 120 I = 1, IELS
        READ (3,FMT,END=150) ELEM, DUM, SVIC
        IF (IDIFF .EQ. 1) GO TO 120
        P = 1 - EXP(-FACMUL*SVIC)
  100   WRITE (6,110) ELEM, P
  110   FORMAT (' ', 3X, F7.1, 4X, F7.4)
  120 CONTINUE
      READ (3,FMT) SVI
      PFTOT = 1 - EXP(-CONSIS*SOVERS*TOTVOL*SVI)
      WRITE (6,130) PFTOT
  130 FORMAT (' ''*** Total failure propbability', F6.4, ' ***')
      WRITE (6,140) SFILE
  140 FORMAT (' ', /, 'Stress file was', 20A1)
  150 STOP
      END
```

APPENDIX VI

THE ATTEMPTED PHOTOELASTIC ANALYSIS

This section describes the unsuccesful attempt, mentioned in Chapter 8, to perform a photoelastic analysis of the mechanical stresses occurring in a graphite electrode. Funding was not available for a full three dimensional analysis, using a stress freezing technique, so a two-dimensional analysis was attempted. Fig. A6.1 shows the general arrangement.

The interelectrode tightening torque was simulated by tightening screw A, and electrode self-weight effects by hanging weights (B) along the bottom edge. There are several disadvantages to this type of model. Apart from the fact that the axisymmetric stress state is reduced to plane stress (the true stress state is axisymmetric), the large ratio of area to thickness of the model makes the possibility of warping under non-planar loads very real. Stresses so induced of course bear no resemblance to the true situation. Additionally, the method of simulating pretightening torque places a highly concentrated load at the centre of the nipple, which causes inaccuracies. These difficulties would not have occurred with a full three-dimensional model.

Construction of the model was begun by machining a two-dimensional cross-section of the nipple out of 1/4" (6mm) aluminium. A mould was then made (Fig. A6.2) and an

electrode 'female' was cast from silicone rubber. This was then used as a mould for pouring both an araldite nipple, and a silicone rubber nipple. The silicone rubber nipple was used to cast an electrode cross-section in araldite. From this procedure, a cross-sectional slice through both electrode and nipple was produced in araldite. Unfortunately, the finished mouldings were deficient in several respects, as described below.

(a) Examination of the casting in a polariscope showed that the residual stress level was very high.

(b) The electrode moulding could not be produced without cracking despite the use of the recommended releasing agent.

(c) The surface finish of both mouldings was poor and the thread tooth detail was marred by small air bubbles.

(d) Because of the uneven contraction of the araldite, the fit of the nipple in the electrode section was very poor.

Despite many attempts to recast the model, it was found impossible to eradicate all of these defects completely. In view of the fact that such a model is, in any case, a very poor approximation to the full three-dimensional stress field, and considering the difficulties referred to above, this experimental project was reluctantly abandoned.

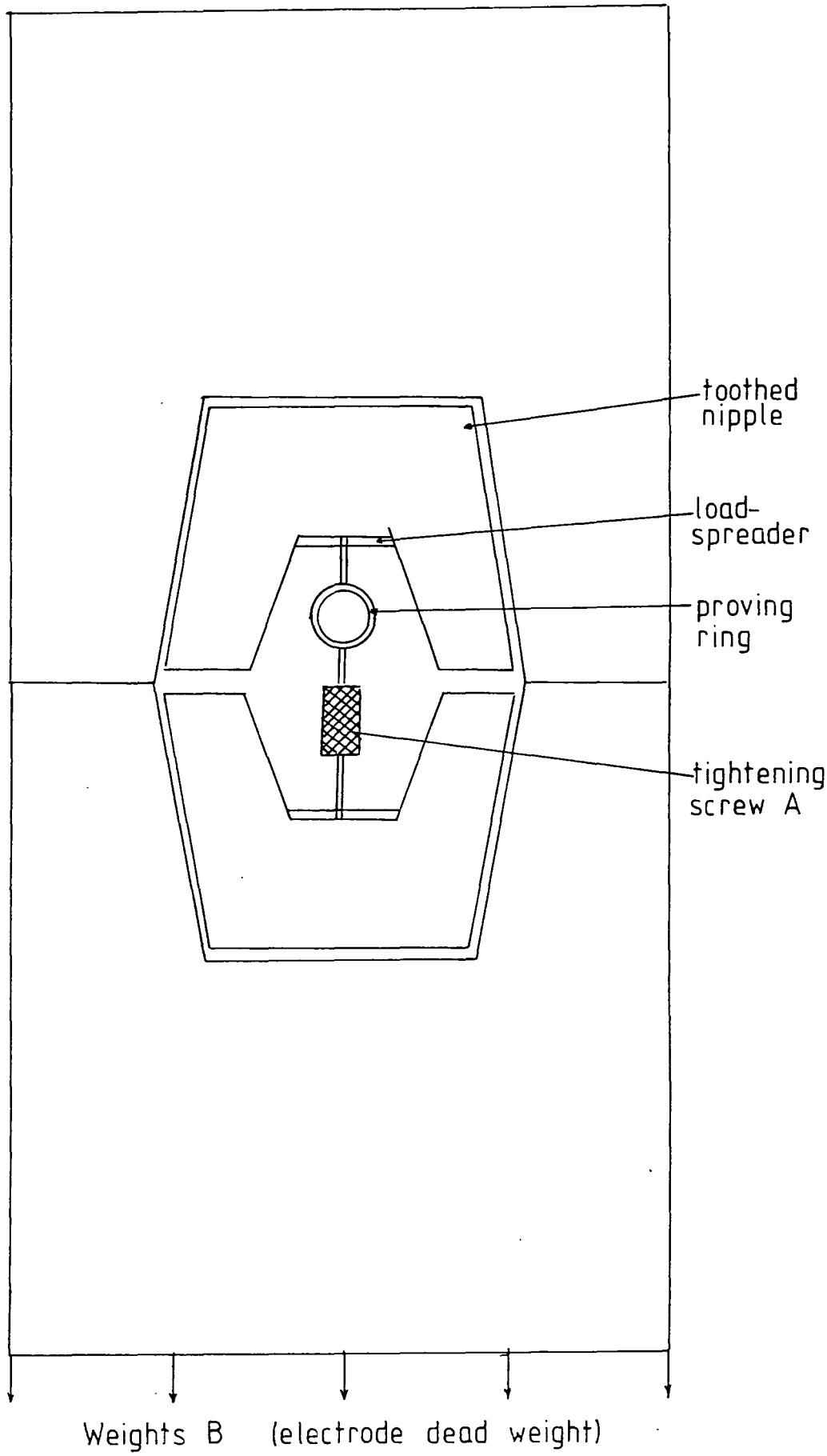

Fig A 6.1 Proposed Photoelastic Model

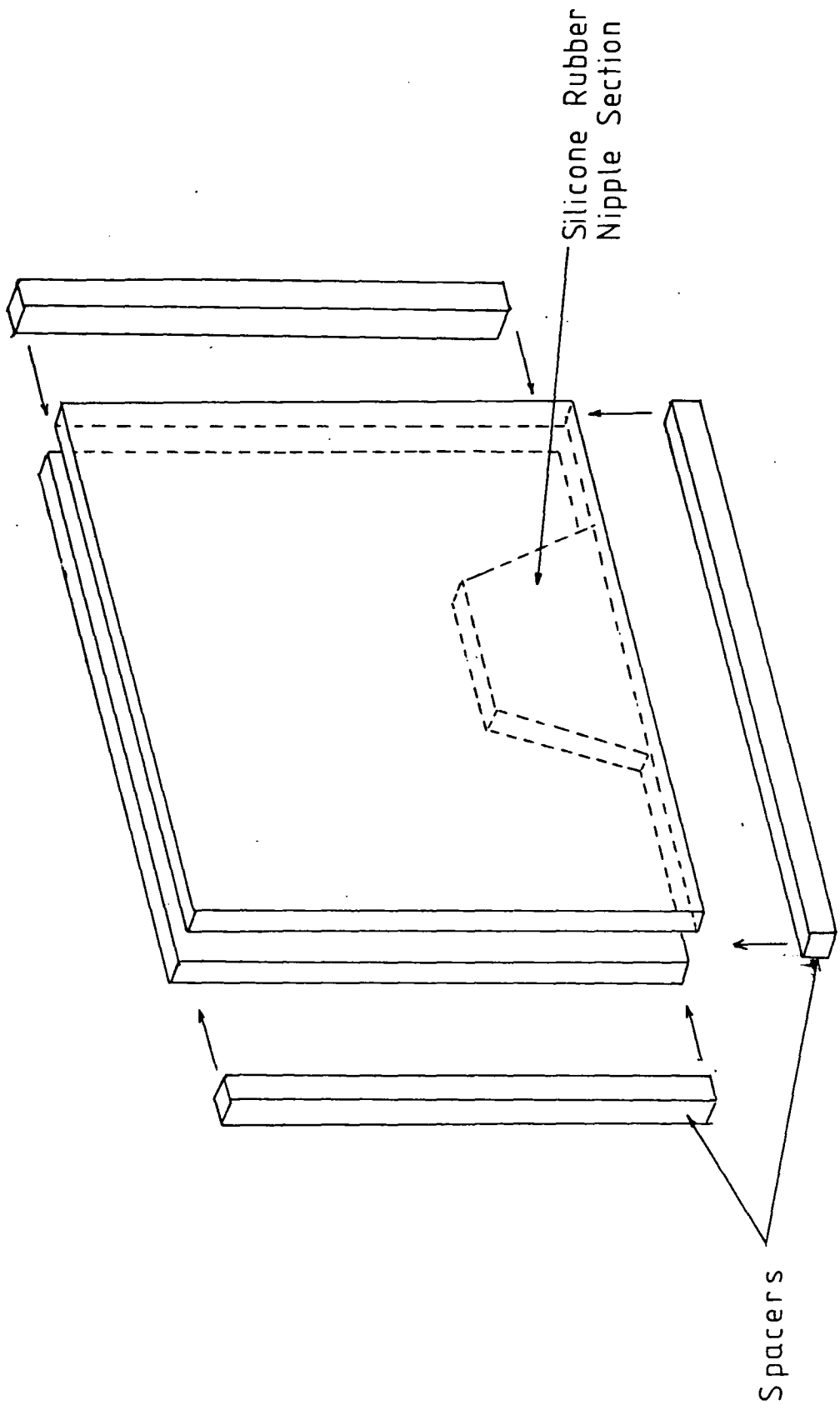

Fig A 6.2 Mould for casting Photoelastic Model

APPENDIX VII

ELECTROMAGNETIC FORCES ACTING UPON AN ELECTRODE

Consider an electrode triad carrying currents I_A, I_B and I_C and let

$$I_A = I_o \cos\omega t$$

$$I_B = I_o \cos(\omega t + 2\pi/3)$$

$$I_C = I_o \cos(\delta t + 4\pi/3)$$

i.e. currents of equal frequency and amplitude with phase differences of 120°.

Forces acting upon electrode A are due to B and C i.e. F_{AB} and F_{AC}, and are given by

$$F_{AB} = -\mu_o I_A I_B/(2\pi a) \quad N/m \quad A7.1$$

and

$$F_{AC} = -\mu_o I_A I_B/(2\pi a) \quad N/m \quad A7.2$$

where, for example, F_{AC} means 'the force on electrode A due to C'.

Resolving horizontally and vertically,

$$F_{A,x} = F_{AC}\cos 60 - F_{AB}\cos 60$$

where $F_{A,x}$ is the force on electrode A in the x-direction. Thus

$$F_{A,x} = (F_{AC} - F_{AB})/2$$

$$= -\mu_o I_A (I_C - I_B)/4\pi a \quad A7.3$$

and

$$F_{B,y} = F_{AC}\cos 30 + F_{AB}\cos 30$$

$$= \sqrt{3}(F_{AC} + F_{AB})/2$$

$$= -\sqrt{3}\mu_o I_A (I_C + I_B) \quad A7.4$$

Now,

$$(I_C - I_B) = I_o[\cos(\omega t + 4\pi/3) - \cos(\omega t + 2\pi/3)]$$

$$= -2I_o \sin(\omega t + \pi)\sin(\pi/3)$$

$$= I_o\sqrt{3}\sin\omega t \qquad \text{A7.5}$$

and

$$(I_C + I_B) = I_o[\cos(\omega t + 4\pi/3) + \cos(\omega t + 2\pi/3)]$$

$$= 2I_o \cos(\omega t + \pi)\cos(\pi/3)$$

$$= -I_o \cos\omega t$$

$$= -I_A \qquad \text{A7.6}$$

(as we would expect, since $I_A + I_B + I_C = 0$)

From A7.3 and A7.4 we obtain

$$F_{A,x} = -(\mu_o/4\pi a) I_o \cos\omega t . I_o\sqrt{3}\sin\omega t$$

$$= -(\sqrt{3}\mu_o I_o^2/4\pi a)\cos\omega t \sin\omega t$$

$$= -(\sqrt{3}\mu_o I_o^2/8\pi a)\sin 2\omega t \qquad \text{A7.9}$$

and

$$F_{A,y} = +(\sqrt{3}\mu_o/4\pi a) I_o \cos\omega t\ I_o \cos\omega t$$

$$= (\sqrt{3}\mu_o/4\pi a)\ I_o^2 \cos^2\omega t$$

$$= (\sqrt{3}\mu_o/8\pi a)\ I_o^2 (1 + \cos 2\omega t) \qquad \text{A7.10}$$

Let $F_o = (\sqrt{3}\mu_o I_o^2/8\pi a)$

then

$$F_{A,x} = F_o \sin 2\omega t$$

$$F_{A,y} = F_o(1 + \cos 2\omega t)$$

$$= F_o \qquad \text{A7.11}$$

We can thus consider the force on each electrode as a constant outward force of magnitude F_o, accompanied by a force rotating at 100 Hz, value $F_o \cos 2\omega t$.

—